THÈSE

Pour obtenir le grade de

DOCTEUR DE LA COMMUNAUTE UNIVERSITE GRENOBLE ALPES

Spécialité : **Chimie Physique Moléculaire et Structurale**

Arrêté ministériel : 25 mai 2016

Présentée par

Long LE QUANG

Thèse dirigée par **Jérôme CHAUVIN, Maître de Conférences, Université Grenoble Alpes**, et
codirigée par **Vincent MAUREL, Ingénieur de Recherche, CEA-Grenoble**

préparée au sein du **Département de Chimie Moléculaire**
dans **l'École Doctorale Chimie et Sciences du Vivant**

Nanomatériaux hybrides TiO$_2$/[Ru(bpy)$_3$]$^{2+}$ associés à [Cr(ttpy)$_2$]$^{3+}$ ou [Mn(ttpy)(CO)$_3$Br] ou au pyrrole: synthèse, études spectroscopiques et applications pour la conversion de l'énergie solaire

Thèse soutenue publiquement le **21 décembre 2017**
devant le jury composé de :

M. Cyrille TRAIN
Professeur, Université Grenoble Alpes   Président
Mme. Bélèn ALBELA
Maître de Conférences, Ecole Normale Supérieure de Lyon   Rapportrice
M. Fabien MIOMANDRE
Professeur, Ecole Normale Supérieure de Cachan   Rapporteur
Mme. Hynd REMITA
Directrice de Recherche, Université Paris-Sud   Examinatrice
M. Vincent MAUREL
Ingénieur de Recherche, CEA-Grenoble   Co-encadrant
M. Jérôme CHAUVIN
Maître de Conférences, Université Grenoble Alpes   Directeur de thèse

Acknowledgements

Table of contents

Chapter III: Chromium(III) bis-tolylterpyridine complexes as electron acceptors 75

3

List of abbreviations

A	Electron Acceptor
AFM	Atomic Force Microscopy
BNAH	1-benzyl-1,4-dihydronicotinamide
BPA	Benzylphosphonic acid
bpy	2,2'-bipyridine
CB	Conduction Band
CE	Counter Electrode
CV	Cyclic Voltammogram
D	Electron Donor
DMF	2,5-dimethylfuran
DFT	Density Functional Theory
EA	Elemental Analysis
EPD	Electrophoretic Deposition
EPR	Electron Paramagnetic Resonance
FRET	Forster Resonance Energy Transfer
FT-IR	Fourier transformed Infrared
FTO	Fluorine-doped Tin Oxide
FWHM	Full Width at Half Maximum
GC	Gas Chromatography
HOMO	Highest Occupied Molecular Orbital
HPLC	High-Performance Liquid Chromatography
IC	Internal Conversion
ISC	Intersystem Crossing
ITO	Indium Tin Oxide
KWW	Kohlrausch – Williams – Watts
LC	Ligand-Centered
LUMO	Lowest Unoccupied Molecular Orbital
MC	Metal-Centered
MeCN	Acetonitrile
MLCT	Metal-to-Ligand Charge Transfer

MS	Mass Spectroscopy
NMR	Nuclear Magnetic Resonance
NPs	Nanoparticles
PS	Photosensitizer
pyr	pyrrole
QCM-D	Quartz Crystal Microbalance with Energy Dissipation
RE	Reference Electrode
RT	Room Temperature
(FE)SEM	(Field-Emission) Scanning Electron Microscopy
TAS	Transient Absorption Spectroscopy
TBABF$_4$	tetrabutylammonium tetrafluoroborate
TBAP	tetrabutylammonium perchlorate
TBAPF$_6$	tetrabutylammonium hexafluorophosphate
TCSPC	Time-Correlated Single Photon Counting
TEOA	Triethanolamine
TEM	Transmission Electron Microscopy
TOF	Turnover Frequency
TON	Turnover Number
tpy	2,2':6',2"-terpyridine
ttpy	4'-(*p*-tolyl)-2,2':6',2"-terpyridine
UV-vis	Ultraviolet-visible
VB	Valence Band
WE	Working Electrode
XPS	X-ray Photoelectron Spectroscopy
XRD	X-ray Diffraction

CHAPTER 1

GENERAL INTRODUCTION

This thesis focuses on the use of TiO_2 nanoparticles (NPs) modified with a $[Ru(bpy)_3]^{2+}$ (bpy = 2,2'-bipyridine) photosensitizer (PS) and a functional complex / organic entity for applications in photocatalysis and photocurrent generation. TiO_2 is a semiconductor which has been extensively investigated in photocatalysis and photodegradation of organic pollutants in water. Here we propose to use TiO_2 NPs (i) as a platform to immobilize different entities proximally, and (ii) as an electron relay between immobilized redox PS and an electron acceptor (A) to obtain a $PS/TiO_2/A$ hybrid triad. In this thesis, $[Ru(bpy)_3]^{2+}$ is employed as the visible PS and a metal complex is used as the electron acceptor. $[Ru(bpy)_3]^{2+}$ is one of the most investigated redox PS, notably because of its good absorption in the visible domain, long-lived excited state and reversible redox properties in both oxidation and reduction. In this chapter we will first highlight some important properties of TiO_2 semiconductor and $[Ru(bpy)_3]^{2+}$ PS that are relevant to our studies. Afterwards, some examples of hybrid systems containing TiO_2, $[Ru(bpy)_3]^{2+}$ and a functional entity for photocatalytic applications will be presented.

I.1.   Semiconducting TiO₂ nanoparticles

TiO_2 is probably the most studied semiconductor, particularly in the field of photocatalysis. One of the earliest works on TiO_2 as a photocatalyst was dated back in 1921 by Renz[1]. The author observed a color change of TiO_2 powder from white to a darker color when TiO_2 was irradiated with sunlight in the presence of glycerol. In this section we will highlight some of the most important properties of TiO_2 semiconductor, together with a few relevant works using TiO_2 as a photocatalyst. We will not discuss the quantum confinement effect of TiO_2 as the NPs mentioned in this section are sufficiently large. For more information on the properties and applications of TiO_2 NPs, the reader is kindly referred to recent reviews by Burda[2], Henderson[3] and Fujishima[4].

I.1.1.   Crystal phases

Three main types of TiO_2 crystal phases are often mentioned in literature namely anatase, rutile and brookite. They can be described as distorted TiO_6 octahedra with different symmetries or arrangements (**Figure I-1**). In the anatase structure, two TiO_6 octahedra are connected via a common edge, whereas in rutile and brookite structures both corner and edge are shared between two TiO_6 units. As a result, the three structures differ in Ti-O bond length which plays a critical role in their electronic properties.
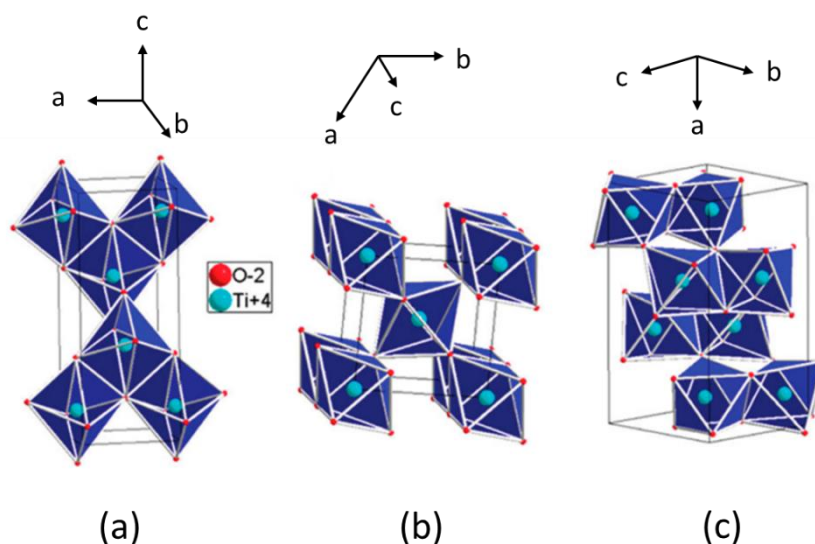
Figure I-1. Representation of TiO_2 crystal phases: (a) anatase: tetragonal, $a = 3.785$ Å, $c = 9.513$ Å; (b) rutile: tetragonal, $a = 4.593$ Å, $c = 2.959$ Å); (c) brookite: orthorhombic, $a = 9.181$ Å, $b = 5.455$ Å, $c = 5.142$ Å. Adapted from reference 2

The phase transformation in the bulk TiO_2 has been extensively studied by Diebold.[5] The author concluded that rutile is the only thermodynamically stable phase, while anatase and brookite are metastable and can be transformed to rutile when heated. However, the phase stability of TiO_2 NPs heavily depends on the particle size. For example, in the range of 325-750 ^{0}C, anatase is the most stable phase for particles smaller than 11 nm, brookite is the most stable phase for particles with diameter from 11 nm to 35 nm, and rutile is the most stable phase for particles larger than 35 nm.[6]

I.1.2. Photophysical properties of TiO_2 particles

The electronic structure of a semiconductor consists of a valence band (VB) and a conduction band (CB). They are separated by a bandgap where there are no electron states. The bandgap thus corresponds to the energy difference between the upper edge of the VB and the lower edge of the CB. In the ground state, all the electrons are located in the VB. Upon absorption of a photon with energy higher than the bandgap, an electron can be promoted to the CB, leaving a positively charged hole in the VB. Consequently, the material becomes conductive due to the electrons in the CB.[4] When the electron and hole recombine, a photon can be emitted. The positions of the CB and VB of several semiconductors are shown in **Figure I-2**.
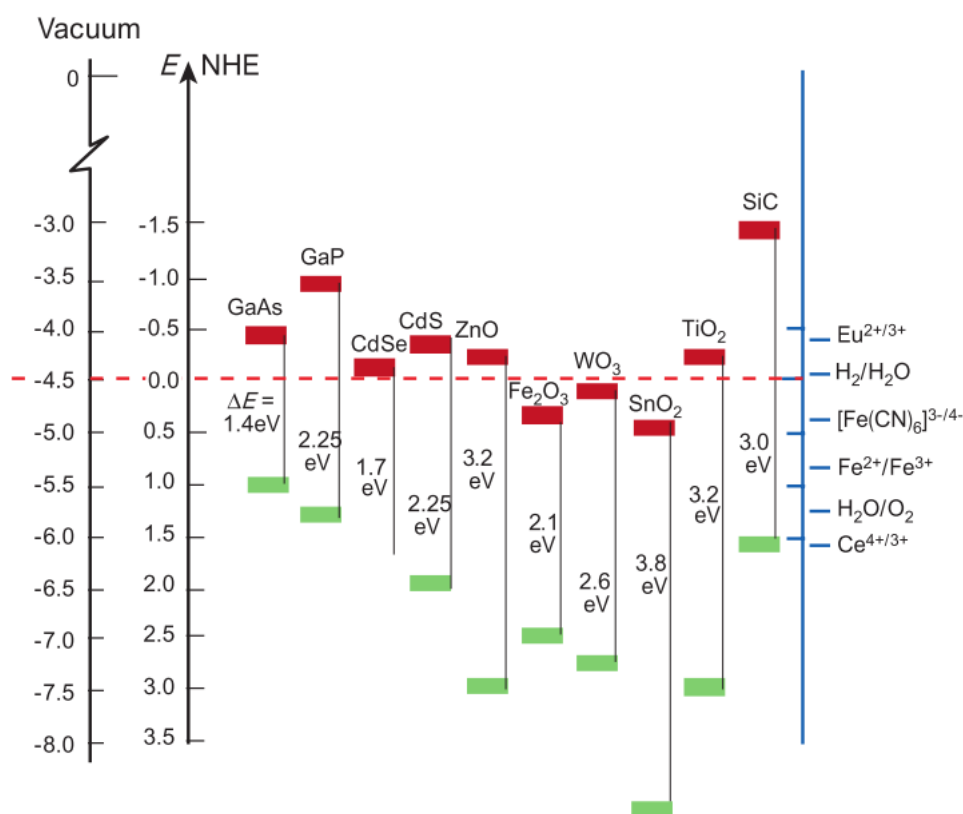
Figure I-2. Positions of the upper edge of the valence band (green) and the lower edge of the conduction band (red) of several semiconductors in contact with aqueous electrolyte at pH 1. Adapted from reference 7

The bandgap of bulk TiO_2 depends on the crystal phase. Anatase and rutile phases show a bandgap E_g = 3.2 eV and 3.0 eV, respectively.[3] The bandgap in anatase and rutile phases is also indirect and direct, respectively. The bandgap in brookite is reported in the range of 3.1-3.4 eV[8] and is indirect[2]. A direct bandgap corresponds to the promotion of an electron from the VB to the CB without changing its momentum, whereas an indirect bandgap requires a change in the electron momentum. Consequently, when the electron and hole recombine, a photon is directly emitted in the rutile phase, while in the anatase phase the electron needs to pass through an intermediate state to transfer the momentum to the crystal lattice. The intermediate state is also referred as "electron trap" or "hole trap", which is located inside the bandgap at energy levels higher or lower than the Fermi level $E_F = (E_{CB} + E_{VB})/2$, respectively. The traps are induced by crystal defects, which create extra states inside the bandgap.[2] In the anatase phase, the recombination between CB electrons and trapped holes to emit photons is conventionally referred as "type 1" emission, while the recombination between trapped electrons and VB holes is called "type 2" emission. Both type 1 and type 2 emissions depend strongly on the energy of the defect sites, meaning the way to synthesize TiO_2 particles. Usually the emission wavelength maximum is observed at ~ 550 nm for anatase phase and ~ 840 nm for rutile phase.[2] **Figure I-3** schematically describes the photon

absorption and emission processes in anatase and rutile phases. It is noted that the two phases only differ in the position of the CB and not the VB.[9]
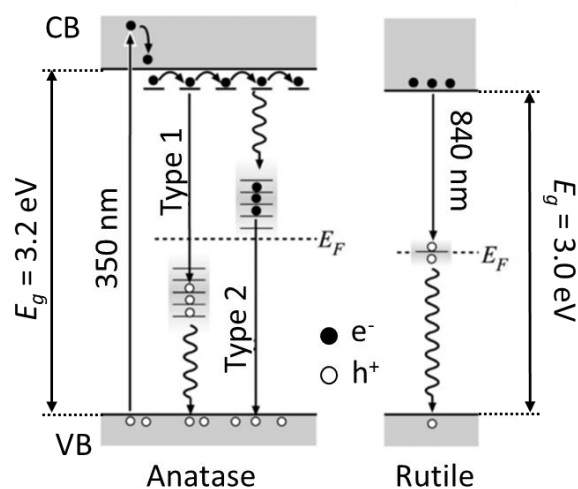
Figure I-3. Representation of the photon absorption and emission of TiO_2 in anatase and rutile phases. Straight and wavy lines indicate radiative and non-radiative decays, respectively. Adapted from reference 2

Direct observations of CB electrons, trapped electrons and trapped holes can be achieved with a variety of spectroscopic techniques. For example, infrared (IR) spectroscopy can detect the CB electrons, and electron paramagnetic resonance (EPR) spectroscopy can be used to observed trapped holes in oxygen atoms (denoted as $O^{\bullet-}$) and trapped electrons in Ti atoms (denoted as Ti^{3+}).[2]

Dynamics of these charge carriers has also been studied with transient absorption spectroscopy (TAS). Tamaki et al.[10] reported that upon the bandgap excitation, photo-induced holes are trapped within 100 fs at sites near the surface of anatase TiO_2 NPs, while photo-induced electrons are first trapped at shallow sites near the surface before relaxing into deeper trapping sites in the bulk within ~ 500 ps. Kinetics of the charge recombination is complicated. An early work by Gratzel et al.[11] in 1987 showed that the radiative recombination occurs within 30 ns for anatase TiO_2 colloid with diameter smaller than 12 nm. Recombination rate also depends on the size of TiO_2 NPs and the number of e^-/h^+ pairs that have been generated, meaning the power of the excitation light. For example, the recombination rate was estimated at 1×10^{11} $cm^3.s^{-1}$ for 2 nm anatase NPs and 3×10^7 $cm^3.s^{-1}$ for 27 nm NPs.[3] Another approach to study the charge recombination process was reported by Colbeau-Justin et al.[12] using time-resolved microwave photoconductivity method. The authors concluded that there is a competition between a fast recombination process and a fast trapping process of a part of the charge carriers in anatase. The trapping process reduces the number of holes, thus increases the lifetime of the electrons on the CB. All of these information are

important for the applications of TiO_2 as a photocatalyst. Generally, a fast excitation rate and a slow charge recombination rate are required so that the electrons and holes will have enough time to react with substrates in solution.

I.1.3.   TiO₂ as a photocatalyst

As mentioned above, the photoexcitation of TiO_2 results in the free electrons and holes as well as $O^{\bullet-}$ radicals, which are all reactive. They offer TiO_2 capability to reduce or oxidize a variety of organic and inorganic species on the surface of the NPs. We choose three types of reactions, namely water oxidation, CO_2 reduction and decomposition of aqueous pollutants, where TiO_2 NPs have been tested as a photocatalyst.

❖ *Water oxidation reaction*

Light-induced water splitting reaction consists of two half-reactions: oxidation of water to O_2 at the photoanode and reduction of water to H_2 at the photocathode. As shown in **Figure I-2**, it is thermodynamically more favorable for the positively charged holes on the TiO_2 CB to oxidize water than for the CB electrons to reduce water. The water (or OH^-) oxidation by VB holes can occur as follows:

$$4\,h^+ \; + \; 2\,H_2O \; \rightarrow \; O_2 \; + \; 4\,H^+$$
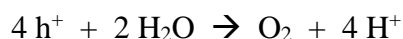
The first attempt to construct a photoelectrochemical cell for water splitting was proposed in 1972 by Fujishima and Honda using a n-type TiO_2 electrode as photoanode and a Pt counter electrode.[13] Under UV light, the holes generated on the VB of TiO_2 are used to oxidize water whereas the electrons on the CB are collected through an external circuit to the Pt electrode where protons are reduced to form H_2. Despite the fact that the process is highly thermodynamically favorable, no publication has shown direct experimental evidence for the water oxidation reaction on TiO_2. It has been proposed that the required nucleophilic attack of water to a trapped surface hole is not achieved.[3] The mechanism of the water oxidation reaction by TiO_2 photocatalyst was investigated by Kavan, Gratzel et al.[9] using anatase $TiO_2(101)$ and rutile $TiO_2(001)$ single crystal deposited onto an electrode. An anodic current was observed when the electrodes were irradiated with UV light at zero bias. Cyclic voltammograms were taken in the dark for the electrodes before and after they were exposed to UV irradiation. The authors observed an irreversible cathodic peak in the CVs of both anatase and rutile electrodes after UV light exposure, which was attributed to the reduction of a surface-bound peroxide intermediate. However, no exhaustive water oxidation experiment was mentioned.

❖ *CO₂ photoreduction*

Although many works on the photoreduction of CO_2 have been made based on TiO_2, they require a co-catalyst or thermal activation of TiO_2 and not the direct photoexcitation of TiO_2.[3] The only publication using TiO_2 as a photocatalyst to reduce CO_2 was conducted by Anpo et al.[14] The authors studied anatase TiO_2 NPs and rutile NPs in the presence of CO_2 + H_2O gas mixture. UV irradiation of the solid TiO_2 NPs at 275 K resulted in the formation of CH_4 as the main product together with traces of C_2H_4 and C_2H_6 in the gas phase. These gas products were not present without the UV light. The photocatalytic activity of TiO_2 was found to depend on the crystal phase and particle size of TiO_2 NPs, as well as the ratio of CO_2/H_2O in the gas phase. **Table I-1** summarizes the amount of CH_4 produced and some relevant characteristic parameters of these TiO_2 photocatalysts. The anatase phase was found to be more catalytically active than the rutile phase for small NPs. Increasing the particle size to several hundred nanometers lead to the decrease in the amount of CH_4, probably due to the reduced surface area and, consequently, reduced number of available sites for CO_2 molecules to be adsorbed.

Table I-1. Summary of the photocatalytic reduction of CO_2 using TiO_2 NPs mentioned in reference 14

Catalyst*	Crystal phase	Particle size (nm)	Surface area (m².g⁻¹)	CO₂ adsorbed (μmol.g⁻¹)	Bandgap (eV)	Amount of CH₄ (μmol.h⁻¹.g⁻¹)
JRC-TIO-2	Anatase	400	16	1	3.47	0.03
JRC-TIO-3	Rutile	30-50	51	17	3.32	0.02
JRC-TIO-4	Anatase	21	49	10	3.50	0.17
JRC-TIO-5	Rutile	640	3	0.4	3.09	0.04

* Japan TiO_2 reference catalyst

❖ *Decomposition of aqueous pollutants*

A wide variety of aqueous pollutants can be decomposed by TiO_2 particles under UV irradiation, such as alkanes, aliphatic alcohols, carboxylic acids, alkenes, aromatics, polymers, surfactants, herbicides, pesticides and dyes.[4] The decomposition of pollutants occurs via the formation of highly oxidative hydroxyl ($OH^•$) and hydroperoxyl ($HO_2^•$) radicals in water following the UV irradiation of TiO_2 (**Scheme I-1**). These radicals can oxidize organic compounds to CO_2 and H_2O.

$$TiO_2 \ (Ti^{4+}\text{-}OH^-) \ + \ h\nu \ \longrightarrow \ Ti^{3+} \ + \ OH^{\bullet}$$

$$Ti^{3+} \ + \ O_2 \ \longrightarrow \ Ti^{4+}\text{-}O_2^{\bullet-}$$

$$Ti^{4+}\text{-}O_2^{\bullet-} \ + \ H_2O \ \longrightarrow \ Ti^{4+}\text{-}OH^- \ + \ HO_2^{\bullet}$$
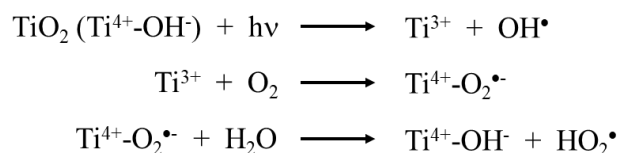
Scheme I-1. Generation of $OH^{\bullet}$ and $HO_2^{\bullet}$ radicals in water by photoinduced e^- and h^+ on TiO_2

Only UV light and O_2 are required for this type of photocatalysis; the reactions can occur at room temperature. However, the quantum yield and efficiency depend on many factors such as the crystal phase and size of TiO_2 photocatalyst, concentration, pH, light intensity, etc.[4] For example, when studying the quantum yields of liquid-solid photocatalytic reactions using TiO_2 slurry catalysts, Serpone et al.[15] found that the maximum quantum yield was obtained with low light intensity and high substrate concentration. The maximum quantum yield of 14 % was reached at 365 nm for phenol degradation using Degussa P25 TiO_2 NPs (rutile/anatase = 3/1, $d = 25$ nm) at pH 3.

To summarize, although TiO_2 shows some photocatalytic activities, it only works under UV light and the selectivity is low. The visible domain of the solar spectrum is not efficiently utilized. To address the former issue, an additional PS capable of absorbing visible light can be anchored on TiO_2 NPs to better harvest the solar light. A suitable PS is $[Ru(bpy)_3]^{2+}$, which will be described in **Section I.2**. Meanwhile the selective issue can be solved by incorporating a more efficient and selective catalyst onto the surface of TiO_2 NPs. This TiO_2/catalyst system will be mentioned in **Section I.3**.

I.2. Ru(II) tris-bipyridine: a prototypical photosensitizer

A PS is a molecule capable of absorbing photons, leading to an excited state which is able to interact with its surrounding media. The $[Ru(bpy)_3]^{2+}$ (**Figure I-4**) has been one of the most studied PS in the last decades due to its excellent properties such as chemical stability, redox reversibility, long-lived excited state and strong luminescence. In this section we will discuss in detail about these properties, which are fundamental for further studies in this thesis.
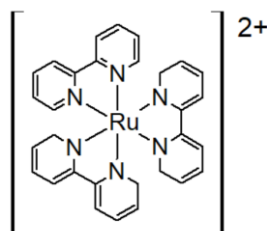
Figure I-4. Molecular structure of $[Ru(bpy)_3]^{2+}$ photosensitizer

I.2.1. Electrochemical properties

The redox properties of $[Ru(bpy)_3]^{2+}$ complex was first studied with cyclic voltammetry by Matsumoto et al.[16] in MeCN solution containing tetraethylammonium perchlorate (TEAP) as electrolyte (**Figure I-5**). In the anodic part, a reversible one-electron oxidation wave is observed at $E_{1/2} = 1.25$ V *vs* NHE which is attributed to the metal oxidation to Ru^{III} species with a low spin $4d^5$ configuration.[17] In the cathodic part, three successive one-electron reduction processes are observed, with the first one centered at around -1.40 V *vs* NHE. All the added electrons are localized on the bpy ligands.[17] No ligand dissociation has been reported. Therefore, the $[Ru(bpy)_3]^{2+}$ PS exhibits rich and reversible redox properties.
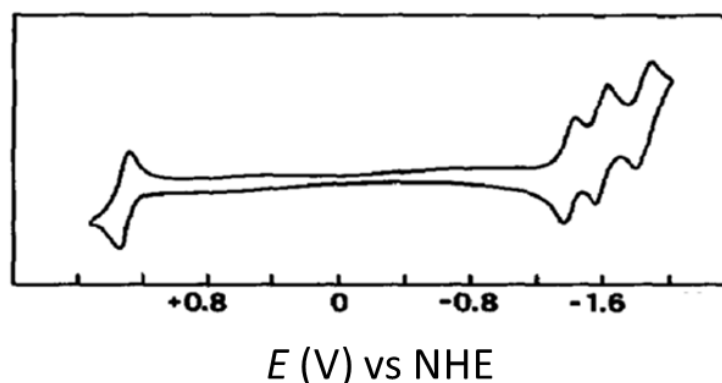
Figure I-5. Cyclic voltammogram (CV) of $[Ru(bpy)_3]^{2+}$ in MeCN + 0.2 M TEAP (tetraethylammonium perchlorate) solution. Adapted from references 16,17

I.2.2.   Photophysical properties

As described by Balzani et al.[18], Ru^{2+} has the d^6 electronic configuration, while the polypyridine ligands are usually colorless molecules possessing σ donor orbitals localized on the nitrogen atoms and π donor and $π^*$ acceptor orbitals more or less delocalized on aromatic rings. In the $[Ru(bpy)_3]^{2+}$ complex, the bpy ligands are high field, thus inducing the configuration shown in **Figure I-6a**, where the valence electrons are distributed on the $t_{2g}(M)$ orbitals. Upon photon absorption in the visible region of the spectrum, a singlet metal to ligand charge transfer (^1MLCT) state is populated which corresponds to the transfer of an electron from the metal-centered (MC) $t_{2g}(M)$ orbital (HOMO) to the ligand-centered (LC) $π^*(L)$ orbital (LUMO). This electron transfer is accompanied by a fast intersystem crossing to change the spin state, resulting in the first triplet state ^3MLCT with a quantum efficiency of 1 (**Figure I-6b**). This new excited state can be deactivated via either photon emission (called phosphorescence), or non-radiative decay (loss of heat), or through the population of a triplet metal-centered (^3MC) state. The latter state is non-emissive and can give rise to the loss of a bpy ligand.[19]
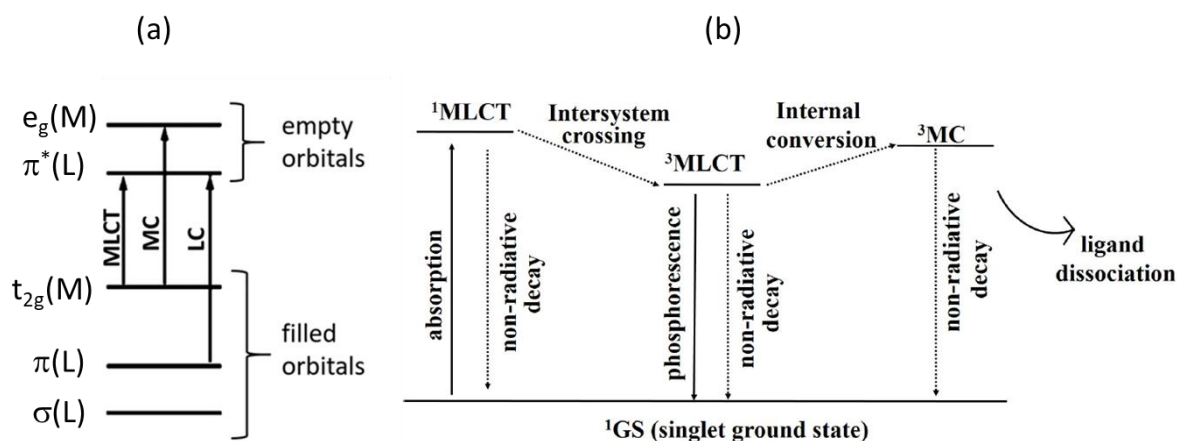
Figure I-6. (a) Simplified molecular orbital diagram of octahedral Ru(II) polypyridine complexes with arrows indicating electronic transitions occuring in the UV-vis region.[18] (b) Simplified Jablonski diagram indicating radiative and non-radiative decays of the excited states of Ru(II) polypyridine complexes.[20] MLCT = metal-to-ligand charge transfer, MC = metal-centered transition, LC = ligand-centered transition, GS = ground state.

To characterize the excited state, it is important to introduce two parameters namely lifetime $τ$ and emission quantum yield $φ$. They are defined by the following equations:[18]

$$\tau = \frac{1}{k_r + k_{nr}}$$
(Eq I-1)

$$\phi = \frac{k_r}{k_r + k_{nr}}$$
(Eq I-2)

where k_r and k_{nr} are the rate constants of radiative and non-radiative decays, respectively.

The UV-vis absorption and emission spectra of $[Ru(bpy)_3]^{2+}$ are shown in **Figure I-7** together with proposed assignments for the electronic transitions.[17] In the absorption spectrum (**Figure I-7a**), the strong band at 285 nm is assigned to spin allowed LC $\pi \rightarrow \pi^*$ transition. The two broad bands at 240 nm and 450 nm are attributed to the MLCT d $\rightarrow \pi^*$ transitions. The shoulders at 322 and 344 nm are assigned to the MC d $\rightarrow$ d transitions. Excitation of $[Ru(bpy)_3]^{2+}$ in any of its absorption bands leads to the emitting ^{3}MLCT state. This emission is centered at around 600 nm where its energy, intensity and lifetime are dependent on the temperature and the solvent (**Figure I-7b**). In deaerated acetonitrile and at room temperature the lifetime of this luminescence is estimated to be around 1 µs with a quantum yield of $\Phi_{em}=$ 0.06.
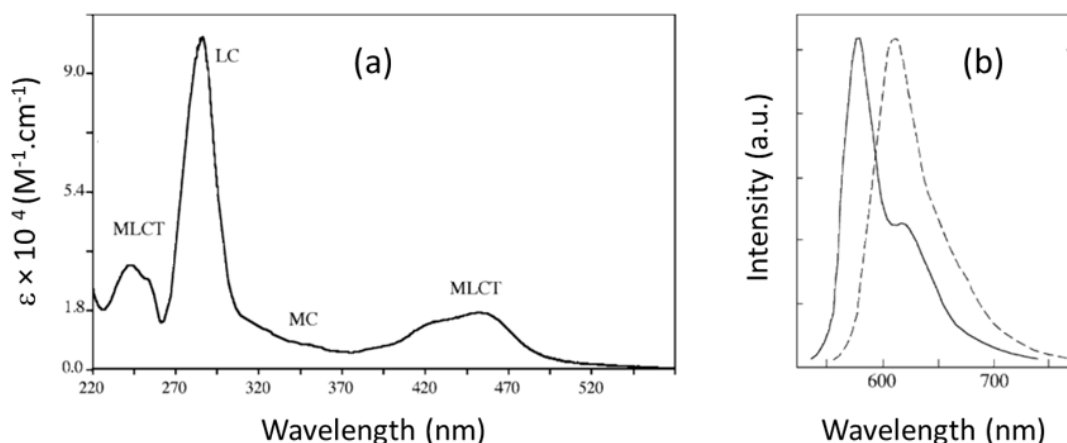
Figure I-7. (a) Electronic absorption spectrum of $[Ru(bpy)_3]^{2+}$ in alcoholic solution. (b) Emission spectrum of $[Ru(bpy)_3]^{2+}$ in alcoholic solution at 77 K (solid line) and room temperature (dashed line). Adapted from reference 18

I.2.3.   Quenching of the $[Ru(bpy)_3]^{2+*}$ excited state

In the presence of suitable electron donors (D) and acceptors (A), the ^{3}MLCT excited state of $[Ru(bpy)_3]^{2+}$ can take part in bimolecular reactions resulting in the quenching of its luminescence. The quenching reaction is governed by the nature of the quenchers. It can occur via an energy transfer reaction, oxidative or reductive quenching reaction as follows:

$[Ru(bpy)_3]^{2+*} + Q \rightarrow [Ru(bpy)_3]^{2+} + Q^*$ Energy transfer

$[Ru(bpy)_3]^{2+*} + Q \rightarrow [Ru(bpy)_3]^{3+} + Q^-$ Oxidative quenching

$[Ru(bpy)_3]^{2+*} + Q \rightarrow [Ru(bpy)_3]^{+} + Q^+$ Reductive quenching
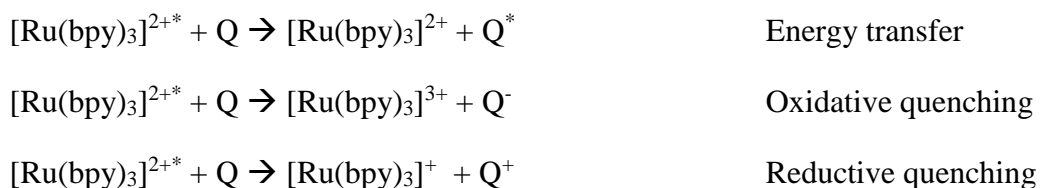
I.2.3.1. Photo-induced energy transfer mechanisms

The energy transfer can be described by different mechanisms that involve either radiative or non-radiative transition between two excited states. A prerequisite for the energy transfer to occur is a good overlap between the emission spectrum of the donor and the absorption spectrum of the acceptor. The energy of the excited state of the donor should be higher than that of the acceptor. The energy transfer can occur via either Dexter[21] or Forster[22] mechanisms (**Figure I-8**).
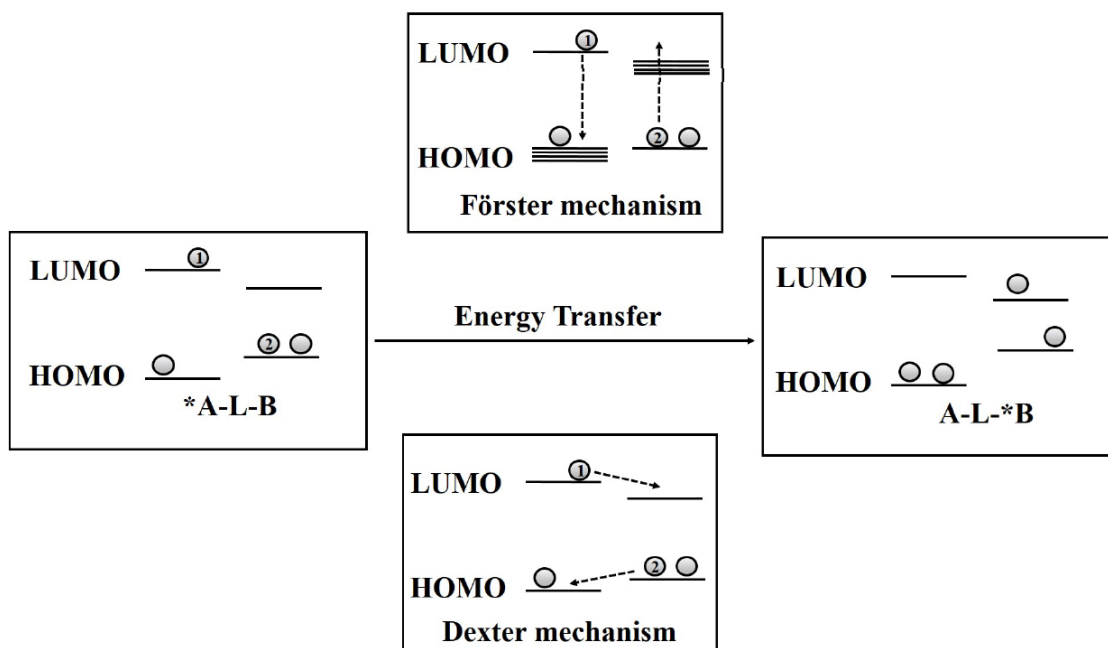
Figure I-8. Illustration of the Forster and Dexter energy transfer mechanisms[23]

The Dexter mechanism, also known as the exchange mechanism, involves a double electron exchange between the donor and the acceptor molecules. An electron moves from the LUMO of the donor to the LUMO of the acceptor, accompanied by a simultaneous electron transfer from the HOMO of the acceptor to the HOMO of the donor. This electron exchange requires a strong overlap between the orbitals of the donor and the acceptor, hence it strongly depends on the nature of the linker connecting the two entities. The rate constant of the Dexter energy transfer process k_{Dexter} depends on the distance r between the donor and the acceptor as described by **Equation I-3**:[21]

$$k_{Dexter} \propto KJ \exp(-\beta r) \qquad\qquad\qquad \text{(Eq I-3)}$$

where K is related to specific orbital interactions, J is the normalized spectral overlap integral between the emission spectrum of the donor and the absorption spectrum of the acceptor, and β is the attenuation factor which is specific for each linker.

The Forster mechanism, also called Coulombic mechanism, is a long range mechanism, which means that there is no requirement for a physical contact between the donor and the acceptor. In this context, the electronic nature of the linker between the donor and the acceptor, if present, does not affect the energy transfer rate. The rate constant of the Forster energy transfer process $k_{Forster}$ is expressed by **Equation I-4**:[22]

$$k_{Forster} \propto \frac{J\phi_D}{\tau_D r^6} \qquad \text{(Eq I-4)}$$

where ϕ_D and τ_D are the emission quantum yield and luminescence lifetime of the donor, r is the distance between the donor and the acceptor.

I.2.3.2. *Photo-induced electron transfer mechanisms*

Electron transfer reactions involve an exchange of electron(s) between two molecules in which one is oxidized while the other is simultaneously reduced. Photo-induced electron transfer reactions are only possible when the redox potentials of the two molecules are well aligned so that the overall process is thermodynamically favorable ($\Delta G < 0$). The process is governed by the redox potential of the excited state of the PS and the oxidation / reduction potential of the electron donor / acceptor, respectively. The redox potential of the PS excited state is estimated by the Rehm-Weller equation:[24]

$$E_{1/2}^{*\ ox} = E_{1/2}^{\ ox} - E_{00} \qquad \text{(Eq I-5)}$$

$$E_{1/2}^{*\ red} = E_{1/2}^{\ red} + E_{00} \qquad \text{(Eq I-6)}$$

where $E^*_{1/2}$ is the reduction or oxidation potential of the excited state, $E_{1/2}$ is the reduction or oxidation potential of the ground state and E_{00} is the difference in energy between the zeroth vibrational states of the ground and excited states. The values of $E_{1/2}$ can be experimentally determined from a cyclic voltammetry experiment. The zero-zero excitation energy E_{00} is usually approximated by the emission energy E_{em} of the compound at 77 K (**Figure I-9**). As an approximation, E_{00} value can be estimated from the emission energy at room temperature in the case of $[Ru(bpy)_3]^{2+*}$ excited state. The Rehm-Weller equations can be re-written as follows:

$$E(Ru^{III}/Ru^{II*}) = E(Ru^{III}/Ru^{II}) - \frac{hc}{\lambda_{em,77\,K}e} \approx E(Ru^{III}/Ru^{II}) - \frac{1240}{\lambda_{em,RT}(nm)} \qquad \text{(Eq I-7)}$$

$$E(Ru^{II*}/Ru^{I}) = E(Ru^{II}/Ru^{I}) + \frac{hc}{\lambda_{em,77\,K}e} \approx E(Ru^{II}/Ru^{I}) + \frac{1240}{\lambda_{em,RT}(nm)} \qquad \text{(Eq I-8)}$$

where h is the Planck's constant, c is the speed of light in vacuum, e is the charge of an electron, $\lambda_{em,77\ K}$ and $\lambda_{em,RT}$ are the emission wavelength maximum at 77 K and room temperature, respectively.
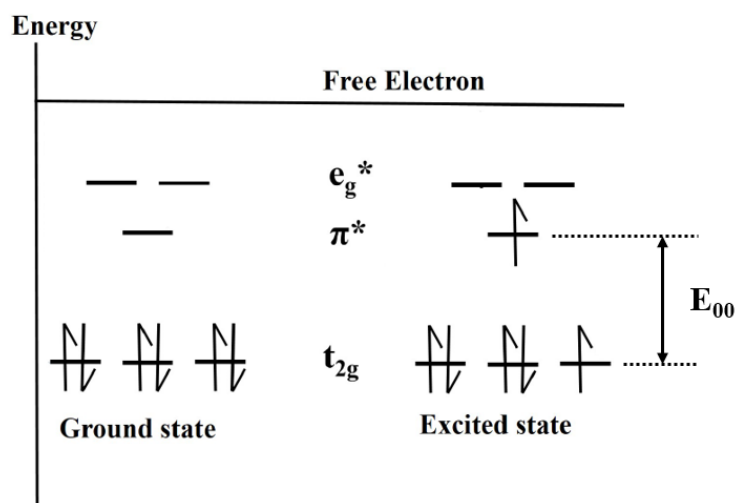
Figure I-9. Electronic configuration of the $[Ru(bpy)_3]^{2+}$ complex in ground state and excited state

After calculation of the potentials of all the redox couples which could be involved, a first approximation of the exergonicity of the photo-induced electron transfer process can be evaluated using the derived equation by Weller:[25]

$$\Delta G = e\left[E_{ox}(D) - E_{red}(A)\right] - E_{00} - \frac{e^2}{4\pi\varepsilon_0\varepsilon_s R_C} - \frac{e^2}{8\pi\varepsilon_0}\left(\frac{1}{r_{D^+}} + \frac{1}{r_{A^-}}\right)\left(\frac{1}{37.5} - \frac{1}{\varepsilon_s}\right) \quad \text{(Eq I-9)}$$

In this equation, ΔG represents the free enthalpy of the reaction, $E_{ox}(D)$ and $E_{red}(A)$ are the oxidation potential of the donor and the reduction potential of the acceptor respectively, ε_s is the solvent dielectric constant, r_{D^+} and r_{A^-} are the ionic radii and R_C is the center-to-center separation distance between the donor and the acceptor. E_{00} is the singlet or triplet state energy determined by the emission maximum at 77 K. The third term represents the Coulombic interaction between the two charged moieties. The last term corrects the difference in the ion-pair solvation in which the redox potentials were measured. This expression can be also written in a more simplified form as follows:

$$\Delta G = -nF\left[E_{1/2}^{ox}(D)^* - E_{1/2}^{red}(A)\right] \text{ or } \Delta G = -nF\left[E_{1/2}^{ox}(D) - E_{1/2}^{red}(A)^*\right] \quad \text{(Eq I-10)}$$

where $E_{1/2}^{ox}(D)^*$ or $E_{1/2}^{red}(A)^*$ is the excited state potential of the photosensitizer, corresponding to the oxidative or reductive quenching of the photosensitizer excited state, respectively. If $\Delta G < 0$, the photo-induced electron transfer reaction is thermodynamically favorable.

I.2.4. Anchoring functional groups to graft a metal complex onto a surface

Grafting a metal complex onto a surface can be achieved by modifying the complex ligands with suitable anchoring groups, which depend on the nature of the surface. **Table I-2** summarizes some common anchoring groups reported in literature for several surfaces such as TiO_2, Au, SiO_2, ZrO_2 and ITO. The surfaces can be either a macroelectrode or NPs.

Table I-2. Common anchoring groups for various surfaces

Surface	Anchoring groups	References
TiO_2	Phosphonic acid $R–PO_3H_2$	26
	Carboxylic acid R-COOH	27
	Catechol Ph-$(OH)_2$	27
Au	Thiol R-SH	28
SiO_2	Silane $R_3–SiH$	29
	Phosphonic acid $R–PO_3H_2$	30
ZrO_2	Phosphonic acid $R–PO_3H_2$	26
	Silane $R-SiH_3$	31
ITO	Phosphonic acid $R–PO_3H_2$	32
	Carboxylic acid R-COOH	33

In this thesis, we focus on using the TiO_2 NPs as a platform to immobilize different species (PS, D, A). Although some early works about grafting $[Ru(bpy)_3]^{2+}$ PS on TiO_2 NPs employed carboxylic acid,[34] in recent years the phosphonic acid has emerged as a more suitable anchoring group. Since the pioneering work by Gao et al.[26] in 1996, numerous publications have been made using phosphonic acid to graft different species onto TiO_2 NPs.[30] Herein, we summarize some critical details for the grafting of a species onto TiO_2 NPs using the phosphonic acid groups.

On a computational point of view, the binding mode between $–P(O)(OH)_2$ and TiO_2 surface is still on debate. Using phosphonic acid as a model to study the grafting on anatase and rutile TiO_2, Luschtinetz et al.[35] concluded that the bidentate mode was more stable than the tridentate one. However, Nilsing et al.[36] claimed that the most stable mode of binding was the monodentate when they used another computational method. It is also experimentally challenging to distinguish between the three binding modes.

On an experimental point of view, a recent publication by Hirsch et al.[27] compares the adsorption process of different derivatives of phosphonic acid or carboxylic acid on TiO_2

anatase NPs ($d \sim 34$ nm). Thermogravimetric analysis (TGA) was employed to quantitatively determine adsorption parameters. **Figure I-10** shows some structures mentioned in this publication. **Table I-3** summarizes important adsorption parameters such as monolayer grafting density θ, adsorption constant K_{ads} and free binding energy ΔG.
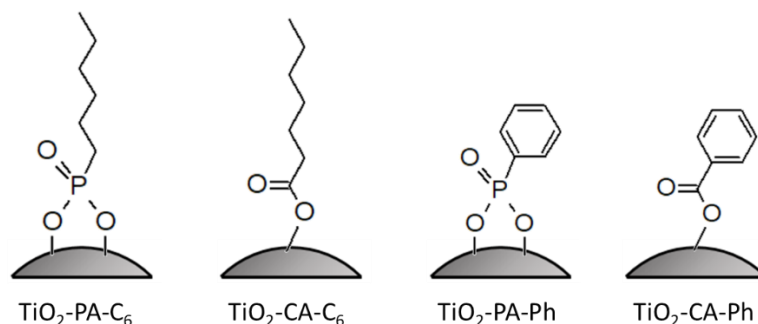
Figure I-10. Structures of some derivatives of phosphonic anc carboxylic acids anchored on TiO$_2$ NPs[27]

Table I-3. Calculated adsorption parameters: monolayer grafting density θ, adsorption constant K_{ads} and free binding energy ΔG mentioned in reference 27

System	θ (nm^{-2})	K_{ads} (M^{-1})	ΔG (kJ.mol^{-1})
TiO$_2$-PA-C$_6$	3.2	6092	-21.6
TiO$_2$-CA-C$_6$	4.6	253	-13.7
TiO$_2$-PA-Ph	3.1	6811	-21.9
TiO$_2$-CA-Ph	4.6	141	-12.3

As shown in **Table I-3**, the grafting density is slightly lower when phosphonic acid is used to graft the species on TiO$_2$ instead of carboxylic acid. However, the phosphonic acid groups exhibit significantly stronger bonds with the surface as indicated by the adsorption constant K_{ads} and free energy ΔG. Negligible differences are found when a phenyl or a hexyl chain is grafted on TiO$_2$ NPs. This work provides experimental evidence for the advantages of using phosphonic acid as anchoring group compared with carboxylic acid.

I.2.5. Photo-induced charge transfer processes on TiO$_2$ NPs sensitized with [Ru(bpy)$_3$]$^{2+}$

In this section we will highlight some relevant studies on the kinetics of photo-induced charge transfer processes on TiO$_2$ NPs modified with [Ru(bpy)$_3$]$^{2+}$ PS (denoted as TiO$_2$/Ru^{II}). The TiO$_2$/Ru^{II} NPs can be either dispersed in colloidal solutions or deposited on a nanocrystalline TiO$_2$ thin film electrode. The carboxylic or phosphonic acid is used as anchoring group. For a comprehensive overview in this topic, the reader is kindly referred to

several excellent reviews for studies in colloidal solutions[37,38] and on mesoporous thin film electrodes[2,38]

I.2.5.1. *In colloidal solutions*
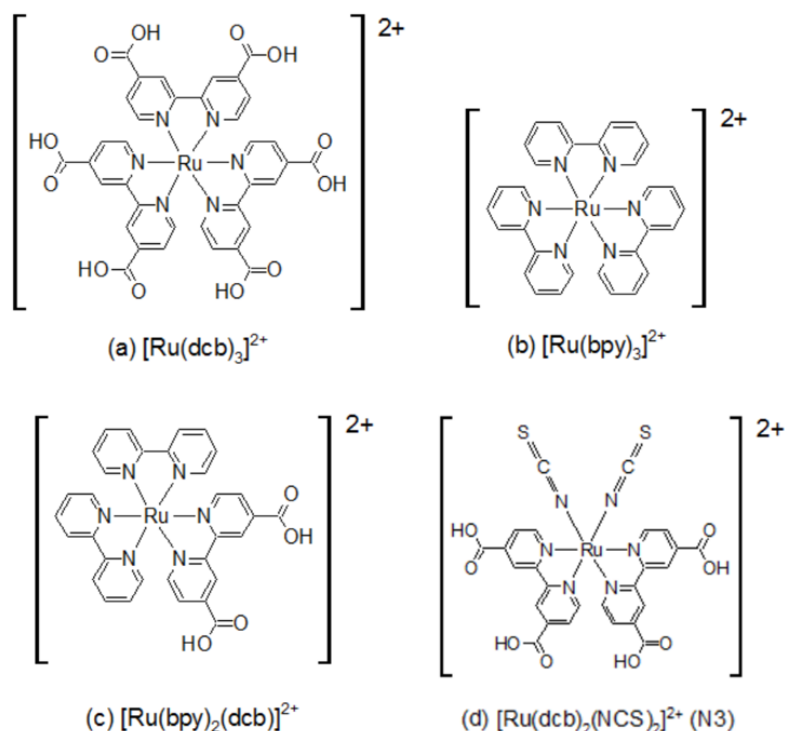
Scheme I-2. Photosensitizers described in **Section I.2.5.1**.

One of the pioneering works on the kinetics of photo-induced charge transfer processes in TiO_2/Ru^{II} colloidal solution was published by Desilvestro et al.[34] The authors grafted $[Ru(dcb)_3]^{2+}$ (dcb=2,2'-bipyridine-4,4'-dicarboxylic, **Scheme I-2a**) on anatase TiO_2 NPs ($d = 6$ nm) and studied the charge transfer in aqueous solution at pH 2 by means of time-resolved emission and transient absorption spectroscopies (TAS). Following an excitation at 530 nm, TiO_2/Ru^{II*} exhibited a rate of electron injection to TiO_2 of 3.2×10^7 s^{-1}. The acidic media of $2.5 < pH < 6$ allowed for the existence of the complex. In comparison, a mixture of $[Ru(bpy)_3]^{2+}$ (**Scheme I-2b**) and TiO_2 NPs did not show any quenching of the excited state Ru^{II*} in acidic solution. At pH 10 $[Ru(bpy)_3]^{2+}$ could be physisorbed to TiO_2 due to electrostatic interaction between the cation dye molecules and negatively charged surface. The electron injection rate was significantly slower, at only 1.5×10^5 s^{-1}. The recombination rate of $(e^-)TiO_2$ and Ru^{3+} was similarly slow in both cases, around 4×10^5 s^{-1}. The work emphasized the importance of covalently linking the dye to TiO_2 semiconductor to enhance the electron injection to TiO_2.

Argazzi et al.[39] reported a long-lived charge separated state when they irradiated $TiO_2/[Ru(bpy)_2(dcb)]^{2+}$ (**Scheme I-2c**) NPs in aqueous solution at pH 2. The emission of

$[Ru(bpy)_2(dcb)]^{2+*}$ was efficiently quenched by electron injection to TiO_2 colloids with $k_{inj} >$ 5×10^7 s^{-1} and $> 80\%$ efficiency. Back electron transfer occurred in a microsecond time scale, with $k_b \sim 10^5$ - 10^6 s^{-1}. In the presence of phenothiazine (PTZ) as an electron donor, the oxidized dye was efficiently reduced at a rate of $k_D = 3 \times 10^8$ s^{-1} before the back electron transfer with $(e^-)TiO_2$. The charge separated state $(e^-)TiO_2$ and PTZ^+ remained stable in a millisecond lifetime.

The nature of photo-induced, trapped electrons on anatase TiO_2 sites (Ti^{3+}) has been investigated by Rittmann-Frank et al.[40] using X-ray Absorption Spectroscopy. A $[Ru(dcb)_2(NCS)_2]^{2+}$ dye (Dye N3, **Scheme I-2d**) was anchored on 20-nm anatase TiO_2 colloidal solution. The trapping sites, located on the surface, were shown to be completely populated within 70 ps. The lifetime of the trapped electrons was found to be slightly higher for dye-sensitized TiO_2 NPs than bare TiO_2, lying on a nanosecond time scale. Two types of surface trapping sites were distinguished as sixfold- and fivefold-coordinated Ti^{3+} sites located at energies of 1.6 eV and 1.2 eV below the CB respectively.

I.2.5.2. On TiO₂ mesoporous thin film electrodes

(a) $[Ru(dcb)_2(\mu\text{-}(CN)Ru(CN)(bpy)_2)_2]^{6+}$

(b) $[Ru(bpy)_2(bpy\text{-}(PO_3H_2)_2)]^{2+}$

(c) $[Ru(bpy)_2(bpy\text{-}(CH_2\text{-}PO_3H_2)_2)]^{2+}$

(d) $[Ru(bpy)_{3-x}(bpy\text{-}(CH_2\text{-}PO_3H_2)_x)]^{2+}$, x = 1, 2, 3
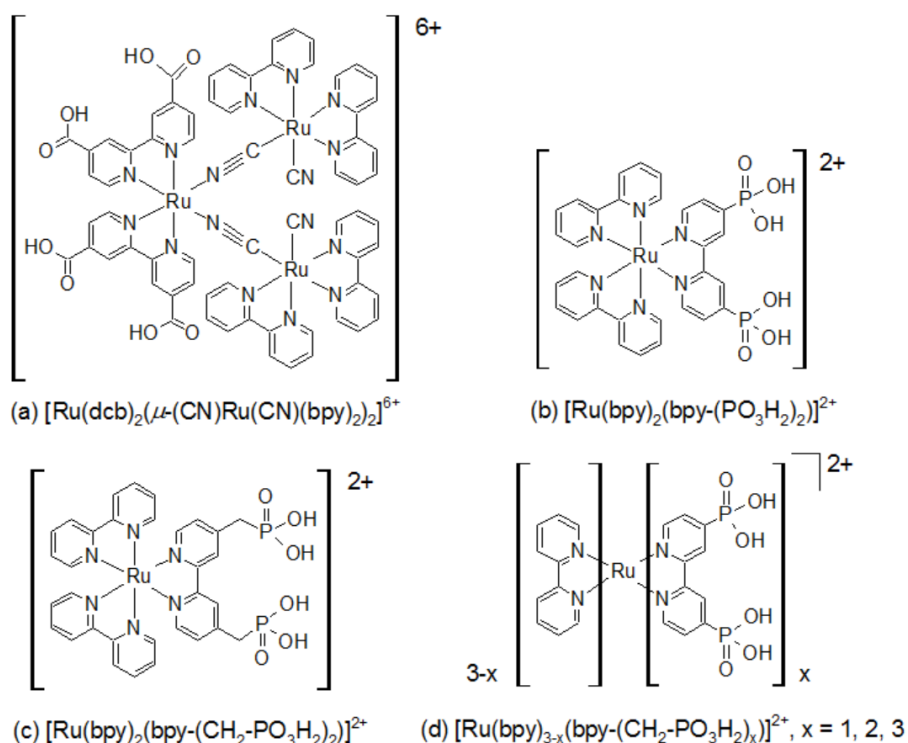
Scheme I-3. Photosensitizers described in **Section I.2.5.2**.

The breakthrough in mesoporous, nanocrystalline TiO_2 thin film electrodes sensitized with a metal complex dye is the report by O'Regan and Gratzel in 1991,[41] where they deposited a monolayer of $[Ru(dcb)_2(\mu\text{-}(CN)Ru(CN)(bpy)_2)_2]^{6+}$ complex (**Scheme I-3a**) on 10-μm thick layer of TiO_2 NPs. The modified electrode combined the high area surface of the

film and excellent UV-vis absorption properties of the dye to yield an incident photon-to-current efficiency (IPCE) of > 80 % and light-to-electric energy conversion of > 7 %, together with great stability. The rate of charge injection was estimated to exceed 10^{12} s^{-1} in this photovoltaic cell, while that of complex decomposition was smaller than 2×10^4 s^{-1}.

Since the O'Regan and Gratzel's paper, there have been numerous extensive studies on the photo-induced kinetics of dye-sensitized solar cells (DSSC). Wang et al.[42] constructed a series of conducting, rigid-rod linkers to immobilize $[Ru(bpy)_3]^{2+}$ on TiO$_2$ NPs thin films to study the dependence of charge transfer processes on the distance between Ru^{2+} sites and the semiconductor. The interfacial electron transfer was strongly pH-dependent: $k_{inj} > 10^8$ s^{-1} (pH 1, unable to be time-resolved) and $k_{inj} = 1 \times 10^7$ s^{-1} (pH 11). The injection quantum yield was found to decrease as the distance increased. Back electron transfer was, on the contrary, independent of the linker length, remaining at ~ 5×10^5 s^{-1}.

Gillaizeau-Gauthier et al.[43] reported the adsorption of $[Ru(bpy)_2(bpy-(PO_3H_2)_2)]^{2+}$ and $[Ru(bpy)_2(bpy-(CH_2-PO_3H_2)_2)]^{2+}$ (**Scheme I-3b and c**) on nanocrystalline TiO$_2$ thin film electrodes. Electron injection kinetics was found to be > 10^8 s^{-1} while the recombination occurred on a millisecond time scale in MeCN + 0.1 M LiClO$_4$ under Ar. The quantum yield of the electron injection was less than unity, which was attributed to the competition between electron injection and vibrational relaxation of the excited state of the Ru-dye on the same time scale. The additional methylene group induced a decrease in the electron injection quantum yield associated by an increase in the lifetime of the $[Ru(bpy)_3]^{2+*}$ excited state. The methylene group also shifted the redox potential of Ru^{III}/Ru^{II} to 100 mV less positive.

Hanson et al.[44] studied the effect of the phosphonic anchoring group on the charge recombination process. The authors prepared a series of $[Ru(bpy)_3]^{2+}$ dyes bearing 2, 4 or 6 phosphonic groups (**Scheme I-3d**) and studied the TiO$_2$/$[Ru(bpy)_3]^{2+}$ thin film electrodes by means of TAS in deaerated 0.1 M HClO$_4$ aqueous solution. As the number of phosphonic groups increased, the electro- and photochemical stability of the dye-sensitized film were enhanced while the electron injection quantum yield was reduced. The recombination process for each dye followed a multiexponential kinetics, from which an average lifetime of ~ 10 µs was found regardless of the number of phosphonic groups.

The mechanism of charge injection and recombination of an adsorbed dye on TiO$_2$ has been reviewed in detail by Sang et al.[2] The injection may occur via two pathways, named after the sequential steps leading to the charge injection: (i) excitation-electron transfer, or (ii) excitation-relaxation of excited state-electron transfer. The former, called "hot injection", can occur without any intersystem crossing (ISC) relaxation of the excited dye because the charge

injection is kinetically faster than the ISC. The electron injection usually occurs on the fs-ps time scale, with multiexponential kinetics. The latter pathway occurs from a less energetic configuration of the excited state of the dye, which has been formed after ISC. Followed the injection, charge recombination at the TiO_2 surface has been described as a non-trivial process where the distribution of the injected electrons should be taken into consideration. Two models have been proposed: random flight model and localized distribution model. The former describes a homogeneous distribution of trapped electrons on the surface, while the latter relies on the trapped sites in the vicinity of the excited dye. Experimental studies showing a size-independent charge recombination rate seem to support the latter model.[45]

Benko et al.[46] studied the mechanism and kinetics of electron injection from N3 dye to TiO_2 nanocrystalline film by femtosecond polarization spectroscopy. Following the photoexcitation of the dye-sensitized film, the electron injection which occurred directly from the ^{1}MLCT delocalized excited state was too fast to be observed, suggesting a sub-hundred femtosecond process. The injection from the ^{3}MLCT state of the attached bpy was also not detectable. The slower component of the injection occurred from the thermalized triplet excited state in a multiexponential fashion with time constants ranging from 1 to 50 ps. This slower process results from an excited state localized on a bpy ligand of the Ru(II) dye that is not attached to the TiO_2 surface. This electron needs to be first transferred to the attached bpy ligand by interligand charge transfer (ILCT) and then injected to TiO_2. ILCT efficiency is claimed to control the triplet channel of electron transfer from the dye. It can be changed by chemical modification of the bpy ligand and by the solvent. **Scheme I-4** illustrates the discussed charge injection pathways from the N3 dye to TiO_2 film. Therefore, localization of the initially photoexcited electron from the MLCT state and its orientation with respect to the semiconductor surface play an important role in the kinetics of electron injection.
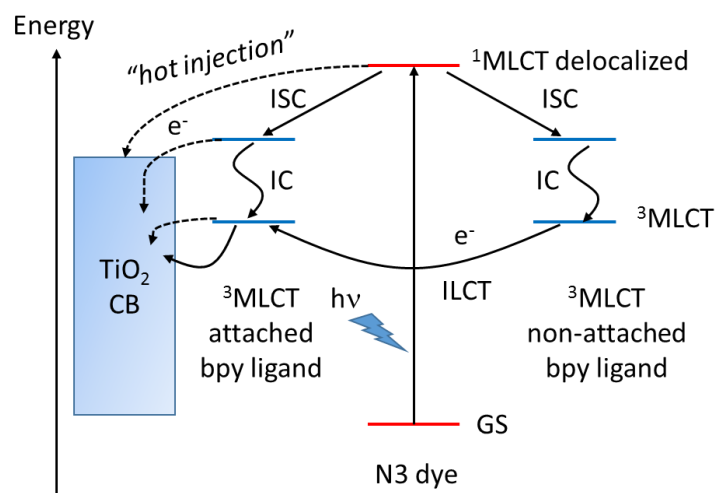
Scheme I-4. Schematic model for electron injection from $[Ru(dcb)_2(NCS)_2]^{2+}$ (N3) dye to TiO_2 nanocrystalline film. GS = ground state, MLCT = metal-to-ligand charge transfer, ILCT = interligand charge transfer, ISC = intersystem crossing, IC = internal conversion, CB = conduction band. Reproduced from reference 46

The size of TiO_2 NPs has been shown to be critical for the kinetics of electron injection.[47] Using N3 dye anchored on a 15-µm thick layer of TiO_2 NPs with various diameters, the authors studied the photo-induced charge separation and recombination processes by means of time-resolved emission spectroscopy and femtosecond TAS. The injection rates lied on ps-ns time scale for all the sizes, but the injection efficiency significantly decreased from ∼ 90 % (diameter < 50 nm) to 30-70 % (diameter > 50 nm). The drop was attributed to the dye aggregation in the space between the large particles. This work highlights the importance of using small TiO_2 NPs (d < 50 nm) to achieve good injection efficiency.

To summarize, the photo-induced charge transfer processes on TiO_2/Ru^{II} dyads have been well studied in colloidal solution and on mesoporous thin film electrodes. In recent years the phosphonic acid to anchor Ru dyes on TiO_2 NPs has gained more attention due to its higher stability than carboxylic acid. However, to the best of our knowledge, there is no publication on the photo-induced charge transfer process in solution when the phosphonic acid is used. We are interested in this topic as it is fundamental for further charge transfer studies in this thesis when another component like an electron donor or acceptor is also immobilized on TiO_2/Ru^{II} NPs.

I.3. Incorporation of a catalyst on TiO₂/Ru^II nanoparticles

As mentioned at the end of **Section I.1**, the photocatalytic reactions induced by TiO_2 suffer from low yields and low selectivity. Therefore, a catalyst can be anchored on TiO_2 NPs for obtaining desired products. For example, a hybrid system comprising metal oxide NPs functionalized with the enzyme carbon monoxide dehydrogenase (CODH) and $[Ru(bpy)_3]^{2+}$ visible PS was synthesized for CO_2 photoreduction (**Scheme I-5**).[48] Under irradiation at λ > 420 nm, the $Ru^{II}/TiO_2/CODH$ hybrid system produced CO as the only product. Anatase and anatase/rutile (3/1) TiO_2 exhibited significantly higher catalytic activity than ZnO and $SrTiO_3$ semiconductors. Meanwhile, the triad based on rutile TiO_2 showed absolutely no activity for the CO_2 reduction. It was attributed to the CB of rutile (-0.32 V *vs* SHE at pH 6) being lower than the CO_2/CO reduction potential (-0.46 V *vs* SHE at pH 6). The alignment of the semiconductor CB with the redox potentials of the PS and the catalyst is shown to be critical for the photocatalytic CO_2 reduction.
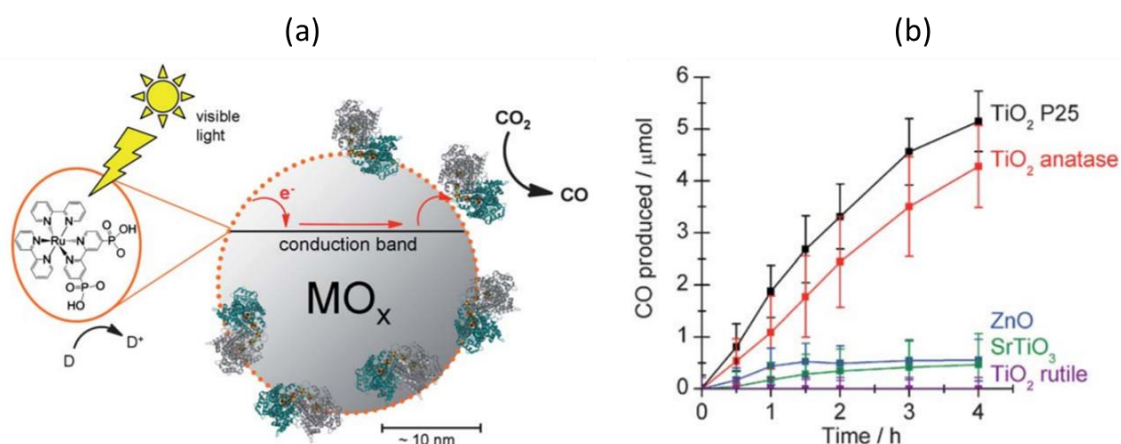
Scheme I-5. (a) Structure of the $Ru^{II}/MO_x/CODH$ hybrid system: MO_x is either TiO_2 (P25), anatase TiO_2, rutile TiO_2, ZnO or $SrTiO_3$ NPs; D is a sacrificial electron donor (2-(*N*-morpholino)ethanesulfonic acid. (b) CO production under visible irradiation using various MO_x substrates.

From a molecular approach, Durrant, Reisner et al.[49] have proposed to graft $[Ru(bpy)_3]^{2+}$ as a PS and cobaloxime as a catalyst on TiO_2 NPs (**Scheme I-6**) for proton reduction reaction. This reaction requires two electrons to produce H_2. Using transient absorption spectroscopy and time-resolved emission spectroscopy, the authors showed that the electron transfer from the Ru^{II*} excited state and Co^{III} site occurs through the conduction band (CB) of TiO_2. The long-lived charge separated state $Ru^{III}/(e^-)TiO_2/Co^{III}$ ($\tau_{1/2}$ ~ 400 ms) allowed the Co^{III} sites to be reduced by the CB electrons of TiO_2. However, there were no experimental evidences for the accumulation of two electrons on the Co^{III} site, although it

should occur as the H_2 product was obtained ($TON_{max} \sim 110$, $TOF = 15\ h^{-1}$) under visible irradiation in the presence of triethanolamine (TEOA) as a sacrificial electron donor.
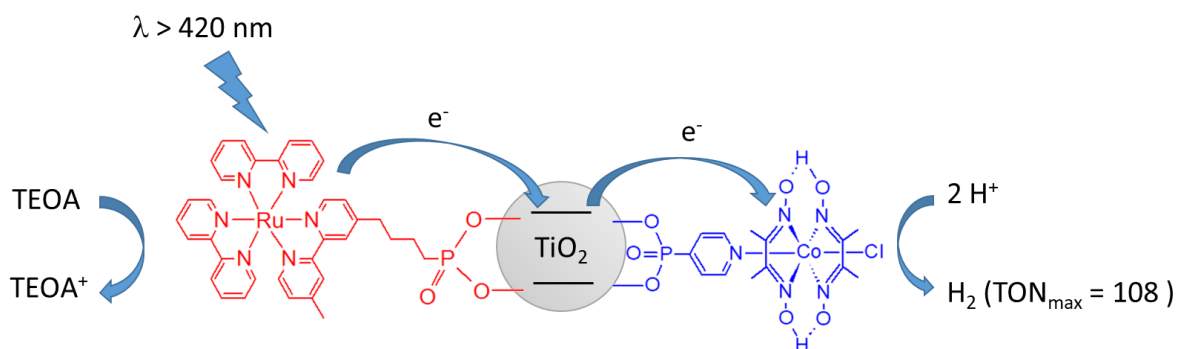
Scheme I-6. Structure of $Ru^{II}/TiO_2/Co^{III}$ (Ru:Co = 3:1 % mol)

This study gives an example for the co-adsorption of a PS and a catalyst on TiO_2 NPs and its photocatalytic application. Similar hybrid systems working as photocatalysts for water oxidation, proton and/or CO_2 reductions can be found in the introduction section of **Chapters 3 and 4**.

I.4.   Scope of this thesis

As mentioned above, since TiO_2 only absorbs UV light, a large portion of the solar spectrum in the visible domain is not efficiently harvested. As $[Ru(bpy)_3]^{2+}$ shows good absorption of visible light, we aim to anchor this PS onto TiO_2 NPs to better harvest light in the solar spectrum. In this case TiO_2 will act as an electron acceptor for the $[Ru(bpy)_3]^{2+*}$ excited state. Due to the advantages of the phosphonic acid anchoring group mentioned above, the $[Ru(bpy)_3]^{2+}$ is functionalized with this group to graft on TiO_2 surface. Under visible light, a charge separated state $(e^-)TiO_2/Ru^{III}$ should occur. In this thesis we aim to use the electrons stored on the CB of TiO_2 NPs or the holes on the Ru^{III} complex to drive specific redox reactions. This thesis is divided into four chapters as follows:

Chapter 2 will focus on the synthesis of a $[Ru(bpy)_3]^{2+}$ PS bearing a phosphonic acid group, the immobilization of this PS onto anatase TiO_2 NPs, and the kinetics of photo-induced charge transfer processes on TiO_2/Ru^{II} dyad. Upon the excitation of $[Ru(bpy)_3]^{2+}$ by visible light, the electron injection from Ru^{2+*} excited state to the CB of TiO_2 and the energy transfer between neighboring Ru^{2+*} sites on the surface will be discussed. Afterwards, kinetics of charge recombination between trapped electrons in TiO_2 and oxidized dye Ru^{3+} will be mentioned. All the kinetics studies were performed in colloidal solution, and the results are fundamental for further studies in subsequent chapters.

Chapter 3 will present a thorough investigation on $[Cr(ttpy)_2]^{3+}$ (ttpy = 4'-(p-tolyl)-2,2':6',2''-terpyridine) complex as an electron acceptor for $[Ru(bpy)_3]^{2+*}$ in homogeneous solution and for $(e^-)TiO_2/Ru^{III}$ hybrid NPs. Both complexes are then grafted on TiO_2 NPs via phosphonic acid groups to form the $Ru^{2+}/TiO_2/Cr^{3+}$ triad where TiO_2 acts as an electron relay. The ability to store multiple reduction equivalents in the $[Cr(ttpy)_2]^{3+}$ complex in homogeneous solution and on the triad will be described.

Chapter 4 will show the electrocatalytic and photocatalytic activity for CO_2 reduction using $[Mn(ttpy)(CO)_3Br]$ catalyst in homogeneous solution. The Mn catalyst and $[Ru(bpy)_3]^{2+}$ PS are then both anchored on TiO_2 NPs to form the $Ru^{II}/TiO_2/Mn^I$ triad. The triad is tested in the photocatalytic CO_2 reduction under visible irradiation, in the presence of a sacrificial electron donor. Some mechanistic studies will also be described.

Finally, in **Chapter 5** we will present the use of the oxidative equivalents stored on the Ru^{III} sites of the photoinduced charge separated state $(e^-)TiO_2/Ru^{III}$ for the polymerization of pyrrole units. The synthesis of a hybrid system consisting of a $[Ru(bpy)_3]^{2+}$ PS bearing two pyrrole moieties immobilized on TiO_2 via phosphonic acid groups will be discussed. The

resulting $TiO_2/[Ru-pyr]^{2+}$ NPs can be photopolymerized under visible light to form a nanocomposite $TiO_2/poly(Ru-pyr)$ where a polypyrrole network is formed around the TiO_2 NPs. In this photopolymerization process, TiO_2 acts as an electron acceptor for $[Ru(bpy)_3]^{2+*}$ excited state, and the electrons injected on TiO_2 are scavenged by O_2. Afterwards, the nanocomposite is deposited onto an electrode for light-to-electricity energy conversion application.

References

1   C. Renz, *Helv. Chim. Acta*, 1921, **4**, 961–968.

2   L. Sang, Y. Zhao and C. Burda, *Chem. Rev.*, 2014, **114**, 9283–9318.

3   M. A. Henderson, *Surf. Sci. Rep.*, 2011, **66**, 185–297.

4   A. Fujishima, X. Zhang and D. A. Tryk, *Surf. Sci. Rep.*, 2008, **63**, 515–582.

5   U. Diebold, *Surf. Sci. Rep.*, 2003, **48**, 53–229.

6   H. Z. Zhang and J. F. Banfield, *J. Phys. Chem. B*, 2000, **104**, 3481–3487.

7   M. Gratzel, *Nature*, 2001, **414**, 338–344.

8   A. Di Paola, M. Bellardita and L. Palmisano, *Catalysts*, 2013, **3**, 36–73.

9   L. Kavan, M. Gratzel, S. E. Gilbert, C. Klemenz and H. J. Scheel, *J. Am. Chem. Soc.*, 1996, **118**, 6716–6723.

10   Y. Tamaki, K. Hara, R. Katoh, M. Tachiya and A. Furube, *J. Phys. Chem. C*, 2009, **113**, 11741–11746.

11   J. Moser, M. Graetzel and R. Gallay, *Helv. Chim. Acta*, 1987, **70**, 1596–1604.

12   C. Colbeau-Justin, M. Kunst and D. Huguenin, *J. Mater. Sci.*, 2003, **38**, 2429–2437.

13   A. Fujishima and K. Honda, *Nature*, 1972, **238**, 37–38.

14   M. Anpo, H. Yamashita, Y. Ichihashi and S. Ehara, *J. Electroanal. Chem.*, 1995, **396**, 21–26.

15   A. V. Emeline, V. K. Ryabchuk and N. Serpone, *J. Phys. Chem. B*, 2005, **109**, 18515–18521.

16   T. Kakutani, Y. Morihiro, M. Senda, R. Takahashi and K. Matsumoto, *Bull. Chem. Soc. Jpn.*, 1978, **51**, 2847–2854.

17   A. Juris, V. Balzani, F. Barigelletti, S. Campagna, P. Belser and A. von Zelewsky, *Coord. Chem. Rev.*, 1988, **84**, 85–277.

18   N. A. P. Kane-Maguire, *Top. Curr. Chem.*, 2007, **280**.

19   I. M. Dixon, E. Lebon, P. Sutra and A. Igau, *Chem. Soc. Rev.*, 2009, **38**, 1621–1634.

20   R. Farran, Université Grenoble-Alpes, 2015.

21   D. L. Dexter, *J. Chem. Phys.*, 1953, **21**, 836–850.

22   T. Forster, *Discuss. Faraday Soc.*, 1959, **27**, 7–17.

23   P. Ceroni, *The Exploration of Supramolecular Systems and Nanostructures by Photochemical Techniques.*, 2012.

24   J. L. Brennan, T. E. Keyes and R. J. Forster, *Langmuir*, 2006, **22**, 10754–10761.

25   J. Kroon, J. W. Verhoeven, M. N. Paddon-Row and A. M. Oliver, *Angew. Chemie, Int. Ed.*, 1991, **30**, 1358–1361.

26   W. Gao, L. Dickinson, C. Grozinger, F. G. Morin and L. Reven, *Langmuir*, 1996, **12**, 6429–6435.

27   L. Zeininger, L. Portilla, M. Halik and A. Hirsch, *Chem. Eur. J.*, 2016, **22**, 13506–13512.

28   H. Nishihara, K. Kanaizuka, Y. Nishimori and Y. Yamanoi, *Coord. Chem. Rev.*, 2007, **251**, 2674–2687.

29   N. Rozlosnik, M. C. Gerstenberg and N. B. Larsen, *Langmuir*, 2003, **19**, 1182–1188.

30   R. Boissezon, J. Muller, V. Beaugeard, S. Monge and J.-J. Robin, *RSC Adv.*, 2014, **4**, 35690–35707.

31   S. Marcinko and A. Y. Fadeev, *Langmuir*, 2004, **20**, 2270–2273.

32   R. Farran, L. Le Quang, D. Jouvenot, F. Loiseau, R. Pansu, A. Deronzier and J. Chauvin, *Inorganica Chim. Acta*, 2017, **454**, 197–207.

33   H. Sugimoto, H. Tsukube and K. Tanaka, *Eur. J. Inorg. Chem.*, 2004, 4550–4553.

34   J. Desilvestro, M. Gratzel, L. Kavan and J. Moser, *J. Am. Chem. Soc.*, 1985, **107**, 2988–2990.

35   R. Luschtinetz, J. Frenzel, T. Milek and G. Seifert, *J. Phys. Chem. C*, 2009, **113**, 5730–5740.

36   M. Nilsing, S. Lunell, P. Persson and L. Ojamae, *Surf. Sci.*, 2005, **582**, 49–60.

37   T. A. Heimer and G. J. Meyer, *J. Lumin.*, 1996, **70**, 468–478.

38   J. M. Stipkala, F. N. Castellano, T. A. Heimer, C. A. Kelly, K. J. T. Livi and G. J. Meyer, *Chem. Mater.*, 1997, **9**, 2341–2353.

39   R. Argazzi, C. A. Bignozzi, T. A. Heimer, F. N. Castellano and G. J. Meyer, *J. Phys. Chem. B*, 1997, **101**, 2591–2597.

40   M. H. Rittmann-Frank, C. J. Milne, J. Rittmann, M. Reinhard, T. J. Penfold and M.

Chergui, *Angew. Chemie, Int. Ed.*, 2014, **53**, 5858–5862.

41   B. O'Regan and M. Gratzel, *Nature*, 1991, **353**, 737–740.

42   D. Wang, R. Mendelsohn, E. Galoppini, P. G. Hoertz, R. A. Carlisle and G. J. Meyer, *J. Phys. Chem. B*, 2004, **108**, 16642–16653.

43   I. Gillaizeau-Gauthier, F. Odobel, M. Alebbi, R. Argazzi, E. Costa, C. A. Bignozzi, P. Qu and G. J. Meyer, *Inorg. Chem.*, 2001, **40**, 6073–6079.

44   K. Hanson, K. M. Brennaman, A. Ito, H. Luo, W. Song, K. A. Parker, R. Ghosh, M. R. Norris, C. R. K. Glasson, J. J. Conception, R. Lopez and T. J. Meyer, *J. Phys. Chem. C*, 2012, **116**, 14837–14847.

45   R. Katoh, A. Furube, A. V. Barzykin, H. Arakawa and M. Tachiya, *Coord. Chem. Rev.*, 2004, 1195–1213.

46   G. Benko, J. Kallioinen, P. Myllyperkio, F. Trif, J. E. I. Korppi-Tommola, A. P. Yartsev and V. Sundstrom, *J. Phys. Chem. B*, 2004, **108**, 2862–2867.

47   L. Du, A. Furube, K. Hara, R. Katoh and M. Tachiya, *J. Phys. Chem. C*, 2010, **114**, 8135–8143.

48   T. W. Woolerton, S. Sheard, E. Pierce, S. W. Ragsdale and F. A. Armstrong, *Energy Environ. Sci.*, 2011, **4**, 2393–2399.

49   F. Lakadamyali, A. Reynal, M. Kato, J. R. Durrant and E. Reisner, *Chem. Eur. J.*, 2012, **18**, 15464–15475.

CHAPTER II

PHOTO-INDUCED CHARGE TRANSFER PROCESSES ON Ru(II) TRIS-BIPYRIDINE SENSITIZED TiO$_2$ NANOPARTICLES

Abstract

In this chapter we will present the electrochemical and photophysical properties of a $[Ru(bpy)_3]^{2+}$ photosensitizer (bpy = 2,2'-bipyridine) bearing a phosphonate group. Afterwards, the phosphonate group is converted to phosphonic acid group to anchor on TiO_2 and SiO_2 nanoparticles. Photo-induced charge and energy transfer processes in TiO_2/Ru^{II} and SiO_2/Ru^{II} colloids under visible light have been studied by time-resolved emission spectroscopy and transient absorption spectroscopy. The electron injection from $[Ru(bpy)_3]^{2+*}$ excited state to the conduction band of TiO_2 occurs in nanosecond time scale to form the charge separated state $(e^-)TiO_2/Ru^{III}$, whereas charge recombination is in millisecond time scale. The trapped electrons on the Ti^{3+} sites of TiO_2 are evidenced by EPR spectroscopy under continuous irradiation. The efficient, long-lived charge separated state $(e^-)TiO_2/Ru^{III}$ provides good opportunities to harvest the charges for subsequent redox reactions, which will be discussed in the remaining chapters.

Résumé

Dans ce chapitre, nous présentons les propriétés électrochimiques et photophysiques d'un nouveau complexe du $[Ru(bpy)_3]^{2+}$ (bpy = 2,2'-bipyridine) portant une fonction d'ancrage de type phosphonate sur une des bipyridines. Par la suite, la fonction phosphonate est hydrolysée en acide phosphonique pour permettre l'immobilisation des complexes du ruthénium sur des nanoparticules de TiO_2 et SiO_2. Les processus de transfert de charge et d'énergie induits par irradiation lumineuse dans les systèmes hydrides colloïdes TiO_2/Ru^{II} et SiO_2/Ru^{II} sous lumière visible ont été étudiés par spectroscopie d'émission résolus en temps et spectroscopie d'absorption transitoire en régime nanoseconde. L'injection d'électrons de l'état excité du $[Ru(bpy)_3]^{2+*}$ à la bande de conduction de TiO_2 se produit dans l'échelle de temps de la nanoseconde pour former l'état à charge séparée $(e^-)TiO_2/Ru^{III}$, alors que la recombinaison de charge se produit à l'échelle de la milliseconde. L'identification de l'électron sur les sites Ti^{3+} de surface de la matrice TiO_2 a été faite par spectroscopie RPE. La longue durée de vie de l'état à charge séparée $(e^-)TiO_2/Ru^{III}$ offre la possibilité d'engager l'électron ou le "trou" dans des réactions redox prédéfinies, qui seront discutées dans les chapitres suivants.

II.1.   Introduction

Despite the various works on the photo-induced charge transfer processes of nanocrystalline TiO$_2$/Ru^{II} electrodes and TiO$_2$/Ru^{II} colloidal solution mentioned in **Section I.2.5**, to the best of our knowledge there are no investigations of the kinetics of a [Ru(bpy)$_3$]$^{2+}$ dye grafted on TiO$_2$ NPs via a phosphonic acid group in solution. We are interested in the colloids as they resemble the media in photocatalytic studies. Herein, we will present the kinetics of photo-induced charge transfer processes of a phosphonic-derivatized [Ru(bpy)$_3$]$^{2+}$ dye immobilized on TiO$_2$ NPs.

II.2.   Phosphonate-derivatized Ru(II) tris-bipyridine in solution

II.2.1.   Synthesis

The synthesis of [Ru(bpy)$_3$]$^{2+}$-based photosensitizers was adapted from the synthesis of a similar ligand with several modifications.[1] It is schematically described in **Scheme II-1**. In the first step, 4,4'-dimethyl bipyridine was deprotonated by lithium diisopropylamide (LDA, 1.1 equiv) at low temperature, before an alkylation reaction with diethyl(3-bromopropyl)phosphonate to form a bipyridine bearing only one phosphonate group. The ligand was subsequently complexed with [Ru(bpy)$_2$Cl$_2$] following a well-established method[2] to obtain the [Ru-PO$_3$Et$_2$]$^{2+}$ photosensitizer bearing a phosphonate group. It was then deprotected by concentrated HCl solution to form [Ru(bpy)$_2$(bpy-PO$_3$H$_2$)]$^{2+}$, denoted as [RuP]$^{2+}$.
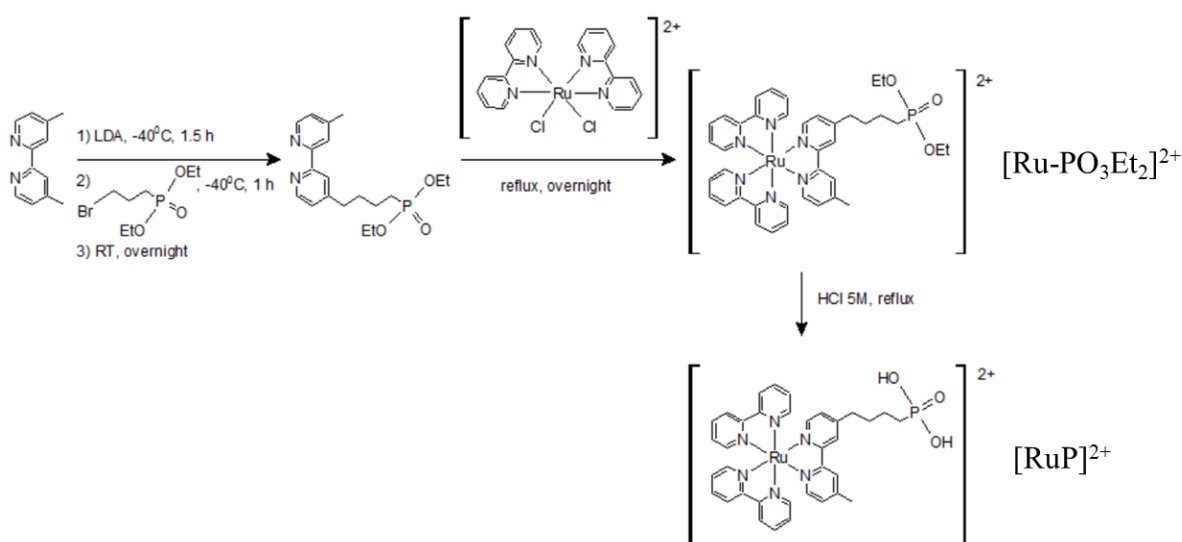
Scheme II-1. Synthesis procedure for [Ru(bpy)$_2$(bpy-PO$_3$Et$_2$)]$^{2+}$ ([Ru-PO$_3$Et$_2$]$^{2+}$) and [Ru(bpy)$_2$(bpy-PO$_3$H$_2$)]$^{2+}$ ([RuP]$^{2+}$)

The phosphonic anchoring group is chosen due to its good affinity with metal oxide surfaces and better stability than carboxylic group as described in **Chapter 1**. The asymmetric

complex bearing only one phosphonic acid group prevents the possible binding to two adjacent nanoparticles, thus it may be potentially helpful for the charge injection to TiO_2 semiconductor and simplifies the kinetics studies. It has also been demonstrated that additional phosphonic groups decrease the rate of photo-induced electron injection to TiO_2 as mentioned in **Chapter 1**.[3] A long alkyl chain separating the $[Ru(bpy)_3]^{2+}$ photosensitizer and TiO_2 substrate may reduce both electron injection and back electron transfer rates between the PS and TiO_2.[4] It is however noted that the Ru-complex with such additional methylene groups may be less electrochemically stable than that bearing a $4,4'-(PO_3H_2)_2$-bpy ligand under an applied potential of 1.5 V *vs* Ag/AgCl for 16 hours.[3]

In order to study the effect of the phosphonic functional group on the electrochemical and photophysical behaviors of $[Ru-PO_3Et_2]^{2+}$ and $[RuP]^{2+}$, $[Ru(bpy)_2(dmbpy)](PF_6)_2$ (dmbpy = $4,4'$-dimethyl-2,2'-bipyridine) complex was also prepared following a similar procedure (**Scheme II-2**). Anion exchange to redox inactive PF_6^- allows the complex to be soluble in MeCN and eliminates the electrochemically active Cl^- species.
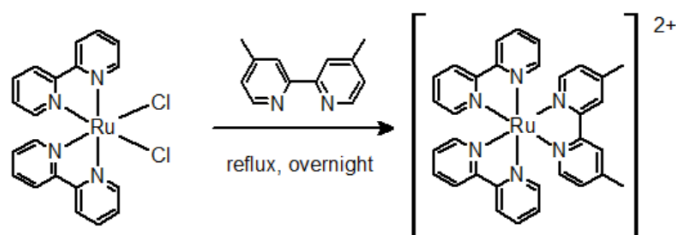
Scheme II-2. Synthesis of $[Ru(bpy)_2(dmbpy)](PF_6)_2$

II.2.2. Photophysical properties

a) UV-vis absorption and emission spectroscopies

To understand the effect of bpy ligand functionalization on the photophysical properties of $[Ru(bpy)_3]^{2+}$ photosensitizer, a comparative study was carried out for $[Ru(bpy)_3]^{2+}$, $[Ru(bpy)_2(dmbpy)]^{2+}$ and $[Ru-PO_3Et_2]^{2+}$ in MeCN under an Ar atmosphere. The $[RuP]^{2+}$ complex is not soluble in MeCN. Their UV-vis absorption and emission spectra are presented in **Figure II-1**. In the absorption spectra, the ^{1}MLCT absorption peak remains similar for the three complexes at 454 nm and the ligand-centered charge transfer (LCCT) peak at 286 nm. The extinction coefficient for the MLCT transition exhibits a minor variation: ε = 13000 $M^{-1}.cm^{-1}$ for $[Ru(bpy)_3]^{2+,5}$ and 14100 $M^{-1}.cm^{-1}$ for $[Ru-PO_3Et_2]^{2+}$.

After photoexcitation at 450 nm, the complexes exhibit a strong emission, with maxima at 608 nm for $[Ru(bpy)_3]^{2+}$ and about 615 nm for the other two complexes. The maximum of emission of $[Ru(bpy)_3]^{2+}$ is in accordance with literature.[6] The shape of the emission spectrum

is broad and identical for all the complexes. The result indicates that the phosphonate group has negligible effect on the emission of this photosensitizer. The substituted alkyl chain is an electron donating group to the bpy ligand. A similar red shift in the emission spectrum has been reported for the methylene group attached to $[Ru(bpy)_3]^{2+}$ complex.[3] Maestri et al.[7] explained the shift as follows: after the photo-induced MLCT process, the HOMO $\pi(t_{2g})$ metal orbital is destabilized causing the HOMO-LUMO gap to reduce. Therefore the emission maximum is shifted to longer wavelengths.
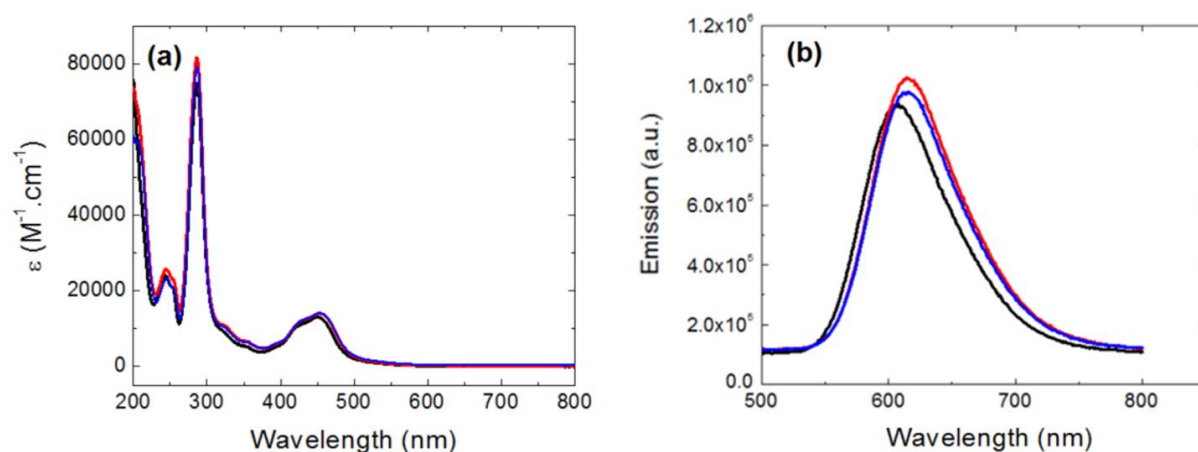
Figure II-1. (a) UV-vis spectra and (b) emission spectra of $[Ru(bpy)_3]^{2+}$ (black), $[Ru(bpy)_2(dmbpy)]^{2+}$ (red) and $[Ru\text{-}PO_3Et_2]^{2+}$ (blue) in MeCN under Ar. Emission spectra were recorded in a fluorescent cuvette after 450 nm light excitation.

The luminescent quantum yield Φ was calculated following an optically diluted methodology using $[Ru(bpy)_3](PF_6)_2$ as a reference (see **Experimental Section**). The luminescent quantum yield Φ shows almost similar values for the reference $[Ru(bpy)_3]^{2+}$ and the substituted $[Ru(bpy)_2(dmbpy)]^{2+}$ and $[Ru\text{-}PO_3Et_2]^{2+}$ (**Table II-1**).

b) *Time-resolved emission spectroscopy*

The time-resolved emission of Ru^{2+*} species was measured by exciting the samples with a 400 nm picosecond pulsed laser and recording the emission decay at the maximum emission wavelength with a Time-Correlated Single Photon Counting (TCSPC) photometer. The signals are shown in **Figure II-2**, together with monoexponential fitting curves. A slight increase in lifetime is observed when the bpy ligand is functionalized with a methyl or alkyl group: 757 ns for $[Ru(bpy)_3]^{2+}$, 986 ns for $[Ru(bpy)_2(dmbpy)]^{2+}$ and 895 ns for $[Ru\text{-}PO_3Et_2]^{2+}$. The photophysical properties of the three complexes are summarized in **Table II-1**. All of these observations prove that the $[Ru\text{-}PO_3Et_2]^{2+}$ retains the characteristics of the prototype $[Ru(bpy)_3]^{2+}$ photosensitizer under visible light, notably a long-lived excited state that can be engaged in electron or energy transfer processes.
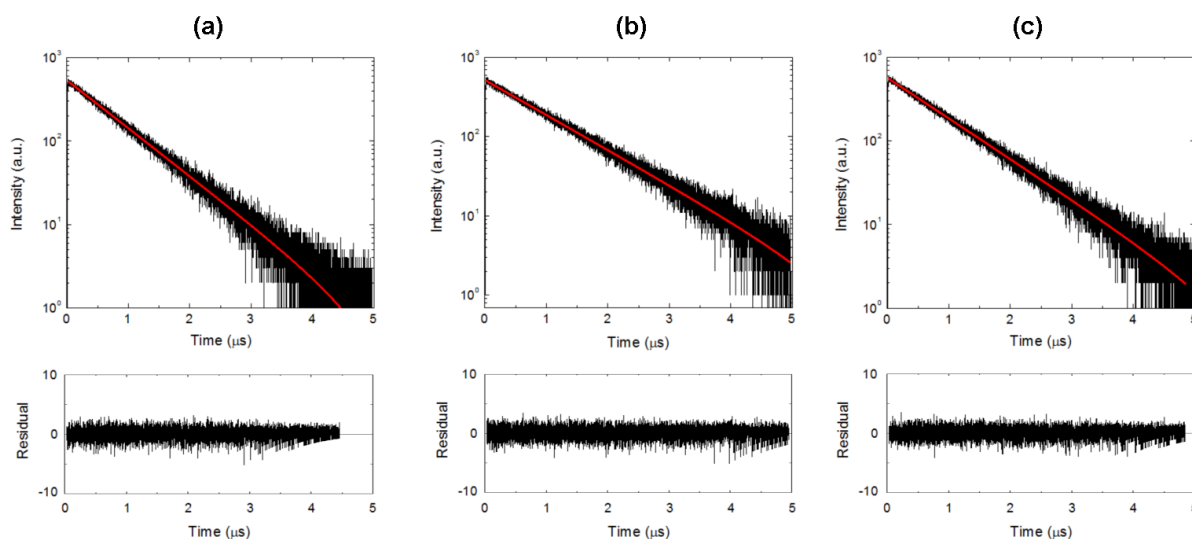
Figure II-2. Time-resolved emission spectra of (a) [Ru(bpy)₃]²⁺*, (b) [Ru(bpy)₂(dmbpy)]²⁺* and (c) [Ru-PO₃Et₂]²⁺* in MeCN under Ar. The samples were excited at 400 nm using a picosecond pulsed laser, while the emitted photons were collected at 610 nm using a TCSPC photometer. The red curves represent the monoexponential fitting of the decays

Table II-1. Summary of photophysical properties of [Ru(bpy)₃]²⁺, [Ru(bpy)₂(dmbpy)]²⁺ and [Ru-PO₃Et₂]²⁺: MLCT absorption peak λ_{abs}, peak of luminescent emission λ_{em}, lifetime τ of the photoexcited Ru²⁺* species and the emission quantum yield Φ.

	LCCT λ_{abs}, nm [ε, M⁻¹.cm⁻¹]	¹MLCT λ_{abs}, nm [ε, M⁻¹.cm⁻¹]	λ_{em}, nm [a]	τ, ns (%) [b]	Φ
[Ru(bpy)₃]²⁺	286 [75000]	451 [13000]	608	757 ± 9	0.062
[Ru(bpy)₂(dmbpy)]²⁺	286 [82000]	454 [14000]	614	986 ± 12	0.070
[Ru-PO₃Et₂]²⁺	286 [80000]	454 [14100]	615	895 ± 10	0.068

[a] *Excitation at 450 nm*

[b] *Excitation by a picosecond pulsed laser at 400 nm*

All measurements were conducted in MeCN solution under Ar at room temperature.

c) Transient absorption spectroscopy

TAS was employed to study the UV-vis absorption of photoexcited [Ru-PO₃Et₂]²⁺* species. Following the excitation by a nanosecond pulsed laser at 532 nm, the complex shows a bleaching at 450 nm which recovers to the initial value after ~2000 ns (**Figure II-3a**). The bleaching is associated with an increased absorbance at 370 nm. The TA spectra are characteristic of the photoexcited state [Ru^III(bpy•⁻)(bpy)(bpy-PO₃Et₂)]²⁺*. The bleaching at 450 nm is fit with monoexponential function to yield a lifetime of 931 ± 5 ns (**Figure II-3b**). This lifetime is in accordance with the one recorded by time-resolved emission spectroscopy.
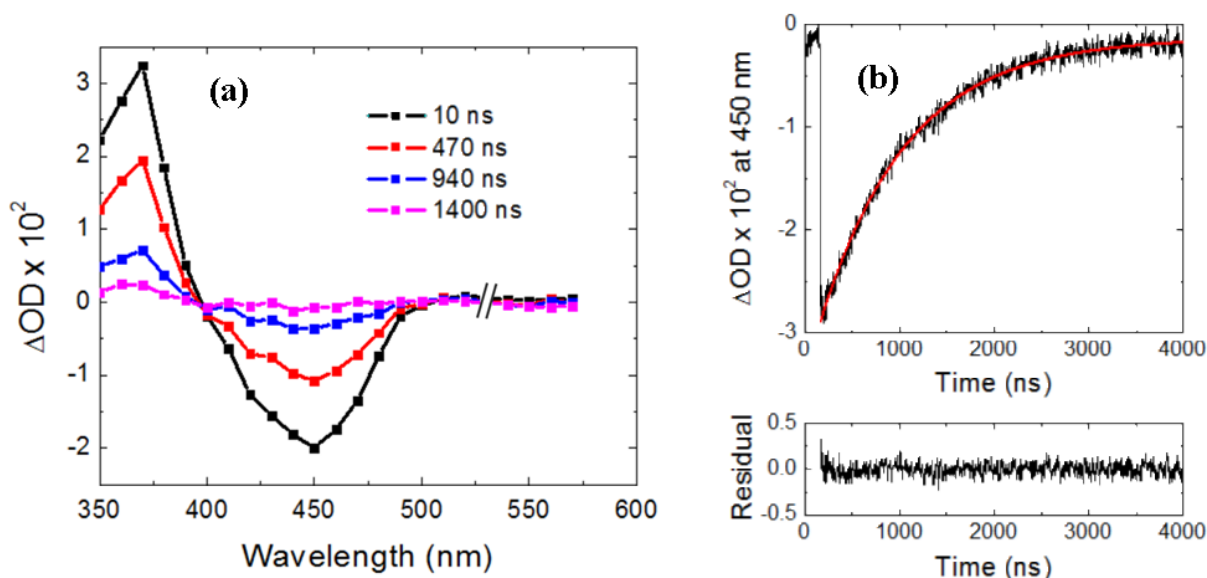
Figure II-3. (a) TA spectra of [Ru-PO₃Et₂]²⁺ complex in Ar-saturated MeCN solution at various time intervals after the sample was photoexcited by a 532 nm nanosecond pulsed laser. The data points at 530 nm have been removed to avoid light scattering from the 532 laser. (b) Signal bleaching at 450 nm (black) fit with a monoexponential function (red) and the fitting residual.

II.2.3. Electrochemical properties

The electrochemical properties of the [Ru(bpy)₃]²⁺-based photosensitizers were characterized with cyclic voltammetry using a glassy carbon electrode (d = 3 mm) as working electrode (WE). The voltammograms of [Ru(bpy)₂(dmbpy)]²⁺ and [Ru-PO₃Et₂]²⁺ are shown in **Figure II-4**, while the redox potentials are collected in **Table II-2**. Both [Ru(bpy)₂(dmbpy)]²⁺ and [Ru-PO₃Et₂]²⁺ complexes exhibit in the anodic part a one-electron reversible oxidation wave centered on the metal at $E_{1/2}$ = 0.91 V. In the cathodic part, they show three successive one-electron reduction processes centered on the bpy ligands at $E_{1/2}$ = -1.66, -1.86 and -2.12 V. The reduction waves are reversible, with the first one producing [Ru^II(bpy•⁻)(bpy)₂]⁺ denoted hereafter as Ru^I.

In the anodic scan, the Ru^II complexes bearing a dimethyl bipyridine group show a shift to lower oxidation potentials compared with the [Ru(bpy)₃]²⁺ reference in accordance with the complex bearing an electron-donating substituted group on bpy ligands.[3] In the cathodic scan, the third reduction potential of the functionalized complexes is significantly shifted to a more negative potential (-2.12 V compared with -2.07 V) whereas the first two reduction potentials are comparable with that of [Ru(bpy)₃]²⁺. This change could be explained by the charge localization on the bpy ligand, while the metal oxidation state remains unchanged.[5] Since the dimethyl is an electron donating group, the first and second reduction processes likely occur

43

on the un-substituted bpy ligands, and the last reduction is on the bpy bearing the dimethyl group.
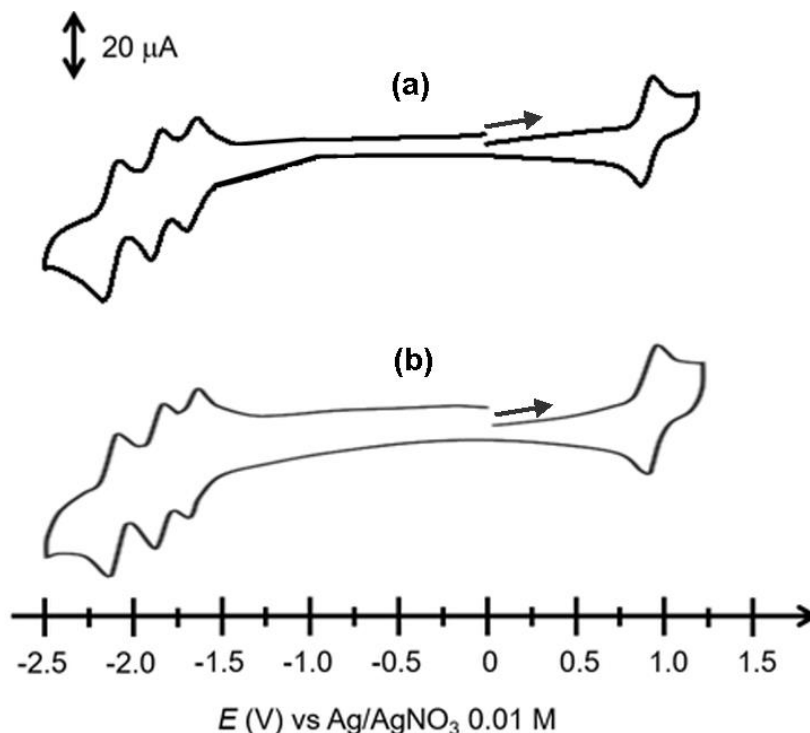
Figure II-4. Cyclic voltammograms of (a) $[Ru(bpy)_2(dmbpy)]^{2+}$ and (b) $[Ru\text{-}PO_3Et_2]^{2+}$ (0.5 mM) in MeCN + 0.1 M TBAPF₆. WE = C disk (d = 3 mm), CE = Pt, RE = Ag/AgNO₃ 0.01 M, v = 100 mV.s⁻¹

Table II-2. Summary of electrochemical properties of $[Ru(bpy)_3]^{2+}$, $[Ru(bpy)_2(dmbpy)]^{2+}$ and $[Ru\text{-}PO_3Et_2]^{2+}$ complexes

$E_{1/2}$ (ΔE_p), V	E_{ox}	E_{red} (1)	E_{red} (2)	E_{red} (3)
$[Ru(bpy)]^{2+,5}$	0.94	-1.67	-1.83	-2.07
$[Ru(bpy)_2(dmbpy)]^{2+}$	0.91 (0.06)	-1.66 (0.06)	-1.86 (0.06)	-2.12 (0.08)
$[Ru\text{-}PO_3Et_2]^{2+}$	0.92 (0.06)	-1.67 (0.06)	-1.86 (0.06)	-2.12 (0.08)

In this study, $[Ru\text{-}PO_3Et_2]^{2+}$ is used as a photosensitizer to inject an electron to the conduction band (CB) of TiO₂ NPs under visible irradiation, forming $(e^-)TiO_2$ and $[RuP]^{3+}$. Therefore, the redox potential of $[RuP]^{III/II*}$ is of great interest to study the photo-induced electron transfer process. From the redox potentials of the ground state and the emission spectra of the complexes, one can estimate the redox potential of $Ru^{III/II*}$ by using the simplified Rehm-Weller equation (**Equation II-1**):

$$E(Ru^{III}/Ru^{II*}) = E(Ru^{III}/Ru^{II}) - \frac{hc}{\lambda_{em,77\,K}e} \approx E(Ru^{III}/Ru^{II}) - \frac{1240}{\lambda_{em,RT}} \qquad \text{(Eq II-1)}$$

where h is the Planck constant, c the speed of light, $\lambda_{em,77\ K}$ and $\lambda_{em,RT}$ the wavelength at emission maximum at 77 K and room temperature, respectively. The redox potential of Ru^{III}/Ru^{II*} is determined to be -1.10 V vs Ag/AgNO$_3$ 0.01 M for both [Ru-PO$_3$Et$_2$]$^{2+}$ and [Ru(bpy)$_3$]$^{2+}$ complexes. It can be concluded that [Ru-PO$_3$Et$_2$]$^{2+}$ complex retains beneficial electrochemical and photoredox properties of the [Ru(bpy)$_3$]$^{2+}$ complex.

II.2.4. Electron paramagnetic resonance spectroscopy

The electron paramagnetic resonance (EPR) spectroscopy is a convenient technique for qualitative and quantitative studies of paramagnetic species, notably free radicals and transition metal complexes. [Ru(bpy)$_3$]$^{n+}$ (n = 3, 2, 1) complexes were chosen as a reference for subsequent studies of the [Ru-PO$_3$Et$_2$]$^{2+}$ grafted on SiO$_2$ or TiO$_2$ NPs. The complexes were electrochemically synthesized by exhaustive electrolysis of [Ru(bpy)$_3$]$^{2+}$ in MeCN + 0.1 M TBAPF$_6$ solution under Ar. The applied potentials were 1.1 V to form [Ru(bpy)$_3$]$^{3+}$ and -1.65 V to form [Ru(bpy)$_3$]$^{+}$. EPR signals of [Ru(bpy)$_3$]$^{n+}$ (n = 3, 1) complexes are presented in **Figure II-5**. The starting complex [Ru(bpy)$_3$]$^{2+}$ possesses a low spin d^6 electronic configuration,[5,8] making it EPR silent. When oxidized to [Ru(bpy)$_3$]$^{3+}$, it is transformed to a d^5 configuration and showing a broad signal over ~ 2000 G. The signal of [Ru(bpy)$_3$]$^{3+}$ (**Figure II-5a**) is featured at 2590 G corresponding to $g_\perp$ = 2.695 In literature the EPR signal of [Ru(bpy)$_3$](PF$_6$)$_3$ at 77 K is characterized with $g_\perp$ = 2.65 and $g_{//}$ = 1.14.[9] The latter g component is not observed in our experiment as it is broad and weak in intensity. The signal is typical for a change in the oxidation state of a transition metal. It is then ascribed to a Ru^{II} → Ru^{III} oxidation.

When singly reduced to [Ru(bpy)$_3$]$^{+}$, the complex shows a much narrower signal (**Figure II-5b**) featured by $g_\perp$ = 2.002 and $g_{//}$ = 1.984, which is ascribed to an electron localized on a bpy ligand, [Ru^{II}(bpy$^{•-}$)(bpy)$_2$]$^{+}$. The signals are also in line with previous studies.[8–10]
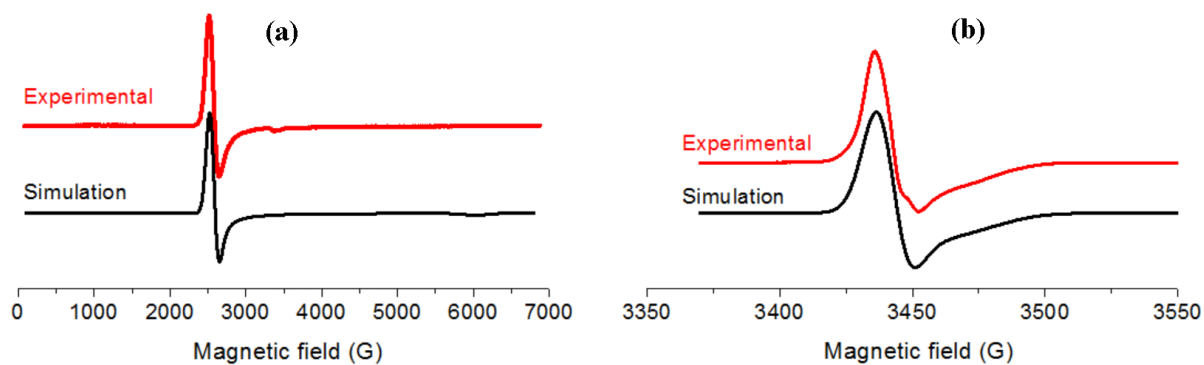
Figure II-5. EPR signals and simulations of (a) [Ru(bpy)$_3$]$^{3+}$ and (b) [Ru(bpy)$_3$]$^+$ produced by exhaustive electrolysis of 1 mM [Ru(bpy)$_3$](PF$_6$)$_2$ in MeCN + 0.1 M TBAPF$_6$. The signals were recorded with an X-band EPR spectrometer ($f \approx 9.65$ GHz, 2 mW) at 10 K (signal a) and 60 K (signal b). They were accumulated in 80 s.

II.3. Immobilization of $[Ru(bpy)_3]^{2+}$ on SiO_2 and TiO_2 nanoparticles

II.3.1. Nanoparticle synthesis

To study the TiO_2/Ru^{II} NPs, we first prepared the analogous SiO_2/Ru^{II} as a reference. In this system there are no charge injections to the SiO_2 due to an extremely negative potential of the conduction band (CB) of SiO_2. The SiO_2 NPs was synthesized from tetraethyl orthosilicate (TEOS) precursor following the Stober's sol-gel procedure[11] with some modifications. The procedure is schematically presented in **Scheme II-3**. The sonication was employed instead of mechanical stirring in order to obtain a higher dispersity.[12] The rate of addition of NH_3 catalyst has been proved to determine the NPs size.[12] With NH_3 dropwise addition, the NPs possess a nearly spherical shape, as shown in the Transmission Electron Microscopy (TEM) and Field Emission Scanning Electron Microscopy (FE-SEM) micrographs (**Figure II-6**). The TEM images also show that the particles are well separated, thus allowing full access to the particle surface for the $[RuP]^{2+}$ dye to adsorb. Both techniques show high polydispersity for the particles. The size distribution is 144 ± 20 (nm), determined from the TEM images (**Figure II-7**).
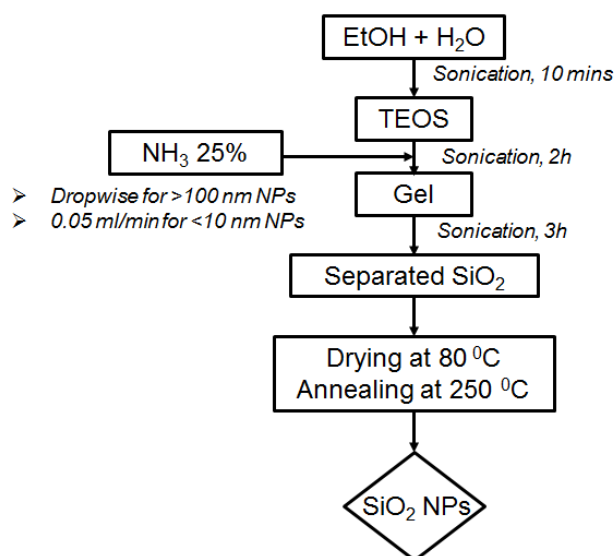
Scheme II-3. Synthesis procedures of SiO_2 NPs with various sizes
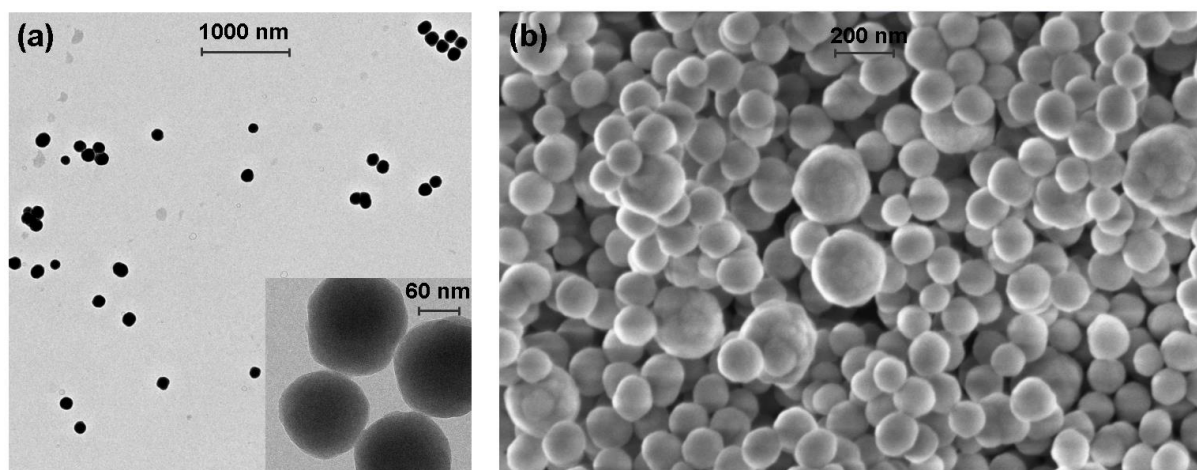
Figure II-6. (a) TEM and (b) FE-SEM micrographs of SiO$_2$ NPs with diameter > 100 nm
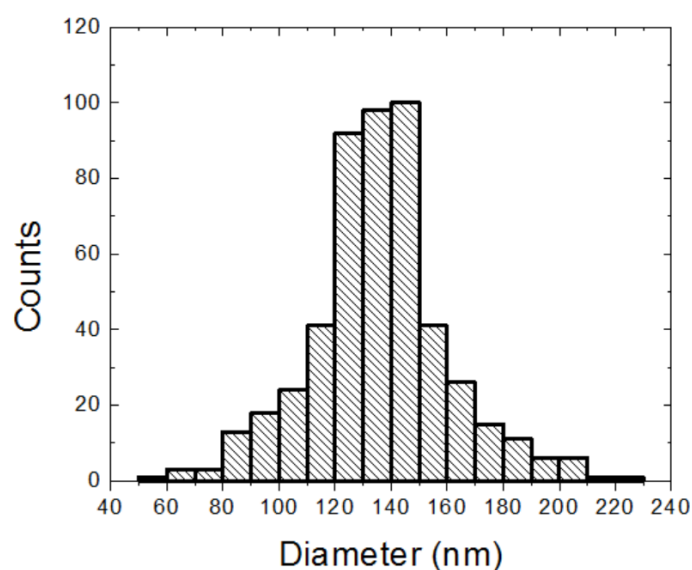
Figure II-7. Size distribution of SiO$_2$ NPs with diameter > 100 nm calculated from TEM

At a slower addition of NH$_3$ at 0.05 ml/min, the SiO$_2$ NPs with significantly smaller diameters are achieved. Their TEM and FE-SEM micrographs are presented in **Figure II-8**, showing a strong aggregation tendency regardless of the solvent used to prepare the suspension. In fact, the low conductivity and small size of the particles make it challenging to analyze the TEM images for size distribution calculation. The FE-SEM images shows the co-existence of two different sizes > 350 nm and < 10 nm.
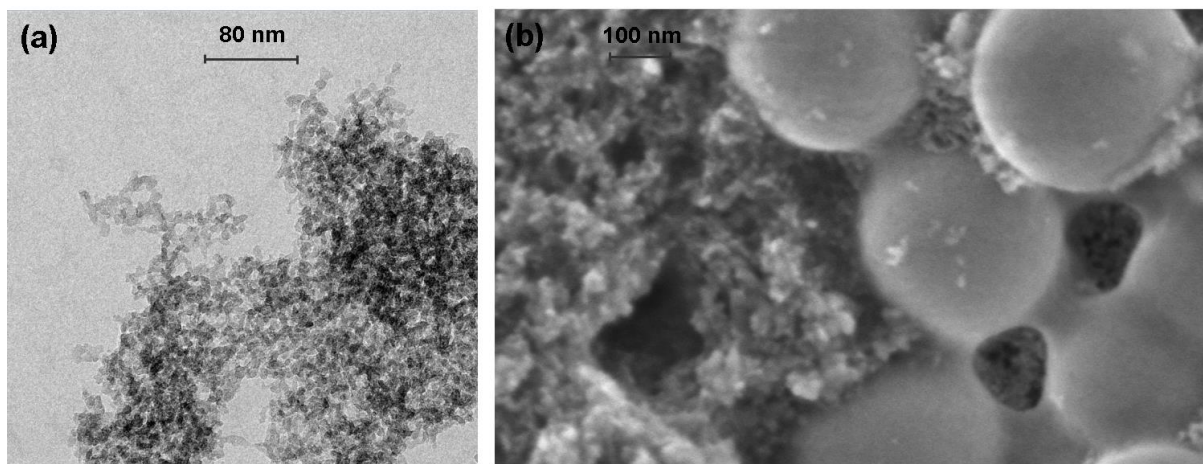
Figure II-8. (a) TEM and (b) FE-SEM micrographs of SiO$_2$ NPs with diameter < 10 nm

The synthesis of TiO$_2$ NPs also followed a sol-gel procedure in an acidic condition with titanium(IV) isopropoxide (TTIP) as precursor.[13] The synthesis route is schematically demonstrated in **Scheme II-4**. TiO$_2$ exhibits three main crystalline phases: anatase, rutile and brookite. The synthesis was carried out with a high water-to-titanium ratio, aiming at obtaining uniform, sub-20 nm anatase TiO$_2$ particles.[13] The slow addition of HCl catalyst has been shown to be critical for obtaining nanometer-sized particles. The anatase phase of TiO$_2$ was chosen in this study for (i) being a better photocatalyst than rutile,[14] and (ii) having less types of surface charge traps than P25 Degussa TiO$_2$ NPs, facilitating the study of charge transfer mechanisms on/through the semiconducting particles. It should however be noted that the P25 TiO$_2$ comprising ~75 % anatase and 25 % rutile has been demonstrated as the best TiO$_2$ photocatalyst.[15]

The anatase TiO$_2$ was readily formed by annealing the as-synthesized powder at 450 ^{0}C for 2 hours. For a comparative study, we also prepared the anatase/rutile mixed phase TiO$_2$ by annealing at 700 ^{0}C. It has been reported that the anatase to rutile phase transformation occurs at around 700 – 800 ^{0}C[16] because the rutile is more thermodynamically stable than anatase.[17]
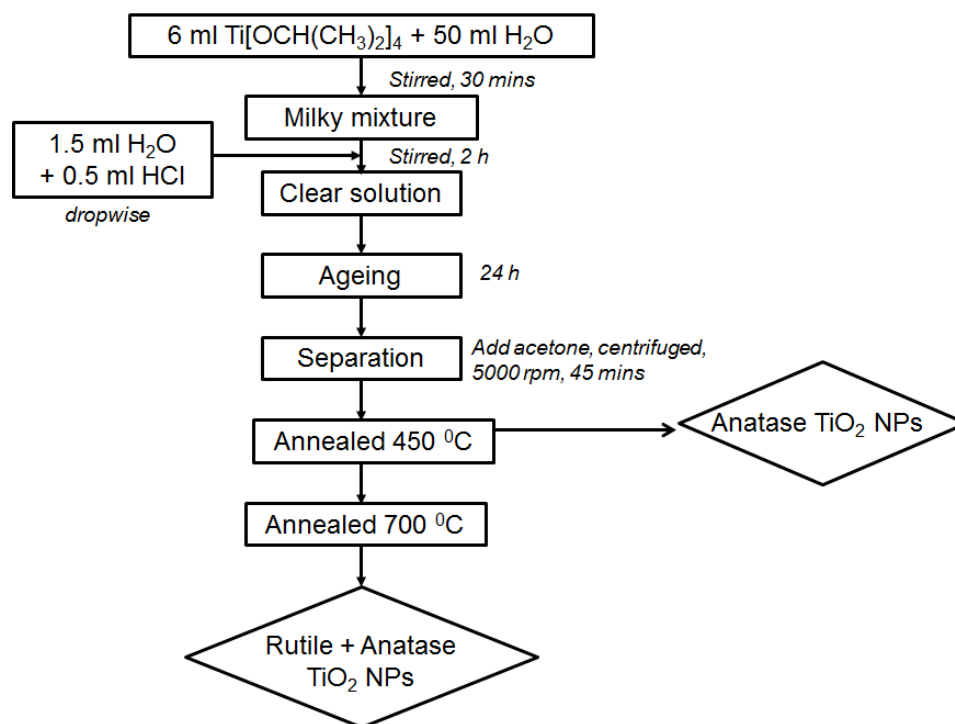
Scheme II-4. Synthesis procedures of TiO₂ NPs with anatase and/or rutile phases

In collaboration with Prof. Isabelle Gautier-Luneau (Institut Néel – Grenoble, CNRS), the morphology of the two TiO₂ NPs were studied with X-ray diffraction (XRD) and compared with the standard values recorded in JCPDS No. 21-1272 (anatase), JCPDS No. 21-1276 (rutile) and JCPDS No. 29-1360 (brookite). XRD patterns of the two TiO₂ samples are presented in **Figure II-9**. The sample annealed at 450 ^{0}C shows XRD peaks at $2\theta = 25.3^0$, 37.9^0, 48.1^0, 54.0^0 and 55.0^0 which could be ascribed to the (101), (103)+(004)+(112), (200), (105) and (211) lattice planes of the anatase phase, respectively. The sample annealed at 700 ^{0}C exhibits, beside the mentioned peaks of anatase, additional peaks at $2\theta = 27.4^0$, 36.1^0, 41.2^0, 54.3^0 and 56.6^0 (marked with asterisks). These peaks could be assigned to the (110), (101), (111), (211) and (220) lattice planes of the rutile phase, respectively. Integrating the area under the anatase and rutile characteristic peaks shows the ratio of anatase/rutile = 8/2. In both samples, the characteristic peak of brookite (30.8^0) is not observed.

The crystallite size of the NPs can be estimated from their XRD patterns using the Scherrer equation:[17]

$$d = \frac{0.9\lambda}{(\beta - \beta_0)\cos\theta} \qquad\qquad \text{(Eq II-2)}$$

where λ is the X-ray wavelength (1.5406 Å for CuKα), β_0 is the instrumental line broadening ($\beta_0 = 0.12$ rad), β (rad) is the line broadening at half of the maximum intensity (FWHM) and θ (degree) is the Bragg angle. The XRD peaks become narrower when the size is larger. The

crystallite size is, therefore, estimated as 10 nm for anatase TiO_2 NPs. For anatase/rutile TiO_2 NPs, the sizes of anatase and rutile domains are 91 nm and 204 nm, respectively.
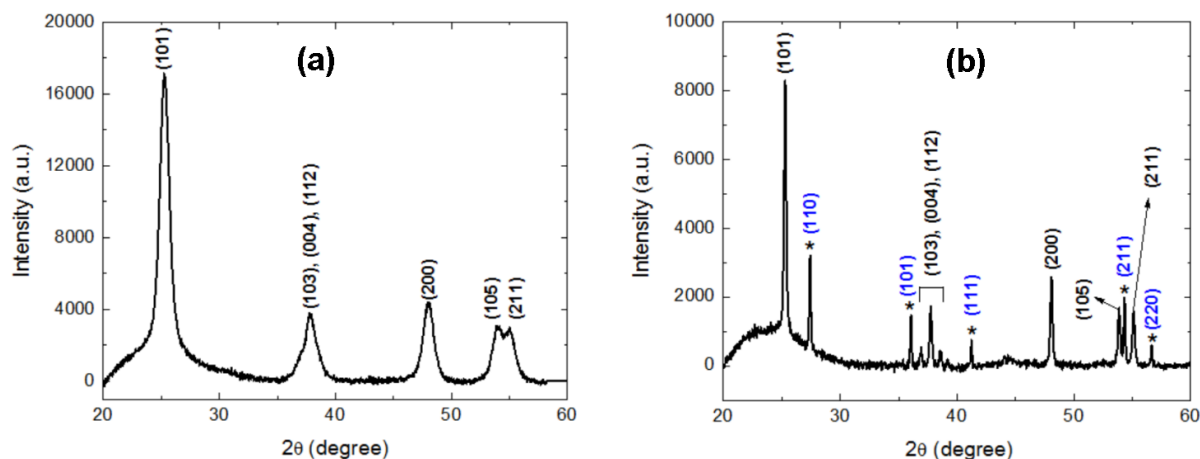
Figure II-9. XRD patterns of TiO_2 NPs annealed at (a) 450 ^0C and (b) 700 ^0C. The black and blue numbers indicate anatase and rutile lattices, respectively. The asterisks mark the peaks of the rutile phase.

Figure II-10 shows the FE-SEM micrographs of the synthesized anatase and anatase/rutile TiO_2 NPs. The primary particle size is estimated to be <10 nm for anatase TiO_2 and 30-40 nm for anatase/rutile TiO_2. The increased size of TiO_2 NPs due to thermal treatment is in accordance with literature.[17] The aggregation of the NPs offers larger crystallite domains than individual particle size. The aggregation precludes statistical studies of size distribution.
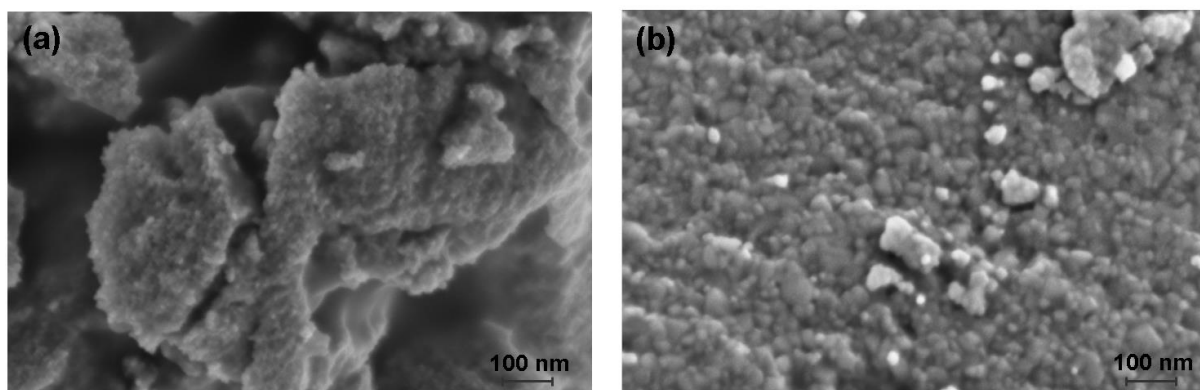
Figure II-10. FE-SEM micrographs of TiO_2 NPs annealed at (a) 450 ^0C and (b) 700 ^0C

II.3.2. *In situ* observation of $[RuP]^{2+}$ dye adsorption on surface

Before grafting the $[RuP]^{2+}$ photosensitizer on SiO_2 and TiO_2 NPs, we studied the dye adsorption on their analogous flat surfaces to determine the dye concentration, temperature and time required, as well as surface coverage. The adsorption is conveniently monitored by Quartz Crystal Microbalance with Energy Dissipation (QCM-D) technique, which is based on the change in vibrational frequency of the quartz crystal upon the adsorption of an analyte.

The technique allows to quantify not only mass change in nanogram scale upon adsorption events but also rigidity of the adsorbed layers by dissipated energy. In the case of a homogeneous, quasi-rigid film, the mass of adsorbents per unit area can be linearly related to the frequency resonance shift by the Sauerbrey relation[18] (**Equation II-3**):

$$m_{QCM} = \text{-}C\Delta f \qquad \text{(Eq II-3)}$$

where Δf (Hz) is the frequency shift, m_{QCM} (ng) the mass uptake and C the mass sensitivity ($C = 17.7$ ng.cm^{-2}.Hz^{-1} at $f_1 = 5$ MHz. If the film is solvated, its acoustic areal mass density consists of the areal mass densities of the adsorbate, m_{ads}, and the hydrodynamically coupled solvent, $m_{solvent}$ (**Equation II-4**).

$$m_{QCM} = m_{ads} + m_{solvent} \qquad \text{(Eq II-4)}$$

The QCM-D responses for the adsorption of $[RuP]^{2+}$ onto SiO_2 and TiO_2 surfaces are shown in **Figure II-11**. Frequency shifts are estimated to be -1.3 and -14.4 (Hz) for SiO_2 and TiO_2 sensor, respectively. Using the **Equation II-3**, one can calculate the increased mass of 23 ng.cm^{-2} (SiO_2) and 255 ng.cm^{-2} (TiO_2). The surface coverage is then calculated as $\Gamma = 2.3 \times 10^{-11}$ mol.cm^{-2} and 2.5×10^{-10} mol.cm^{-2} for SiO_2 and TiO_2, respectively, provided that the mass of coupled solvent is neglected. They are equal to 0.1 molecule.nm^{-2} for SiO_2 and 1.5 molecules.nm^{-2} for TiO_2. The contact angle of the modified surfaces with water is found to be quite identical: $(24.4 \pm 1.6)^0$ for SiO_2/Ru^{II} and $(22.4 \pm 1.7)^0$ for TiO_2/Ru^{II}, implying a similar outer layer. It also suggests a similar degree of solvation for both films. Given the initial surfaces having a contact angle of $\sim 10^0$ (SiO_2) and $\sim 4^0$ (TiO_2), the modified ones become clearly more hydrophobic, due to the bpy ligands. The experiments prove that the dye adsorption onto SiO_2 and TiO_2 surfaces could be achieved under ambient conditions within several hours. The TiO_2 surface coverage is an order of magnitude higher than SiO_2 as the mass of coupled solvent is expected to be the same for both films. It could be explained by the higher stability of the Ti-O-P bond than Si-O-P one.[19]
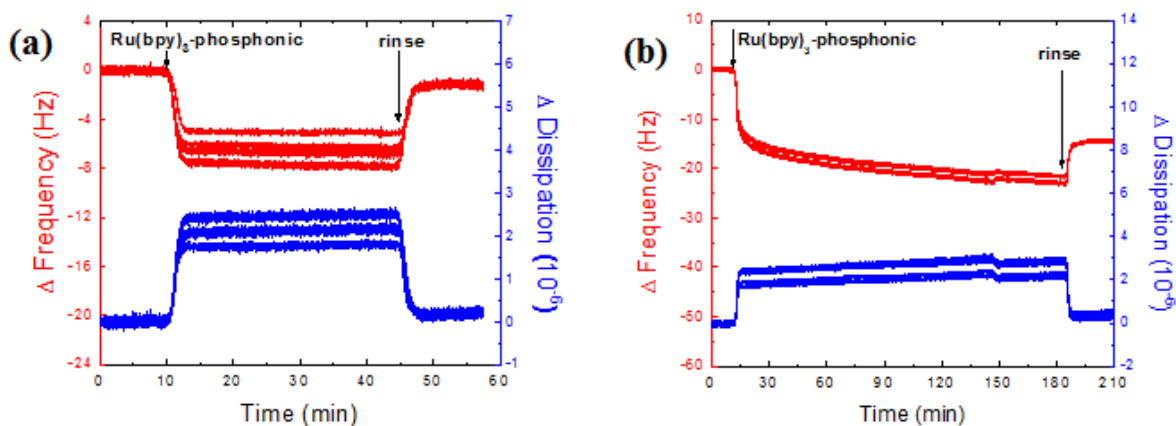
Figure II-11. QCM-D responses for the adsorption of [RuP]$^{2+}$ complex on (a) SiO$_2$ and (b) TiO$_2$ coated sensors. Red and blue lines represent changes in frequency and dissipated energy, respectively, at various overtones. All experiments were run at 21 ^{0}C.

II.3.3.   Dye sensitization with [RuP]$^{2+}$ on colloidal nanoparticles

The [RuP]$^{2+}$-dye sensitization of TiO$_2$ and SiO$_2$ NPs was achieved by mixing the particles and the complex in ethanol/acetone (8/2 v/v) solution at room temperature. The NPs were then centrifuged and washed with the solution multiple times until the ungrafted complex in the supernatant solution cannot be detected anymore with UV-vis spectroscopy. By measuring the UV-vis absorbance of the solution after each centrifugation, we estimate the Ru^{II} loading as 0.19 mmol.g^{-1} TiO$_2$ (both anatase and anatase/rutile) and 0.02 mmol.g^{-1} SiO$_2$ (< 10 nm) NPs. It is in good agreement with the QCM-D experiment on the flat surfaces where the surface coverage on TiO$_2$ is about ten times higher than SiO$_2$.

The main advantage of the heterogenization of the photosensitizer complex on NPs is their high surface area and high dispersibility in a variety of solvents. However, both the intact and sensitized NPs with diameter less than 10 nm show rapid precipitation in many solvents such as MeCN, ethanol, acetone, DMF and water. Large aggregates of bare NPs were observed with SEM and TEM. The precipitation prohibits the formation of a stable colloid for further studies.

As a comparative study, we then employed commercially available nanopowders of SiO$_2$ (d < 25 nm) and anatase TiO$_2$ (d < 20 nm) produced by Aldrich, which show better dispersibility in MeCN and water. After the dye sensitization with [RuP]$^{2+}$, the particles still retain their dispersibility, forming a colloid stable for several days. The loading of Ru^{II} on these NPs is estimated as 0.21 mmol.g^{-1} TiO$_2$ and 0.076 mmol.g^{-1} SiO$_2$. Thanks to the great dispersibility of these NPs, they were chosen for further studies in this thesis.

Table II-3 summarizes the [RuP]$^{2+}$ dye loading values on commercially available SiO$_2$ and anatase TiO$_2$ NPs. The loadings per particle and per nm^2 are roughly estimated by

assuming the diameter of TiO$_2$ and SiO$_2$ as 25 nm and 20 nm, respectively. For more detail the reader is kindly referred to the **Experimental Section**. The loadings per nm^2 for both kinds of NPs are in agreement with the loadings obtained with flat surfaces of SiO$_2$ and TiO$_2$ described in **Section II.3.2**.

Table II-3. Loading of [RuP]$^{2+}$ dye on commercially available SiO$_2$ and TiO$_2$ (anatase) NPs.

	Loading (mmol.g^{-1})	Molecules per particle	Molecules per nm^2
SiO$_2$/Ru^{II} NPs	0.076	460	0.5
TiO$_2$/Ru^{II} NPs	0.21	4000	2.0

II.3.4. Infrared spectroscopy

Figure II-12 presents the FT-IR spectra of SiO$_2$/Ru^{II} (a) and TiO$_2$/Ru^{II} NPs (b), in comparison with the phosphonic-derivatized dye, [RuP]$^{2+}$, and naked SiO$_2$ and TiO$_2$ NPs. The complex spectrum shows the P=O stretch at 1250 cm^{-1}, which disappears in the spectrum of TiO$_2$/Ru^{II}. A shoulder at ~1150 cm^{-1} for TiO$_2$/Ru^{II} (shown as a peak in the subtracted spectrum 4) is attributed to the bidentate surface linkage of –P(O)(O$^-$)$_2$.[20] The spectral changes are characteristic of the grafting of [RuP]$^{2+}$ on TiO$_2$ surface.

In the case of SiO$_2$/Ru^{II}, a strong, broad Si-O stretching band at about 1100 cm^{-1} precludes the detection of the phosphonate surface linkage, which is expected at ~1150 cm^{-1}.[21] However the spectrum of SiO$_2$/Ru^{II} displays a broader signal in this region compared to that of naked SiO$_2$ NPs. The P=O stretch at 1250 cm^{-1} partially remains on SiO$_2$/Ru^{II}. The grafting of [RuP]$^{2+}$ is then expected to be more stable on TiO$_2$ than on SiO$_2$.
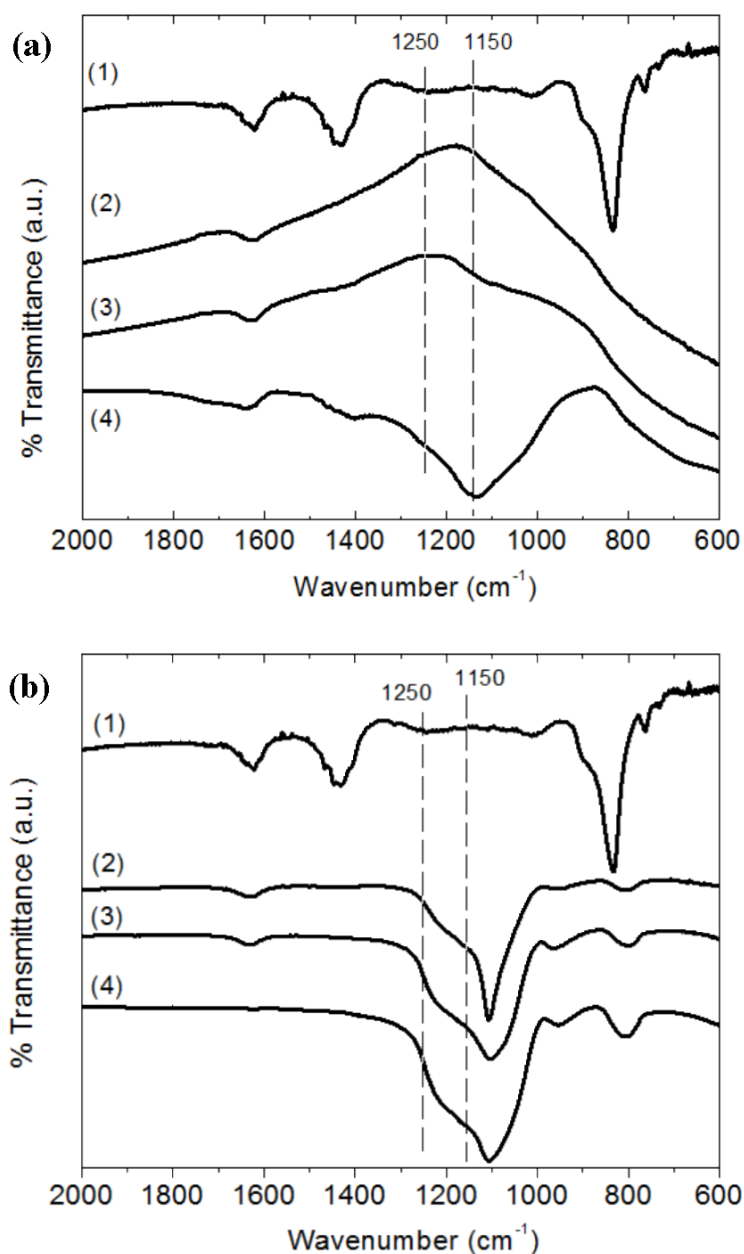
Figure II-12. (a) FT-IR spectra of: (1) $[RuP]^{2+}$, (2) anatase TiO_2, (3) TiO_2/Ru^{II}, (4) the subtraction of signal (2) from (3). (b) IR spectra of: (1) $[RuP]^{2+}$, (2) SiO_2, (3) SiO_2/Ru^{II}, (4) the subtraction of signal (2) from (3). Samples were measured in KBr pellets at room conditions.

II.3.5. Electrochemical properties

a) [RuP]²⁺ grafted on FTO

The electronic communication between grafted $[RuP]^{2+}$ and a metal oxide electrode was studied using a Fluorine-doped Tin Oxide (FTO) coated glass electrode. FTO was chosen because (i) the phosphonic group is suitable to be grafted on the surface,[22] and (ii) it is rather redox inactive in the range of Ru^{III}/Ru^{II} and Ru^{II}/Ru^{I} potentials. **Figure II-13a** presents the CV of the FTO/Ru^{II} electrode. Reversible waves at $E_{1/2}$ = 0.93 V and -1.76 V (ΔE = 60 mV) are attributed to Ru^{III}/Ru^{II} and Ru^{II}/Ru^{I} couples, which is in accordance with the protected

$[Ru\text{-}PO_3Et_2]^{2+}$ complex in MeCN solution (see **Section II.2.3**). A linear relationship between the anodic peak current I_{pa} vs scan rate v (**Figure II-13b**) for the Ru^{III}/Ru^{II} peak proves that the complex has been successfully grafted onto the electrode.

A quasi-reversible reduction peak at -1.25 V associated by an oxidation on the reversed scan at -0.65 V was detected. This system is attributed to the reduction of phosphonate anchoring group. For instance the CV of unprotected $[RuP]^{2+}$ in $MeCN:H_2O$ (95:5 v/v) mixture shows an irreversible reduction peak at -1.20 V (**Figure II-13c**) that is not present in the CV of protected $[Ru\text{-}PO_3Et_2]^{2+}$ complex (see **Figure II-4b**). In literature, when monolayers of *n*-alkane phosphonic acids are anchored on gold, a desorption peak was observed at -1.26 V *vs* SCE.[23] For $[RuP]^{2+}$ grafted on FTO, the reduction of phosphonate accompanied by an oxidation peak at -0.65 V shows better stability of the phosphonate group on metal oxide than gold.
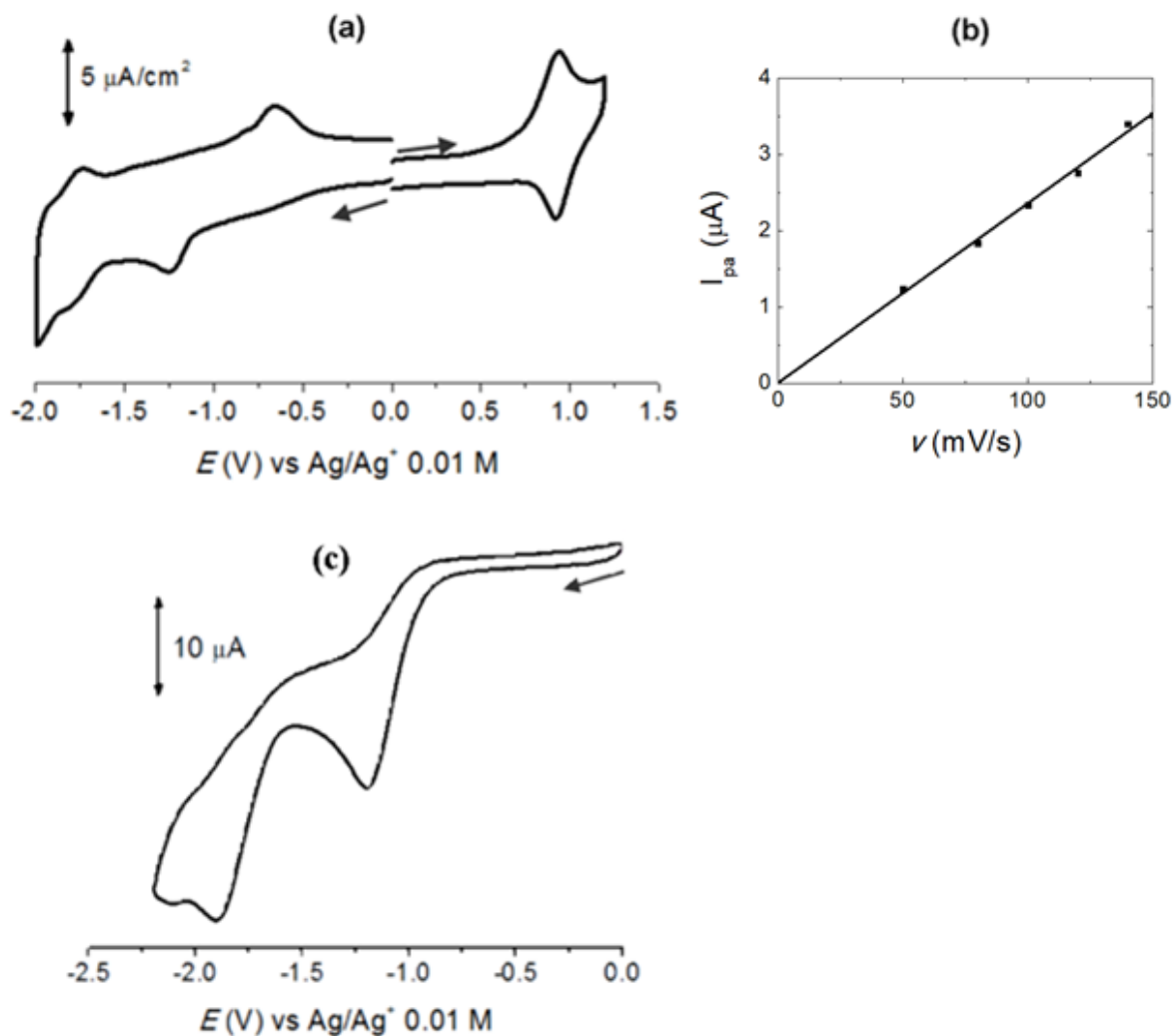
Figure II-13. (a) CV of FTO/Ru^{II} electrode, recorded in MeCN + 0.1 M TBAPF$_6$ under Ar, v = 100 mV.s^{-1}. (b) I_{pa}-v plot of Ru^{III}/Ru^{II} oxidation peak shows a linear relationship, R^2 = 0.999. (c) CV of $[Ru\text{-}PO_3H_2](PF_6)_2$ in MeCN/H_2O (95/5 v/v) solution containing 0.1 M TBAP under Ar, WE = C disk (d = 3 mm), v = 100 mV.s^{-1}

b) [RuP]$^{2+}$ on TiO$_2$ and SiO$_2$ NPs

Our attempts to characterize the electrochemical properties of SiO$_2$/Ru^{II} and TiO$_2$/Ru^{II} in colloidal solution with C, Pt disk electrodes or C sponge electrode were unsuccessful due to low conductivity of TiO$_2$ and SiO$_2$ and low coverage of the redox active species on the electrode surface. Therefore, SiO$_2$/Ru^{II} and TiO$_2$/Ru^{II} NPs were examined in powder form by cyclic voltammetry using a microcavity Pt working electrode ($d = 50$ µm). In the anodic portion, the SiO$_2$/Ru^{II} exhibits a reversible redox wave at $E_{1/2} = 0.92$ V ($\Delta E_p = 60$ mV) (**Figure II-14a**), whereas the TiO$_2$/Ru^{II} shows a quasi-reversible wave at $E_{1/2} = 0.98$ V ($\Delta E_p = 130$ mV) (**Figure II-14c**). The waves can be attributed to the Ru^{III}/Ru^{II} couple. The redox potential of Ru^{II} complex anchored on SiO$_2$ is similar to that of [Ru-PO$_3$Et$_2$]$^{2+}$ free complex in MeCN and FTO/Ru^{II} electrode, while there is a shift to a more positive oxidation potential when the complex is anchored on TiO$_2$. Positive shifts of the redox potential of Ru^{III}/Ru^{II} complexes grafted on a nanocrystalline TiO$_2$ thin film *versus* free complexes in solution have also been reported for phosphonate[3]- and carboxylate[24]-derivatized complexes.

In the cathodic portion of SiO$_2$/Ru^{II} NPs (**Figure II-14a**), the Ru^{II}/Ru^{I} peak at *ca.* -1.7 V of the precursor [Ru-PO$_3$Et$_2$]$^{2+}$ is not observed. In the case of TiO$_2$/Ru^{II} (**Figure II-14b**), the direct charge injection to the CB of TiO$_2$ starts at about -1.0 V *vs* Ag/Ag$^+$ 0.01 M. A similar CV for TiO$_2$ film deposited onto a graphite electrode (**Figure II-15**) shows that the charge injection to the CB occurs at around -0.6 V *vs* SCE (-0.9 V *vs* Ag/AgNO$_3$ 0.01 M).[25] In the CV of TiO$_2$/Ru^{II} NPs, the peak due to the reduction of TiO$_2$ NPs is so intense that the detection of a small quantity of [Ru(bpy)$_3$]$^+$ centered at -1.6 V, if any, is unfeasible.
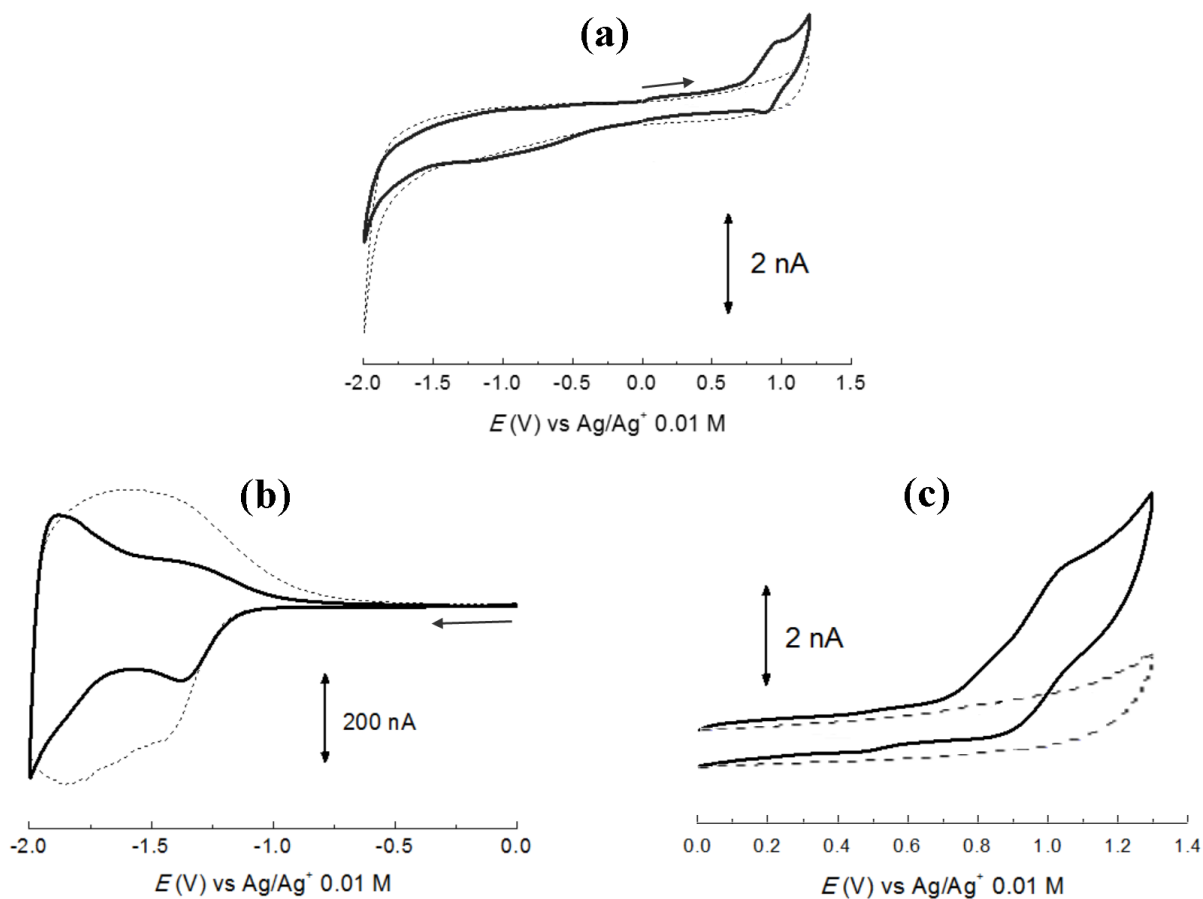
Figure II-14. (a) CVs of SiO_2/Ru^{II} (solid line) and bare SiO_2 (dotted line). (b) CVs of TiO_2/Ru^{II} (solid line) and bare TiO_2 (dotted line) in the cathodic region. (c) CVs of TiO_2/Ru^{II} (solid line) and bare TiO_2 (dotted line) in the anodic region. The CVs were recorded with a microcavity Pt electrode ($d = 50$ µm) in MeCN + 0.1 M TBAPF₆ under Ar, $v = 100$ mV.s⁻¹ .
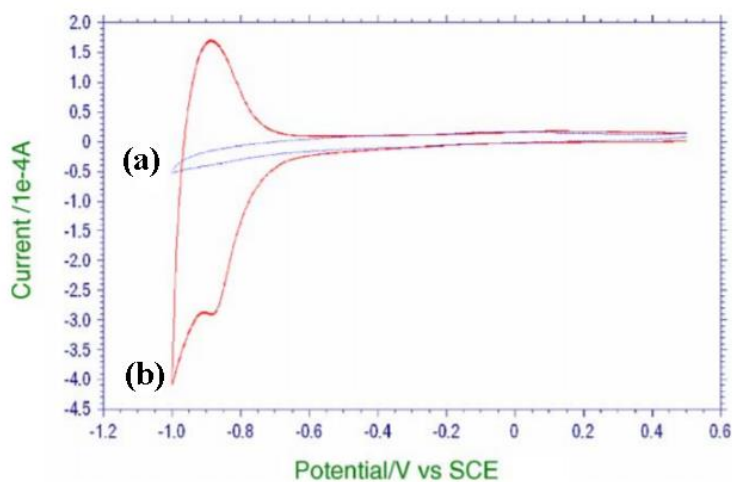
Figure II-15. CVs of bare graphite electrode (a) and a TiO_2 film deposited on graphite electrode (b) at pH 6. The CVs are taken from reference 25

II.3.6. Photophysical properties

a) UV-vis absorption spectroscopy and emission spectroscopy

The UV-vis absorption of SiO_2/Ru^{II} and TiO_2/Ru^{II} NPs was investigated in solid state using an integration sphere. The powders were dispersed in a KBr pellet as a transparent substrate in the UV-vis region. **Figure II-16a** presents their absorption after subtracting the absorbance of KBr + NPs. The peaks at ~450 nm of both functionalized NPs can be attributed to the ^{1}MLCT of $[Ru(bpy)_3]^{2+}$, as the $[Ru-PO_3Et_2]^{2+}$ shows a similar peak. The LCCT peak at 286 nm is evidenced for the SiO_2/Ru^{II} NPs. For TiO_2/Ru^{II} NPs, the absorption overlap between Ru^{II} dye and TiO_2 in the UV region makes it impossible to observe the LCCT at 286 nm for the dye. In fact, the absorption of TiO_2 NPs starts at ~392 nm (dotted line). This absorption of TiO_2 allows for the bandgap calculation: $E_g = \dfrac{1240}{\lambda_g} = \dfrac{1240}{392} = 3.2$ (eV) . The value is in accordance with the bandgap of bulk anatase TiO_2, since quantum confinement effects which cause larger bandgaps only take place where the diameter of the particles is below 1 nm.[26]

The emission of grafted Ru^{II*} excited state was normalized and shown in **Figure II-16b**. Both SiO_2/Ru^{II} and TiO_2/Ru^{II} NPs show a similar broad emission spectrum after being excited at 450 nm. While the emission peak of the former (612 nm) is comparable to the $[Ru-PO_3Et_2]^{2+}$ complex (615 nm), that of the latter is red-shifted to 627 nm. Since the Ru^{II} loading on TiO_2 is 3 times higher than on SiO_2 NPs, the redshift could be a consequence of a self-quenching process between adjacent Ru^{II} species on the same NP. Using **Equation II-1**, the oxidation potential of grafted Ru^{II*} excited state is calculated as -1.11 V for SiO_2/Ru^{II} and -1.00 V for TiO_2/Ru^{II}.
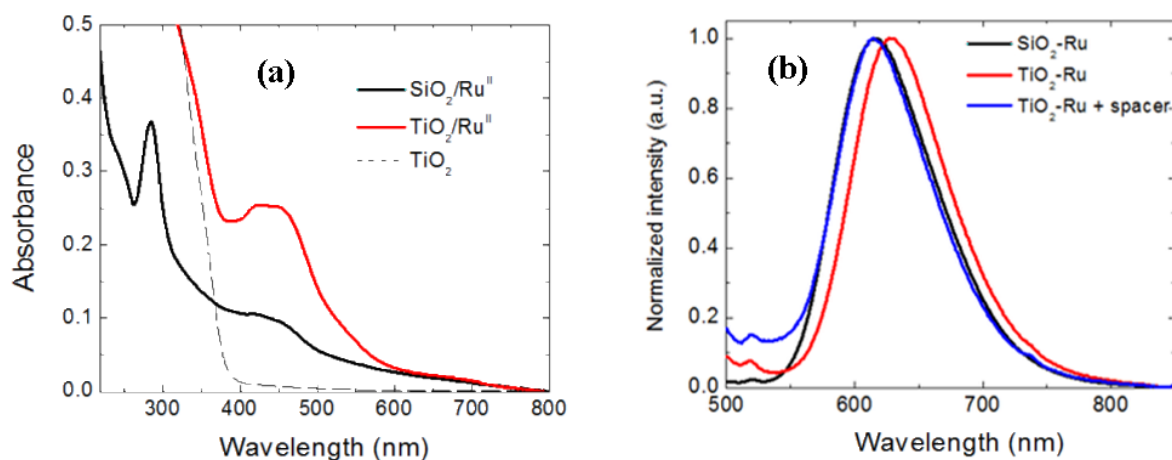
Figure II-16. (a) Solid state UV-vis and (b) emission spectra of SiO_2/Ru^{II} and TiO_2/Ru^{II} NPs.

In order to gain more insight into this emission shift, a mixture of $[RuP]^{2+}$ (10%) and benzylphosphonic acid (BPA, 90%) was immobilized onto TiO$_2$ NPs. The BPA acts as a lateral spacer to separate the Ru^{II} species on the particles. The resulting NPs, denoted as [TiO$_2$/Ru^{II} + spacers], display an emission peak at 615 nm (**Figure II-16b**) similar to that of SiO$_2$/Ru^{II} and [Ru-PO$_3$Et$_2$]$^{2+}$. Hence, the red-shift emission of TiO$_2$/Ru^{II} NPs could be attributed to the enhanced energy transfer between neighboring Ru^{II*} and Ru^{II} species.

Our attempts to measure the luminescence quantum yield of SiO$_2$/Ru^{II} and TiO$_2$/Ru^{II} colloids in MeCN were not successful. In order to measure it correctly, the absorbance of Ru^{II} species grafted on the NPs at 450 nm needs to be approximately equal to that of [Ru(bpy)$_3$](PF$_6$)$_2$ reference. However, the light scattering, which gradually raises the absorbance as the probe light is swept from long to short wavelengths, strongly affects the Ru^{II} absorbance at 450 nm. Mathematical attempts to subtract this light scattering effect from the real absorption of Ru^{II} species are not efficient. The effect makes it impossible to correctly determine the amount of Ru^{II} anchored on SiO$_2$ and TiO$_2$ NPs, thus the quantum yields are not measured.

b) Time-resolved emission spectroscopy

The time-resolved emission spectra of SiO$_2$/Ru^{II*} and TiO$_2$/Ru^{II*} were recorded after excitation by a 400 nm pulsed laser. The decays of the Ru^{II*} excited states are presented in **Figure II-17**. The signal of SiO$_2$/Ru^{II} NPs (black line) can be fit with a monoexponential decay to give a lifetime of 838 ns, which is comparable to that of the [Ru-PO$_3$Et$_2$]$^{2+}$ complex in Ar-saturated MeCN solution (907 ns). The signal of TiO$_2$/Ru^{II} (red line), however, can only be fit with a biexponential function to give two lifetime values: 366 ns and 32 ns. The fractional amplitudes of these lifetimes are 12% and 88%, respectively. The [TiO$_2$/Ru^{II} + spacers] NPs also exhibit a biexponential decay and two lifetimes with corresponding fractional amplitudes: 488 ns (2%) and 8 ns (98%). Hence, the short lifetime component of TiO$_2$/Ru^{II*} NPs is attributed to the electron injection from the Ru^{II*} to the CB of TiO$_2$, which is not observed for SiO$_2$/Ru^{II} NPs. The photo-induced electron transfer process from the Ru^{II*} state to TiO$_2$ is not total, as evidenced by the presence of a second component in the decay. This longer component still remains shorter than the excited state lifetime of [Ru-PO$_3$Et$_2$]$^{2+}$ free complex in solution, which may be a consequence of an additional energy transfer deactivation pathway between adjacent Ru^{II} centers on the NPs. The time-resolved luminescence decay shows that the energy quenching is more pronounced for TiO$_2$/Ru^{II} than SiO$_2$/Ru^{II}. It is probably due to the higher loading of Ru^{II} on TiO$_2$ than on SiO$_2$: about 2 molecules/nm^2 TiO$_2$ surface area compared with 0.5 molecules/nm^2 SiO$_2$ surface area.

Comparing the lifetimes of TiO$_2$/Ru^{II*} state with or without BPA spacers, one can observe a significant drop in the lifetime value (32 to 8 ns) associated with an increase in the fractional amplitude. It could be explained by the separation of grafted Ru^{II} species favoring the electron injection to TiO$_2$ and diminishing the energy transfer pathway.
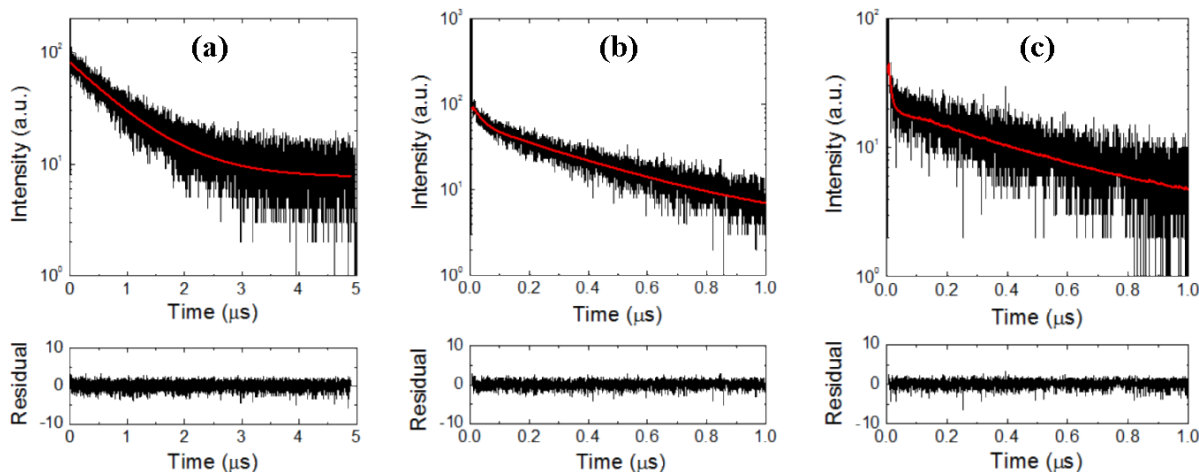
Figure II-17. Time-resolved emission spectra of (a) SiO$_2$/Ru^{II}, (b) TiO$_2$/Ru^{II} and (c) Ru^{II}/TiO$_2$/BPA (10% Ru^{II} and 90% BPA as spacer) in MeCN under Ar. The samples were excited by 400 nm picosecond pulsed laser, emitted photons were recorded at 610 nm using a TCSPC photometer. The red curves represent the monoexponential fitting of the decays

Using SiO$_2$/Ru^{II} lifetime as a reference where there are no electron injections, the kinetics of electron injection from Ru^{II*} to TiO$_2$ substrate, k_{inj}, can be calculated by **Equation II-5**:

$$k_{inj} = \frac{1}{\tau_1} - \frac{1}{\tau_{SiO_2/Ru}}$$ (Eq II-5)

where τ_1 and $\tau_{SiO_2/Ru}$ (s) are the short lifetime of TiO$_2$/Ru^{II*} and the lifetime of SiO$_2$/Ru^{II*}, respectively. Similarly, the kinetics of energy quenching of Ru^{II*} by neighboring Ru^{II}, k_q, referenced to [Ru-PO$_3$Et$_2$]$^{2+}$ free complex in solution, can be estimated by **Equation II-6**:

$$k_q = \frac{1}{\tau_2} - \frac{1}{\tau_{[Ru-PO_3Et_2]^{2+}}}$$ (Eq II-6)

where τ_2 and $\tau_{[Ru-PO_3Et_2]^{2+}}$ (s) are the long lifetime of TiO$_2$/Ru^{II*} and the lifetime of [Ru-PO$_3$Et$_2$]$^{2+}$, respectively. The kinetics values, together with the photophysical properties of the NPs, are collected in **Table II-4**.

Table II-4. Summary of photophysical properties of SiO$_2$/Ru^{II} and TiO$_2$/Ru^{II} colloids in MeCN

	^{1}**MLCT** λ_{abs}, nm	λ_{em}, **nm**	τ, **ns (%)** [a]	k_{inj}, **s^{-1}** [b]	k_q, **s^{-1}** [c]
[Ru-PO$_3$Et$_2$]$^{2+}$	450	615	895 ± 10	-	-
SiO$_2$/Ru^{II} NPs	450	612	838 ± 43	-	7.6×10^4
TiO$_2$/Ru^{II} NPs	450	627	366 ± 7 (12%)	3.0×10^7	1.6×10^6
			32 ± 0.6 (88%)		
Ru^{II}/TiO$_2$/BPA	450	615	488 ± 33 (2%)	1.2×10^8	9.5×10^5
(Ru:BPA = 1:9)			8 ± 0.4 (98%)		

[a] Emission lifetime recorded at 610 nm after excitation by 400 nm nanosecond pulsed laser
[b] Kinetics of electron injection from Ru^{II*} to TiO$_2$
[c] Kinetics of energy transfer from Ru^{II*} to a neighboring Ru^{II}

As seen in **Table II-4**, the rate of energy transfer on SiO$_2$/Ru^{II} NPs is significantly slower than on TiO$_2$/Ru^{II} due to lower loading of the [RuP]$^{2+}$ dye on SiO$_2$ (0.076 mmol.g^{-1}) than on TiO$_2$ (0.21 mmol.g^{-1}). The charge injection rates of TiO$_2$/Ru^{II} NPs to TiO$_2$ are significantly lower than that reported for a phosphonic-derivatized Ru-dye immobilized on a nanocrystalline TiO$_2$ electrode,[27] but they are in accordance with previous works in colloidal solutions.[28,29] The rates of energy transfer are comparable to a Ru-carboxylic dye grafted on a TiO$_2$ thin film electrode.[30] In the presence of a lateral spacer, the electron injection is significantly enhanced in terms of kinetics and percentage. **Table II-5** summarizes the kinetics of electron injection and kinetics of energy transfer for similar systems in the aforementioned works.

Table II-5. Summary of k_{inj} and k_q values obtained in literature for similar systems

Systems	k_{inj} or k_q (s^{-1})	Note	Ref.
on FTO/TiO₂ thin film	$k_{inj} = 3.3 \times 10^{13}$ (x = 1, 3) $k_{inj} = 2.0 \times 10^{13}$ (x = 2)	Injection from the ^{1}MLCT state. Measured with TAS in aqueous solution (pH = 6.7)	27
on FTO/TiO₂ thin film	$k_{inj} = 4.5 \times 10^{11}$ (x = 1) $k_{inj} = 2.0 \times 10^{11}$ (x = 2) $k_{inj} = 9.4 \times 10^{10}$ (x = 2)	Injection from the "hot electrons" on ^{3}MLCT state. Measured with TAS in aqueous solution (pH = 6.7)	27
In anatase TiO₂ colloid (*d* = 6 nm)	$k_{inj} = 3.2 \times 10^7$	Measured in aqueous solution at pH 2 by time-resolved emission spectroscopy	28
In anatase TiO₂ colloid (*d* = 7 nm)	$k_{inj} > 5.0 \times 10^7$ (> 80 % efficiency)	Measured in aqueous solution at pH 2 by TAS	29
On FTO/TiO₂ thin film	$k_q = 9.1 \times 10^6$	Measured in Ar-purged MeCN solution, modeled by Dexter quenching mechanism	30
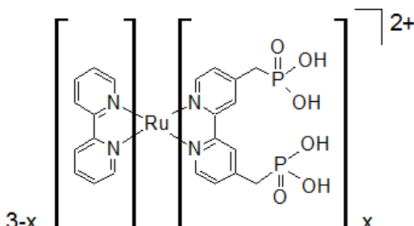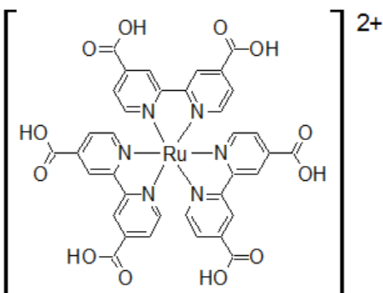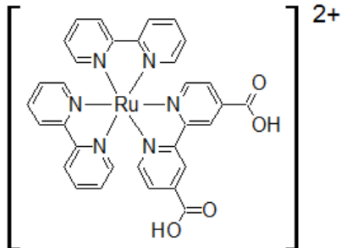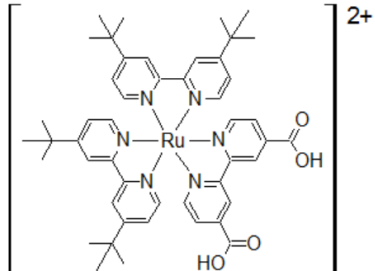
The lifetime component of the Ru^{II*} state due to energy quenching can also be used to estimate the average distance between neighboring Ru^{II} sites (*r (Ru-Ru)*) on the particle surface. Assuming a pure Forster resonance energy transfer (FRET) mechanism, the distance *r* can be estimated from the efficiency of the energy transfer process according to **Equation II-7**:[31]

$$Efficiency = \frac{R_0^6}{R_0^6 + r^6} = 1 - \frac{\tau_{DA}}{\tau_D} \qquad \text{(Eq II-7)}$$

where R_o is the Forster radius, τ_{DA} and τ_D (ns) are the luminescent lifetimes of the donor in the presence and absence of an acceptor, respectively. The τ_D value is determined by the lifetime of $[Ru\text{-}PO_3Et_2]^{2+*}$ in MeCN (895 ns).

The Forster radius is defined as the Ru-Ru distance where the efficiency of Forster energy quenching is equal to 50%. The Forster radius R_0 (nm) is calculated by **Equation II-8**:[31]

$$R_0^6 = 8.8 \times 10^{17} \left(\kappa^2 n^{-4} \phi_D J \right) \qquad \text{(Eq II-8)}$$

where Φ_D is the quantum yield of the donor, *n* is the refractive index of the solvent, κ is the orientation factor (usually equal to 2/3 for a chromophore free to rotate in solution) and *J* ($M^{-1}.cm^3$) is the overlap integral between the absorbance and emission spectra. *J* is calculated from **Figure II-18** and **Equation II-9**:

$$J = \frac{\int F_D(\lambda)\varepsilon_A(\lambda)\lambda^4 d\lambda}{\int F_D(\lambda)d\lambda} \qquad \text{(Eq II-9)}$$
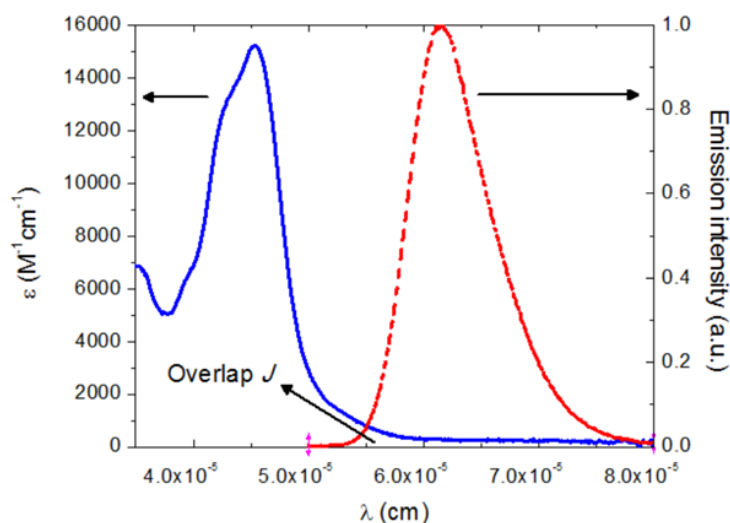
Figure II-18. Overlap between the absorption (blue solid line) and emission (red broken line) spectra of $[Ru\text{-}PO_3Et_2]^{2+}$, recorded in deaerated MeCN.

The overlap integral J is thus determined to be 4.4×10^{-15} M^{-1}.cm^3 and the Forster distance R_o is 1.9 nm. The FRET efficiency and Ru-Ru distance on SiO$_2$ and TiO$_2$ are summarized in **Table II-6**.

Table II-6. Forster resonance energy transfer: lifetime, efficiency and the distance between neighboring Ru^{II} species on TiO$_2$ and SiO$_2$ surfaces

	τ, ns	Efficiency	r (Ru-Ru), nm
[Ru-PO$_3$Et$_2$]$^{2+}$	895		
SiO$_2$/Ru^{II} NPs	838	0.06	2.5
TiO$_2$/Ru^{II} NPs	366	0.60	1.8
Ru^{II}/TiO$_2$/BPA	488	0.45	2.0

It is noted that the energy quenching of SiO$_2$/Ru^{II*} is drastically lower than TiO$_2$/Ru^{II*}, which is explained by a greater distance between the Ru^{II} sites. As expected, the addition of BPA spacers reduces the FRET efficiency. It is however still substantially higher than that of SiO$_2$/Ru^{II}. The Ru^{II} loading on the surfaces is estimated to be 0.076 mmol.g^{-1} for SiO$_2$/Ru^{II} and 0.02 mmol.g^{-1} for [TiO$_2$/Ru^{II} + spacers]. The higher Ru^{II} loading but lower FRET efficiency and greater Ru-Ru distance of SiO$_2$/Ru^{II} suggest then a more uniform distribution of [RuP]$^{2+}$ on SiO$_2$ than on TiO$_2$.

It should also be mentioned that taking into account the calculated average distances, the Dexter quenching mechanism cannot be totally excluded. Statistically speaking, some pairs of complex molecules can be in contact and their orbitals may overlap to exchange electrons. However, the distances calculated by the FRET method are in line with the surface loading of Ru^{II} species (see **Section II.3.3**): 0.5 molecules/nm^2 for SiO$_2$/Ru^{II} and 2 molecules/nm^2 for TiO$_2$/Ru^{II}.

c) Transient absorption spectroscopy

TA measurements were performed in order to study the absorption spectrum of photo-excited state of SiO$_2$/Ru^{II*} and TiO$_2$/Ru^{II*} and the kinetics of charge recombination. For that reason we chose to work with MeCN solvent under Ar to avoid any photocatalytic reactions involving the injected electrons on the CB of TiO$_2$ or the oxidized Ru^{3+} species. Diluted suspensions of NPs in MeCN were required to reduce light scattering effect by the NPs. Excitation light was chosen at 532 nm and a UV filter was placed in front of the lamp to avoid direct bandgap excitation of TiO$_2$ NPs.

We first investigated the TA spectrum of $[RuP]^{2+}$ complex grafted on SiO_2 NPs and compare it with the spectrum of $[Ru\text{-}PO_3Et_2]^{2+}$ free complex which has been presented in **Section II.2.2c**. The transient spectrum of SiO_2/Ru^{II*} 20 ns after excitation at 532 nm is shown in **Figure II-19a**. Signal bleaching at 450 nm is observed which is similar to the TA spectrum of $[Ru\text{-}PO_3Et_2]^{2+}$ free complex (see **Section II.2.2**). The bleaching is assigned to the absorption of the ground state of $[Ru(bpy)_3]^{2+}$ core which has been depopulated upon absorption of 532 nm photons. Attempts to record the full TA spectra after the laser excitation are not successful due to precipitation of the NPs over a time period longer than 15 minutes.

Figure II-19b shows the time profile of the absorbance change of SiO_2/Ru^{II} 20 ns after the laser excitation. The signal has been averaged from 40 measurements due to weak absorption of the NPs. The signal recovers to the initial value within 10 µs. The signal was fit with a monoexponential function to yield a lifetime of 3630 ± 480 ns. It is surprisingly four times longer than the lifetime of SiO_2/Ru^{II*} state recorded with the time-resolved emission spectroscopy (838 ns). However, this experiment is reproducible to give similar lifetimes regardless of the colloid concentration.
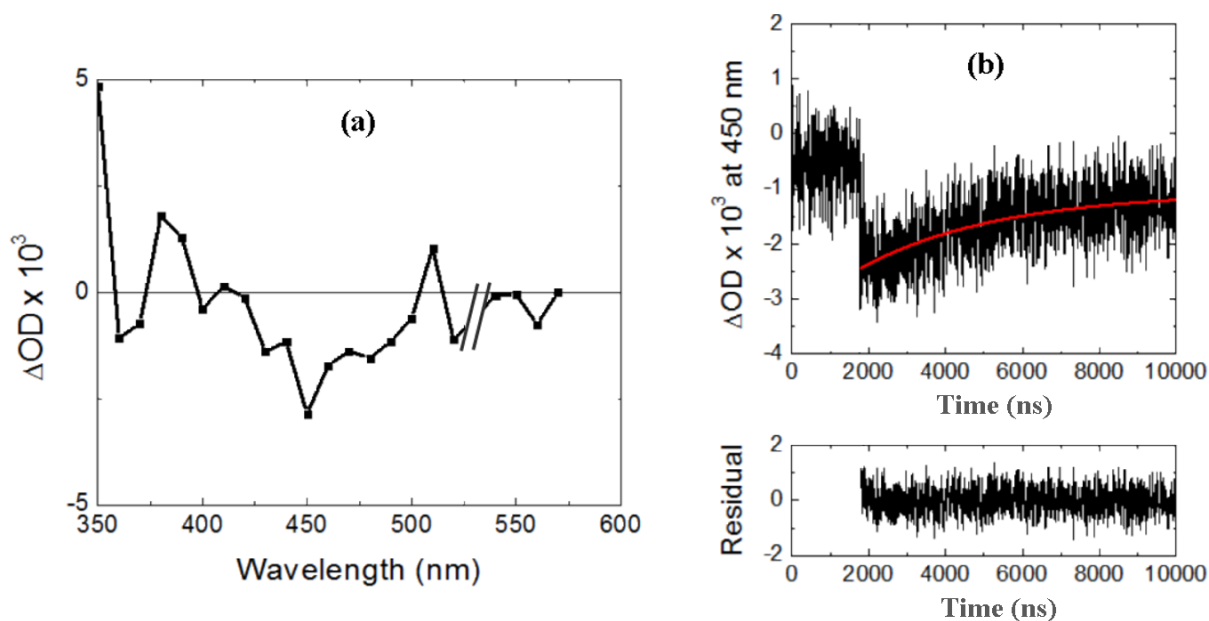
Figure II-19. (a) TA spectrum of SiO_2/Ru^{II} NPs in MeCN under Ar 20 ns after excitation by a nanosecond pulse laser at 532 nm. The data point at 530 nm has been removed to eliminate the scattering of excitation light by the NPs. (b) Signal bleaching at 450 nm (black) fit with a monoexponential function (red) and the fitting residual. The signal has been averaged from 40 measurements.

The charge recombination of $(e^-)TiO_2$ and Ru^{3+} species was then studied by the TA measurements. Following the excitation at 532 nm, the absorbance change was recorded 20 ns after the laser pulse (**Figure II-20a**). The spectrum exhibits a broad, featureless positive

change in optical density (OD) from 450 nm to 570 nm. A decay at 450 nm, which has been averaged for 20 measurements is also shown in the inset. The experiment is reproducible regardless of the concentration of TiO_2/Ru^{II} NPs.

The positive change in OD at 450 nm is surprising for us since we expect a negative change as in the case of $[Ru-PO_3Et_2]^{2+}$ free complex or SiO_2/Ru^{II*} NPs. Since the charge injection from grafted Ru^{2+*} to TiO_2 occurs in nanosecond time scale to reduce the amount of ground state Ru^{2+} while Ru^{3+} absorbs less than Ru^{2+} at 450 nm[5], the negative OD change at 450 nm is anticipated. We therefore conclude that the positive OD change is due to the absorption of injected electrons on TiO_2, $(e^-)TiO_2$. G. Meyer[27,32] and E. Reisner[33] observed the absorption of anatase $(e^-)TiO_2$ at wavelengths between 600 nm and 750 nm. Nevertheless, their results have been based on $[Ru(bpy)_3]^{2+}$-sensitized mesoporous TiO_2 thin films deposited on FTO electrodes, whereas we work with colloids in MeCN solution.

The analysis of recombination kinetics is complicated because the diffusion of both trapped electrons and oxidized dye molecules need to be taken into account. This diffusion mechanism leads to multiple pathways for the charges to recombine. Therefore, the kinetics was fit with the Kohlrausch – Williams – Watts (KWW) model as a stretched exponential equation[30] (**Equation II-10**):

$$\Delta OD = \Delta OD_{max} \exp\left[-\left(\frac{t}{\tau_{KWW}}\right)^{\beta_{KWW}}\right] \qquad \text{(Eq II-10)}$$

where ΔOD is the absorbance change, τ_{KWW} and β_{KWW} the apparent lifetime and power of the stretched exponential function ($0 \leq \beta_{KWW} \leq 1$). To facilitate the fitting process, this equation can be transformed to:

$$-\ln\left(\frac{\Delta OD}{\Delta OD_{max}}\right) = \left(\frac{t}{\tau_{KWW}}\right)^{\beta_{KWW}} \qquad \text{(Eq II-11)}$$

This equation is conveniently fit with a power function. **Figure II-20b** presents the *-ln(ΔOD/ΔOD_{max}) vs t* plot and the fitting curve.
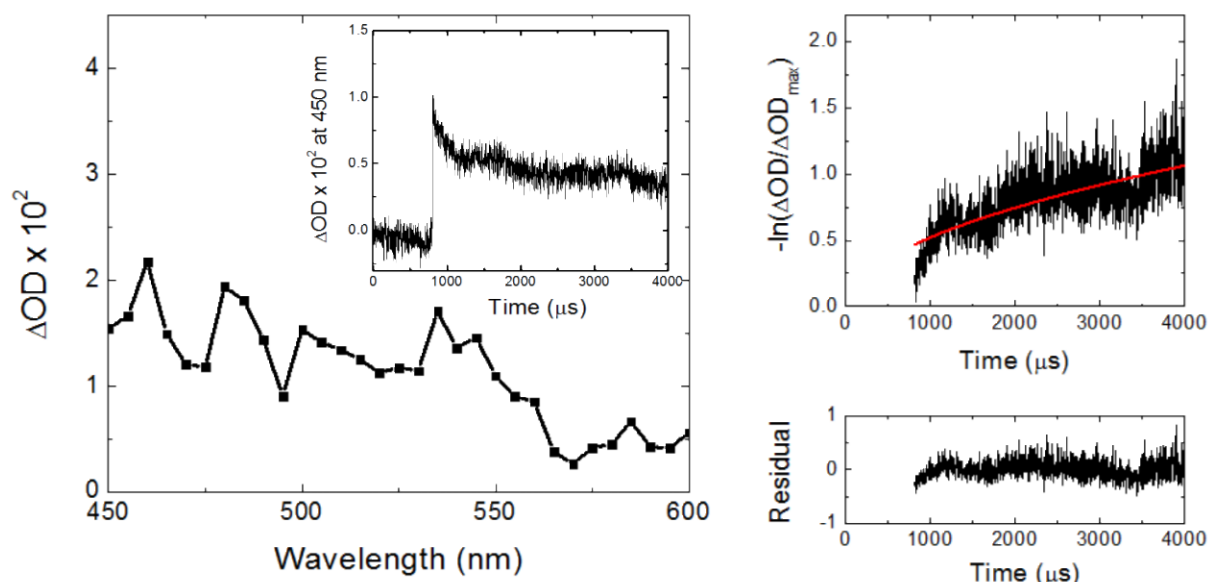
Figure II-20. (a) TA spectrum of TiO$_2$/Ru^{II} NPs in MeCN under Ar 20 ns after excitation by a nanosecond pulse laser at 532 nm. Inset shows the decay at 450 nm. (b) *–ln(ΔOD/ΔOD$_{max}$) versus t* plot (black line) obtained at 450 nm and fit with a power function (red line).

From the KWW model fitting, the parameters τ_{KWW} = (3770 ± 800) µs and β_{KWW} = (0.51 ± 0.01) are obtained. The fact that β_{KWW} value is far from 1 justifies the stretched exponential model. In a similar study[30] concerning [Ru(dtb)$_2$(dcb)]$^{2+}$ dye (dtb = 4,4'-C(CH$_3$)$_3$)$_2$-2,2'-bipyridine and dcb = 4,4'-(COOH)$_2$-2,2'-bipyridine) grafted on mesoporous TiO$_2$ thin film, β_{KWW} was found to be 0.14 and τ_{KWW} was 0.14 µs. A representative charge recombination kinetics k_{cr} is then calculated as follows:[32]

$$k_{cr} = \left[\frac{1}{k_{KWW}\beta_{KWW}} \Gamma\left(\frac{1}{\beta_{KWW}}\right) \right]^{-1} = \left[\frac{\tau_{KWW}}{\beta_{KWW}} \Gamma\left(\frac{1}{\beta_{KWW}}\right) \right]^{-1} \tag{Eq II-12}$$

The recombination kinetics is estimated as (140 ± 30) s^{-1}. This result suggests the recombination kinetics 5 orders of magnitude slower than the kinetics of electron injection to TiO$_2$. It also shows that a longer linker between the [Ru(bpy)$_3$]$^{2+}$ PS and phosphonic goup reduces the charge recombination rate more significantly than shorter linkers: for example without methylene groups the [Ru(dtb)$_2$(dcb)]$^{2+}$ grafted on TiO$_2$ thin film exhibits recombination kinetics of ~1 × 10^3 s^{-1}.[32] Such a very slow recombination process allows efficient charge injection and utilization of the photo-generated CB electrons and oxidized "hole" dye molecules on TiO$_2$ surface in successive redox reactions.

II.3.7. Electron paramagnetic resonance spectroscopy

Electron paramagnetic resonance (EPR) spectroscopy has been employed to identify the sites of photo-induced trapped electrons on TiO$_2$ NPs as they are paramagnetic. Upon photon

absorption at 455 nm by the $[Ru(bpy)_3]^{2+}$ dye, an electron is injected to the CB of TiO_2 and then trapped in Ti^{3+} sites, which will be called here "electron traps". The charge separated state $(e^-)TiO_2/Ru^{3+}$ was then created and directly observed with the EPR spectroscopy at 20 K. We first examined different irradiation methods:

- *Ex situ* irradiating an EPR tube containing TiO_2/Ru^{II} colloid in water or MeCN by a 455 nm LED for 2-3 hours, then freezing the tube with liquid nitrogen
- *In situ* irradiating an EPR tube containing the powder or colloid of interest by immersing an optical fiber inside

Our experiments show that the *ex situ* irradiation method does not produce enough paramagnetic species to be observed. It is probably due to charge recombination between $(e^-)TiO_2$ and Ru^{3+} sites occurring when the tube is transferred from the dewar to the EPR cavity. *In situ* irradiation with a fiber immersed inside the tube containing TiO_2/Ru^{II} in powder form or in colloid does not improve the signal. Comparing the powder form and colloid, we found that the colloid gives better signal, possibly due to its better ability to diffuse light throughout the sample. Therefore, a colloid in MeCN and *in situ* irradiation from the wall of the EPR cavity have been chosen for further studies. MeCN solvent was used in order for the EPR experiment to be consistent with previously described characterizations. Details of the experimental setup can be found in the **Experimental Section**.

Figure II-21 presents its EPR signal, as well as the signal simulation of the trapped electrons on Ti^{3+} anatase sites. The signal remains stable for a few minutes after the light is switched off. It is also reproducible when the sample is raised to room temperature, then frozen again and irradiated with the laser. The electron traps are characterized by two *g* values: $g_\perp = 1.990$ and $g_{//} = 1.959$ as shown by the simulation in **Figure II-21**. The *g* values have been corrected with 2,2-diphenyl-1-picrylhydrazyl (DPPH) reference (*g*=2.0036). As a comparison, the EPR signal of naked anatase TiO_2 NPs remains unchanged under the 455 nm irradiation. Therefore, the recorded signal is attributed to the trapped electrons on Ti^{3+} sites,[34,35] while the electrons on the CB of TiO_2 are EPR silent.[36] There are also no trapped holes (usually denoted as $O^{\bullet-}$ centers in literature)[35] detected in this study, proving that the electron transfer from Ru^{2+*} to TiO_2 generates the signal instead of electron promotion from the VB to the CB of TiO_2. The signal of Ru^{3+} is, however, not detectable. This can be explained by the fact that its EPR spectrum is around 70 times broader than the spectrum of Ti^{3+} (~3500 G for Ru^{3+} compared with ~50 G for Ti^{3+}), so the EPR signal corresponding to Ru^{3+} should appear roughly $70 \times 70 = 4900$ times smaller than the EPR signal corresponding

to Ti^{3+}. Therefore, the Ru^{3+} signal is not detectable. The signal reproducibility upon changing temperature proves that the electron transfer process is reversible.

In **Figure II-21** one can observe the presence of additional four EPR lines (1:3:3:1 ratio) separated by 23 G, which are marked by asterisks. The lines are assigned to •CH$_3$ radicals.[37] In our process it may come from the photocatalytic degradation of ethanol[38,39] as it may not be completely removed by heating in an oven at 80 ^{0}C.
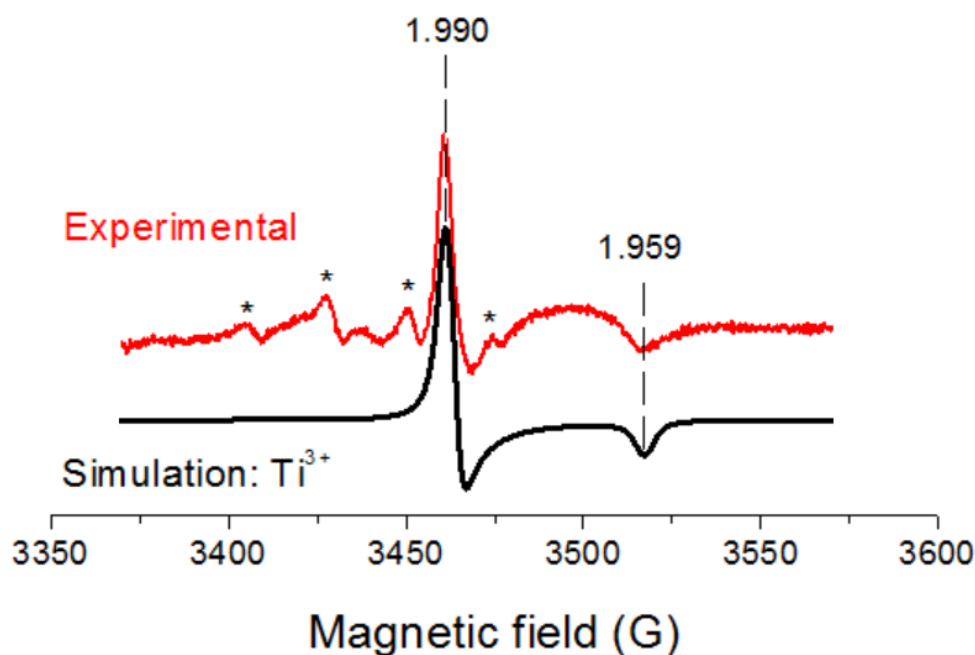
Figure II-21. EPR signal of photo-induced charge separation on TiO$_2$/Ru^{II} colloid (10 mg/mL) in MeCN glass (red line) and the simulation of trapped electrons on Ti^{3+} sites of anatase TiO$_2$ (black line). Asterisks show the signal of •CH$_3$ radicals. The sample was irradiated *in situ* by a 455 nm LED. The spectrum was taken at 20 K with an X-band EPR spectrometer (f = 9.65208 GHz, 2 mW, 5 G modulation), accumulated for 30 minutes.

II.4. Conclusion

In **Chapter 2** we have reported the study of a [Ru(bpy)$_3$]$^{2+}$-based photosensitizer bearing a phosphonic group to be grafted onto the surface of TiO$_2$ and SiO$_2$ NPs. The phosphonate-derivatized precursor [Ru-PO$_3$Et$_2$]$^{2+}$ has been extensively characterized in MeCN solution using electrochemistry, UV-vis spectroscopy, luminescent emission spectroscopy and time-resolved emission spectroscopy. The results show that it retains excellent properties of the prototype [Ru(bpy)$_3$]$^{2+}$ photosensitizer after ligand modifications.

Functionalization of NPs with [RuP]$^{2+}$ dye has been proved to be more efficient on TiO$_2$ than SiO$_2$, reaching the [RuP]$^{2+}$ loading of 0.21 mmol/g TiO$_2$ and 0.076 mmol/g SiO$_2$ NPs. The successful grafting of [RuP]$^{2+}$ on SiO$_2$ and TiO$_2$ surfaces has been proved by the QCM-D and FT-IR experiments. After being anchored, the [RuP]$^{2+}$ complex shows a similar oxidation potential as the [Ru-PO$_3$Et$_2$]$^{2+}$ free complex in solution. The wavelength of emission maximum is almost unchanged. The kinetics of visible light-induced electron transfer from Ru^{II*} units to TiO$_2$ and energy transfer from Ru^{II*} to Ru^{II} immobilized on the surfaces of TiO$_2$ and SiO$_2$ have been studied in colloids with time-resolved emission spectroscopy and TAS. The results indicate a nanosecond injection rate from Ru^{II*} to TiO$_2$ with ~ 90 % yield, followed by a millisecond charge recombination rate, thus proving an efficient, long-lived charge separated state. The addition of lateral spacers to separate neighboring Ru^{II} species shows a marked increase in the kinetics and the yield of electron injection to TiO$_2$, which is attributed to the reduced energy transfer between the photosensitizers. The FRET study also reveals an average distance of 2.5 nm (SiO$_2$/Ru^{II}) and 1.8 nm (TiO$_2$/Ru^{II}) between neighboring Ru^{II} species on the surface. Finally, the photo-induced charge separated state (e$^-$)TiO$_2$/Ru^{3+} has been directly observed *in situ* by EPR spectroscopy. The mechanistic studies in this Chapter serves as a fundamental basis for the following chapters where additional redox active components are anchored on the TiO$_2$ NPs.

References

1   H.-Y. Wang, J. Liu, J. Zhu, S. Styring, S. Ott and A. Thapper, *Phys. Chem. Chem. Phys.*, 2014, **16**, 3661–3669.

2   F. P. Dwyer, H. A. Goodwin and E. C. Gyarfas, *Aust. J. Chem.*, 1963, **16**, 544–548.

3   K. Hanson, K. M. Brennaman, A. Ito, H. Luo, W. Song, K. A. Parker, R. Ghosh, M. R. Norris, C. R. K. Glasson, J. J. Conception, R. Lopez and T. J. Meyer, *J. Phys. Chem. C*, 2012, **116**, 14837–14847.

4   Y. Gao, L. Zhang, X. Ding and L. Sun, *Phys. Chem. Chem. Phys.*, 2014, **16**, 12008–12013.

5   A. Juris, V. Balzani, F. Barigelletti, S. Campagna, P. Belser and A. von Zelewsky, *Coord. Chem. Rev.*, 1988, **84**, 85–277.

6   N. E. Tokel-Takvoryan, R. E. Hemingway and A. J. Bard, *J. Am. Chem. Soc.*, 1973, **95**, 6582–6589.

7   M. Maestri, N. Armaroli, V. Balzani, E. C. Constable and A. M. W. C. Thompson, *Inorg. Chem.*, 1995, **34**, 2759–2767.

8   A. G. Motten, K. Hanck and M. K. DeArmond, *Chem. Phys. Lett.*, 1981, **79**, 541–546.

9   R. E. DeSimone and R. S. Drago, *J. Am. Chem. Soc.*, 1970, **92**, 2343–2352.

10   D. E. Morris, K. W. Hanck and M. K. DeArmond, *J. Am. Chem. Soc.*, 1983, **105**, 3032–3038.

11   W. Stober and A. Fink, *J. Colloid Interface Sci.*, 1968, **26**, 62–69.

12   I. A. Rahman, P. Vejayakumaran, C. S. Sipaut, J. Ismail, M. A. Bakar, R. Adnan and C. K. Chee, *Colloids Surfaces A Physicochem. Eng. Asp.*, 2007, **294**, 102–110.

13   G. Oskam, A. Nellore, R. L. Penn and P. C. Searson, *J. Phys. Chem. B*, 2003, **107**, 1734–1738.

14   T. Luttrell, S. Halpegamage, J. Tao, A. Kramer, E. Sutter and M. Batzill, *Sci. Rep.*, 2014, **4**, 1–8.

15   M. A. Henderson, *Surf. Sci. Rep.*, 2011, **66**, 185–297.

16   W. Li and C. Ni, *J. Appl. Phys.*, 2004, **96**, 6663–6668.

17   X. Chen and S. S. Mao, *Chem. Rev.*, 2007, **107**, 2891–2959.

18   G. Sauerbrey, *Z. Phys.*, 1959, **155**, 206–222.

19   R. Boissezon, J. Muller, V. Beaugeard, S. Monge and J.-J. Robin, *RSC Adv.*, 2014, **4**, 35690–35707.

20   B. J. Brennan, M. J. L. Portoles, P. A. Liddell, T. A. Moore, A. L. Moore and D. Gust, *Phys. Chem. Chem. Phys.*, 2013, **15**, 16605–16614.

21   W. A. Pliskin, *Appl. Phys. Lett.*, 1965, **7**, 158–159.

22   X. Marguerettaz and D. Fitzmaurice, *Langmuir*, 1997, **13**, 6769–6779.

23   J. F. Cabrita, A. S. Viana, F.-P. Montforts and L. M. Abrantes, *Surf. Sci.*, 2011, **605**, 1412–1419.

24   Q. Wang, S. M. Zakeeruddin, M. K. Nazeeruddin, R. Humphry-Baker and M. Gratzel, *J. Am. Chem. Soc.*, 2006, **128**, 4446–4452.

25   J. Zhang, C. Yang, G. Chang, H. Zhu and M. Oyama, *Mater. Chem. Phys.*, 2004, **88**, 398–403.

26   Y. Ma, X. Wang, Y. Jia, X. Chen, H. Han and C. Li, *Chem. Rev.*, 2014, **114**, 9987–10043.

27   P. G. Giokas, S. A. Miller, K. Hanson, M. R. Norris, C. R. K. Glasson, J. J. Concepcion, S. E. Bettis, T. J. Meyer and A. M. Moran, *J. Phys. Chem. C*, 2013, **117**, 812–824.

28   J. Desilvestro, M. Gratzel, L. Kavan and J. Moser, *J. Am. Chem. Soc.*, 1985, **107**, 2988–2990.

29   R. Argazzi, C. A. Bignozzi, T. A. Heimer, F. N. Castellano and G. J. Meyer, *J. Phys. Chem. B*, 1997, **101**, 2591–2597.

30   S. Ardo and G. J. Meyer, *J. Am. Chem. Soc.*, 2011, **133**, 15384–15396.

31   S. Acikgoz, G. Aktas, N. M. Inci, H. Altin and A. Sanyal, *J. Phys. Chem. B*, 2010, **114**, 10954–10960.

32   R. N. Sampaio, A. V. Muller, A. S. Polo and G. J. Meyer, *ACS Appl. Mater. Interfaces*, 2017, **9**, 33446–33454.

33   F. Lakadamyali, A. Reynal, M. Kato, J. R. Durrant and E. Reisner, *Chem. Eur. J.*, 2012, **18**, 15464–15475.

34   R. F. Howe and M. Gratzel, *J. Phys. Chem.*, 1987, **91**, 3906–3909.

35   C. P. Kumar, N. O. Gopal, T. C. Wang, M.-S. Wong and S. C. Ke, *J. Phys. Chem. B*, 2006, **110**, 5223–5229.

36   T. Berger, M. Sterrer, O. Diwald, E. Knozinger, D. Panayotov, T. L. Thompson and J. T. Yates, *J. Phys. Chem. B*, 2005, **109**, 6061–6068.

37   M. Kaise, H. Nagai, K. Tokuhashi, S. Kondo, S. Nimura and O. Kikuchi, *Langmuir*, 1994, **10**, 1345–1347.

38   V. Brezova, P. Tarabek, D. Dvoranova, A. Stasko and S. Biskupic, *J. Photochem. Photobiol. A Chem.*, 2003, **155**, 179–198.

39   D. Dvoranova, Z. Barbierikova and V. Brezova, *Molecules*, 2014, **19**, 17279–17304.

CHAPTER III

CHROMIUM(III) BIS-TOLYLTERPYRIDINE COMPLEXES AS ELECTRON ACCEPTORS

Abstract

In this chapter, the rich electrochemical and photophysical properties of $[Cr(ttpy)_2]^{3+}$ (ttpy = 4'-(*p*-tolyl)-2,2':6',2''-terpyridine) complex will be discussed. Different redox states of $[Cr(ttpy)_2]^{n+}$ (n = 3, 2, 1, 0) complex have been studied with UV-vis absorption spectroscopy and Electron Paramagnetic Resonance (EPR) spectroscopy. DFT calculations show that all the reduction steps occur on the ttpy ligands. The $[Cr(ttpy)_2]^{3+}$ complex can be doubly reduced to $[Cr(ttpy)_2]^{+}$ by $[Ru(bpy)_3]^{2+}$ photosensitizer under visible irradiation in presence of triethanolamine (TEOA), showing its ability to store two reduction equivalents on the Cr complex. This multi-electron storage ability can also be achieved with a mixture of TiO_2/Ru^{II} nanoparticles (NPs), $[Cr(ttpy)_2]^{3+}$ and TEOA in solution. Furthermore, the doubly reduced $[Cr(ttpy)_2]^{+}$ complex shows some activity as a catalyst for the proton reduction reaction in a non-aqueous solution. Afterwards, the $[Cr(ttpy)_2]^{3+}$ alone or in association with the $[Ru(bpy)_3]^{2+}$ complexes are grafted on TiO_2 NPs via phosphonic acid as anchoring group to form $TiO_2/[Cr2P]^{3+}$ dyad and $Ru^{II}/TiO_2/[Cr2P]^{3+}$ triad structures. In contrast to the free $[Cr(ttpy)_2]^{3+}$ complex in solution, the $Ru^{II}/TiO_2/[Cr2P]^{3+}$ triad does not show the ability to store electrons on the $[Cr2P]^{3+}$ units under continuous irradiation in the presence of TEOA. It may be due to accelerated kinetics of back electron transfer between grafted transient $[Cr2P]^{2+}$ and Ru^{3+} species in close proximity at the surface of the NPs.

Résumé

Dans ce chapitre, les propriétés électrochimiques et photophysiques du complexe $[Cr(ttpy)_2]^{3+}$ (ttpy = 4'-(*p*-tolyl)-2,2':6',2''- terpyridine) sont décrites. Différents états redox du complexe $[Cr(ttpy)_2]^{n+}$ (n = 3, 2, 1, 0) ont été étudiés par spectroscopie d'absorption UV-vis et spectroscopie par résonance paramagnétique électronique (RPE). Les calculs DFT confirment que toutes les étapes de réduction se produisent sur les ligands ttpy. Le complexe $[Cr(ttpy)_2]^{3+}$ peut être doublement réduit sous la forme $[Cr(ttpy)_2]^{+}$ par irradiation dans le visible en présence de triéthanolamine (TEOA) comme donneur d'électron sacrificiel. La réaction est accélérée en ajoutant le $[Ru(bpy)_3]^{2+}$ dans le milieu. La réaction de photoréduction à également lieu entre les nanoparticules hybride TiO_2/Ru^{II} et le complexe $[Cr(ttpy)_2]^{3+}$ libre en solution en présence de TEOA. En outre, le complexe $[Cr(ttpy)_2]^{+}$ doublement réduit présente une activité catalytique vis à vis de la réduction des protons en solution organique. Les complexes de $[Cr(ttpy)_2]^{3+}$ seul ou avec le $[Ru(bpy)_3]^{2+}$ ont aussi été immobilisées à la surface des nanoparticules de TiO_2 pour former des systèmes de dyade hybride $TiO_2/[Cr2P]^{3+}$ et de triade $Ru^{II}/TiO_2/[Cr2P]^{3+}$. Contrairement aux systèmes précédents, la triade $Ru^{II}/TiO_2/[Cr2P]^{3+}$ ne permet pas de stocker des électrons sur les unités $[Cr2P]^{3+}$ sous irradiation continue en présence de TEOA. Cela peut être dû à une cinétique rapide du transfert d'électrons en retour entre les espèces transitoire $[Cr2P]^{2+}$ et Ru^{III} greffées, à proximité en surface des nanoparticules.

III.1. Introduction

III.1.1. Chromium(III) polypyridyl complexes

Among the polypyridyl complexes of first-row transition metals, Cr(III) complexes still remain underexplored in comparison with notably Co(III) and Fe(II) complexes.[1] Herein, the photophysics and electrochemistry of $[Cr(tpy)_2]^{3+}$ (tpy = 2,2':6',2''-terpyridine) and $[Cr(bpy)_3]^{3+}$ (bpy = 2,2'-bipyridine) complexes will be briefly summarized to emphasize its rich properties. For more detail the reader is kindly referred to recent reviews by Kane-Maguire[2] and Ford[3].

The hexacoordinated Cr(III) complexes possesses an $[Ar]3d^3$ configuration of the metal ion and an octahedral symmetry.[2] A simplified Jablonski energy diagrams of relevant energy levels is shown in **Scheme III-1**. In the ground state, the three electron occupy three t_{2g} orbitals rendering the spin state $S = 3/2$. The quartet ground state is hence denoted $^4A_{2g}$. Upon photon absorption, an electron can be promoted from a t_{2g} orbital to one of the two unoccupied e_g orbitals without changing its spin state. Depending on the orientation of the t_{2g} and e_g orbitals involved in this electron promotion, two energy levels are formed, namely $^4T_{2g}$ and $^4T_{1g}$. The former has a lower energy level. As the electron is relaxed to the lowest energy level $^4T_{2g}$, it can return to the ground state by fluorescence emission or non-radiative decays. The $^4T_{2g} \rightarrow {}^4A_{2g}$ transition, however, is rarely observed due to very fast, efficient $^4T_{2g} \rightarrow {}^2E_g$ intersystem crossing. The latter transition requires a change in spin state to form a doublet. From the ^2E_g state the electron can relax to the ground state via phosphorescence emission and non-radiative decays as well. Several Cr(III) complexes exhibit relatively long-lived phosphorescence emission at room conditions ($\tau > 100$ ns).[2]
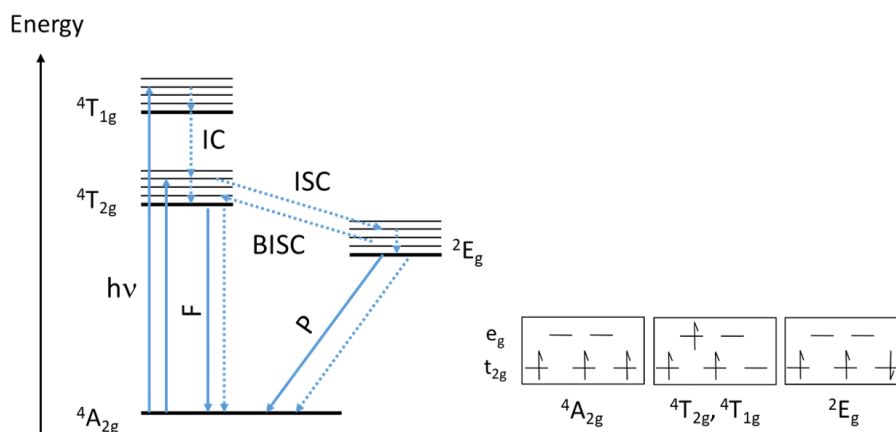
Scheme III-1. Simplified Jablonski energy diagram for octahedral Cr(III) polypyridyl complexes. IC = internal conversion, ISC = intersystem crossing, BISC = back intersystem crossing, F = fluorescence, P = phosphorescence. Solid arrows indicate processes involving photon absorption or emission, while dotted arrows show processes that do not involve the photon absorption and emission. Adapted from reference 2

Homoleptic Cr(III) bipyridine and terpyridine complexes have shown rich photophysical properties. In a pioneering paper published in 1979, Serpone et al.[4] studied the photophysical behavior of the $[Cr(bpy)_3]^{3+}$ and $[Cr(tpy)_2]^{3+}$ complexes. In nitrogen-purge aqueous solution, emission lifetime of ^2E_g state of $[Cr(bpy)_3]^{3+*}$ (63 µs) is considerably longer than that of $[Cr(tpy)_2]^{3+*}$ (~ 50 ns). An analogous pairs, $[Ru(bpy)_3]^{2+*}$ and $[Ru(tpy)_2]^{2+*}$ complexes, also exhibit a similar trend. The authors proposed that due to a more open structure in the tpy complexes, the metal core is more exposed to solvent molecules which can enhance the non-radiative relaxation of its excited state. Consequently, the emission lifetime is lower than in the bpy complexes. In addition, quenching of the ^2E_g states of $[Cr(bpy)_3]^{3+*}$ by I^-, Fe^{2+} or O_2 has also been shown to be efficient. The bimolecular quenching rate is ranging from 10^7 $M^{-1}.s^{-1}$ (for O_2) to 10^9 $M^{-1}.s^{-1}$ (for I^-).

Furthermore, homoleptic Cr(III) bipyridyl and terpyridyl complexes also show rich electrochemical properties. For example, Wieghardt and co-worker[5] reported that $[Cr(tpy)_2]^{3+}$ shows four reversible one-electron reduction processes. Based on density functional theory (DFT) calculations supported by a wide range of spectroscopic techniques, they attributed all the four added electrons to ligand-reduction processes while Cr remains +3. The study suggests the possibility to accumulate multiple electrons on the complex, which is a crucial step towards multi-electron catalysis such as proton or CO_2 reduction. The complex has also been proposed as a potential candidate for the water reduction because water molecules, in solid state, are found to stay close to the Cr(III) core of the $[Cr(tpy)_2]^{3+}$ complex encompassed by two orthogonal tpy ligands.[6] However, this proposed catalytic reaction has not been published yet.

An important and recent progress in this field is the successful synthesis of heteroleptic Cr(III) polypyridyl complexes.[7,8] It opens a new route to functionalize the tpy ligands with suitable anchoring groups to graft the complex onto surfaces or to synthesize dyads in order to explore its capability of storing multiple charges at a single Cr(III) site.

III.1.2. Accumulation of multiple redox equivalents in molecular – semiconductor hybrid systems

In the search for sustainable energy sources to replace traditional but polluted fossil fuels, hydrogen produced by proton reduction reaction arises as an absolutely clean source. Besides, the capture and conversion of the infamous greenhouse gas CO_2 into more value-added energy sources has also received particular attention in recent years. However, both the water reduction to form H_2 and CO_2 reduction using molecular catalysts require the accumulation of more than one electron on the catalytic sites. For instance the proton

reduction to H_2 is a two electron reduction process. We are interested in molecular systems capable of accumulating multiple redox equivalents under visible light. In this part we will highlight the challenges associated with the multiple charge accumulation processes and some recent advances in the field, with a focus on a novel class of molecular-semiconductor hybrid systems. Detailed reviews on the multi-charge storage and catalytic applications can be found in literature.[9,10]

According to Hammarstrom,[9] the multiple charge accumulation can be attained in molecular structures consisting of an Electron Donor (D) – Photosensitizer (PS) – Electron Acceptor (A) covalently linked together. Under light irradiation, this triad architecture allows to separate positive and negative charges over a long distance to reduce the rate of back electron transfer. The resulting charge separated state D^+-PS-A^- can be again photoexcited followed by another charge separation step to form the multiple charge separated state D^{2+}-PS-A^{2-}. **Scheme III-2** illustrates the charge separation steps and possible charge recombination pathways.
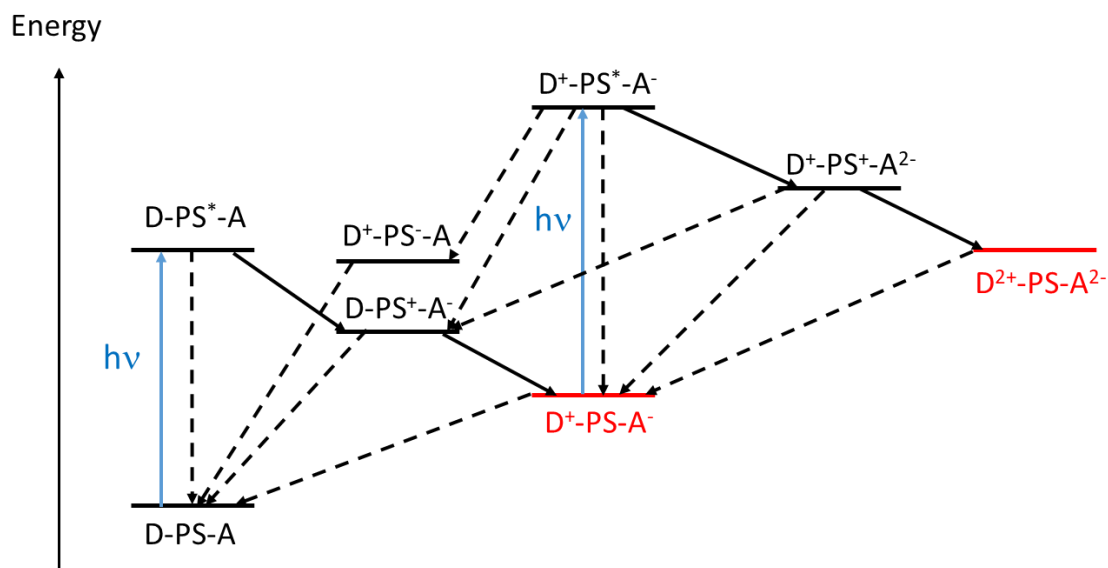
Scheme III-2. Generic scheme for a photo-induced, sequential charge transfer process leading to multiple charge accumulation in D-PS-A triad. Solid blue and black arrows indicate transformations involving a photon or an electron, respectively. Dashed arrows indicate possible charge recombination pathways. Adapted from reference 9

The charge accumulation faces several major challenges such as: (i) efficient PS to harvest light and to selectively inject the photo-excited electron to A, (ii) suitable energy levels of the components, (iii) sufficient long lifetime of the charge separated state D^+-PS-A^-, (iv) chemically stable A^- and D^+ species. Therefore, it is challenging to design purely molecular systems for the charge accumulation. Redox relays are sometimes required to

suppress the back electron transfer steps. The competing back electron transfer processes and the difficulties to synthesize these supramolecules are of the main barriers.

Meanwhile, molecular – semiconductor (TiO_2) hybrid systems have several advantages over the purely molecular systems such as: (i) easier synthesis of individual components, (ii) long-lived charge separated state $(e^-)TiO_2/Ru^{3+}$ (see **Chapter 2**), (iii) TiO_2 as a scaffold for grafting a wide range of complexes. This chapter is hence dedicated to this hybrid material class (two examples have already been described in **Section I.3**).

a) Accumulation of multiple oxidative equivalents

The first example for the accumulation of multiple oxidative equivalents using a regenerative PS and a multi-electron donor has been reported by Hammarstrom and co-workers[11]. The authors covalently linked a $[Ru(bpy)_2(CN)]^{2+}$ PS to an oligo(triarylamine) (OTA) electron donor, and the Ru-OTA complex was grafted onto TiO_2 nanoparticles (NPs) (**Scheme III-3**). After the first laser pulse excitation at 510 nm, the Ru^{2+*} state injects an electron to TiO_2 to form $(e^-)TiO_2/Ru^{3+}$ within 5 ps. A single electron transfer from OTA regenerates the Ru^{2+} dye in less than 1 ns. The charge separated state $(e^-)TiO_2/Ru^{II}$-OTA^+ is then formed with ~ 100 % yield. Afterwards, the second laser pulse at 480 nm excites the Ru^{2+} dye and another electron is injected to TiO_2, followed by the rapid reduction of Ru^{3+} by OTA^+ ($\tau \ll 15$ ns). The resulting multiple charge separated state, $(2e^-)TiO_2/Ru^{2+}$-OTA^{2+}, has been shown to be formed with remarkable nearly 100 % yield and attributed to the efficient separation between the A sites (TiO_2) and D sites (OTA). The photo-induced electron transfer is schematically described in **Scheme III-3**.
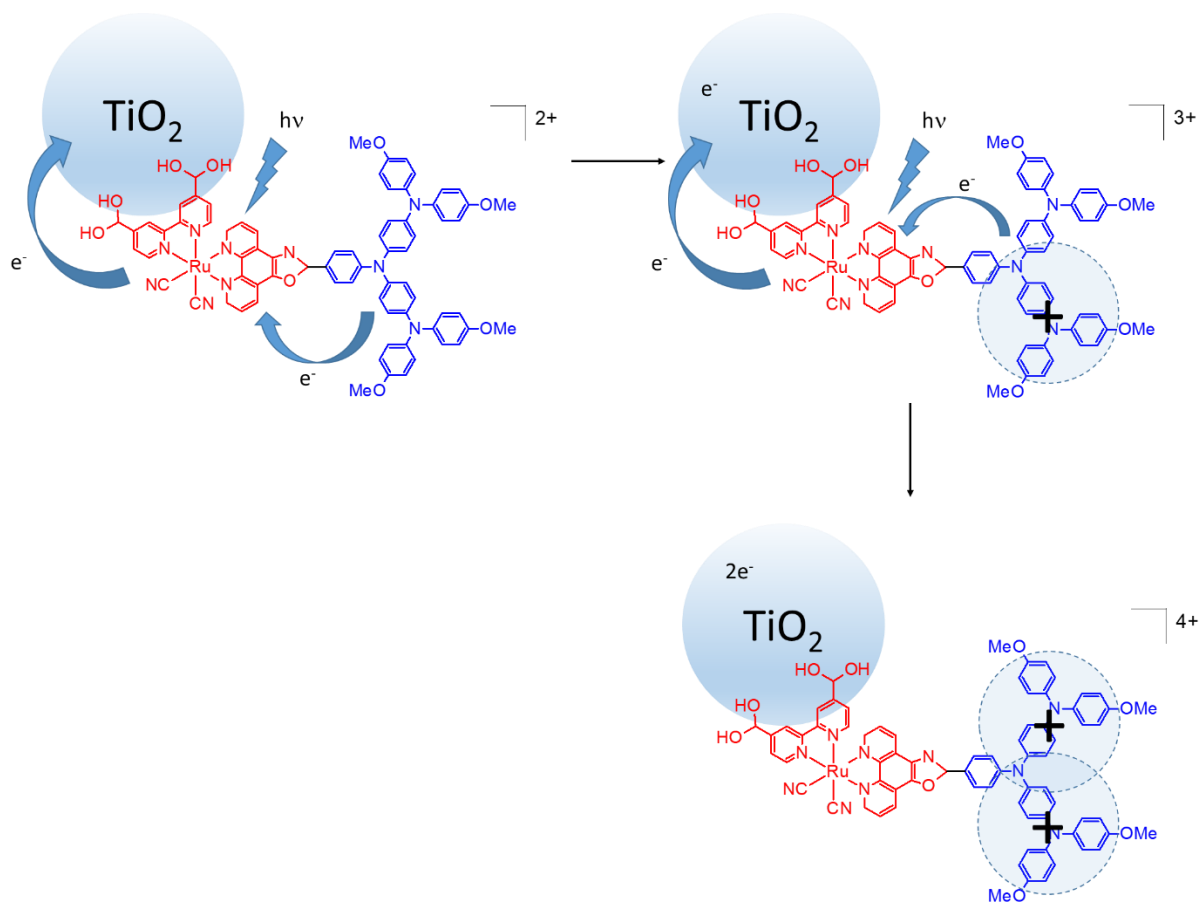
Scheme III-3. Accumulation of two oxidative equivalents on OTA site of TiO_2/Ru-OTA NPs which is mentioned in reference 11. *Note:* OTA$^+$ and OTA^{2+} oxidative charges are delocalized over the whole OTA unit.

The pioneering work by Hammarstrom's group has motivated other researchers to develop this D-PS-A design for catalytic applications. For example, T. J. Meyer and co-workers reported a PS – molecular catalyst dyad anchored on TiO_2 thin film electrode for water oxidation in aqueous solution[12] (**Scheme III-4a**). They covalently grafted a Ru_a^{II}-Ru_b^{II}-OH_2 dinuclear complex on mesoporous TiO_2 thin film electrode, where Ru_a^{II} acts as a visible light PS and Ru_b^{II}-OH_2 is a known pre-catalyst for water oxidation to produce O_2.[13] Steady-state and transient spectroscopic studies have been conducted to probe the formation of transient species under irradiation and their associated electron transfer kinetics. After the first laser pulse, the Ru_a^{II} PS is excited and quickly injects an electron to TiO_2 film in less than 20 ns, followed by the electron transfer from Ru_b^{II} site to transiently form $(e^-)TiO_2$/Ru_a^{II}-Ru_b^{III}-OH species with ~ 10 % quantum yield. When a bias is applied to pre-oxidize the system to form TiO_2/Ru_a^{II}-Ru_b^{III}-OH, the irradiation excites an electron of the Ru_a^{II} PS, followed by electron injection to TiO_2. Subsequently, another mono-electron transfer occurs between Ru_b^{III}-OH and Ru_a^{III} species to form Ru_a^{II} and Ru_b^{IV}=O within 20 ns and < 15 % yield. The work has provided experimental spectroscopic evidence for sequential mono-electron transfer steps towards the accumulation of two oxidative equivalents in Ru^{IV}=O centers, which is the

catalytic center for water oxidation reaction[13]. **Scheme III-4a** schematically illustrates the electron transfer events.

As a comparison, T. J. Meyer and co-workers also applied the similar concept but a Ru_a^{II} PS and Ru_b^{II} molecular catalyst have been co-loaded on TiO_2 thin film electrode (**Scheme III-4b**) instead of being covalently linked together.[14] The first photoexcitation and electron injection also occurs at less than 20 ns. Lateral hole hopping process between Ru_a^{III} and Ru_b^{II}-OH_2 to yield Ru_a^{II} and Ru_b^{III}-OH is accomplished within hundreds of microseconds, which is significantly lower than the covalently linked Ru_a-Ru_b-OH_2 complex. However, when the Ru_b^{II}-OH_2 is pre-oxidized to Ru_b^{III}-OH by an applied bias, no signal of Ru_b^{IV}=O has been detected when the Ru_a/Ru_b molar ratio is around 1.8:1. It is attributed to the increased recombination rate between $(e^-)TiO_2$ and oxidized Ru_a^{III} or Ru_b^{III}-OH species. Increasing the Ru_a/Ru_b ratio to 6.4:1 has indeed allowed for the formation of the desired Ru_b^{IV}=O species.
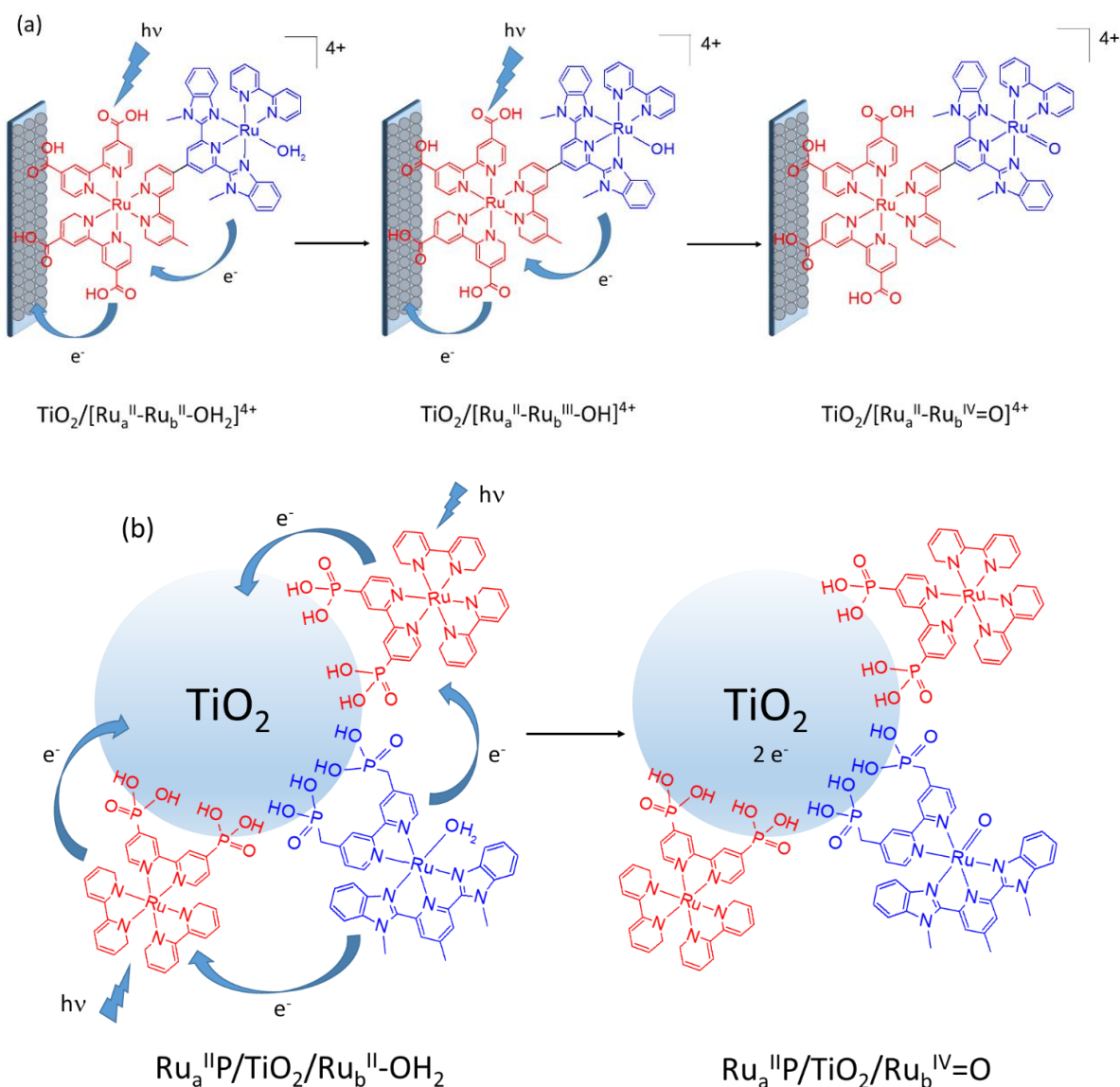
Scheme III-4. Multiple oxidative equivalents accumulated on single molecular site for photocatalytic water oxidation: (a) $[Ru_a\text{-}Ru_b\text{-}OH_2]^{4+}$ PS-catalyst assembly immobilized on mesoporous TiO_2 thin film electrode mentioned in reference 12; (b) $Ru_a/TiO_2/Ru_b\text{-}OH_2$ PS/TiO_2/catalyst assembly (Ru_a:Ru_b = 6.4:1 % mol) mentioned in reference 14.

b) Accumulation of multiple reductive equivalents

On the other hand, efforts have been made to accumulate multiple reductive equivalents under visible light. From a purely molecular approach, Wasielewski and co-workers[15] made the first report using perylene bis(carboxyimide) (PBDCI) as an electron acceptor connected with two porphyrins (P2H) as PS (**Scheme III-5**). Under laser excitation, both P2H units can be simultaneously excited to the singlet state, then sequentially transferring an electron to PBDCI moiety to achieve a doubly reduced species, PBDCI^{2-}. The resulting charge separated state, $^+$H2P-PBDCI^{2-}-P2H$^+$, shows a relatively short lifetime of ~ 5 ns. Interestingly, this work

emphasizes the role of excitation light intensity for the charge accumulation on the PBDCI unit.
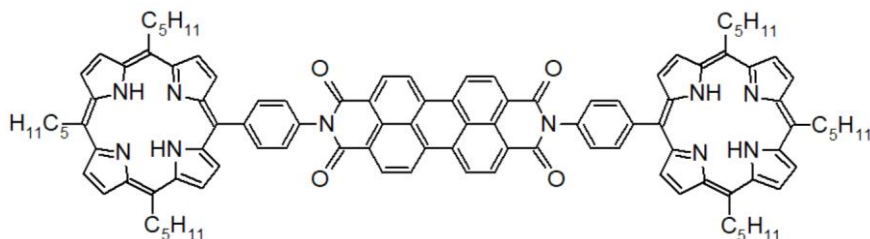
Scheme III-5. Molecular structure of H2P-PBDCI-P2H mentioned in reference 15

To date, most of the works rely on purely molecular systems.[9,10,16,17] Very few publications have been made using semiconducting NPs like TiO_2 as an electron relay in the PS-TiO$_2$-A architecture to suppress the back electron transfer process and to accumulate multiple electrons on the A sites. In 2012, Durrant, Reisner et al.[18] have proposed to use TiO_2 NPs as an electron relay between $[Ru(bpy)_3]^{2+}$ PS and a cobaloxime as a catalyst (**Scheme III-6**) for proton reduction reaction, which has already been described in **Section I.3**. However, no direct evidence for the accumulation of two electrons on the Co^{III} site was observed, although the authors obtained H_2 with $TON_{max} = 108$, and the proton reduction to H_2 is a two-electron process.
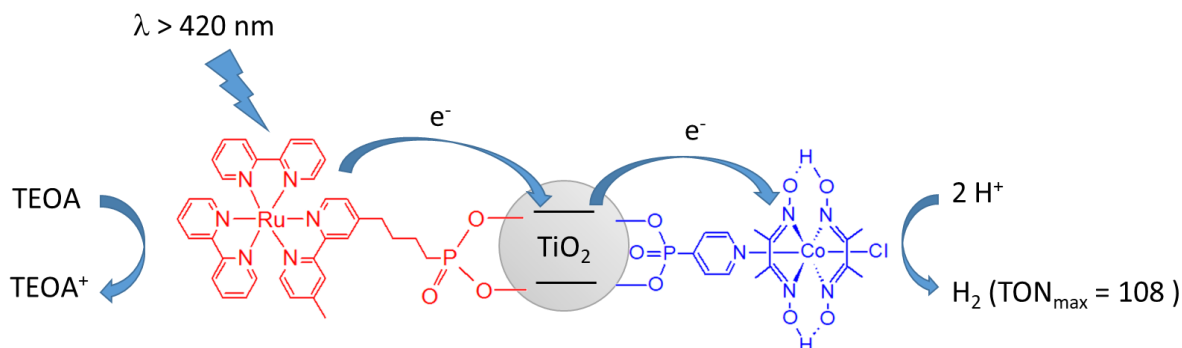
Scheme III-6. Structure of $Ru^{II}/TiO_2/Co^{III}$ (Ru:Co = 3:1 % mol) mentioned in reference 18

In this chapter we will first discuss the electrochemical and photophysical properties of $[Cr(ttpy)_2]^{3+}$ (ttpy = 4'-(*p*-tolyl)-2,2':6',2''-terpyridine) complex. The ttpy instead of tpy ligand has been chosen for the convenience of subsequent functionalization of the methyl group with phosphonic acid to be anchored on TiO_2. Multiple electron storage induced by visible light will also be mentioned. The electrocatalytic activity of the homogeneous complex towards proton reduction will be addressed as well. Afterwards, the building and characterization of TiO_2/Cr^{3+} and $Ru^{2+}/TiO_2/Cr^{3+}$ NPs following the PS-TiO$_2$-A design will be thoroughly described.

III.2. Chromium(III) bis-tolylterpyridine complexes in solution

III.2.1. Synthesis

The synthesis of $[Cr(ttpy)_2]^{3+}$ complex with ClO_4^- counter anions is depicted in **Scheme III-7**. Starting material has been chosen to be $CrCl_2$ thanks to the lability of the metal ion. Indeed, Cr^{3+} is known to be inert, which makes it difficult for complexation. After the complexation between Cr^{2+} salt and ttpy ligand under Ar atmosphere, an excess amount of $NaClO_4$ was added to precipitate the complex out of water/ethanol solvent. The reaction mixture was then bubbled with air to yield the desired product $[Cr(ttpy)_2]^{3+}$. It has been shown that this strategy may prevent the dissociation of the ttpy ligand in the presence of water, as water can coordinate with the Cr^{3+} metal core.[19] As the sample is paramagnetic, it cannot be investigated with ^1H NMR spectroscopy.
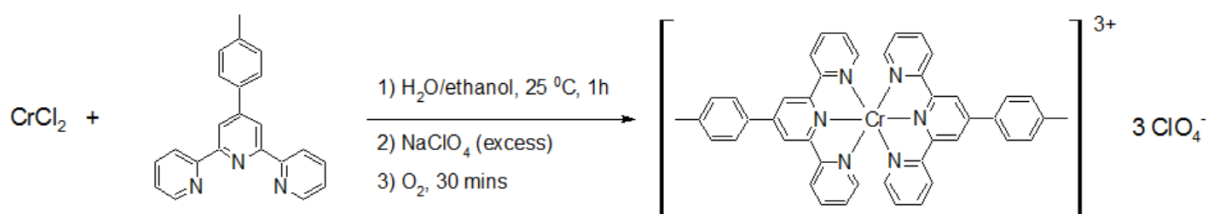
Scheme III-7. Synthesis procedure for $[Cr(ttpy)_2]^{3+}$ complex

III.2.2. Electrochemical properties

The electrochemical properties of $[Cr(ttpy)_2]^{3+}$ complex have been studied by cyclic voltammetry (**Figure III-1**, black line) and the redox potentials are collected in **Table III-1**. The complex shows no oxidation waves when the potential is swept until 1.5 V *vs* Ag/AgNO₃ 0.01 M. In the cathodic scanning, it shows four successive one-electron reduction processes at $E_{1/2}$ = -0.47, -0.85, -1.35 and -2.25 V. All the waves show peak-to-peak splitting ΔE_p around 60 – 70 mV, indicating electrochemically reversible processes. The redox potentials are in accordance with literature.[7] The analogous $[Cr(tpy)_2]^{3+}$ complex also shows comparable redox potentials: $E_{1/2}$ (V) = -0.44, -0.86, -1.36 and -2.28 *vs* Ag/AgNO₃ 0.01 M reference electrode.[20] Although the ttpy ligand in this studies contains tolyl substituting group at the *para* position which is a weak electron donating group, its effect on the redox potentials is negligible.

Meanwhile, the ttpy ligand alone (**Figure III-1**, green line) shows a reduction wave at $E_{1/2}$ = -2.35 V which is less reversible (ΔE_p = 90 mV). We thus assign the fourth reduction process to the reduction of the complex rather than free ttpy ligand.

$$[Cr(ttpy)_2]^{3+} + e^- \rightleftharpoons [Cr^{III}(ttpy)(ttpy^{\bullet-})]^{2+} \qquad E_{1/2} = -0.47 \text{ V}$$

$$[Cr(ttpy)_2]^{2+} + e^- \rightleftharpoons [Cr^{III}(ttpy^{\bullet-})(ttpy^{\bullet-})]^{+} \qquad E_{1/2} = -0.85 \text{ V}$$

$$[Cr(ttpy)_2]^+ \ + \ e^- \ \rightleftharpoons \ [Cr^{III}(ttpy^{\bullet-})(ttpy^{2-})]^0 \qquad\qquad E_{1/2} = -1.35 \text{ V}$$

$$[Cr(ttpy)_2]^0 \ + \ e^- \ \rightleftharpoons \ [Cr^{III}(ttpy^{2-})(ttpy^{2-})]^- \qquad\qquad E_{1/2} = -2.25 \text{ V}$$
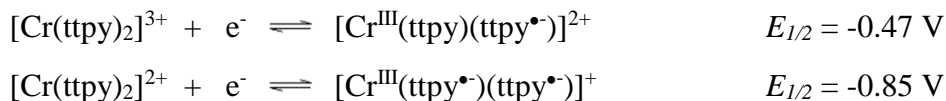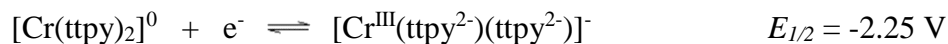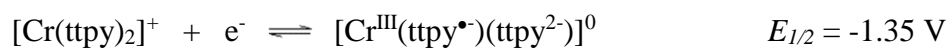
Since the Cr^{III} core is thought to be redox inert, the added electrons are localized on the ttpy ligands.[5] However, to simplify the notations we will use those on the left side hereafter unless it is necessary to clarify:

$$[Cr(ttpy)_2]^{2+} \ = \ [Cr^{III}(ttpy)(ttpy^{\bullet-})]^{2+}$$

$$[Cr(ttpy)_2]^+ \ = \ [Cr^{III}(ttpy^{\bullet-})(ttpy^{\bullet-})]^+$$

$$[Cr(ttpy)_2]^0 \ = \ [Cr^{III}(ttpy^{\bullet-})(ttpy^{2-})]^0$$

$$[Cr(ttpy)_2]^- \ = \ [Cr^{III}(ttpy^{2-})(ttpy^{2-})]^{1-}$$
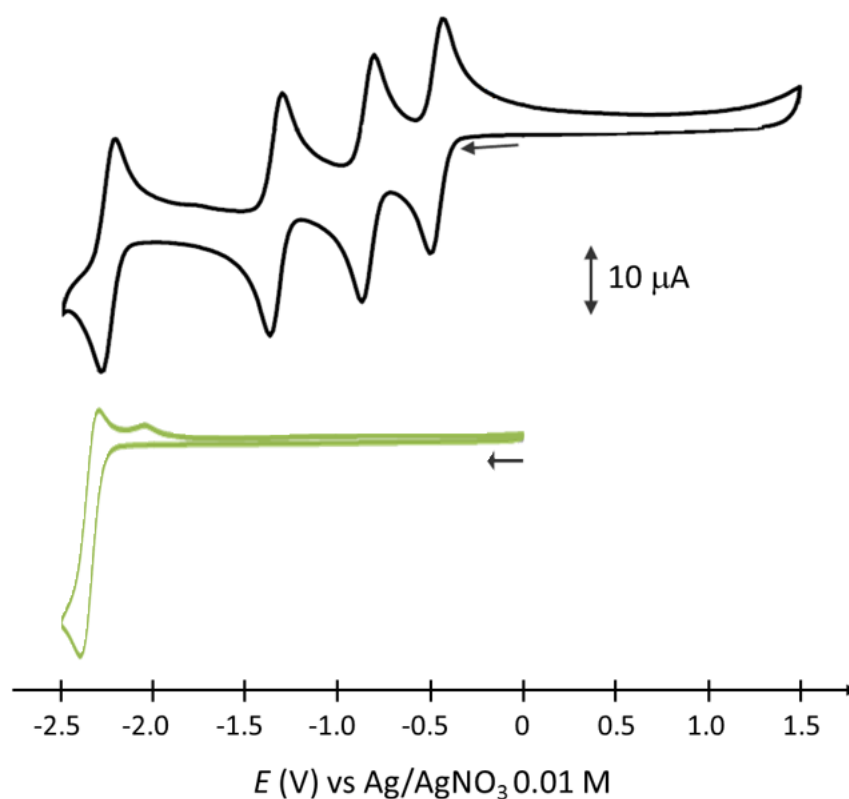
Figure III-1. CVs of $[Cr(ttpy)_2]^{3+}$ (1 mM, black line) and ttpy ligand (1mM, green line) recorded in MeCN + 0.1 M TBAPF$_6$. WE = C disk (d = 3 mm), v = 100 mV.s^{-1}

Table III-1. Redox potentials of $[Cr(ttpy)_2]^{2+}$ complex and ttpy ligand

$E_{1/2}\ (\Delta Ep),\ V$	$E_{red}\ (1)$	$E_{red}\ (2)$	$E_{red}\ (3)$	$E_{red}\ (4)$
$[Cr(ttpy)_2]^{3+}$	-0.47 (0.07)	-0.85 (0.07)	-1.35 (0.07)	-2.25 (0.07)
ttpy	-2.35 (0.09)	-	-	-

86

In order to get insight into the charge distribution during subsequent reduction steps, DFT calculations have been performed by Dr. Jean-Marie Mouesca (CEA Grenoble/ INAC/ SyMMES/ CAMPES). The GGA (Generalized Gradient Approximation) exchange-correlation potential was used to obtain the Mulliken charge and spin population distribution over the $[Cr(ttpy)_2]^{n+}$ (n = 3, 2, 1, 0, -1) complexes. The spin populations on Cr atom compose of α and β spins in its d orbitals which are aligned with or against an external magnetic field, respectively. The β spin number partly quantifies how much the electron(s) localized on the ttpy ligand will spread onto the Cr empty d orbitals. The Mulliken charge and spin populations on Cr of different oxidation states are summarized in **Table III-2**.

Table III-2. Mulliken charge and spin populations on Cr atoms of $[Cr(ttpy)_2]^{n+}$ complexes. GS = ground state, ES = excited state

Complex oxidation state	Spin state	Mulliken (Cr) Charge population	Mulliken (Cr) Spin population	α spin (Cr) population	β spin (Cr) population
+3	3/2	1.22	3.06	3.62	0.79
+2	1	1.17	2.50	3.41	1.08
+1	1/2	1.14	2.11	3.25	1.26
0	0 (GS)	1.12	1.10	2.80	1.77
	1 (ES)	1.17	2.26	3.31	1.19
-1	1/2 (GS)	1.14	1.55	3.00	1.55
	3/2 (ES)	1.18	2.48	3.41	1.08

It can be seen that the α spin number remains around 3 in all the series, suggesting the oxidation state of Cr atom is always +3. The β spin number slightly increases from the +3 to -1 oxidation states, i.e. up to four-electron reduction. Furthermore, the excited states of $[Cr(ttpy)_2]^0$ and $[Cr(ttpy)_2]^{-1}$ complexes have also been investigated. The result suggests that all four added electrons are mainly localized on the ttpy ligands. Therefore, the electronic structure of $[Cr(ttpy)_2]^{n+}$ complexes at ground states can be described as:

n = 2 $[Cr^{III}(ttpy)(ttpy^{\bullet-})]^{2+}$

n = 1 $[Cr^{III}(ttpy^{\bullet-})_2]^{+}$

n = 0 $[Cr^{III}(ttpy^{\bullet-})(ttpy^{2-})]^0$ (ground state)

n = -1 $[Cr^{III}(ttpy^{2-})(ttpy^{2-})]^{1-}$ (ground state)
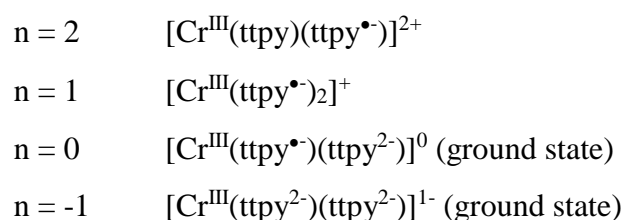
The result of these ground states are in accordance with Wieghardt et al.[5] on analogous complexes $[Cr(tpy)_2]^{n+}$ (tpy = 2,2':6',2"-terpyridine) using the B3LYP functional calculation. **Figure III-2** shows the α and β spin numbers of these complexes. In all the cases the α spin is ~3 while added electrons are sequentially localized on the two tpy ligands. Therefore, the authors concluded that the oxidation state of Cr remains +3. For the neutral, triply reduced complex $[Cr(tpy)_2]^0$ (**Figure III-2d**), since the Cr^{III} is not reduced, the third electron is thought to be delocalized over two reduced (tpy$^{\bullet-}$) ligand. This could be a reason for a relatively facile reduction step from $[Cr(tpy)_2]^+$ to $[Cr(tpy)_2]$ ($E_{1/2}$ = -1.36 V). When the fourth electron is introduced (**Figure III-2e**), all the electrons are localized on the tpy ligands. However, the two ligands differ in spin state: one singlet (tpy^{2-})$^{2-}$ and one triplet (tpy$^{\bullet\bullet}$)$^{2-}$.
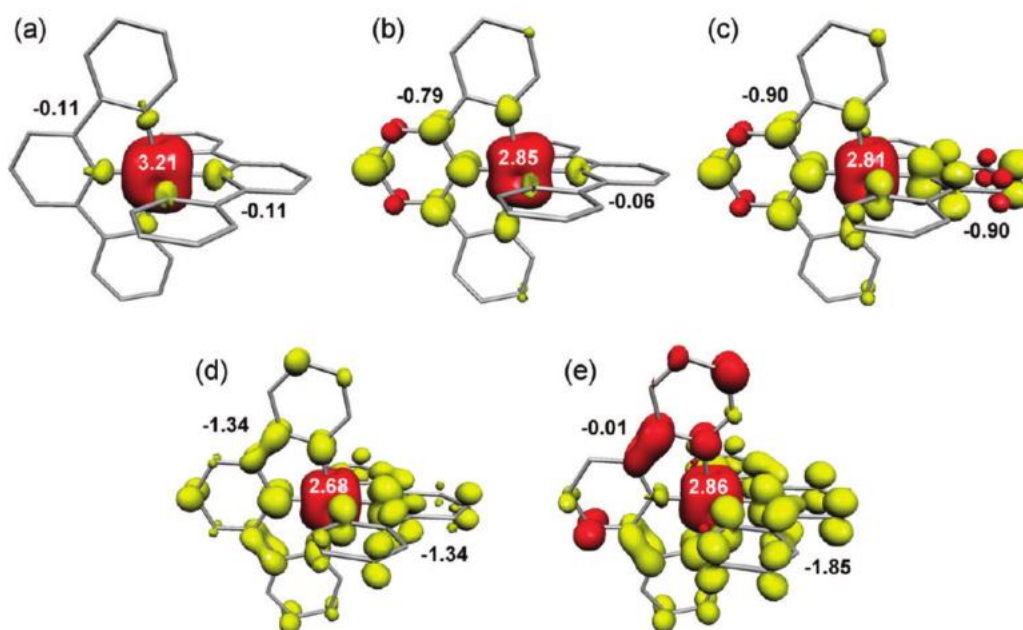
Figure III-2. Calculated Mulliken spin density distribution in $[Cr(tpy)_2]^{n+}$ complexes: (a) n = 3, (b) n = 2, (c) n = 1, (d) n = 0 and (e) n = -1. Adapted from reference 5

III.2.3. Photophysical properties

a) *UV-vis absorption spectroscopy*

The UV-vis absorption spectra of $[Cr(ttpy)_2]^{n+}$ (n = 3, 2, 1, 0) complexes have been extensively studied by Rajaa FARRAN, a former PhD student in our group, by means of spectroelectrochemistry.[19] Here is the summary of the results.

The UV-vis absorption spectra of $[Cr(ttpy)_2]^{n+}$ (n = 3, 2, 1, 0) complexes are shown in **Figure III-3**. They were measured after exhaustive electrolysis of the initial $[Cr(ttpy)_2]^{3+}$ complex at suitable potentials: -0.65 V for n = 2, -1.0 V for n = 1 and -1.7 V for n = 0. It is important to note that due to the solubility issue, we investigated the electroreduction in the presence of two different electrolytes: TBABF$_4$ for n = 3, 2 and 1; TBAClO$_4$ for n = 0.

The spectrum of $[Cr(ttpy)_2]^{3+}$ (line a) shows strong absorption in the UV region at 370 nm and small absorption at 475 nm, which are assigned to the ligand-centered (LC) and metal-centered (MC) transitions, respectively.[4] $[Cr(ttpy)_2]^{2+}$ state (line b) exhibits two strong absorption peaks at 500 nm and 584 nm and a broad band centered at 800 nm. The broad band in the near infrared region is assigned to $\pi \rightarrow \pi^*$ transition of the ttpy radical anion by comparison with a study of $[Cr(tpy)_2]^{2+}$.[5] $[Cr(ttpy)_2]^+$ state (line c) displays enhanced absorption in the visible region with two peaks at 524 nm and 560 nm, which is accompanied by a characteristic absorption peak at 723 nm. Using perchlorate as electrolyte, the $[Cr(ttpy)_2]^0$ complex (line d) is produced and precipitates with time. It is evidenced by an increase at all wavelengths in the absorption spectrum. The characteristic absorption wavelengths and extinction coefficients of all the redox states are collected in **Table III-3**.
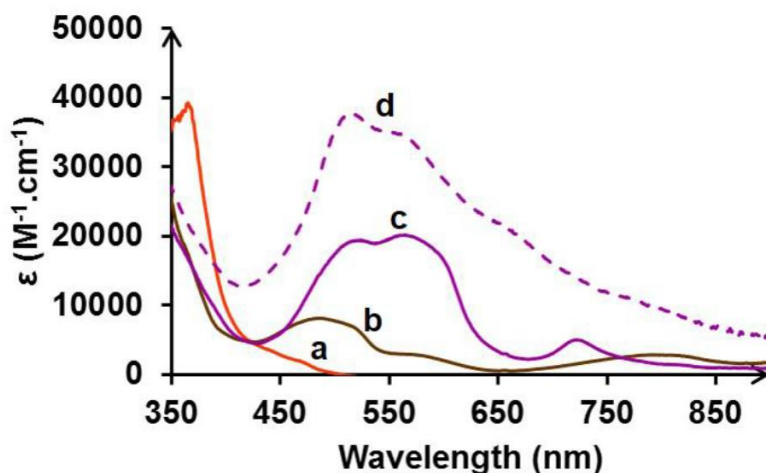
Figure III-3. UV-vis absorption spectra of various oxidation state of $[Cr(ttpy)_2]^{n+}$: (a) n=3, (b) n=2, (c) n=1, (d) n=0. Spectra were recorded by exhaustive electrolysis of $[Cr(ttpy)_2]^{3+}$ in (a, b and c) MeCN + 0.1 M TBABF$_4$ or (d) MeCN + 0.1 M TBAClO$_4$ under Ar at suitable potentials

Table III-3. UV-vis extinction coefficients of $[Cr(ttpy)_2]^{n+}$: n = 3, 2, 1, 0

Complex	λ_{abs}, nm [ε, M^{-1}.cm^{-1}]
$[Cr(ttpy)_2]^{3+}$	370 [36500], 441 [3500], 475 [1500]
$[Cr(ttpy)_2]^{2+}$	500 [7700], 584 [2600], 800 [2800]
$[Cr(ttpy)_2]^+$	524 [20200], 560 [19500], 723 [5000]
$[Cr(ttpy)_2]^0$	520 [37500], 571 [33600], 670 [19900], 776 [10500]

Time-Dependent (TD) DFT calculations have also been carried out by Dr. Jean-Marie Mouesca for the assignment of the UV-vis absorption peaks of the $[Cr(ttpy)_2]^{n+}$ complexes to corresponding electronic transitions. The SAOP (Statistical Average of Orbital Potentials) exchange-correlation potential[21], which is especially suited for the TD-DFT calculations, has

been used. The complex oxidation states have been converged from GGA solutions mentioned above before using the SAOP method to ensure the continuity between the GGA and SAOP calculations. The results are summarized in **Table III-4**.

Table III-4. Experimental and calculated electronic transition energies for $[Cr(ttpy)_2]^{n+}$ (n = 2, 1) complexes, together with the assignment of their electronic transitions

Complex	Experimental λ_{abs} (nm)	Experimental energies (cm^{-1})	Calculated energies (cm^{-1})	Assignment
$[Cr(ttpy)_2]^{2+}$	500	20000	18800	
	584	17120		
	800 (broad)	12500	13000 and 12100	LMCT
$[Cr(ttpy)_2]^{+}$	524	19100	20600	
	560	17900	17900	
	723	13800	13000	LMCT

For the $[Cr(ttpy)_2]^{2+}$ singly reduced complex, $[Cr^{III}(ttpy)(ttpy^{\bullet-})]^{2+}$, calculations have been performed for transitions at 828 nm and 767 nm, which are in accordance with the broad absorption band centered at 800 nm. Electronic transitions at these wavelengths are shown in **Figure III-4**. It is surprising that in the ground state of $[Cr(ttpy)_2]^{2+}$, the electron is localized on the tolyl substituting group rather than the tpy part. The transition at 828 nm corresponds to the intraligand charge transfer between the tolyl and tpy groups. The transition at 767 nm is assigned to the charge transfer between tolyl and metal center. Therefore, the overall broad absorption band at 800 nm is a consequence of different charge transfer processes which finally leads to the charge transfer between ttpy ligand and Cr metal center. The whole process is thus described as ligand-to-metal charge transfer (LMCT). The calculation also shows a strong electronic transition at 532 nm (18800 cm^{-1}) which can be assigned to the strong absorption peak at 500 nm.

828 nm (12100 cm^{-1})

767 nm (13000 cm^{-1})
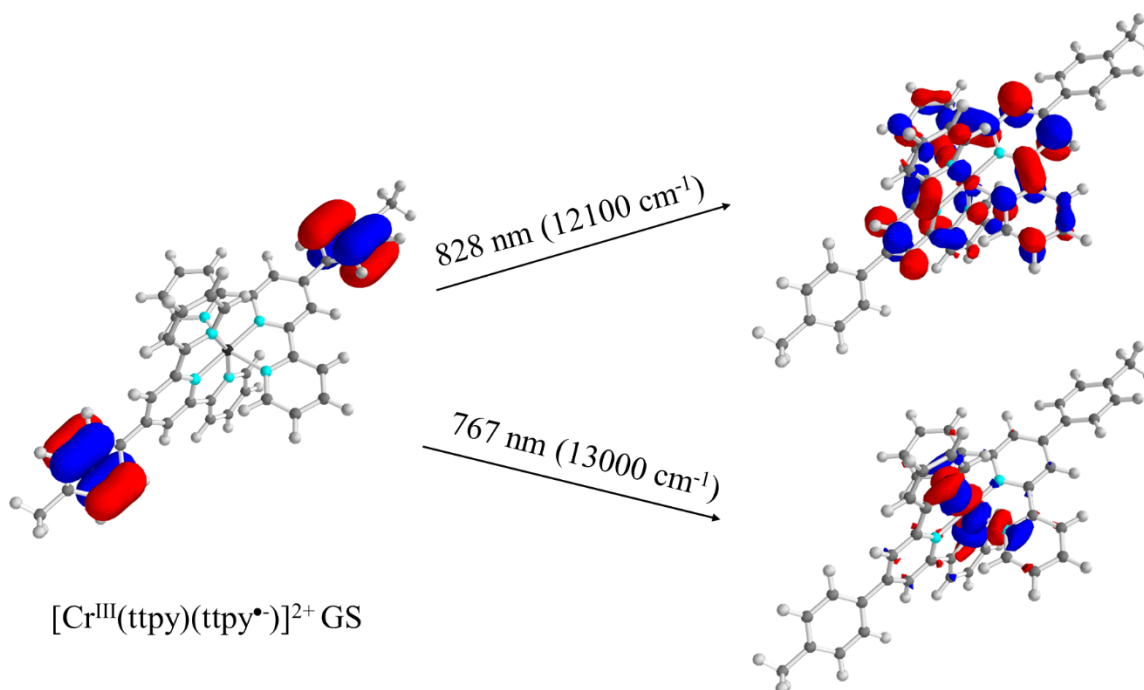
$[Cr^{III}(ttpy)(ttpy^{\bullet-})]^{2+}$ GS

Figure III-4. Calculated electronic transitions for $[Cr(ttpy)_2]^{2+}$ singly reduced complex. GS = ground state

For the $[Cr(ttpy)_2]^+$ doubly reduced complex, $[Cr^{III}(ttpy^{\bullet-})_2]^{2+}$, calculations have been focused on the transition at 767 nm, which can be assigned to the experimental absorption peak at 723 nm. Electronic transitions at this wavelength are shown in **Figure III-5**. The calculated transition is a combination between processes (a) and (b) with equal contribution. In the $[Cr(ttpy)_2]^+$ ground state, the two electrons are localized on the two tpy ligands and equally distributed between the tpy (a) and tolyl (b) parts. The process (a) corresponds to a fully LMCT transition: π(tpy) → d. The process (b) corresponds to the intraligand CT between the tolyl and tpy moieties. Therefore, the whole process can also be described as a LMCT transition. Moreover, this calculation also shows a strong electronic transition at 485 nm (20600 cm^{-1}) and 559 nm (17900 cm^{-1}) which can be assigned to the strong absorption peak at 524 nm and 560 nm.

(a)

767 nm (13000 cm^{-1})

50 %

(b)

767 nm (13000 cm^{-1})

50 %
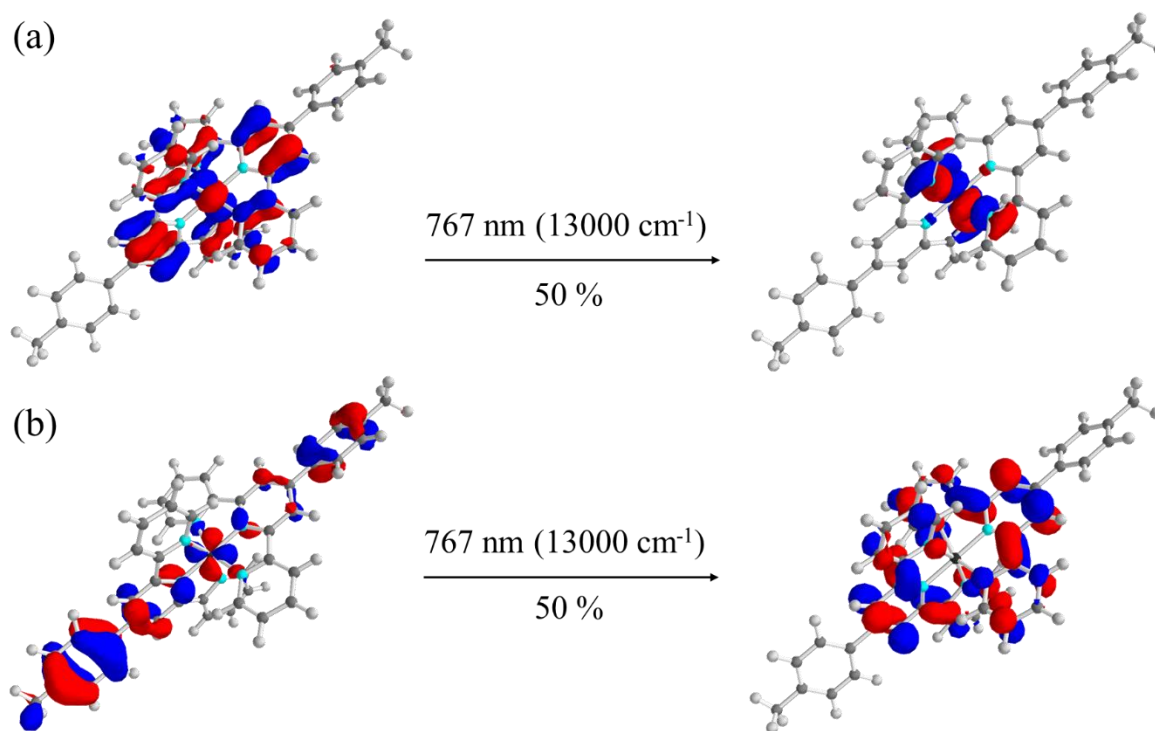
Figure III-5. Calculated electronic transitions for [Cr(ttpy)$_2$]$^+$ doubly reduced complex.

b)   *Steady-state and time-resolved emission spectroscopy*

The steady state luminescence emission of [Cr(ttpy)$_2$]$^{3+}$ complex in MeCN solution under Ar has been studied by irradiating the sample at 370 nm. This wavelength was chosen as it is the absorption maximum of the complex. The emission spectrum is shown as dotted line in **Figure III-6**, in comparison with the absorption spectrum of the complex (solid line). The emission, whose maximum is at 770 nm, is very weak. Its quantum yield at room temperature is estimated to be less than 10^{-3} and attributed to the relaxation of the ^2E_g state to the $^4A_{2g}$ ground state.[22] The shoulder at around 730 nm could be due to the relaxation of the $^4T_{2g}$ state.[22]
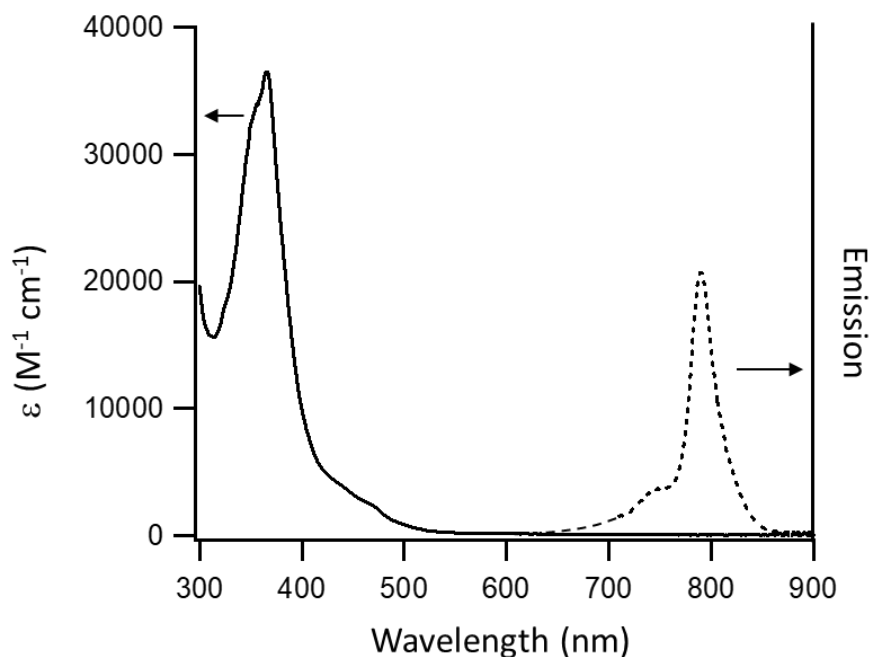
Figure III-6. UV-vis absorption spectrum (solid line) and emission spectrum (dotted line) of $[Cr(ttpy)_2]^{3+}$ complex in MeCN under Ar.

The redox potential of excited state $E(Cr^{III*}/Cr^{II})$ can be estimated by assuming an energy diagram similar to that of $[Cr(diamine)_3]^{3+}$ complexes as shown in literature.[2] The diagram is shown in **Scheme III-8**.
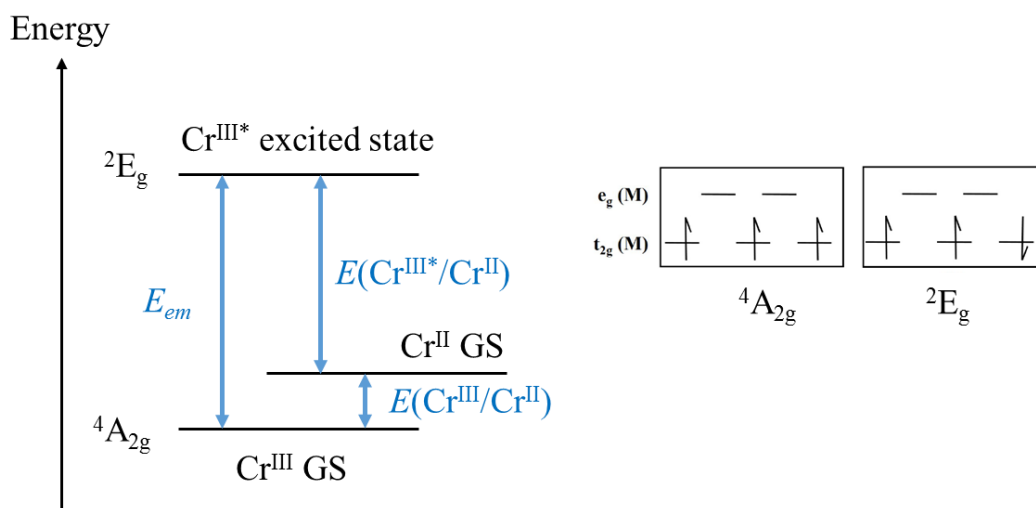
Scheme III-8. Schematic illustration of the energetics associated with (^2E_g) Cr^{III*} state. GS = ground state. Adapted from reference 2

From the diagram one can calculate the oxidizing power of Cr^{III*} state, $E(Cr^{III*}/Cr^{II})$, as follows:

$$E(Cr^{III*}/Cr^{II}) = E_{em} + E(Cr^{III}/Cr^{II})$$

$$E(\mathrm{Cr^{III*}/Cr^{II}}) = \frac{hc}{\lambda_{em,77\ K}\ e} + E(\mathrm{Cr^{III}/Cr^{II}}) \approx \frac{1240}{\lambda_{em,RT}(nm)} + E(\mathrm{Cr^{III}/Cr^{II}}) \qquad \text{(Eq III-1)}$$

where h is the Planck constant, c the speed of light, e the charge of an electron, $\lambda_{em,77\ K}$ and $\lambda_{em,RT}$ (nm) the wavelength at emission maximum at 77 K and room temperature, respectively. Taking into account $E(\mathrm{Cr^{III}/Cr^{II}}) = -0.47$ V, the redox potential $E(\mathrm{Cr^{III*}/Cr^{II}})$ is thus estimated as 1.14 V, making the excited state $\mathrm{Cr^{III*}}$ a strong oxidant. The result is in line with literature for the same complex ($E(\mathrm{Cr^{III*}/Cr^{II}}) = 1.06$ V)[22]. A previous work[2] on $[\mathrm{Cr(bpy)_3}]^{3+}$ in aqueous solution showed $E(\mathrm{Cr^{III*}/Cr^{II}}) = 1.44$ V *vs* NHE (about 0.89 V *vs* Ag/AgNO$_3$ 0.01 M), hence the $[\mathrm{Cr(bpy)_3}]^{3+*}$ is a weaker oxidant than $[\mathrm{Cr(ttpy)_2}]^{3+*}$.

Time-resolved emission spectroscopy was also carried out to study the emission decay in nanosecond time scale. The decay recorded at 770 nm is shown in **Figure III-7**. It is well fit with a biexponential function (red curve), giving a short lifetime of 3 ns and a long lifetime of 270 ns. The 3 ns lifetime could be due to the fluorescence process from $^4\mathrm{T_{2g}}$ to $^4\mathrm{A_{2g}}$ state, whereas the phosphorescence decay of $^2\mathrm{E_g}$ state occurs with the 270 ns lifetime. The lifetime of 270 ns is significantly shorter than that of $[\mathrm{Cr(bpy)_3}]^{3+}$ in N$_2$-purged aqueous solution (63 μs)[4] but in accordance to the lifetime of $[\mathrm{Cr(ttpy)_2}]^{3+}$ (400 ns)[22]. The reduced lifetime for the tpy ligand compared to the bpy one can be due to a more exposed $\mathrm{Cr^{III}}$ metal core, which may allow solvent molecules to quench the excited state more efficiently.[4]
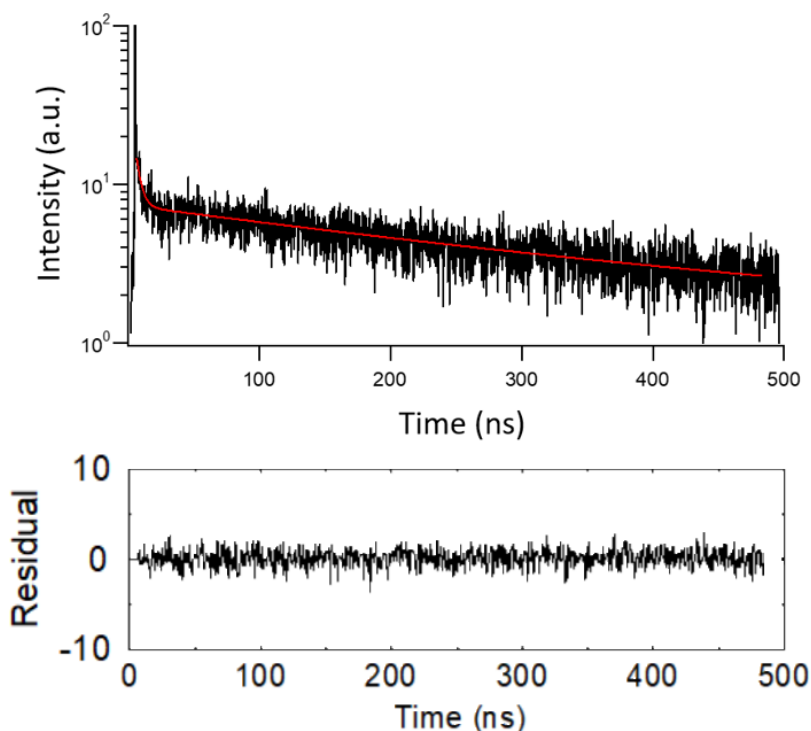
Figure III-7. Decay of $[\mathrm{Cr(ttpy)_2}]^{3+*}$ excited state recorded at 770 nm in MeCN under Ar after excitation at 400 nm by a picosecond pulsed laser

c)   *Transient absorption spectroscopy (TAS)*

In order to study the excited state absorption spectrum, TAS measurement of $[Cr(ttpy)_2]^{3+}$ complex has been carried out. The spectra is presented in **Figure III-8a**. Upon excitation by a 355 nm nanosecond pulsed laser and under Ar, the complex exhibits a negative ΔOD at 370 nm accompanied by a positive band centered at ~ 550 nm. Both features recover to zero after about 2 µs. The negative ΔOD value at 370 nm is assigned to the bleaching of the ground state of $[Cr(ttpy)_2]^{3+}$ complex. The transient absorption band at 550 nm is attributed to the population of the ^2E_g metal centered excited state.

The disappearance of the 550 nm absorption band *versus* time is shown in **Figure III-8b**. The decay is fit with a monoexponential function to give a lifetime of (295 ± 4) ns. This lifetime is in agreement with the aforementioned emission lifetime (270 ns). Such a long-lived excited state may be useful for subsequent charge or energy transfer reactions.
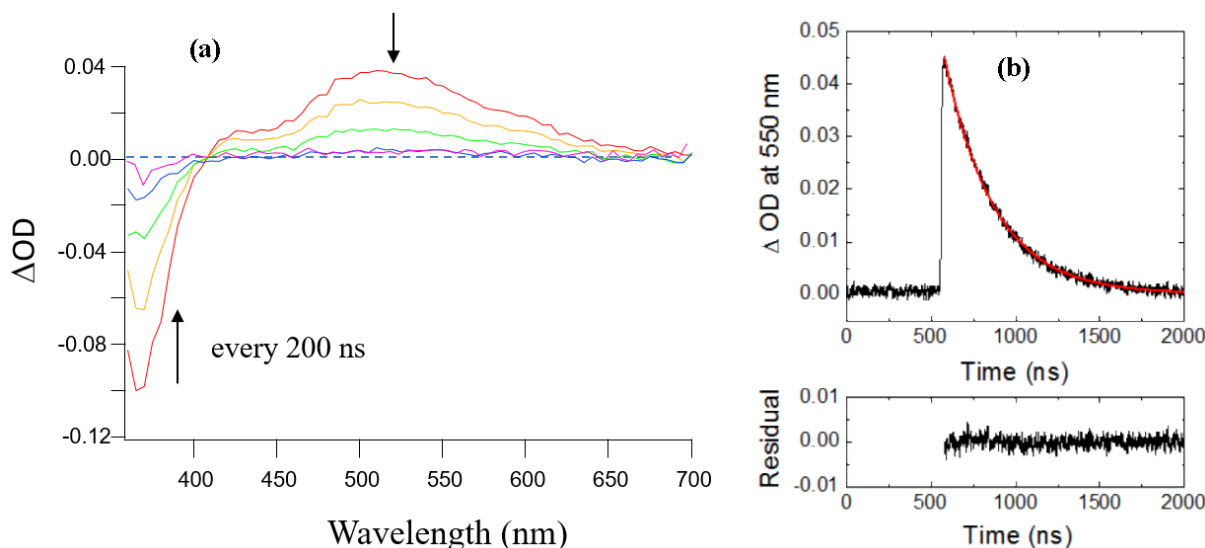
Figure III-8. (a) TA spectra of $[Cr(ttpy)_2]^{3+}$ complex in MeCN under Ar at different time intervals after laser excitation at 355 nm. Arrows indicate temporal spectral changes. (b) TA decay at 550 nm. Excitation was done by nanosecond laser pulses at 355 nm. Red line represents a monoexponential fitting with lifetime of (295 ± 4) ns.

III.2.4.   Electron paramagnetic resonance spectroscopy

Since the $[Cr(ttpy)_2]^{n+}$ (n = 3, 2, 1) complexes are all paramagnetic, we employed electron paramagnetic resonance (EPR) spectroscopy to study changes in spin state when the original complex $[Cr(ttpy)_2]^{3+}$ is reduced. All samples have been prepared by exhaustive electrolysis of $[Cr(ttpy)_2]^{3+}$ (1 mM) in MeCN + 0.1 M TBAPF$_6$ solution under Ar at suitable potentials: -0.7 V for n = 2, -1.1 V for n = 1, -1.6 V for n = 0. The spectra of $[Cr(ttpy)_2]^{3+}$ and

$[Cr(ttpy)_2]^+$ detected with an X-band EPR spectrometer are shown as black lines in **Figure III-9**.
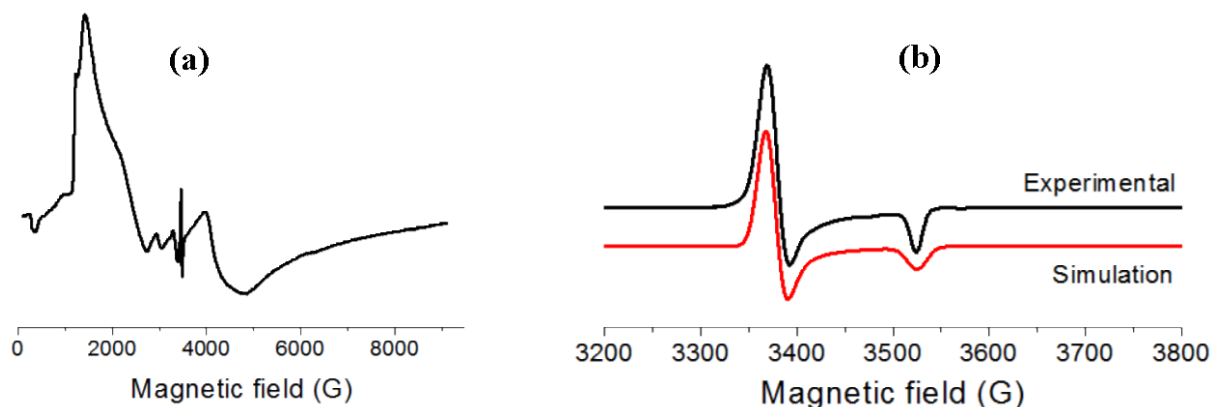
Figure III-9. EPR spectra of $[Cr(ttpy)_2]^{n+}$ at various oxidation states: (a) n = 3, (b) n = 1 which were produced by exhaustive electrolysis of 1 mM $[Cr(ttpy)_2]^{3+}$ in MeCN + 0.1 M TBAPF$_6$. They were recorded with an X-band EPR spectrometer ($f \approx 9.6553$ GHz) with following parameters: (a) 20 mW, 10 K, modulation: 10 G, accumulation time: 50 mins; (b) 0.02 mW, 20 K, modulation: 2 G, accumulation time: 70 mins. Red line represents the simulation of $[Cr(ttpy)_2]^+$ complex.

Considering stepwise monoelectronic reductions of the original complex $[Cr(ttpy)_2]^{3+}$, the expected spin state of these complexes is as follows: $[Cr(ttpy)_2]^{3+}$: $S = 3/2$; $[Cr(ttpy)_2]^{2+}$: $S = 1$; $[Cr(ttpy)_2]^+$: $S = 1/2$ and $[Cr(ttpy)_2]^0$: $S = 0$. Therefore, we should expect that all the complexes except the last one are paramagnetic and detectable by EPR spectroscopy. However, the $[Cr(ttpy)_2]^{2+}$ complex is EPR silent when an X-band EPR spectrometer is used to record the signal. A similar study for $[Cr(tpy)_2]^{2+}$ complex also shows no EPR signal, but its spin state of $S = 1$ has been confirmed by SQUID (Superconducting Quantum Interference Device) measurement.[5] The $[Cr(ttpy)_2]^{3+}$ complex ($S = 3/2$) exhibits a very broad EPR spectrum showing multiple signals spread over more than 6000 G. The spectrum of $[Cr(ttpy)_2]^{3+}$ is in accordance with literature for an analogous $[Cr(tpy)_2]^{3+}$ complex.[23]

Amongst the redox states, the doubly reduced $[Cr(ttpy)_2]^+$ complex is of great interest. Its EPR signal shows anisotropy of the *g*-values: *g* = (2.043, 2.043, 1.955). No clear evidence for the hyperfine coupling to the ^{53}Cr ($I = 3/2$) naturally occurred isotope is observed. The *g*-values are slightly smaller than that of $[Cr(tpy)_2]^+$.[5] It is important to note that the anisotropy of the *g*-values of $[Cr(tpy)_2]^+$ are more pronounced: *g* = (2.0537, 2.0471, 1.9603) than $[Cr(ttpy)_2]^+$.

The EPR experiments clearly show that different oxidized states of $[Cr(ttpy)_2]^{n+}$ (n = 3, 2, 1) possess unique EPR signature. This method can be very helpful to identify the oxidation state of the Cr complex when it is photoreduced by TiO$_2$ or TiO$_2$/Ru^{II} NPs, which will be discussed in **Sections III.3** and **III.4**.

III.2.5. Photoreduction of $[Cr(ttpy)_2]^{3+}$ in the presence of TEOA

❖ *Photoreduction of $[Cr(ttpy)_2]^{3+}$ by TEOA under continuous visible irradiation*

In order to study the reactivity of $[Cr(ttpy)_2]^{3+*}$ excited state, we have carried out the exhaustive photoreduction experiment using an excess amount of TEOA (300 equivalents) under continuous visible irradiation. Triethanolamine (TEOA) is known as a sacrificial electron-donating quencher. Changes in UV-vis absorption spectra during the irradiation period are shown in **Figure III-10**.
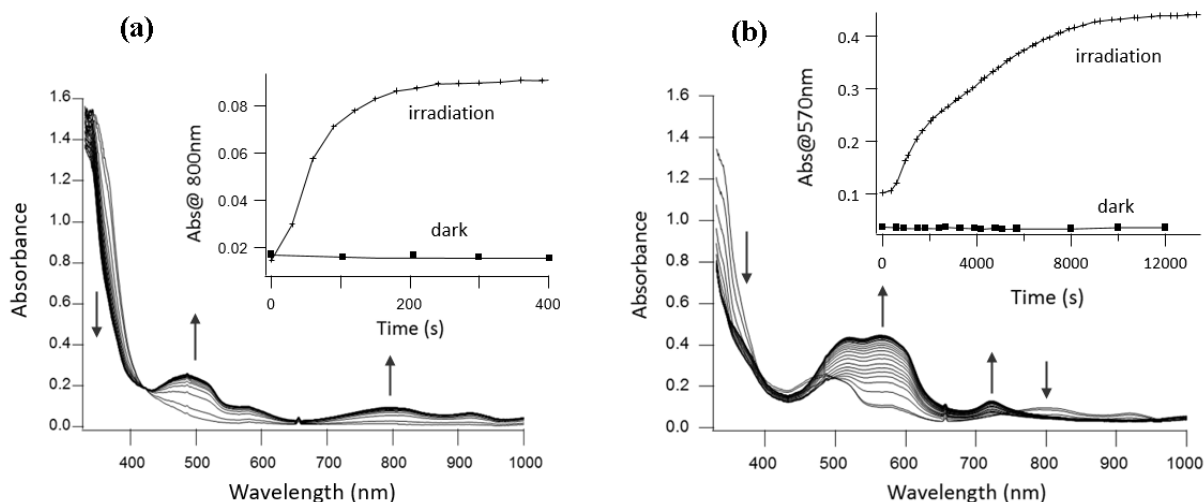
Figure III-10. UV-vis absorption spectra of $[Cr(ttpy)_2]^{3+}$ complex in Ar-saturated MeCN solution containing 300 equivalents of TEOA during 400 s (a) and 200 min (b). They were taken at different time intervals under continuous visible irradiation (400 nm $< \lambda <$ 750 nm). Arrows indicate temporal spectral changes during the irradiation. Inset in graph (a) shows temporal changes in the absorbance at 800 nm, which represents the formation of $[Cr(ttpy)_2]^{2+}$ species. Inset in graph (b) shows temporal changes in the absorbance at 570 nm, which represents the formation of $[Cr(ttpy)_2]^+$ species.

During the first 400 s (**Figure III-10a**), the peaks at 800 nm and 500 nm are gradually formed and increased while the band at ~ 370 nm decreases. These changes corresponds to the $[Cr(ttpy)_2]^{3+} \rightarrow [Cr(ttpy)_2]^{2+}$ reduction. The inset shows temporal change in absorbance at 800 nm. A plateau is observed after ~250 s, indicating a complete chemical transformation. Taking into account the absorbance of the newly formed $[Cr(ttpy)_2]^{2+}$ at 800 nm as its characteristic peak, we estimate the transformation to occur with a quantitative yield. Meanwhile, a blank experiment has also been carried out in dark, which shows no changes in the absorption spectrum of $[Cr(ttpy)_2]^{3+}$.

When the irradiation time is prolonged (**Figure III-10b**), new peaks at ~ 560 nm and 723 nm are recorded, associated with the gradual disappearance of the 800 nm band. These changes satisfactorily correspond to the $[Cr(ttpy)_2]^{2+} \rightarrow [Cr(ttpy)_2]^+$ reduction process. It is important to note that although the 723 nm peak is characteristic of $[Cr(ttpy)_2]^+$ species, its

very low extinction coefficient and absorbance induce low signal-to-noise ratio. Therefore, the absorbance at 570 nm has been chosen to follow the temporal spectral changes in detail. The inset shows a plateau after ~ 10000 s, suggesting the transformation has been complete. Based on the absorbance at 723 nm we estimate the second reduction step to occur with around 80 % yield.

❖ *Quenching of [Cr(ttpy)₂]³⁺* state by TEOA studied by Stern-Volmer experiment*

To get insight into the quenching mechanism, we conducted a Stern-Volmer experiment. In terms of thermodynamics, the oxidizing power of $[Cr(ttpy)_2]^{3+*}$ excited state ($E(Cr^{3+*}/Cr^{2+})$ = 1.14 V, see **Section III.2.3b**) is strong enough to oxidize TEOA ($E(TEOA^+/TEOA)$ = 0.42 V *vs* Ag/AgNO₃ 0.01 M)[24] as follows:

$$[Cr(ttpy)_2]^{3+} + h\nu \rightarrow [Cr(ttpy)_2]^{3+*}$$
$$[Cr(ttpy)_2]^{3+*} + TEOA \rightarrow [Cr(ttpy)_2]^{2+} + TEOA^+$$
$$TEOA^+ \rightarrow \text{degraded products}$$
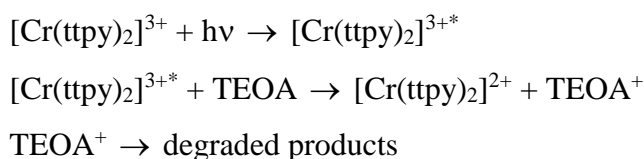
The photoinduced electron transfer reaction between Cr^{3+*} and TEOA is largely exergonic (ΔG = -0.72 eV). Without light this reaction is not favourable since the oxidizing power of $[Cr(ttpy)_2]^{3+}$ ground state ($E(Cr^{3+}/Cr^{2+})$ = -0.47 V) is much lower than the redox potential of TEOA.

Upon the TEOA addition, the emission maximum of $[Cr(ttpy)_2]^{3+*}$ is gradually reduced (**Figure III-11a**) under continuous light excitation at 360 nm. The peak position and shape remain unchanged. When a picosecond pulsed laser was used to excite the sample, the lifetime τ of $[Cr(ttpy)_2]^{3+*}$ was found to decline. A plot of τ_0/τ *vs* [TEOA] is shown in **Figure III-11b**. The experimental data is fit with the Stern-Volmer equation[25]:

$$\frac{\tau_0}{\tau} = 1 + K_{SV}[TEOA] = 1 + k_q\tau_0[TEOA] \qquad \text{(Eq III-2)}$$

where τ_0 and τ are the lifetime of $[Cr(ttpy)_2]^{3+*}$ in the absence and presence of TEOA quencher respectively (τ_0 = 295 ns from the TAS result), K_{SV} the Stern-Volmer constant and k_q the quenching constant. The linear fitting is shown as the red line in **Figure III-11b**.
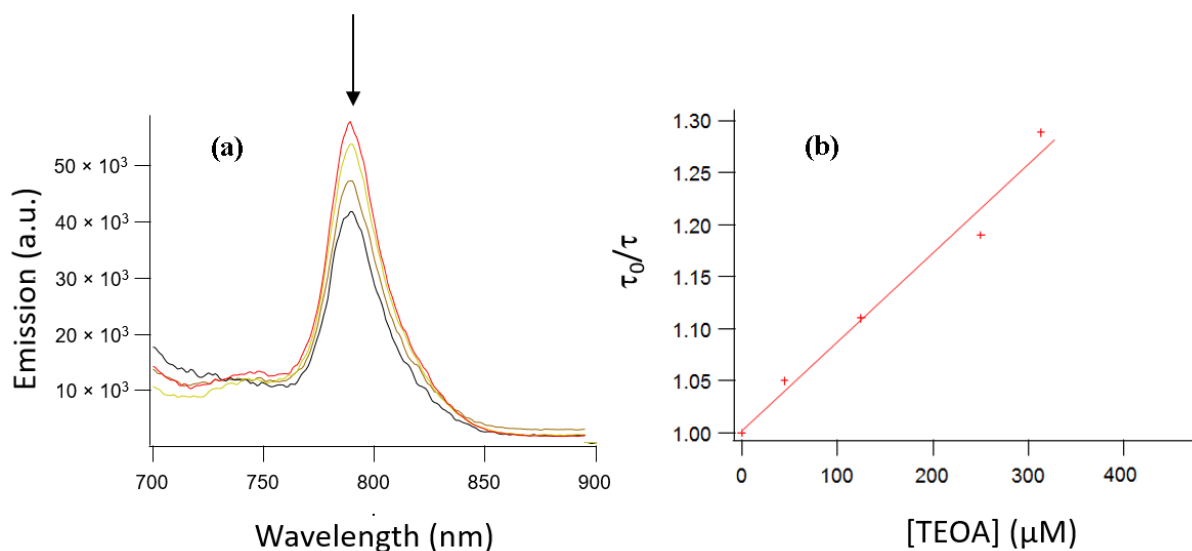
Figure III-11. (a) Quenching of the emission of $[Cr(ttpy)_2]^{3+}$ (1.3×10^{-5} M) excited state upon increasing concentration of TEOA in Ar-purged MeCN solution. The sample was excited at 360 nm. (b) Stern-Volmer plot for the quenching of $[Cr(ttpy)_2]^{3+*}$ by TEOA. The sample was excited by a 400 nm picosecond pulsed laser and emitted photons were recorded at 770 nm.

As predicted by thermodynamics, TEOA reductively quenches the $[Cr(ttpy)_2]^{3+*}$ excited state. Since the UV-vis absorption spectrum of TEOA and the emission spectrum of $[Cr(ttpy)_2]^{3+*}$ do not overlap, the quenching pathway should be only via electron transfer. From the Stern-Volmer plot one can extract $K_{SV} = 850$ M^{-1} and hence $k_q = 3 \times 10^9$ M^{-1}.s^{-1}. The high quenching constant indicates that TEOA is a good quencher for the $[Cr(ttpy)_2]^{3+*}$ state.

This quenching rate is close to the limit of the diffusion rate of species in solution, which is usually around 10^{10} M^{-1}.s^{-1}. In literature, a similar result was obtained for the quenching of $[Cr(ttpy)_2]^{3+*}$ by a mononucleotide base.[26] The authors recorded K_{SV} constants ranging from 1.7×10^4 with guanine to 10^3 with thynine base. Moreover, at high nucleotide concentrations, the Stern-Volmer plot shows an upward curvation indicating an additional deactivation pathway for $[Cr(ttpy)_2]^{3+*}$ excited state involving static quenching due to a nucleotide-bound Cr(III) complex. In our study, the quenching of $[Cr(ttpy)_2]^{3+*}$ by TEOA seems purely dynamic.

To summarize, the photoreduction of $[Cr(ttpy)_2]^{3+}$ by TEOA leads to the formation of $[Cr(ttpy)_2]^+$ after two electron transfer steps under continuous irradiation. The reaction occurs through the formation of the transient $[Cr(ttpy)_2]^{2+}$ species, suggesting that this species can also be photoactive. On a thermodynamic point of view, $[Cr(ttpy)_2]^+$ can reduce any species with a potential higher than -0.85 V *vs* Ag/AgNO$_3$ 0.01 M (around -0.30 V *vs* NHE).

III.2.6. Photoreduction of $[Cr(ttpy)_2]^{3+}$ in the presence of $[Ru(bpy)_3]^{2+}$ and TEOA

❖ *Photoreduction of $[Cr(ttpy)_2]^{3+}$ by $[Ru(bpy)_3]^{2+}$ and TEOA under continuous visible irradiation*

The previous section shows that $[Cr(ttpy)_2]^{3+}$ complex can be excited by visible light and then be photoreduced. However it is not a good PS due to its low absorbance in the visible region. Therefore, the quest for a better PS is necessary. A recent publication has proposed to substitute the ttpy ligand with a strong electron donor group to shift the absorption of the Cr(III) complex to the visible domain.[22] In our study we focus on the $[Ru(bpy)_3]^{2+}$ PS as it possesses great properties of a PS: high absorbance in visible region ($\varepsilon = 13000$ $M^{-1}.cm^{-1}$ at 450 nm), strong emission and long lifetime ($\tau = 608$ ns in MeCN under Ar, see **Chapter 2**). Moreover, its photochemical and redox properties have been well established.[27]

The photoreduction experiment of $[Cr(ttpy)_2]^{3+}$ has been performed in MeCN solution under Ar in the presence of $[Ru(bpy)_3]^{2+}$ as additional PS and TEOA as sacrificial electron donor. Temporal UV-vis spectral changes are shown in **Figure III-12a** during the irradiation period. First, the 800 nm band is formed (black arrow) associated with a peak at 500 nm, which is characteristic of $[Cr(ttpy)_2]^{2+}$ formation. This step seems to finish within 10 s where the next absorption spectrum is taken, showing a very fast rate. Without the $[Ru(bpy)_3]^{2+}$ PS the $[Cr(ttpy)_2]^{2+}$ formation is accomplished only after 250 s under the same irradiation conditions (**Figure III-10a**).

Afterwards, the band at 800 nm gradually disappears while a peak at ~ 720 nm and a shoulder at ~ 560 nm are formed and increase in intensity. These changes correspond well to the $[Cr(ttpy)_2]^{+}$ species. During the experiment, the peak at 450 nm, which is assigned to the ^{1}MLCT absorption maximum of $[Ru(bpy)_3]^{2+}$ PS, remains almost unaffected. The experiment clearly demonstrates that $[Cr(ttpy)_2]^{3+}$ complex can be doubly reduced to $[Cr(ttpy)_2]^{+}$ in the reaction conditions, and the $[Ru(bpy)_3]^{2+}$ PS has been well regenerated by the sacrificial agent TEOA. Prolonged irradiation does not lead to the formation of $[Cr(ttpy)_2]^{0}$ species.

Figure III-12b presents the temporal absorbance change at 720 nm (red line), which is the UV-vis signature of the $[Cr(ttpy)_2]^{+}$ species. A plateau has been reached after about 4000 s, signaling the double reduction reaction has been completed with 100 % conversion for the $[Cr(ttpy)_2]^{3+}$ to $[Cr(ttpy)_2]^{+}$ transformation. Without the $[Ru(bpy)_3]^{2+}$ PS, the reaction has been completed after ~ 10000 s with 80 % conversion. Therefore, the use of this PS accelerates the photoreduction reaction as expected.
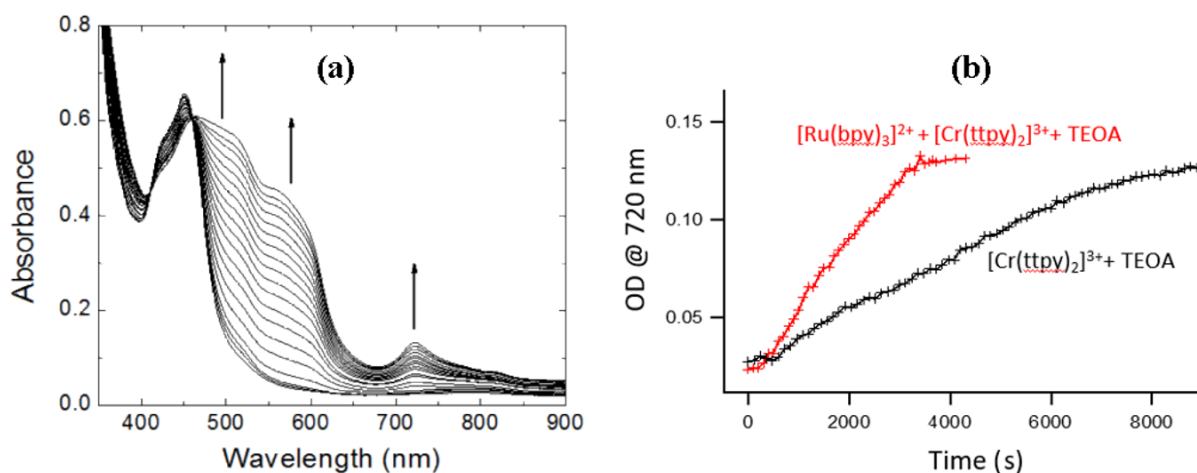
Figure III-12. (a) UV-vis absorption spectra of a mixture of $[Ru(bpy)_3]^{2+}$ (4×10^{-5} M), $[Cr(ttpy)_2]^{3+}$ (2×10^{-5} M) and TEOA (1.5×10^{-2} M) in Ar-saturated MeCN solution. The spectra were taken every 100 s under continuous irradiation at 400 nm $< \lambda <$ 750 nm. Arrows indicate the formation of the $[Cr(ttpy)_2]^+$ species. (b) Comparison of temporal changes in the absorbance at 720 nm in the presence (red line) and absence (black line) of $[Ru(bpy)_3]^{2+}$ complex.

As the irradiation light is between 400 and 750 nm where both $[Ru(bpy)_3]^{2+}$ and $[Cr(ttpy)_2]^{3+}$ complexes absorb the light, hence both are excited. The thermodynamically possible electron transfer reactions between the two complexes are as follows:

(1) $[Ru(bpy)_3]^{2+*}$ + $[Cr(ttpy)_2]^{3+}$ $\longrightarrow$ $[Ru(bpy)_3]^{3+}$ + $[Cr(ttpy)_2]^{2+}$ ΔG_1 = -0.63 eV

(2) $[Ru(bpy)_3]^{2+}$ + $[Cr(ttpy)_2]^{3+*}$ $\longrightarrow$ $[Ru(bpy)_3]^{3+}$ + $[Cr(ttpy)_2]^{2+}$ ΔG_2 = -0.20 eV

(Note : $E(Ru^{3+}/Ru^{2+})$ = 0.94 V, $E(Ru^{3+}/Ru^{2+*})$ = -1.10 V, $E(Cr^{3+}/Cr^{2+})$ = -0.47 V, $E(Cr^{3+*}/Cr^{2+})$ = 1.14 V vs Ag/AgNO$_3$ 0.01 M).

It is clear that in both cases, the products are the same. The reaction (1) is more energetically favorable. The $[Ru(bpy)_3]^{2+}$ complex also absorbs more than the $[Cr(ttpy)_2]^{3+}$ complex in the visible region due to higher spectral coverage and extinction coefficient. Therefore, we assume that the reaction (1) is the main quenching mechanism. However, to verify whether the reaction (2) can occur or not, we need to find a non-photoactive, redox chemical to replace $[Ru(bpy)_3]^{2+}$. This chemical should also have a similar redox potential as the Ru^{3+}/Ru^{2+} couple ($E_{1/2}$ = 0.94 V). Triphenylphosphine (PPh$_3$) with E_{pa} (POPh$_3$/PPh$_3$) = 0.91 V[28] in MeCN solution has been chosen since it does not absorb in the visible region.

❖ *Photoreduction of [Cr(ttpy)$_2$]$^{3+*}$ by PPh$_3$ under continuous visible irradiation*

The monoelectronic photoreduction of $[Cr(ttpy)_2]^{3+}$ complex by PPh$_3$ under visible irradiation has been monitored by spectrophotometry. Changes in UV-vis absorption spectra are shown in **Figure III-13**.
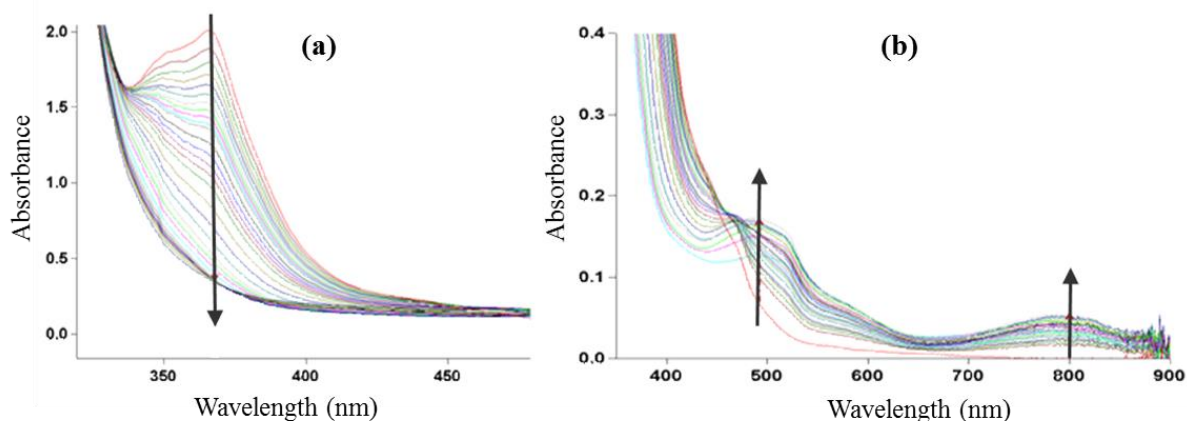
Figure III-13. (a) UV-vis absorption spectra of a mixture of $[Cr(ttpy)_2]^{3+}$ and PPh$_3$ (1000 equivalents) in Ar-saturated MeCN solution. The spectra were taken every 60 s under irradiation at 400 nm $< \lambda <$ 750 nm. Arrow shows the disappearance of the $[Cr(ttpy)_2]^{3+}$ complex. (b) Zoom-in from 400 nm to 900 nm to show the formation of the $[Cr(ttpy)_2]^{2+}$ complex indicated by arrows.

During the irradiation, the absorption maximum of $[Cr(ttpy)_2]^{3+}$ complex at 370 nm gradually decreases accompanied by an increase of a peak at $\sim$ 500 nm and a broad band centered at 800 nm. These changes correspond to the formation of the $[Cr(ttpy)_2]^{2+}$ species. The experiment can be explained by the following reaction:

$$2\ [Cr(ttpy)_2]^{3+*} + PPh_3 + H_2O \rightarrow 2\ [Cr(ttpy)_2]^{2+} + POPh_3 + 2\ H^+ \qquad \Delta G = -0.23\ \text{eV}$$

Stern-Volmer experiment for the quenching of $[Cr(ttpy)_2]^{2+*}$ by PPh$_3$ shows a quenching constant $k_q = 3 \times 10^8$ M^{-1}.s^{-1}.[19] In this case prolonged irradiation does not lead to $[Cr(ttpy)_2]^+$ doubly reduced species. The oxidation power of $[Cr(ttpy)_2]^{2+*}$ is probably not strong enough to oxidize PPh$_3$.

In our study, when $[Ru(bpy)_3]^{2+}$ complex is used instead of PPh$_3$ (reaction 2 mentioned above), the quenching of $[Cr(ttpy)_2]^{3+*}$ by $[Ru(bpy)_3]^{2+}$ can then be possible.

❖ *Quenching of $[Ru(bpy)_3]^{2+*}$ excited state by $[Cr(ttpy)_2]^{3+}$*

In order to study the kinetics of the quenching reaction between $[Ru(bpy)_3]^{2+*}$ and $[Cr(ttpy)_2]^{3+}$ (reaction 1 above), the Stern-Volmer experiment has been carried out.[19] A linear plot of τ_0/τ *vs* the concentration of $[Cr(ttpy)_2]^{3+}$ was obtained upon excitation at 460 nm and the quenching constant k_q was found to be $\sim 3 \times 10^9$ M^{-1}.s^{-1}. As there are no overlaps between the emission spectrum of $[Ru(bpy)_3]^{2+*}$ and the absorption spectrum of $[Cr(ttpy)_2]^{3+}$, the quenching reaction cannot occur via an energy transfer mechanism. Therefore, we attribute this quenching process to an electron transfer mechanism. When $[Cr(bpy)_3]^{3+}$ was used instead of $[Cr(ttpy)_3]^{3+}$, a very similar k_q value was found ($k_q = 3.3 \times 10^9$ M^{-1}.cm^{-1}).[29] This quenching constant is one order of magnitude higher than the constant for the quenching of

$[Cr(ttpy)_2]^{2+*}$ by PPh_3. Therefore, in our study the reaction 1 between $[Ru(bpy)_3]^{2+*}$ and $[Cr(ttpy)_2]^{3+}$ is probably the main quenching mechanism in our study as it is more favorable than reaction 2 in terms of both thermodynamics and kinetics.

As another approach to confirm the reaction 1, we have conducted a flash photolysis experiment for the mixture of $[Cr(ttpy)_2]^{3+}$ and $[Ru(bpy)_3]^{2+}$ complexes. Transient absorption (TA) spectral changes are shown in **Figure III-14a** after the sample has been excited at 532 nm where only $[Ru(bpy)_3]^{2+}$ species absorb. A negative ΔOD value is observed at ~ 450 nm which corresponds to the absorption maximum of $[Ru(bpy)_3]^{2+}$ ground state. A concomitant positive ΔOD band centered at ~ 520 nm is recorded, which can be due to the absorption of the photogenerated $[Cr(ttpy)_2]^{2+}$ complex (see **Figure III-3**). After 1700 ns all the ΔOD values return to zero. Therefore, the spectral changes are attributed to the back electron transfer reaction between the transient $[Cr(ttpy)_2]^{2+}$ and $[Ru(bpy)_3]^{3+}$ species leading to $[Cr(ttpy)_2]^{3+}$ and $[Ru(bpy)_3]^{2+}$.
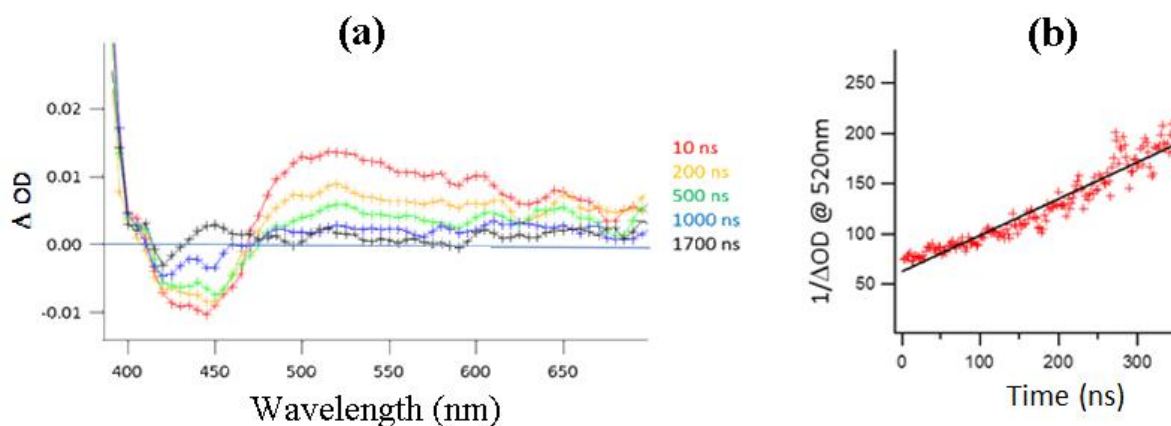
Figure III-14. (a) TA spectra of $[Cr(ttpy)_2]^{3+}$ and $[Ru(bpy)_3]^{2+}$ mixture (molar ratio = 1:1) in MeCN solution under Ar at different time intervals after the sample was excited by a 532 nm nanosecond pulsed laser. (b) Plot of $1/\Delta OD$ *vs* τ at 520 nm (red), fit with a linear function (black).

If the back electron transfer is a bimolecular process, ΔOD at 520 nm should follow the equation:

$$\frac{1}{\Delta OD} = \frac{1}{\Delta OD_0} + \frac{k_{BET}}{\varepsilon l}t \qquad \text{(Eq III-3)}$$

where k_{BET} ($M^{-1}.s^{-1}$) is the kinetics of the back electron transfer reaction, ΔOD the change in optical density at 520 nm at the moment t after the excitation (ΔOD_0 corresponding to $t = 0$), l the optical length ($l = 1$ cm) and ε the variation of the extinction coefficient of the mixture at 520 nm. Since $[Ru(bpy)_3]^{3+}$ and $[Cr(ttpy)_2]^{3+}$ complexes do not absorb at this wavelength, we attribute this ε value due to $[Cr(ttpy)_2]^{2+}$ only ($\varepsilon = 7000$ $M^{-1}.cm^{-1}$ at 520 nm). **Figure III-14b**

presents the plot of $1/\Delta OD$ *vs* t and its linear fitting. The data seems not to completely follow the linear relationship between $1/\Delta OD$ and t. From the slope and known ε value, we estimate $k_{BET} = 2 \times 10^{11}$ $M^{-1}.s^{-1}$. Meanwhile, the diffusion kinetics k_d of non-charged molecular reactants having the same size can be roughly estimated by a derivative of the Smoluchowski's equation:[30]

$$k_d = \frac{8RT}{3\eta} \qquad \text{(Eq III-4)}$$

where η is the solvent viscosity (η = 0.341 mPa.s for MeCN at RT)[31] and T (K) the temperature. The value of k_d is estimated to be 1.9×10^{10} $M^{-1}.s^{-1}$. In fact, as they are both positively charged, electrostatic repulsion makes it harder for the molecules to diffuse towards each other, thus real k_d value should be smaller. Therefore, the rate of back electron transfer is significantly faster than the rate of diffusion. It can be imagined as a fast electron transfer reaction happening in a solvent cage where both transient $[Ru(bpy)_3]^{3+}$ and $[Cr(ttpy)_2]^{2+}$ complexes are artificially linked to each other. In this case a monoexponential model (**Equation III-5**) can better describe the TA decay than the bimolecular model. **Figure III-15** shows the monoexponential fitting of the decay at 520 nm.

$$\Delta OD = \Delta OD_0 \exp(-k_{BET}t) \qquad \text{(Eq III-5)}$$
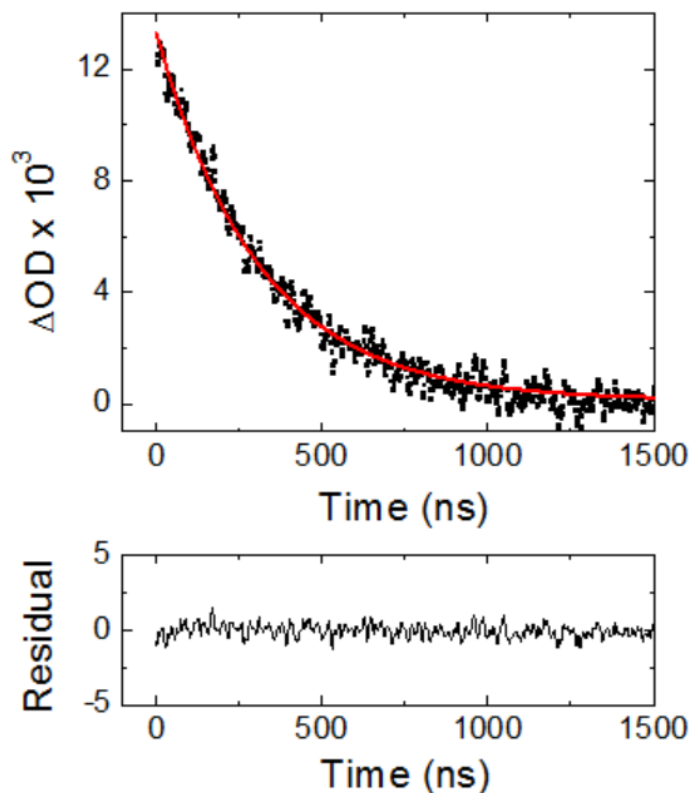
Figure III-15. Decay of the transient absorption maximum at 520 nm (black dots) fit by a monoexponential function (red line), together with the fitting residual.

It can be seen that the monoexponential function is a better fitting model. The kinetics of back electron transfer is estimated to be $(3.2 \pm 0.1) \times 10^6 \text{ s}^{-1}$.

❖ *Mechanism of the photoreduction of [Cr(ttpy)$_2$]$^{3+}$ in the presence of [Ru(bpy)$_3$]$^{2+}$ and TEOA*

Since TEOA, a sacrificial electron donor, is present in the exhaustive photoreduction experiment mentioned above, there are two possible photoreduction pathways for the quantitative photogeneration of [Cr(ttpy)$_2$]$^+$ complex:

- *Pathway 1: [Ru(bpy)$_3$]$^{2+*}$ state is first quenched by [Cr(ttpy)$_2$]$^{3+}$ (oxidative quenching)*

(1) $[Ru(bpy)_3]^{2+} \xrightarrow{\text{h}\nu} [Ru(bpy)_3]^{2+*}$

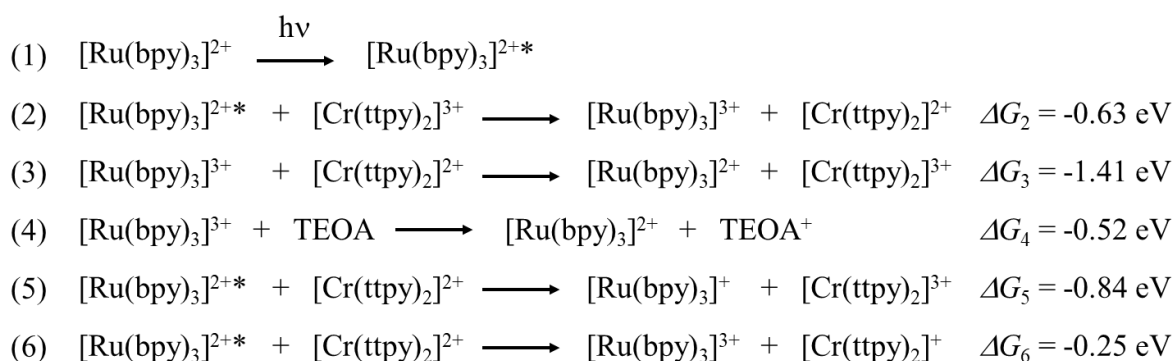(2) $[Ru(bpy)_3]^{2+*} + [Cr(ttpy)_2]^{3+} \longrightarrow [Ru(bpy)_3]^{3+} + [Cr(ttpy)_2]^{2+}$ $\Delta G_2 = -0.63$ eV

(3) $[Ru(bpy)_3]^{3+} + [Cr(ttpy)_2]^{2+} \longrightarrow [Ru(bpy)_3]^{2+} + [Cr(ttpy)_2]^{3+}$ $\Delta G_3 = -1.41$ eV

(4) $[Ru(bpy)_3]^{3+} + \text{TEOA} \longrightarrow [Ru(bpy)_3]^{2+} + \text{TEOA}^+$ $\Delta G_4 = -0.52$ eV

(5) $[Ru(bpy)_3]^{2+*} + [Cr(ttpy)_2]^{2+} \longrightarrow [Ru(bpy)_3]^{+} + [Cr(ttpy)_2]^{3+}$ $\Delta G_5 = -0.84$ eV

(6) $[Ru(bpy)_3]^{2+*} + [Cr(ttpy)_2]^{2+} \longrightarrow [Ru(bpy)_3]^{3+} + [Cr(ttpy)_2]^{+}$ $\Delta G_6 = -0.25$ eV

- *Pathway 2: [Ru(bpy)$_3$]$^{2+*}$ state first quenched by TEOA (reductive quenching)*

(1) $[Ru(bpy)_3]^{2+} \xrightarrow{\text{h}\nu} [Ru(bpy)_3]^{2+*}$

(2) $[Ru(bpy)_3]^{2+*} + \text{TEOA} \longrightarrow [Ru(bpy)_3]^{+} + \text{TEOA}^+$ $\Delta G_2 = 0.05$ eV

(3) $[Ru(bpy)_3]^{+} + [Cr(ttpy)_2]^{3+} \longrightarrow [Ru(bpy)_3]^{2+} + [Cr(ttpy)_2]^{2+}$ $\Delta G_3 = -1.20$ eV

(4) $[Ru(bpy)_3]^{+} + [Cr(ttpy)_2]^{2+} \longrightarrow [Ru(bpy)_3]^{2+} + [Cr(ttpy)_2]^{+}$ $\Delta G_4 = -0.82$ eV

(5) $[Ru(bpy)_3]^{2+*} + [Cr(ttpy)_2]^{2+} \longrightarrow [Ru(bpy)_3]^{+} + [Cr(ttpy)_2]^{3+}$ $\Delta G_5 = -0.84$ eV

(6) $[Ru(bpy)_3]^{2+*} + [Cr(ttpy)_2]^{2+} \longrightarrow [Ru(bpy)_3]^{3+} + [Cr(ttpy)_2]^{+}$ $\Delta G_6 = -0.25$ eV

(7) $[Ru(bpy)_3]^{3+} + \text{TEOA} \longrightarrow [Ru(bpy)_3]^{2+} + \text{TEOA}^+$ $\Delta G_7 = -0.52$ eV
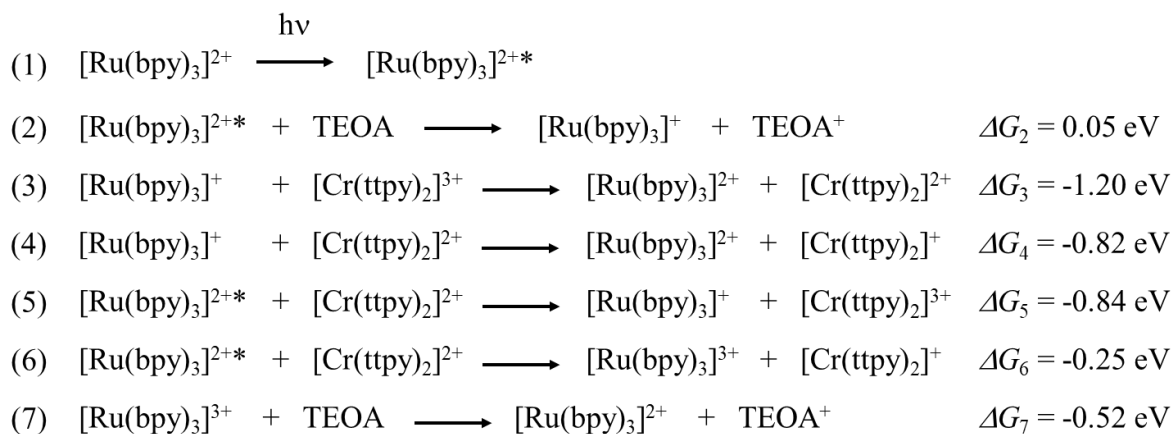
(Note : $E(Ru^{3+}/Ru^{2+}) = 0.94$ V, $E(Ru^{2+}/Ru^{+}) = -1.67$ V, $E(Ru^{2+*}/Ru^{+}) = 0.37$ V, $E(Ru^{3+}/Ru^{2+*})$ = -1.10 V, $E(Ru^{3+}/Ru^{2+*}) = -1.10$ V, $E(Cr^{3+}/Cr^{2+}) = -0.47$ V, $E(Cr^{2+}/Cr^{+}) = -0.85$ V, $E_{pa}(\text{TEOA}^+/\text{TEOA}) = 0.42$ V *vs* Ag/AgNO$_3$ 0.01 M).

For the formation of [Cr(ttpy)$_2$]$^{2+}$, the two proposed pathways are concerned with whether the first quenching step of [Ru(bpy)$_3$]$^{2+*}$ excited state is by [Cr(ttpy)$_2$]$^{3+}$ (pathway 1) or TEOA (pathway 2). Comparing the step 2 of these pathways, it is clear that the quenching reaction by [Cr(ttpy)$_2$]$^{3+}$ is thermodynamically more favourable as the quenching reaction by TEOA is slightly endergonic. The quenching rate of [Ru(bpy)$_3$]$^{2+*}$ by [Cr(ttpy)$_2$]$^{3+}$ is very high

(k_q = 3 × 10^9 $M^{-1}.s^{-1}$) as mentioned above. Meanwhile, the reductive quenching of $[Ru(bpy)_3]^{2+*}$ by TEOA is not detected.[32] Together with our calculated ΔG values, we conclude that the pathway 1 is more favorable than pathway 2 in terms of both thermodynamics and kinetics.

In the pathway 1, after the formation of $[Cr(ttpy)_2]^{2+}$, the back electron transfer reaction between $[Cr(ttpy)_2]^{2+}$ and $[Ru(bpy)_3]^{3+}$ (step 3, ΔG_3 = -1.41 eV) is even more favorable than the quenching reaction (ΔG_2 = -0.63 eV). This back electron transfer step has been proved to be very fast by the flash photolysis experiment mentioned above. Since we observe the net formation of $[Cr(ttpy)_2]^{2+}$ and then $[Cr(ttpy)_2]^{+}$, we assume that TEOA efficiently scavenges the $[Ru(bpy)_3]^{3+}$ molecules (step 4) to prevent this back electron transfer reaction. In literature, the reduction rate of $[Ru(bpy)_3]^{3+}$ by TEOA is between 6 × 10^6 $M^{-1}.s^{-1}$,[33] or 2 × 10^7 $M^{-1}.s^{-1}$,[34] (in deaerated aqueous solution, C_{TEOA} ~ 0.1 M). Converted to the pseudo first-order kinetics, this rate is comparable to the back electron transfer rate (3.2 × 10^6 s^{-1}). As the amount of TEOA in the exhaustive photoreduction experiment is about 1000 times higher than $[Cr(ttpy)_2]^{3+}$, it is statistically more likely that the $[Ru(bpy)_3]^{3+}$ complex is reduced by TEOA than by $[Cr(ttpy)_2]^{2+}$, suggesting that step 4 is more likely to occur than step 3. Therefore, the back electron transfer is short-circuited by TEOA, allowing $[Cr(ttpy)_2]^{2+}$ complex to be reduced again.

After the $[Cr(ttpy)_2]^{2+}$ singly reduced complex is formed, it can quench the $[Ru(bpy)_3]^{2+*}$ state via either a reductive quenching process (step 5) or an oxidative quenching process (step 6). Although the reductive quenching reaction is more energetically favourable (ΔG_5 = -0.84 eV compared with ΔG_6 = -0.25 eV), as we observed the gradual formation of $[Cr(ttpy)_2]^{+}$ species, the oxidative quenching reaction should be kinetically faster. Furthermore, the TEOA sacrificial agent is known to efficiently reduce $[Ru(bpy)_3]^{3+}$ PS (step 4) to sustain the step 6.

❖ *Conclusion for the photoreduction mechanism of $[Cr(ttpy)_2]^{3+}$ by $[Ru(bpy)_3]^{2+}$ and TEOA:*

To summarize, $[Cr(ttpy)_2]^{3+}$ complex can be reduced twice to form $[Cr(ttpy)_2]^{+}$ with 100 % conversion in the presence of $[Ru(bpy)_3]^{2+}$ PS and TEOA as sacrificial electron donor. The photoreduction of $[Cr(ttpy)_2]^{3+}$ occurs via the pathway 1 where the first reduction step is the reductive quenching of $[Ru(bpy)_3]^{2+*}$ by $[Cr(ttpy)_2]^{3+}$. The back electron transfer reaction between photogenerated species $[Ru(bpy)_3]^{3+}$ and $[Cr(ttpy)_2]^{2+}$ is short circuited by the excess amount of TEOA, which efficiently reduces $[Ru(bpy)_3]^{3+}$ to regenerate the $[Ru(bpy)_3]^{2+}$ PS.

Finally, $[Cr(ttpy)_2]^{2+}$ oxidatively quenches $[Ru(bpy)_3]^{2+*}$ to form the doubly reduced $[Cr(ttpy)_2]^+$ complex.

III.2.7. $[Cr(ttpy)_2]^{3+}$ as an electrocatalyst for proton reduction

Recent works have shown that some first row transition metal complexes with bis-terdentate ligands (**Scheme III-9**) such as $[Co^{II}(tpy)_2]^{2+}$, $[Ni^{II}(tpy)_2]^{2+}$ and $[Fe^{II}(tpy)_2]^{2+}$,[35,36] or $[Co^{II}(dapa)_2]^{2+}$ and $[Ni^{II}(dapa)_2]^{2+}$ (dapa = 2,6-diacetylpyridine-bis(anil))[37] complexes have potential applications in the electrocatalysis of proton or CO_2 reduction reaction. Inspired by that, we have conducted an electrocatalytic study using $[Cr(ttpy)_2]^{3+}$ complex for the proton reduction reaction as the complex has shown the ability to store up to 3 electrons at relatively small negative potentials without degradation. Trifluoroacetic acid (TFA) was chosen as the proton source due to its fairly low pK_a (12.8 in MeCN[38]).

$[M^{II}(tpy)_2]^{2+}$
(M = Co, Ni or Fe)

$[M^{II}(dapa)_2]^{2+}$
(M = Co or Ni)
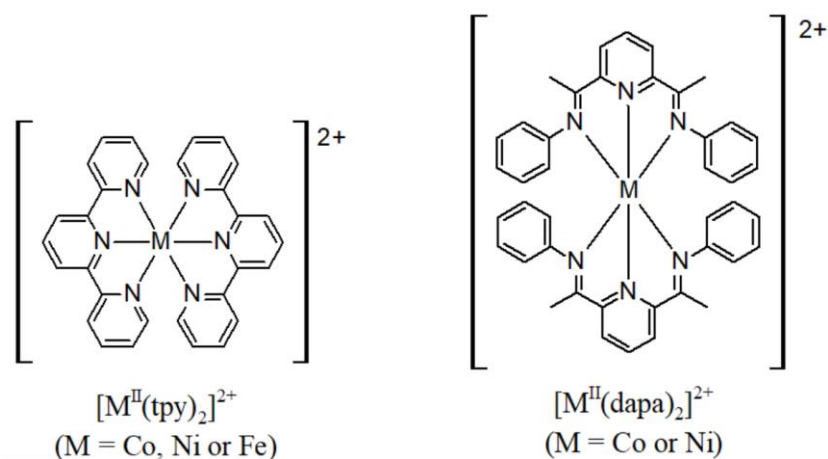
Scheme III-9. Some first row transition metal complexes for catalytic proton reduction reaction

First, the electrochemical behavior of TFA in the absence and presence of $[Cr(ttpy)_2]^{3+}$ complex has been studied by cyclic voltammetry (**Figure III-16a**) with a carbon disk as working electrode (WE). It is clear that the presence of the complex helps to shift the onset of catalytic current towards less negative potential. In terms of energy it corresponds to a gain of about 240 mV. Moreover, in the presence of the Cr complex, the catalytic current onset appears after the second reduction peak of the complex, suggesting the electrocatalytically active species to be $[Cr(ttpy)_2]^+$. In the reverse scan, two oxidation peaks are observed at similar potentials for the $[Cr(ttpy)_2]^{2+}$ and $[Cr(ttpy)_2]^{3+}$ formation.
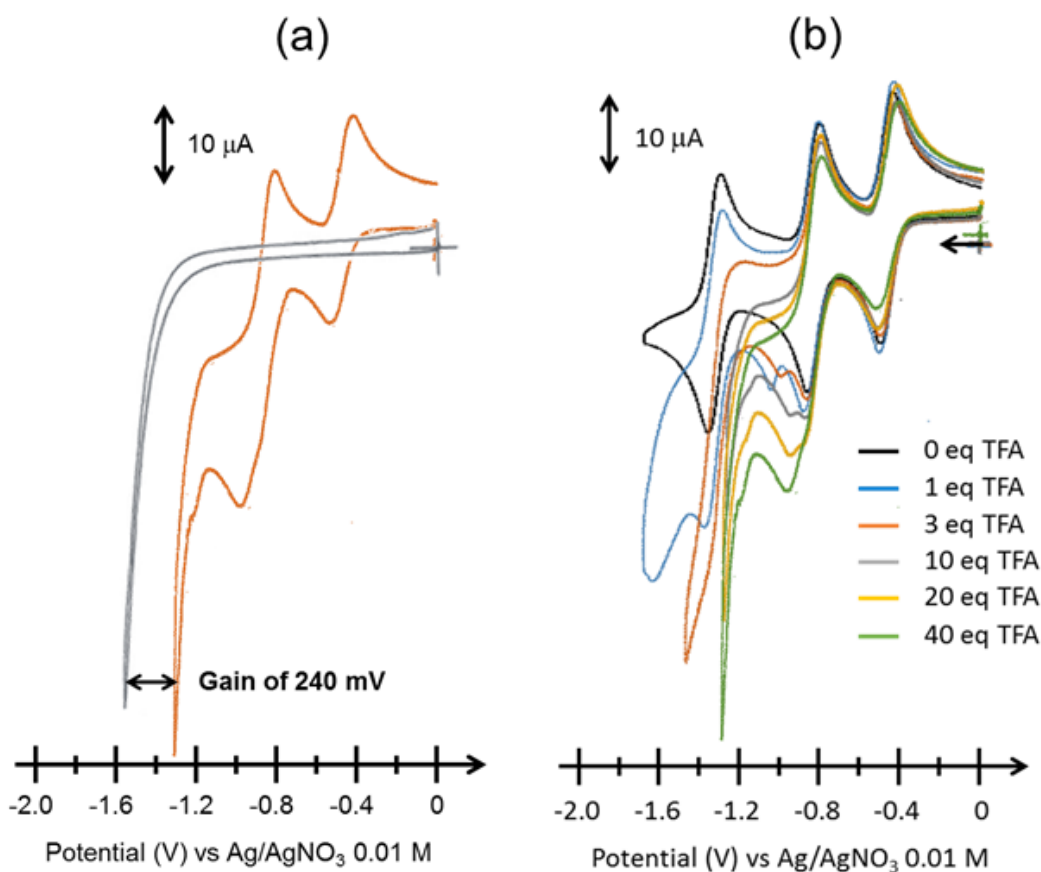
Figure III-16. (a) CV of 1 mM $[Cr(ttpy)_2]^{3+}$ in the presence of TFA (40 equivalents, 40 mM) (red line) and CV of 40 mM TFA alone (grey line). (b) CVs of 1 mM $[Cr(ttpy)_2]^{3+}$ upon the addition of TFA. Experiments were carried out in MeCN + 0.1 M TBAPF$_6$ solution under Ar. WE = C disk (d = 3 mm), $v = 100$ mV.s^{-1}

In order to study the change in electrochemical behavior of the $[Cr(ttpy)_2]^{3+}$ complex in more detail, we recorded its CVs in the presence of different amounts of TFA (**Figure III-16b**). The first and second redox waves remain unchanged, suggesting completely reversible reduction until the $[Cr(ttpy)_2]^+$ complex. After that, two new irreversible reduction waves is formed around -1.0 V and -1.2 V, which may indicate the formation of an intermediate for the electrocatalytic process. The new peak is associated with a complete disappearance of the third redox wave. When the amount of TFA is more than 20 equivalents, the new reduction peak at -1.0 V seems to merge with the reduction peak of Cr^{2+}/Cr^+ couple.

Afterwards, a controlled potential electrocatalysis experiment has been carried out to study the catalytic products. The catalytic test was performed at the bias of -1.20 V in MeCN under Ar using a vitreous carbon plate as WE. The $[Cr(ttpy)_2]^{3+}$ complex was mixed with TFA (50 equivalents). At this potential the direct reduction of TFA on carbon electrode should be negligible (see **Figure III-16a** for its CV). The amount of H$_2$ produced during the experiment was analyzed with a gas chromatograph (GC) and is shown in **Figure III-17**. The amount of H$_2$ gas reaches 45 µmol after 120 mins with around 65 % Faradaic yield. In terms

of turnover number (TON) *versus* the $[Cr(ttpy)_2]^{3+}$ catalyst, it corresponds to TON = 9 after 2 hours. Without the catalyst, the amount of H_2 was only about 4 µmol after 2 hours. Because the H_2 production reaction is a two-electron process, the maximum TON is 25. Therefore, the catalytic process is not limited by the amount of TFA.
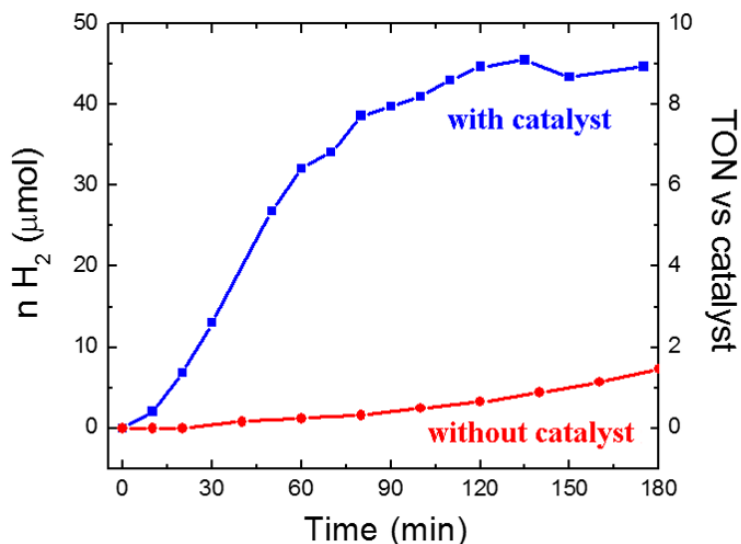
Figure III-17. Electrocatalytic proton reduction by $[Cr(ttpy)_2]^{3+}$ (0.5 mM) in the presence of TFA (50 eq) as proton source at the bias of -1.20 V. Solution: 0.1 M TBAPF$_6$ in MeCN, WE = C plate (8 cm^2).

After 3 hours under the -1.2 V bias, the CV recorded with a clean carbon disk electrode was very similar to that obtained before the experiment, except for declines in intensity of the redox waves. The CV recorded with the carbon plate WE produced unstable responses. After 3 hours, the surface of the carbon plate was covered with a visible layer that was not soluble in MeCN. In the absence of TFA, there is no such layer covering the WE when an exhaustive electrolysis of $[Cr(ttpy)_2]^{3+}$ complex was conducted at a similar potential. It is hence suspected that during a long time under the -1.2 V bias and in the presence of H^+, the $[Cr(ttpy)_2]^+$ complex is partly decomposed, releasing a ttpy ligand that is then deposited onto the WE. This layer blocks the conductivity of the electrode so that the catalytic reaction is stopped. In fact, this electrocatalytic experiment is not reproducible as sometimes the WE was blocked quickly within 1 or 2 hours at the -1.20 V bias. The suspected ttpy layer is always observed.

In an attempt to get insight into the catalytic mechanism, we first created $[Cr(ttpy)_2]^+$ complex by exhaustive electrolysis of the $[Cr(ttpy)_2]^{3+}$ complex in MeCN, then added different amount of TFA. The samples were characterized by EPR spectroscopy and UV-vis spectroscopy (**Figure III-18**). Upon the addition of 1 equivalent of TFA, the EPR signal of $[Cr(ttpy)_2]^+$ is gradually reduced by half. Up to 50 equivalents of TFA the $[Cr(ttpy)_2]^+$ EPR signal completely disappears. No other signals have been found in other region of the X-band

spectrum. The result simply suggests the consumption of $[Cr(ttpy)_2]^+$ species to form EPR-silent species. It is important to note that the $[Cr(ttpy)_2]^{2+}$ in solution is EPR silent although its spin number is $S = 1$. The changes in the UV-vis spectra of $[Cr(ttpy)_2]^+$ species upon the TFA addition correspond to the formation of $[Cr(ttpy)_2]^{2+}$. The EPR and UV-vis spectra suggest that during the reduction of H^+ to H_2, the $[Cr(ttpy)_2]^+$ species are oxidized to $[Cr(ttpy)_2]^{2+}$ rather than $[Cr(ttpy)_2]^{3+}$.
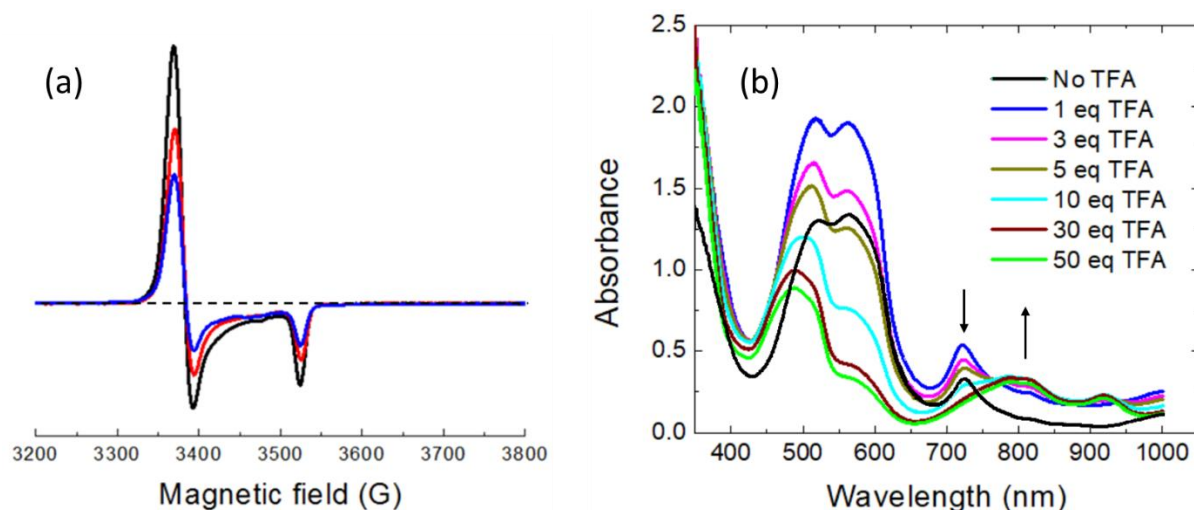
Figure III-18. (a) Changes in the EPR spectrum of $[Cr(ttpy)_2]^+$ upon addition of TFA: no TFA (black), 0.5 eq TFA (red), 1 eq TFA (blue) and 50 eq TFA (dashed line). (b) Changes in the UV-vis spectrum of $[Cr(ttpy)_2]^+$ upon addition of TFA.

We also attempted to use pulsed EPR technique to study the samples mentioned above. The experiment is based on the following assumptions: (i) if another paramagnetic complex formed during the catalytic process has a similar continuous EPR spectrum as $[Cr(ttpy)_2]^+$, it may show changes in spin relaxation time; (ii) if decoordination of ttpy ligands occurs, interaction between the $S = 1/2$ system and the ^{14}N atoms should change as well, which can be detected by the HYSCORE method; (iii) if a hydride complex is an intermediate for H_2 production, interaction between the $S = 1/2$ system and protons should be enhanced in the HYSCORE spectrum. Therefore, we recorded the spin relaxation time and HYSCORE spectra (**Figure III-19**) for 2 samples: $[Cr(ttpy)_2]^+$ complex alone and the complex with 1 equivalent of TFA. However, the two samples show completely similar spin relaxation and HYSCORE spectra, except for the reduced intensities as seen in the continuous X-band EPR spectra.
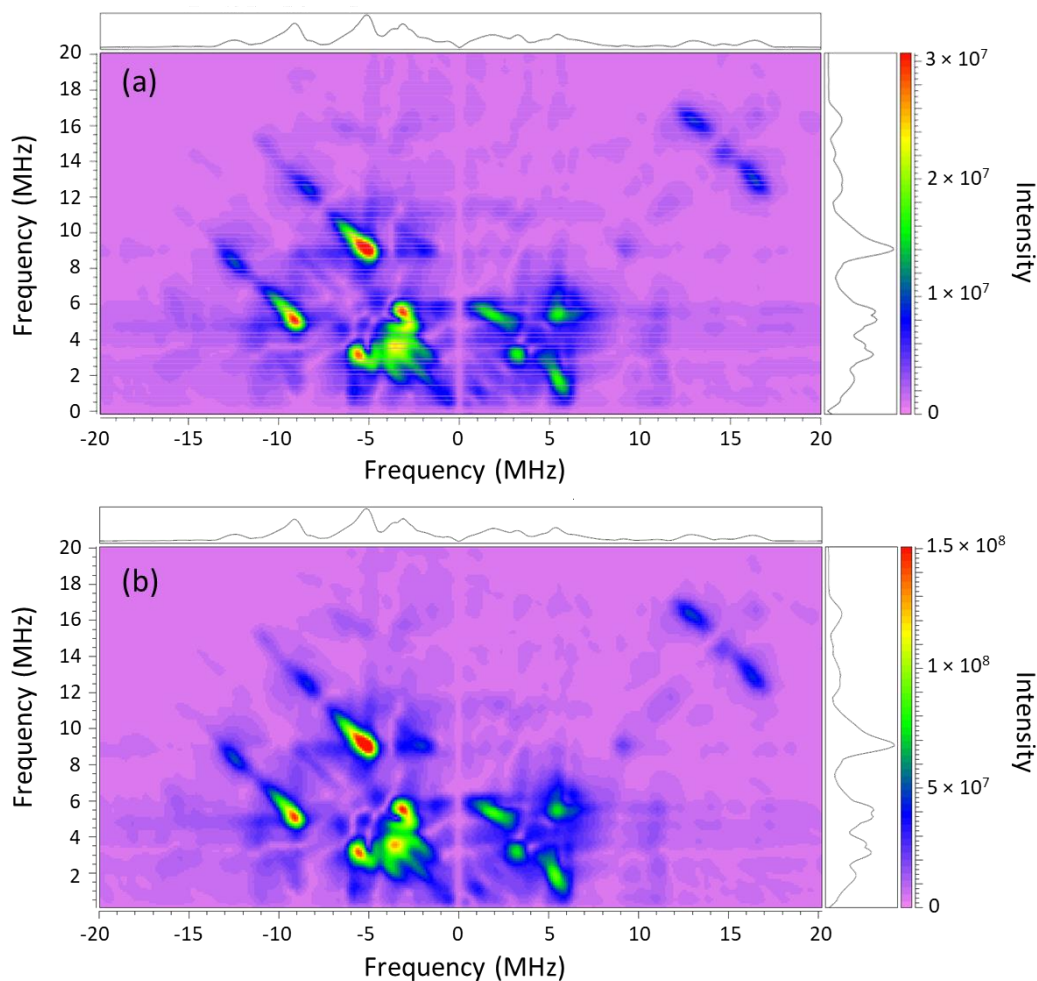
Figure III-19. HYSCORE spectra of $[Cr(ttpy)_2]^+$ complex (1 mM): (a) in the absence of TFA, (b) in the presence of 1 equivalent of TFA, recorded with delay d_1 = 136 ns

Based on the results mentioned above, the mechanism for this electrocatalytic proton reduction process is still not clear. As the HYSCORE spectra of $[Cr(ttpy)_2]^+$ complex in the presence and absence of TFA are identical, formation of a hybrid complex $[Cr^{III}(H)(ttpy^{\bullet-})]^{2+}$ where hydrogen atom is linked to the Cr core is not proved. Moreover, the released ttpy ligand is neutral in charge at -1.2 V bias, thus it is electrochemically inactive and cannot be involved in the proton reduction reaction. Therefore, we tend to attribute the catalytic process to a ligand-based reduction process where a protonated terpyridine complex, $[Cr^{III}(ttpyH)(ttpy^{\bullet-})]^{2+}$, can be an intermediate.

III.3. [Cr(ttpy)₂]³⁺ complex immobilized on TiO₂ nanoparticles

After studying the $[Cr(ttpy)_2]^{3+}$ complex in homogeneous environment, we immobilized it on TiO₂ NPs to study photo-induced charge transfer processes. Using TiO₂ NPs as a support can be more convenient in photocatalytic studies than using an electrode due to higher loading of the catalyst. Another advantage of this TiO₂ NPs support over an electrode surface is that it is also easier to study the evolution of photo-induced paramagnetic species by EPR spectroscopy. Similar to **Chapter 2**, the phosphonic acid was used as anchoring group to the TiO₂ surface.

III.3.1. Synthesis

The synthesis route to ttpy-PO₃Et₂ and ttpy-PO₃H₂ ligands, their complexation with Cr^{2+} salt and subsequent oxidation to form $[Cr(ttpy-PO_3Et_2)]^{3+}$ and $[Cr(ttpy-PO_3H_2)]^{3+}$ (denoted as $[Cr2P]^{3+}$) complexes are shown in **Scheme III-10**. The synthesis of the ttpy-PO₃Et₂ and ttpy-PO₃H₂ ligands follows a similar published procedure.[39] In our study, the ligands have been confirmed by ¹H NMR, ³¹P NMR and mass spectrometry. The complexation between the modified ttpy ligands and CrCl₂ is similar to the reaction to form $[Cr(ttpy)_2]^{3+}$ complex which has been described in **Section III.2.1.** Since both $[Cr(ttpy-PO_3Et_2)]^{3+}$ and $[Cr2P]^{3+}$complexes are paramagnetic, ¹H NMR cannot be used to characterize them. In fact, their presence has been confirmed with electrochemistry and UV-vis absorption spectroscopy, which will be described later.
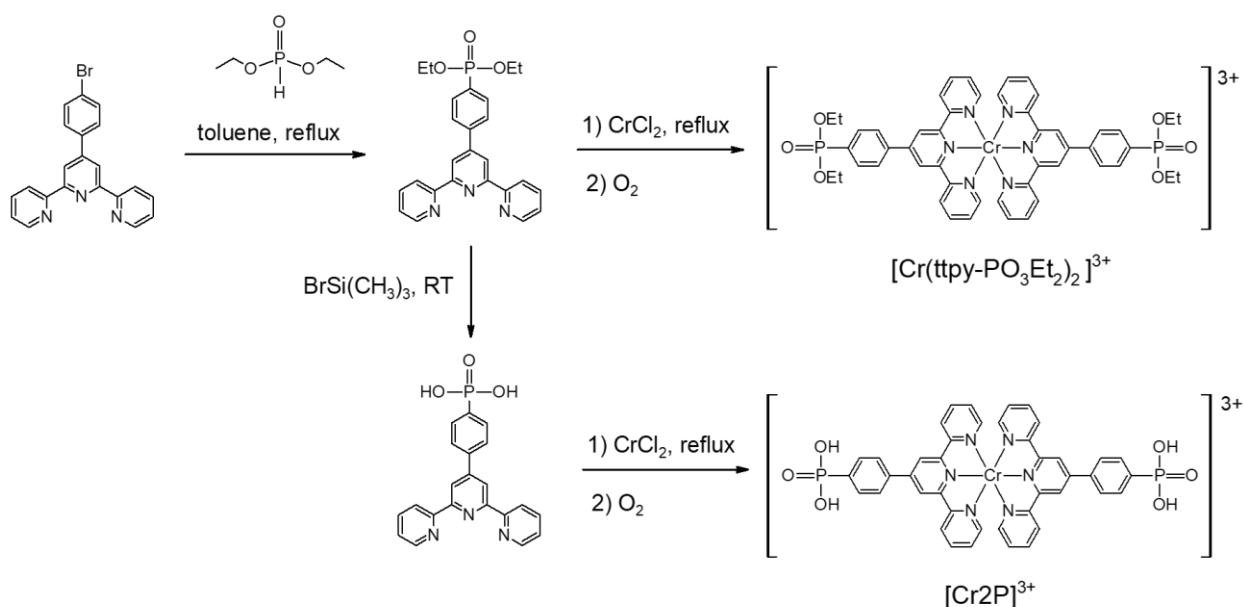
Scheme III-10. Synthesis route for $[Cr(ttpy-PO_3Et_2)_2]^{3+}$ and $[Cr2P]^{3+}$ complexes

Since it should be better if the Cr complex bears only one phosphonic acid group to prevent the possible cross-linking between neighboring NPs, we also attempted to synthesize the asymmetric Cr complex coordinated by a ttpy ligand and a ttpy-PO_3H_2 ligand, $[Cr(ttpy)(ttpy-PO_3H_2)]^{3+}$ ($[Cr1P]^{3+}$). Its synthesis route (**Scheme III-11**) follows a similar procedure in literature for heteroleptic terpyridine Cr complexes.[7,8] However, the synthesis is considered unsuccessful as evidenced by the mass spectrum of $[Cr1P]^{3+}$ complex and the cyclic voltammogram (CV) of ITO/$[Cr1P]^{3+}$ modified electrode.
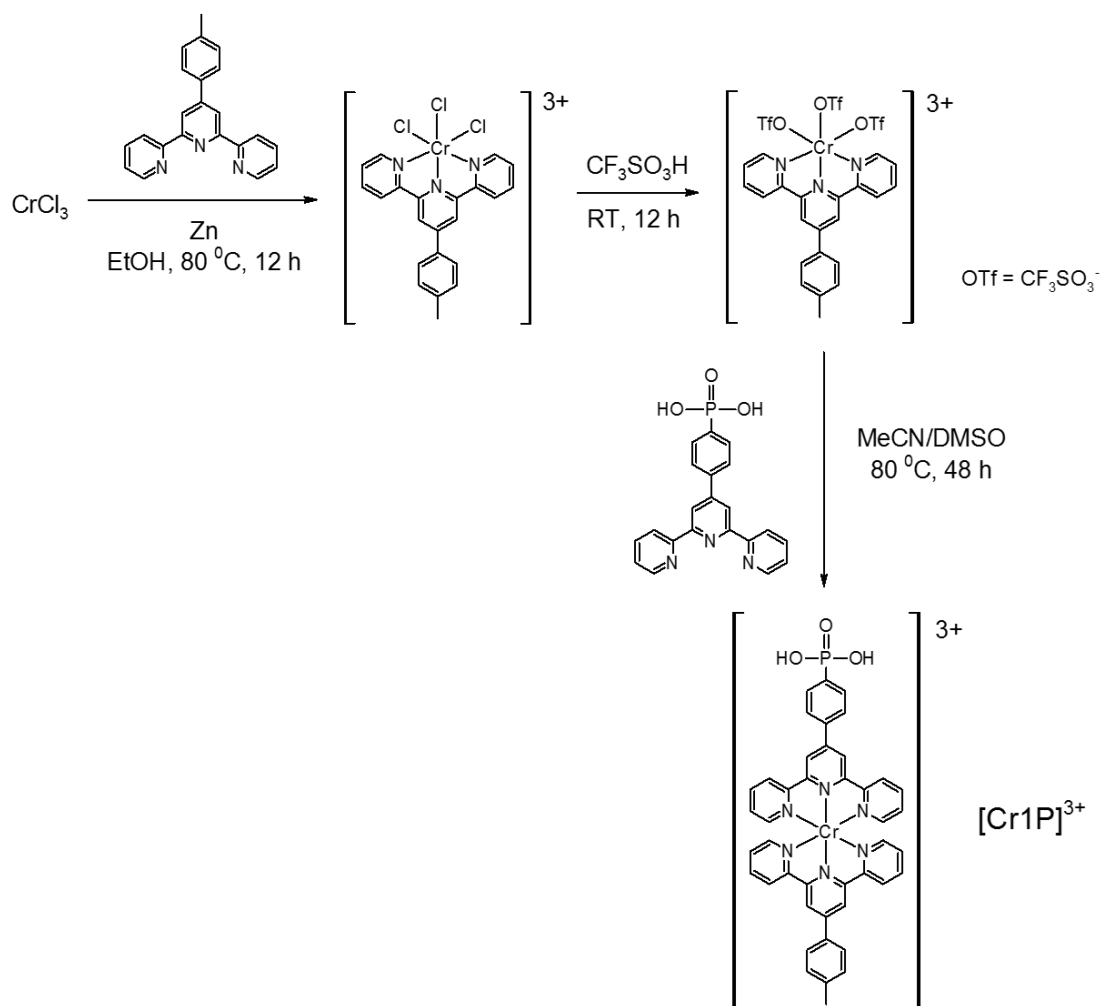
Scheme III-11. Synthesis route for $[Cr1P]^{3+}$ complex

Grafting the $[Cr2P]^{3+}$ complex onto TiO_2 NPs has been achieved by simply mixing the two components in DMF/DMSO mixed solvent at room conditions. The modified NPs were then washed with suitable solvents and separated by centrifugation. They are hereafter called TiO_2/$[Cr2P]^{3+}$. Further details can be found in the experimental section. By measuring the UV-vis absorbance of supernatant solution after each centrifugation step, we estimate the loading of $[Cr2P]^{3+}$ complex to be about 0.20 mmol.g^{-1}, which corresponds to about 3800 $[Cr2P]^{3+}$ molecules per particle or 2 molecules per nm^2 of surface.

III.3.2. Electrochemical properties

III.3.2.1. *ttpy-PO₃Et₂ ligand and [Cr(ttpy-PO₃Et₂)₂]³⁺ complex in solution*

The electrochemical behaviors of the $ttpy\text{-}PO_3Et_2$ ligand and corresponding $[Cr(ttpy\text{-}PO_3Et_2)_2]^{3+}$ complex have been characterized with cyclic voltammetry in order to study the effect of the phosphonate group. **Figure III-20** presents their CVs in comparison with the CV of the ttpy ligand alone. Their redox potentials are collected in **Table III-5** in comparison with the redox potentials of ttpy ligand and $[Cr(ttpy)_2]^{3+}$ complex.
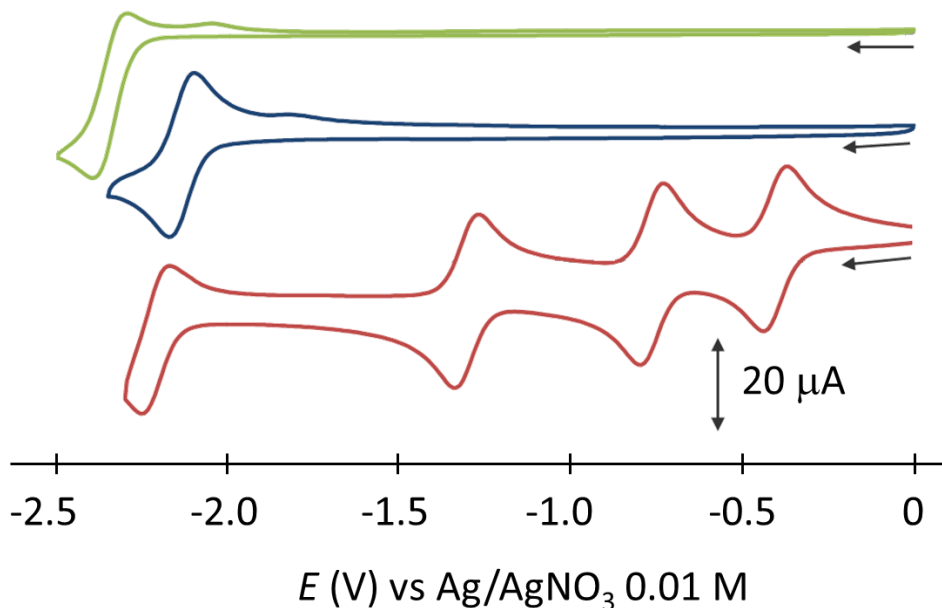
Figure III-20. CVs of ttpy (green), $ttpy\text{-}PO_3Et_2$ (blue) and $[Cr(ttpy\text{-}PO_3Et_2)_2]^{3+}$ (red) in MeCN + 0.1 M TBAPF₆ under Ar. WE = C disk (d = 3 mm), v = 100 mV.s⁻¹

Table III-5. Redox potentials of ttpy and $ttpy\text{-}PO_3Et_2$ ligands, $[Cr(ttpy)_2]^{3+}$ and $[Cr(ttpy\text{-}PO_3Et_2)_2]^{3+}$ complexes

$E_{1/2}$ (ΔEp), V	E_{red} (1)	E_{red} (2)	E_{red} (3)	E_{red} (4)
ttpy	-2.35 (0.09)	-	-	-
$ttpy\text{-}PO_3Et_2$	-2.13 (0.07)	-	-	-
$[Cr(ttpy)_2]^{3+}$	-0.47 (0.07)	-0.85 (0.07)	-1.35 (0.07)	-2.25 (0.07)
$[Cr(ttpy\text{-}PO_3Et_2)_2]^{3+}$	-0.34 (0.05)	-0.77 (0.06)	-1.30 (0.08)	-2.21 (0.08)

Comparing ttpy and $ttpy\text{-}PO_3Et_2$, the phosphonate derivatization increases the reduction potential of the ttpy ligand: from -2.35 V for ttpy to -2.13 V for $ttpy\text{-}PO_3Et_2$. The phosphonate substituent induces an electron withdrawing effect on the π-conjugated system, thus making its reduction easier. The $ttpy\text{-}PO_3Et_2$ ligand also shows a more reversible behavior than the ttpy ligand.

The $[Cr(ttpy-PO_3Et_2)_2]^{3+}$ complex exhibits a very similar CV as the $[Cr(ttpy)_2]^{3+}$ complex, showing four successive one-electron reduction processes centered at $E_{1/2}$ = -0.34, -0.77, -1.30 and -2.21 V. Based on the electrochemical properties of $[Cr(ttpy)_2]^{3+}$ complex, these half-wave potentials are thus attributed to $[Cr(ttpy)_2]^{3+}/[Cr(ttpy)_2]^{2+}$, $[Cr(ttpy)_2]^{2+}/[Cr(ttpy)_2]^{+}$, $[Cr(ttpy)_2]^{+}/[Cr(ttpy)_2]^{0}$ and $[Cr(ttpy)_2]^{0}/[Cr(ttpy)_2]^{-}$ redox couples, respectively. The added electrons are localized on the ligands while the oxidation state of Cr remains +3. These potentials are slightly positively shifted compared with those obtained for $[Cr(ttpy)_2]^{3+}$ complex. This shift is a consequence of the electron withdrawing phosphonate group making it easier to reduce. The fourth reduction process of $[Cr(ttpy-PO_3Et_2)_2]^{3+}$ complex appears at a potential similar to the analogous $[Cr(ttpy)_2]^{3+}$ complex rather than the free ttpy-PO$_3$Et$_2$ ligand. Besides, no signals of the free ttpy-PO$_3$Et$_2$ ligand at -2.13 V are detected.

III.3.2.2.   Grafting [Cr2P]$^{3+}$ complex on ITO

We first attempted to study the unprotected $[Cr2P]^{3+}$ complex directly with cyclic voltammetry to compare with the results mentioned above. However, the $[Cr2P]^{3+}$ complex (with ClO_4^- as counteranion) is not soluble in a variety of non-aqueous solvents like MeCN, DMF and CH_2Cl_2. We therefore chose to anchor the complex onto an ITO electrode to study its electrochemical properties. **Figure III-21a** presents the CV of ITO/[Cr2P]$^{3+}$ modified surface. The half-wave potentials are collected in **Table III-6** in comparison with the redox potentials of the $[Cr(ttpy-PO_3Et_2)_2]^{3+}$ precursor.
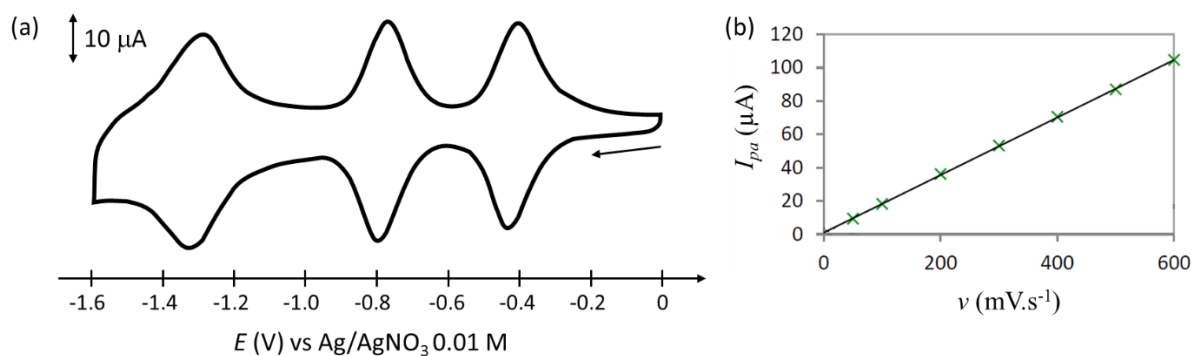
Figure III-21. (a) CV of ITO/[Cr2P]$^{3+}$ modified electrode (area = 1.2 cm^2) recorded in MeCN + 0.1 M TBAPF$_6$, v = 100 mV.s^{-1}. (b) $I_{pa} - v$ plot is fit with a linear function (R^2 = 0.9999).

Table III-6. Redox potentials of ITO/[Cr2P]$^{3+}$ electrode and [Cr(ttpy-PO$_3$Et$_2$)$_2$]$^{3+}$ complex in MeCN + 0.1 M TBAPF$_6$ under Ar

$E_{1/2}$ (ΔEp), V	E_{red} (1)	E_{red} (2)	E_{red} (3)
ITO/[Cr2P]$^{3+}$	-0.42 (0.02)	-0.79 (0.03)	-1.32 (0.03)
[Cr(ttpy-PO$_3$Et$_2$)$_2$]$^{3+}$	-0.34 (0.05)	-0.77 (0.06)	-1.30 (0.08)

The CV of ITO/[Cr2P]$^{3+}$ electrode shows three successive one-electron reduction steps, which are centered at $E_{1/2}$ = -0.42, -0.79 and -1.32 V. These values are similar to those obtained for the [Cr(ttpy-PO$_3$Et$_2$)$_2$]$^{3+}$ complex, therefore the three redox waves are attributed to [Cr2P]$^{3+}$/[Cr2P]$^{2+}$, [Cr2P]$^{2+}$/[Cr2P]$^{+}$ and [Cr2P]$^{+}$/[Cr2P]^{0} couples, respectively. No signs of phosphonic desorption are detected. The surface coverage Γ is estimated at $(6.0 \pm 0.1) \times 10^{-11}$ mol.cm^{-2} (see **Experimental Section** for the calculation). This relatively low Γ value is in the same range with previously reported values for complexes bearing ttpy phosphonic ligands anchored on ITO surface.[39–42]

For a kinetically controlled electron transfer process between a grafted redox species and the electrode, a linear relationship between peak current intensity I_p and scan rate v has been proved as follows:[43]

$$I_p = \frac{n^2 F^2}{4RT} vA\Gamma \qquad \text{(Eq III-6)}$$

where Γ (mol.cm^{-2}) is the surface coverage of the complex. For the first reduction step at -0.42 V, a linear plot between anodic peak current I_{pa} and scan rate v is obtained (**Figure III-21b**). This linear relationship suggests the electronic communication between anchored [Cr2P]$^{3+}$ and ITO electrode is kinetically controlled, thus proving the successful grafting of [Cr2P]$^{3+}$ onto the ITO support.

III.3.2.3. *Grafting [Cr2P]$^{3+}$ complex on TiO$_2$ NPs*

We first attempted to characterize the electrochemical behavior of TiO$_2$/[Cr2P]$^{3+}$ NPs in colloidal solution using C or Pt disk electrode as WE. However our attempts were not successful due to low conductivity of TiO$_2$ NPs and probably low surface coverage. Therefore, we employed a microcavity Pt electrode (d = 50 µm) to study the electrochemical properties of TiO$_2$/[Cr2P]$^{3+}$ in powder form. **Figure III-22** shows the CVs of the TiO$_2$/[Cr2P]$^{3+}$ NPs and bare TiO$_2$ NPs where the potential was swept from 0 to -2 V in anhydrous MeCN solution. The first reduction step to form [Cr2P]$^{2+}$ at around -0.4 V is not observed. It could be due to the fact that the [Cr2P]$^{3+}$ molecules bearing two phosphonic acid

groups are anchored on two TiO_2 NPs, thus are buried inside the TiO_2 matrix, making it difficult to be in contact with the Pt electrode.

As the redox potentials of grafted $[Cr2P]^{3+}$ on TiO_2 NPs are difficult to measure, the potentials of $ITO/[Cr2P]^{3+}$ are taken for further studies.
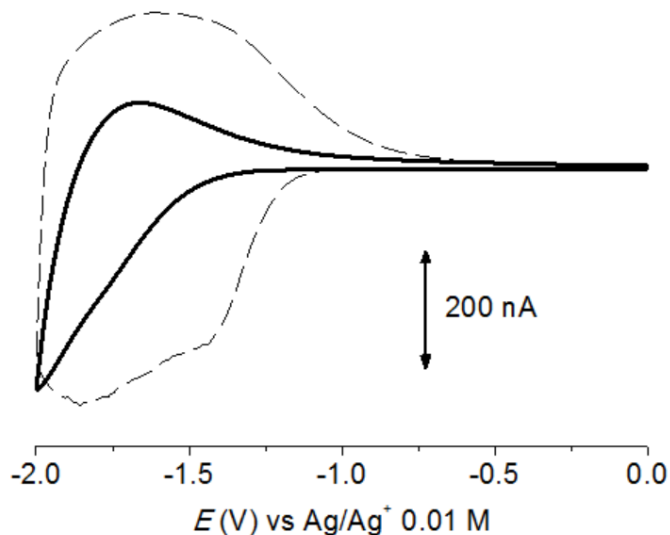
Figure III-22. CVs of $TiO_2/[Cr2P]^{3+}$ NPs (solid line) and TiO_2 (dashed line) recorded in solid state using a microcavity Pt electrode in MeCN + 0.1 M TBAPF$_6$ under Ar, $v = 100$ mV.s^{-1}

III.3.3. UV-vis absorption spectroscopy and emission spectroscopy

Our attempts to measure the UV-vis absorption spectrum of $TiO_2/[Cr2P]^{3+}$ NPs in colloidal solution were not successful due to intense light scattering effect. If the colloid concentration is reduced to such a degree that the light scattering is negligible, there are not enough complex molecules to show a good signal. Therefore, the absorption spectrum of $TiO_2/[Cr2P]^{3+}$ NPs has been recorded in solid form by mixing them with KBr. Its spectrum is presented in **Figure III-23** together with that of bare TiO_2 NPs for comparison.
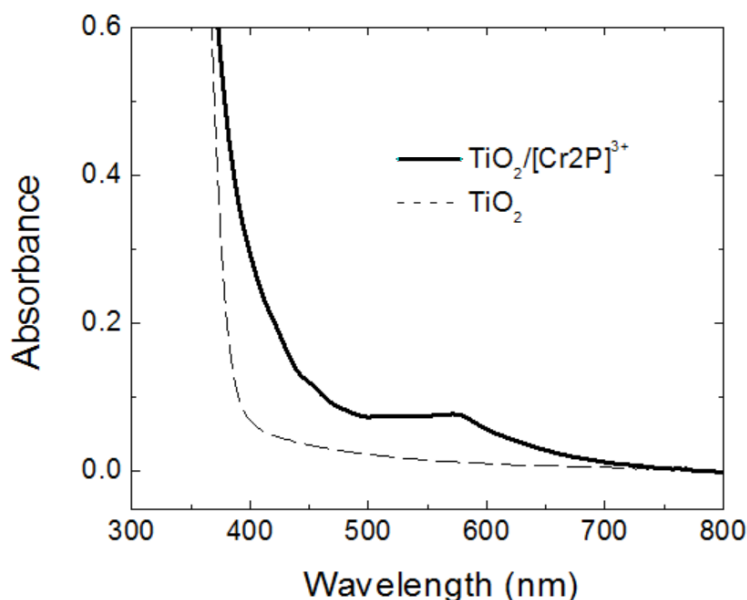
Figure III-23. Solid state UV-vis absorption spectra of $TiO_2/[Cr2P]^{3+}$ (black line) and TiO_2 NPs (dashed line)

The modified $TiO_2/[Cr2P]^{3+}$ NPs shows absorption maximum at 580 nm whereas the bare TiO_2 NPs do not absorb in the visible range. The precursor $[Cr2P]^{3+}$ complex in solid state also exhibits this absorption maximum, which is not present in the spectra of $[Cr(ttpy)_2]^{3+}$ complex or ttpy-PO_3H_2 ligand (**Figure III-24**). Therefore we attribute the 580 nm absorption peak to the immobilized $[Cr2P]^{3+}$ complex on TiO_2.
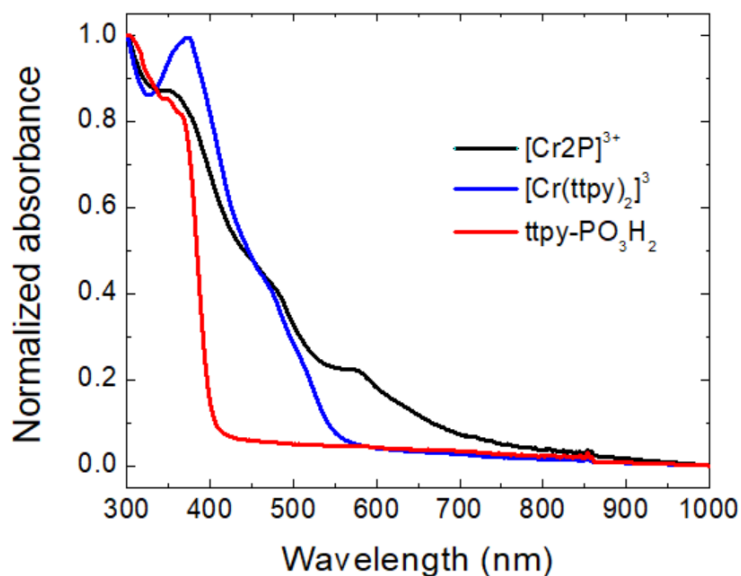
Figure III-24. Normalized UV-vis absorption spectra of $[Cr2P]^{3+}$ complex (black), $[Cr(ttpy)_2]^{3+}$ complex (blue) and ttpy-PO_3H_2 ligand (red) recorded in solid state by mixing them with KBr

The $TiO_2/[Cr2P]^{3+}$ NPs do not emit light in the 600 – 900 nm range after photoexcitation at 580 nm or 450 nm where the anchored $[Cr2P]^{3+}$ complex shows some degree of absorption but not TiO_2 scaffold. The weak luminescence of $[Cr(ttpy)_2]^{3+*}$ excited state seems to be completely quenched after being grafted onto TiO_2 NPs.

III.3.4. Electron paramagnetic resonance spectroscopy

The EPR experiments have been carried out at low temperature to study $TiO_2/[Cr2P]^{3+}$ NPs, which is expected to be paramagnetic in ground state. When the loading of $[Cr2P]^{3+}$ reaches maximum at 0.20 mmol.g^{-1} TiO_2 (about 2 molecules/nm^2), the $TiO_2/[Cr2P]^{3+}$ simply exhibits a broad EPR line centered at $g \sim 2$ (**Figure III-25a**). It is typically attributed to the high concentration of paramagnetic species. However, this line precludes further studies of the magnetic properties of individual $[Cr2P]^{3+}$ species. The $[Cr2P]^{3+}$ complex concentration is estimated to be 1.2 mM, which is comparable to the $[Cr(ttpy)_2]^{3+}$ concentration (1 mM) employed in an analogous EPR experiment for the free complex (see **Section III.2.4**). Therefore, the local concentration on the NP surface is the main cause for this EPR line. This assumption is supported by the estimated loading of 2 $[Cr2P]^{3+}$ molecules per nm^2. The high local concentration of paramagnetic $[Cr2P]^{3+}$ complex provides evidence for the successful grafting of $[Cr2P]^{3+}$ on TiO_2 NPs.

We then prepared $TiO_2/\{[Cr2P]^{3+}+BPA\}$ (BPA = benzylphosphonic acid) NPs containing 2 % Cr and 98 % BPA as lateral spacers. With this dilution, the average distance between Cr sites is expected to significantly increase. **Figure III-25b** shows its EPR response. No signals are observed at other regions of this X-band spectrum. It can be seen that although the broad EPR line is still observed, sub-structures of individual $[Cr2P]^{3+}$ sites start to be detectable. A sharp line at 3440 G and two maxima at ~ 3200 G and 2960 G are similar to the signal of $[Cr(ttpy)_2]^{3+}$ free complex. However, the highest absorption peak of the free complex at ~ 1400 G is not observed in the NPs.
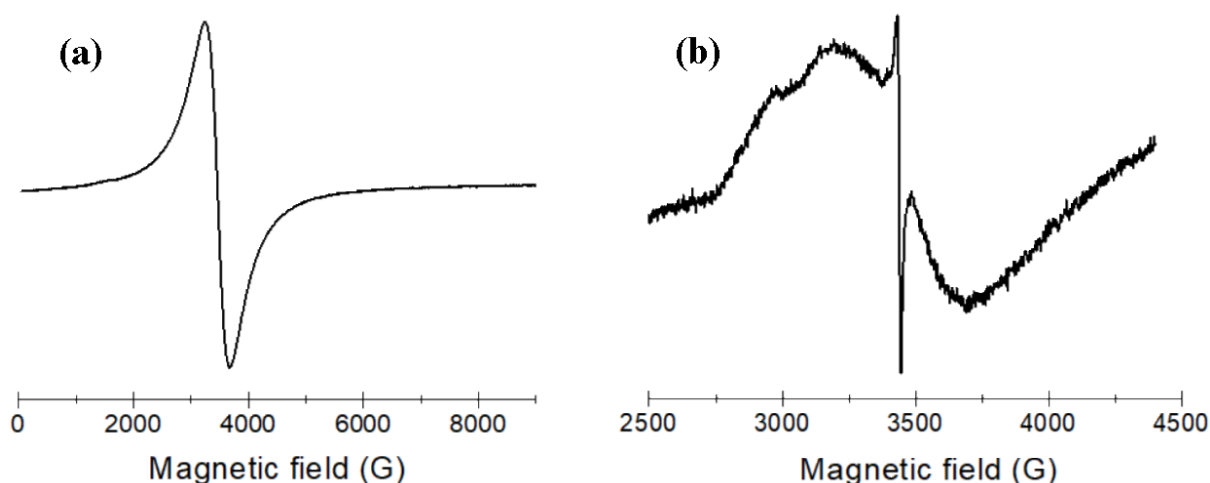
Figure III-25. EPR spectra of $TiO_2/[Cr2P]^{3+}$ colloid in MeCN (C = 6 g.L^{-1}) with (a) 100 % $[Cr2P]^{3+}$ and (b) 2 % $[Cr2P]^{3+}$ + 98 % BPA spacers. They were taken with an X-band EPR spectrometer (f = 9.6538 GHz, 10 G modulation, 20 mW) at 10 K during 84 s.

III.4. $[Cr(ttpy)_2]^{3+}$ and $[Ru(bpy)_3]^{2+}$ complexes co-immobilized on TiO$_2$ nanoparticles

After the electrochemical and photophysical characterizations of TiO$_2$/Ru^{2+} NPs (**Chapter 2**) and TiO$_2$/[Cr2P]$^{3+}$ NPs (**Chapter 3**), we hypothesized that the incorporation of both complexes onto TiO$_2$ NPs may accelerate the rate of photo-induced electron transfer processes thanks to the close distance between the electronic components and long-lived charge separated state between (e$^-$)TiO$_2$ and Ru^{3+} species. The resulting triad, denoted as Ru^{2+}/TiO$_2$/[Cr2P]$^{3+}$ (**Scheme III-12**), was designed to study visible light-induced electron transfer events between: (i) Ru^{2+*} and TiO$_2$ to form Ru^{3+} and (e$^-$)TiO$_2$; subsequently, (ii) (e$^-$)TiO$_2$ and [Cr2P]$^{3+}$ to form TiO$_2$ and [Cr2P]$^{2+}$ species. As $[Cr(ttpy)_2]^{3+}$ complex can be reduced twice by $[Ru(bpy)_3]^{2+*}$ to form $[Cr(ttpy)_2]^+$, we also expected to be able to store two electrons on a single [Cr2P]$^{3+}$ site if the charge transfer rate was fast enough and the back electron transfer was delayed. Furthermore, as the $[Cr(ttpy)_2]^{3+}$ complex has shown promising activity in electrocatalytic H$_2$ production, we presumed the Ru^{2+}/TiO$_2$/[Cr2P]$^{3+}$ triad to be a photocatalyst for the H$_2$ production reaction. All of these hypotheses and experimental results will be discussed in this section.
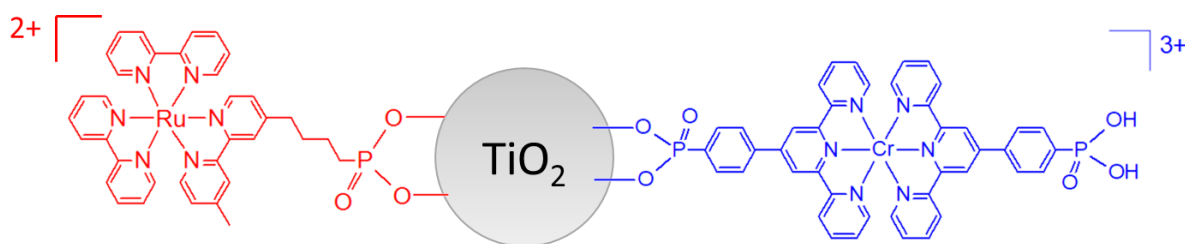
Scheme III-12. Structure of Ru^{2+}/TiO$_2$/[Cr2P]$^{3+}$ triad

III.4.1. Synthesis

The [Cr2P]$^{3+}$ and [RuP]$^{2+}$ complexes have been allowed to chemically adsorb on TiO$_2$ NPs via phosphonic binding groups as they have been shown to be successfully grafted onto the NPs. They were simply mixed with TiO$_2$ NPs in DMF/DMSO solvent and kept in dark for 60 hours to yield the Ru^{2+}/TiO$_2$/[Cr2P]$^{3+}$ triad. In this way the molar ratio of Ru:Cr can be easily controlled by changing the complex concentration. In some experiments where a lateral spacer is required, benzylphosphonic acid (BPA) has been added. In a typical experiment, the molar ratio of Ru:Cr:BPA was set at 20:2:78 (% mol). The loadings of [RuP]$^{2+}$ and [Cr2P]$^{3+}$ complexes are estimated to be 60 µmol.g^{-1} (~ 1000 molecules per NP, 0.6 molecule per nm^2) and 6 µmol.g^{-1} (~ 100 molecules per NP, 0.06 molecule per nm^2), respectively. Further details can be found in the **Experiment Section**.

III.4.2. Photophysical properties

a) UV-vis absorption spectroscopy and emission spectroscopy

Similar to previous UV-vis absorption experiments, the $Ru^{2+}/TiO_2/[Cr2P]^{3+}$ NPs were also mixed with KBr and pressed into a pellet for measurement. As we are interested in the possibility to store multiple electrons at the Cr sites, the molar ratio of Ru to Cr species was set at 10 so that the electron supply from $[RuP]^{2+}$ PS is not a limiting factor for the $[Cr2P]^{3+}$ reduction. BPA, which is optically transparent in the visible region, was also included as lateral spacer to enhance the photo-induced electron injection rate as shown in **Chapter 2**. Another reason for using BPA is to separate the paramagnetic Cr^{3+} sites from each other for the EPR characterization, which will be discussed later in this section. **Figure III-26** presents the absorption spectrum of $Ru^{2+}/TiO_2/[Cr2P]^{3+}$ triad, compared with those of bare TiO_2 NPs and $TiO_2/[Cr2P]^{3+}$ dyad.
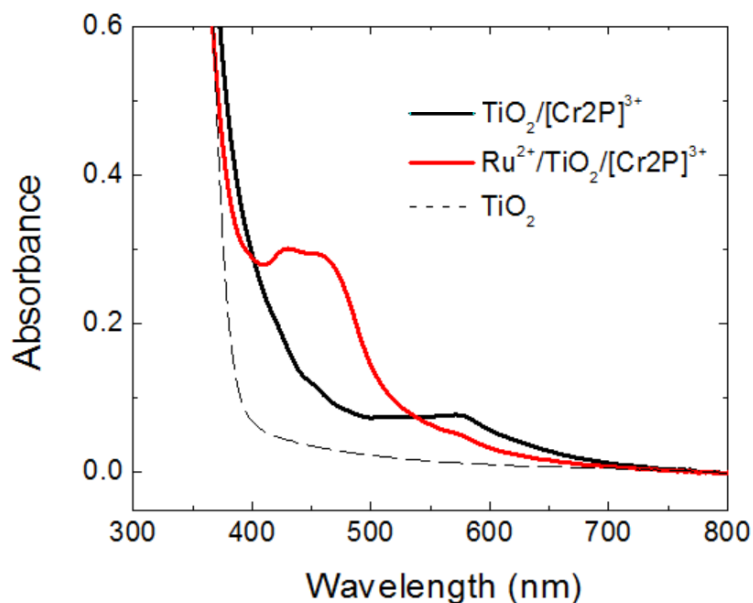
Figure III-26. Solid state UV-vis spectra of $TiO_2/[Cr2P]^{3+}$ (black line), $Ru^{2+}/TiO_2/[Cr2P]^{3+}$ (Ru:Cr:BPA = 20:2:78, % mol) (red line) and TiO_2 NPs (dashed line)

The double peak at around 450 nm is attributed to the ^{1}MLCT absorption of $[Ru(bpy)_3]^{2+}$-type PS as seen in **Chapter 2**. The small absorption maximum at 580 nm is ascribed to the grafted $[Cr2P]^{3+}$ species as shown in **Section III.3**. Only changes in the intensities of the two peaks are observed when the molar ratio of Ru:Cr is changed. The presence of both complexes on the NPs after thorough washing is an evidence for the successful co-grafting process.

b) Emission spectroscopy

The emission of $Ru^{2+}/TiO_2/[Cr2P]^{3+}$ triad has been recorded in steady state after

photoexcitation at 450 nm. **Figure III-27** shows its spectrum in comparison with the spectrum of TiO_2/Ru^{2+} dyad. Both spectra have the same broad, featureless shape, thus it is attributed to the ^{3}MLCT emission of $[RuP]^{2+}$ PS. The peak position of the triad (624 nm) is slightly blue-shifted to that of the dyad (630 nm). The blue-shift has been shown to be due to the separation of the Ru^{2+} PS by BPA lateral spacers. No emission at 770 nm by $[Cr2P]^{3+*}$ excited state has been observed.
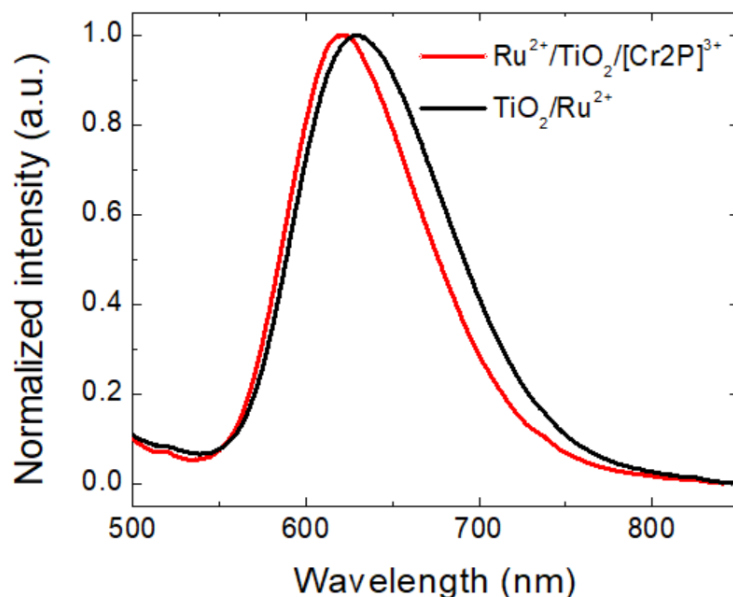
Figure III-27. Normalized emission spectra of $Ru^{2+}/TiO_2/[Cr2P]^{3+}$ triad (Ru:Cr:BPA = 20:2:78, % mol) (red line) and TiO_2/Ru^{2+} dyad (black line) recorded in MeCN under Ar

c) Transient absorption spectroscopy

We initially aimed to use TA technique to record TA spectra of $Ru^{2+}/TiO_2/[Cr2P]^{3+}$ at different time intervals after laser excitation. In order to avoid as much light scattering as possible and maintain a sufficiently stable colloid, the triad concentration was kept very low at 0.04 g.L^{-1} in MeCN solution. Consequently, the full TA spectra need to be accumulated over at least 20 mins to obtain a good signal-to-noise ratio. During this time, however, the NPs begin to precipitate. Therefore, we only focus on the signal decay at 450 nm, which has been ascribed to the charge recombination between (e$^-$)TiO$_2$ and Ru^{3+} species (see **Chapter 2**). The decay (**Figure III-28a**) is very similar in shape as the same decay of TiO$_2$/Ru^{2+} dyad (**Figure II-20**), although in this triad it seems to recover to zero faster than in the dyad.
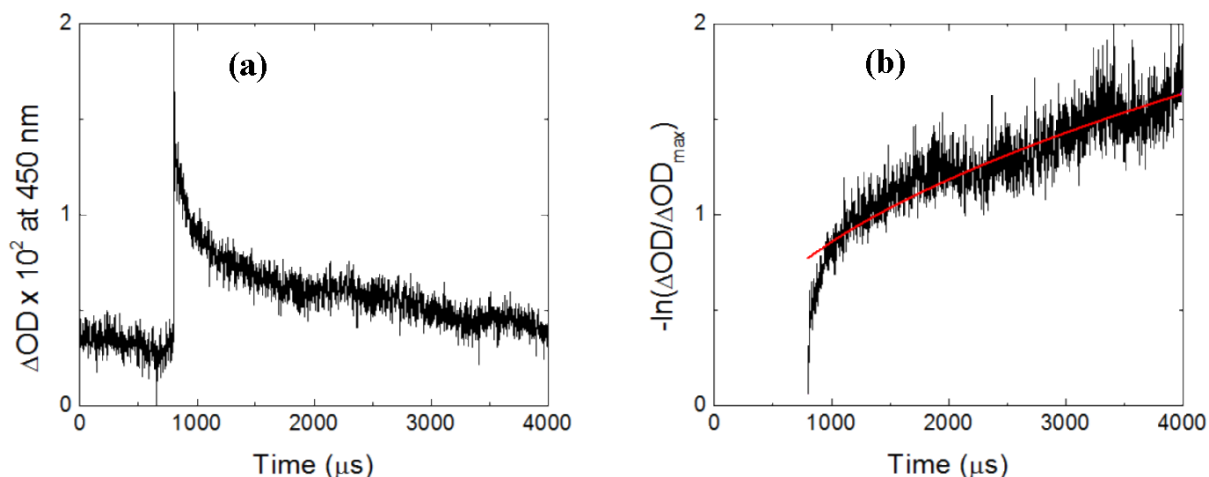
Figure III-28. TA measurement for Ru^{2+}/TiO$_2$/[Cr2P]$^{3+}$ triad (Ru:Cr:BPA = 20:2:78, % mol, C = 0.04 g.L^{-1}) recorded in MeCN under Ar 20 ns after excitation at 532 nm: (a) Signal decay at 450 nm, (b) –*ln(ΔOD/ΔOD$_{max}$) versus t* plot (black line) obtained at 450 nm and fit with a power function (red line).

Similar to **Chapter 2**, as the charge recombination process should take into account the diffusion of both trapped electrons and oxidized PS, its kinetics should be fit with the Kohlrausch – Williams – Watts (KWW)'s stretched exponential equations (**Equations III-7** and **III-8**).[44] **Figure III-28b** shows the fitting (red line) according to the KWW model. The β_{KWW} fitting parameter is close to that obtained with TiO$_2$/Ru^{2+} dyad and far from 1, which justifies the stretch model.

$$\Delta OD = \Delta OD_{max} \exp\left[-\left(\frac{t}{\tau_{KWW}}\right)^{\beta_{KWW}}\right] \qquad \text{(Eq III-7)}$$

$$-\ln\left(\frac{\Delta OD}{\Delta OD_{max}}\right) = \left(\frac{t}{\tau_{KWW}}\right)^{\beta_{KWW}} \qquad \text{(Eq III-8)}$$

From the τ_{KWW} and β_{KWW} parameters, one can estimate a representative charge recombination rate k_{cr} by applying the **Equation III-9**.[45] The KWW fitting parameters (τ_{KWW} and β_{KWW}) as well as the recombination rate k_{cr} are collected in **Table III-7** and compared to those obtained with the TiO$_2$/Ru^{2+} dyad.

$$k_{cr} = \left[\frac{1}{k_{KWW}\beta_{KWW}}\Gamma\left(\frac{1}{\beta_{KWW}}\right)\right]^{-1} = \left[\frac{\tau_{KWW}}{\beta_{KWW}}\Gamma\left(\frac{1}{\beta_{KWW}}\right)\right]^{-1} \qquad \text{(Eq III-9)}$$

Table III-7. KWW fitting parameters (τ_{KWW} and β_{KWW}) and charge recombination rate k_{cr} between $(e^-)TiO_2$ and Ru^{3+} species in $Ru^{2+}/TiO_2/[Cr2P]^{3+}$ triad (Ru:Cr:BPA = 20:2:78, % mol), in comparison with TiO_2/Ru^{2+} dyad

	τ_{KWW} (µs)	β_{KWW}	k_{cr} (s^{-1})	$\tau_{cr} = (k_{cr})^{-1}$ (ms)
$Ru^{2+}/TiO_2/[Cr2P]^{3+}$	1400 ± 150	0.46 ± 0.01	300 ± 30	3.3
TiO_2/Ru^{2+}	3770 ± 800	0.51 ± 0.01	140 ± 30	7.1

At first, the two-fold increase in charge recombination kinetics of $Ru^{2+}/TiO_2/[Cr2P]^{3+}$ triad compared with that of TiO_2/Ru^{2+} dyad was surprising to us, as the presence of an electron acceptor like $[Cr2P]^{3+}$ should scavenge the injected electron on the CB of TiO_2, preventing back electron transfer between $(e^-)TiO_2$ and Ru^{3+} species. However, as we have assigned the signal decay at 450 nm to the $(e^-)TiO_2$ disappearance, two assumptions should be considered in the triad case: (i) the charge recombination process between $(e^-)TiO_2$ and Ru^{3+} is accelerated, or (ii) another electron transfer pathway besides the charge recombination process to consume these trapped electrons. The charge recombination rate between two species should only depend on their nature, distance and the solvent, thus the first assumption is not sensible. As the lifetime of the charge recombination is very long ($\tau_{cr} = (k_{cr})^{-1} = 7.1$ ms), $[Cr2P]^{3+}$ should be able to scavenge the electrons on TiO_2, supporting the second assumption. Therefore, we tend to attribute this two-fold increase in k_{cr} value to the additional electron transfer between $(e^-)TiO_2$ and $[Cr2P]^{3+}$ to transiently form the $Ru^{3+}/TiO_2/[Cr2P]^{2+}$ charge separated species. The rate of electron transfer between $(e^-)TiO_2$ and $[Cr2P]^{3+}$ should be in the same range with the recombination rate between $(e^-)TiO_2$ and Ru^{3+}.

Theoretically, such a transient charge separated state like $Ru^{3+}/TiO_2/[Cr2P]^{2+}$ can also be achieved by lateral electron transfer between Ru^{2+*} and Cr^{3+} species. To verify whether it is formed via the "through particle" or "on particle" mechanism, a redox-inert substrate like SiO_2 NPs can be employed so that only the latter mechanism can govern the electron transfer event. However, the surface coverage of phosphonic anchoring group on SiO_2 surface has been proved to be much lower than on TiO_2. Further reductions in the concentration of adsorbates like that will make it very challenging to characterize with the TA technique. Besides that, the rate of photo-induced electron injection from Ru^{2+*} to TiO_2 is very fast ($k_{inj} \sim 10^7 - 10^9$ s^{-1}, see **Chapter 2**). The quenching of $[Ru(bpy)_3]^{2+*}$ by $[Cr(ttpy)_2]^{3+}$ in solution has been shown to be 3.0×10^9 M^{-1}.s^{-1}.[19] Taking into account the concentration of $[Cr(ttpy)_2]^{3+}$ complex in the range of 10^{-5} M, the pseudo first-order quenching constant will be $\sim 3 \times 10^4$ s^{-1}, which is significantly smaller than the injection rate. Besides, as the complexes are fixed on TiO_2 surface and the concentration of Cr^{3+} is only 2 %, the chance for electron transfer to

occur between Ru^{2+*} species and underlying Ti^{4+} sites should be significantly higher than between Ru^{2+*} and Cr^{3+}. Therefore, it is reasonable to assume the "through particle" charge transfer as the main mechanism for the $Ru^{3+}/TiO_2/[Cr2P]^{2+}$ triad.

III.4.3. Electrochemical properties

a) [Cr2P]$^{3+}$ and [RuP]$^{2+}$ co-immobilized on ITO electrode

In a similar fashion as the previous section, we attempted to study the electrochemical behavior of $[Cr2P]^{3+}$ and $[RuP]^{2+}$ complexes co-grafted on ITO electrode prior to study the $Ru^{2+}/TiO_2/[Cr2P]^{3+}$ triad. An ITO surface was immersed into a solution containing both the complexes with the same concentration of 1 mM for 20 hours in dark, then washed thoroughly before measured with cyclic voltammetry. Its CV is shown in **Figure III-29a**. In the anodic part, a reversible wave at $E_{1/2} = 0.90$ V is attributed to the Ru^{3+}/Ru^{2+} couple. In the cathodic part, three successive reversible waves are detected, corresponding to the reduction of Cr^{3+} to Cr^{2+}, Cr^+ and Cr^0 respectively. This CV can be considered as the superimposition of $ITO/[RuP]^{2+}$ and $ITO/[Cr2P]^{3+}$ CVs. Based on the Ru^{3+}/Ru^{2+} wave at ~ 0.9 V and the Cr^{3+}/Cr^{2+} wave at ~ -0.48 V, the surface coverage Γ of the complexes is calculated to be $(2.0 \pm 0.2) \times 10^{-12}$ mol.cm^{-2} for $[RuP]^{2+}$ and $(5.0 \pm 0.5) \times 10^{-12}$ mol.cm^{-2} for $[Cr2P]^{3+}$. The higher loading of $[Cr2P]^{3+}$ compared with $[RuP]^{2+}$ is probably due to the presence of two phosphonic anchoring group on $[Cr2P]^{3+}$ while $[RuP]^{2+}$ has only one group.

Also based on the two aforementioned redox waves, a plot of $I_{pa} - v$ (**Figure III-29b**) has been obtained for both Ru and Cr species. Linear fittings are well achieved for both species, proving the two complexes have been successfully grafted on ITO.
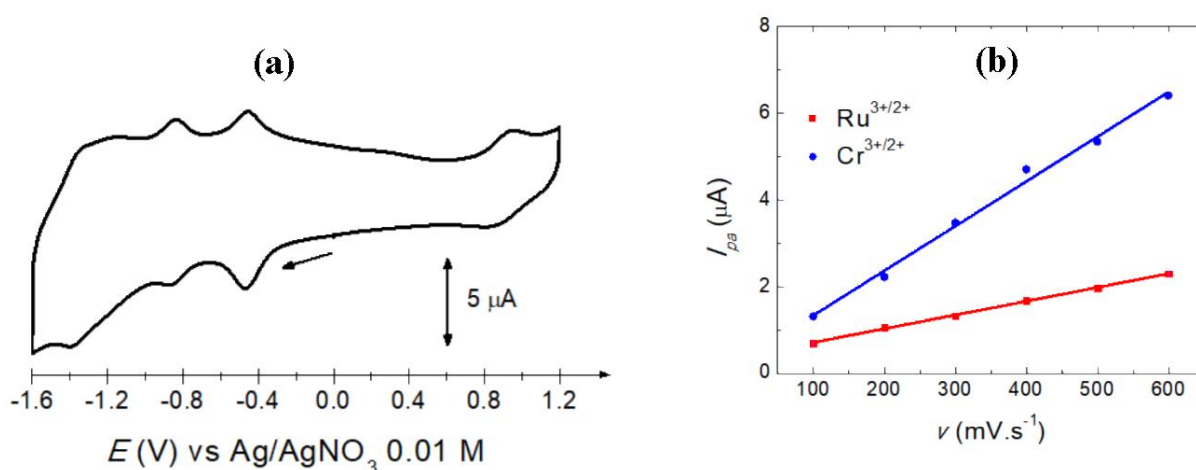
Figure III-29. (a) CV of ITO/{Ru^{2+}+[Cr2P]$^{3+}$} electrode recorded in MeCN + 0.1 M TBAPF$_6$ under Ar, $v = 100$ mV.s^{-1}. (b) $I_{pa} - v$ plot based on the Ru^{3+}/Ru^{2+} (red squares) and Cr^{3+}/Cr^{2+} (blue circles) peaks, together with the linear fitting ($R^2 = 0.999$ for Ru^{3+}/Ru^{2+} and 0.992 for Cr^{3+}/Cr^{2+}).

b) [Cr2P]³⁺ and [RuP]²⁺ co-immobilized on TiO₂ NPs

Our attempts to record the CVs of Ru²⁺/TiO₂/[Cr2P]³⁺ NPs with a microcavity Pt electrode have not been successful as for the TiO₂/[Cr2P]³⁺ dyad. Two kinds of triads have been measured: (i) Ru:Cr = 1:1 (% mol) without BPA spacers, and (ii) Ru:Cr:BPA = 20:2:78 (% mol). The very low surface coverage as shown with ITO electrode (about 10 times lower for the Ru-Cr mixture compared with Cr or Ru alone) makes it difficult to record the CV.

Therefore, the redox potential of grafted [Cr2P]³⁺/[Cr2P]²⁺ couple is assumed to be similar to that of ITO/[Cr2P]³⁺ electrode (-0.42 V) for subsequent studies in this chapter.

III.4.4. Photoreduction of [Cr(ttpy)₂]³⁺ free complex by TiO₂/Ru²⁺ NPs

In a systematic study, we first focus on the photoreduction of [Cr(ttpy)₂]³⁺ free complex by TiO₂/Ru²⁺ dyad before studying the Ru²⁺/TiO₂/[Cr2P]³⁺ triad. We conducted UV-vis absorption measurements with similar experimental conditions as in **Section III.2.6** where [Ru(bpy)₃]²⁺ PS was used instead of TiO₂/Ru²⁺ NPs. The absorption spectra during the irradiation time are shown in **Figure III-30a**. It is important to note that the TiO₂/Ru²⁺ colloid alone does not show the ¹MLCT absorption band of [Ru(bpy)₃]²⁺ with a maximum at 450 nm as in the solid state. Only a shoulder emerges at the foot of the TiO₂ absorption band. The first reduction step to form [Cr(ttpy)₂]²⁺ complex is usually characterized by a broad band centered at 800 nm; however it is not observed in this case as for the photoreduction experiment of [Cr(ttpy)₂]³⁺ by [Ru(bpy)₃]²⁺ in solution (see **Section III.2.6**). The second reduction step to form [Cr(ttpy)₂]⁺ complex is clearly evidenced by the spectral changes indicated by black arrows: the evolution of two absorption maxima at 500 nm and 580 nm, accompanied by the characteristic peak at 723 nm. The experiment proves that the two-electron reduction of [Cr(ttpy)₂]³⁺ to [Cr(ttpy)₂]⁺ is achievable with immobilized Ru²⁺ PS on TiO₂.
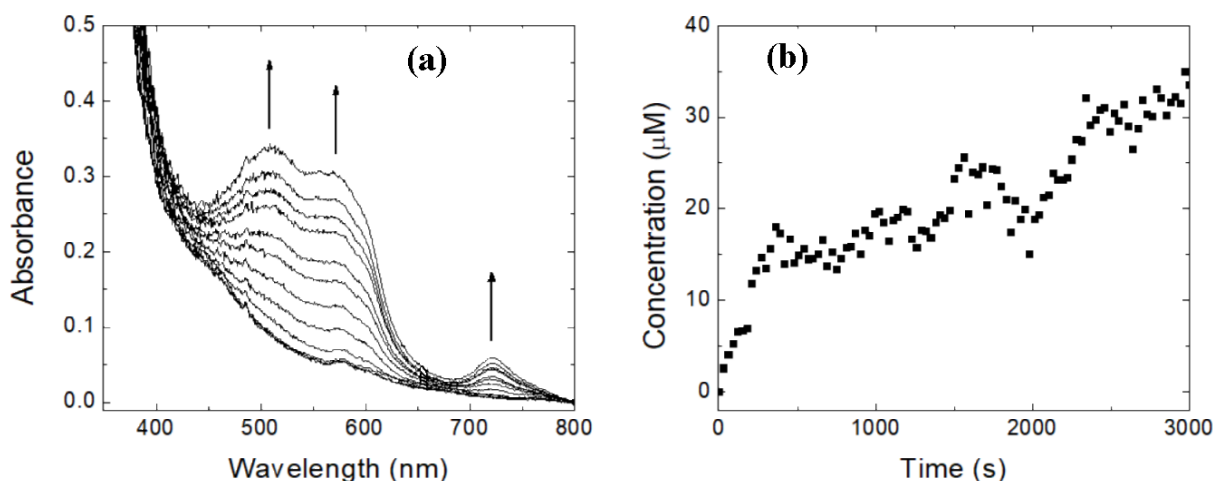
Figure III-30. (a) UV-vis spectra of a mixture of $[Cr(ttpy)_2]^{3+}$ free complex (C = 57 μM) and TiO_2/Ru^{2+} NPs (C = 0.25 g.L^{-1}) in Ar-saturated MeCN solution containing 300 equivalents of TEOA. The spectra were taken every 300 s under irradiation at 400 nm < λ < 750 nm. They have been corrected to exclude the light scattering effect of NPs. Arrows indicate the spectral changes during the experiment. (b) Evolution of $[Cr(ttpy)_2]^+$ complex (measured at 723 nm) during the experiment.

By tracking the 723 nm peak, one can calculate the concentration of the $[Cr(ttpy)_2]^+$ complex as a function of irradiation time (**Figure III-30b**). After 3000 s the conversion from $[Cr(ttpy)_2]^{3+}$ to $[Cr(ttpy)_2]^+$ is only 60 %. As a comparison, when $[Ru(bpy)_3]^{2+}$ is used instead of TiO_2/Ru^{II}, the conversion reaches ~ 90 % after the same time. The concentration of Ru^{2+} PS in both cases is comparable: ~ 5.3×10^{-5} M in this dyad sample and 4×10^{-5} M for $[Ru(bpy)_3]^{2+}$ complex in solution. It is therefore concluded that the photoreduction rate is reduced when immobilized Ru^{2+} dye is used instead of $[Ru(bpy)_3]^{2+}$ complex in solution. We assume that this rate decline is due to the poorer contact between the colloid and the $[Cr(ttpy)_2]^{3+}$ homogeneous complex, therefore anchoring both complexes on TiO_2 NPs may accelerate this rate. This assumption will be checked and discussed in the next section.

III.4.5. Photoreduction of immobilized Cr^{3+} complex in $Ru^{2+}/TiO_2/[Cr2P]^{3+}$ triad

a) Energy diagram

We first examine the energy levels associated with the electronic components in $Ru^{2+}/TiO_2/[Cr2P]^{3+}$ triad. **Scheme III-13** describes the redox potentials of Ru^{3+}/Ru^{2+}, Ru^{3+}/Ru^{2+*}, Cr^{3+}/Cr^{2+}, Cr^{2+}/Cr^+ and the CB of TiO_2, which are relevant to the photo-induced electron transfer cascade in this study. Under visible irradiation, Ru^{2+} PS is excited (step 1) and can inject electrons to the CB of TiO_2 (step 2). The electron injection can occur from either ^{1}MLCT state ("hot injection") or ^{3}MLCT relaxed state of the Ru^{2+} PS. This injection step has been described in detail in **Chapter 2**. Afterwards, in terms of thermodynamics, the electrons on the CB of TiO_2 can reduce $[Cr2P]^{3+}$ complex twice to form $[Cr2P]^+$ (step 3).

Regeneration of Ru^{2+} PS is achieved by sacrificial reductant TEOA (step 4). Possible back electron transfer pathways are between $(e^-)TiO_2$ and Ru^{3+} (step 5) and between $[Cr2P]^{2+}$ or $[Cr2P]^+$ and Ru^{3+} (step 6), which can prevent the two-electron storage on $[Cr2P]^{3+}$ sites. TEOA is expected to short-circuit these back electron transfer pathways as demonstrated with $[Cr(ttpy)_2]^{3+}$ and $[Ru(bpy)_3]^{2+}$ complexes in solution. The following experiments have been designed to study these charge transfer steps.
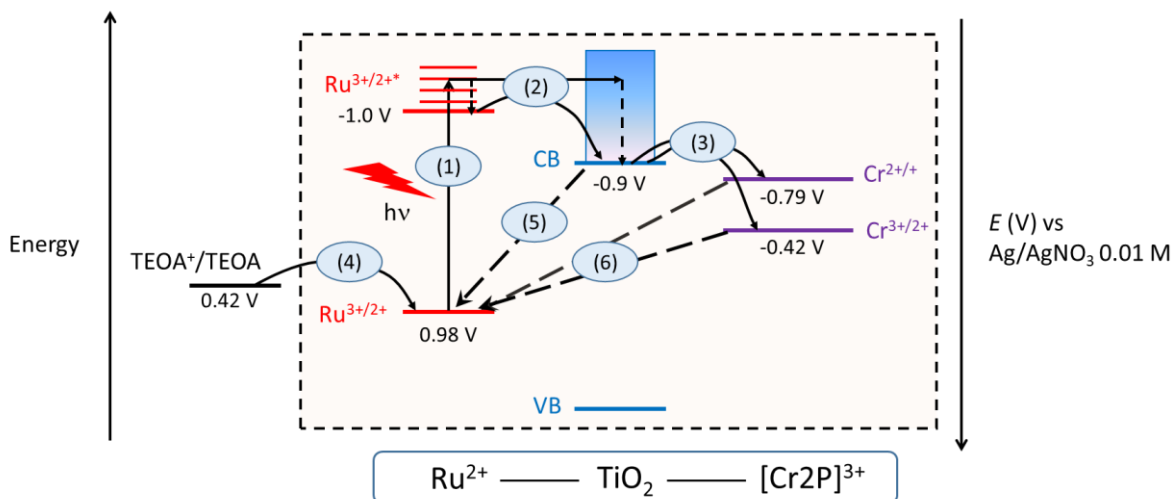
Scheme III-13. Energy diagram of $Ru^{2+}/TiO_2/[Cr2P]^{3+}$ triad and the expected photo-induced electron transfer cascade: (1) photo-excitation of Ru^{2+} dye, (2) electron injection to the CB of TiO_2, (3) sequential electron transfer to reduce $[Cr2P]^{3+}$ to $[Cr2P]^{2+}$ and then $[Cr2P]^+$, (4) regeneration of Ru^{2+} PS by TEOA, (5) back electron transfer between $(e^-)TiO_2$ and Ru^{3+} species, and (6) back electron transfer between $[Cr2P]^{2+}$ or $[Cr2P]^+$ and Ru^{3+} species. Dashed rectangle surrounds the triad components.

b) Charge transfer reactions monitored by UV-vis spectroscopy

In order to compare with the photoreduction experiment described in the previous section, we conducted a similar experiment using $Ru^{2+}/TiO_2/[Cr2P]^{3+}$ triad instead of TiO_2/Ru^{2+} and $[Cr(ttpy)_2]^{3+}$ mixture, in the presence of TEOA. However, no spectral changes are observed. The photoreduction of immobilized $[Cr2P]^{3+}$ is therefore deemed unsuccessful.

c) Charge transfer reactions monitored by EPR spectroscopy

In order to understand why the photoreduction of immobilized $[Cr2P]^{3+}$ in the triad is not accomplished, a light-coupled EPR experiment has been carried out at low temperature and in the absence of TEOA sacrificial donor to study the formation of photo-induced paramagnetic species. Our research hypothesis is that if $[Cr2P]^+$ doubly reduced complex is formed, it can be observed by EPR as in the case of $[Cr(ttpy)_2]^+$ complex ($S = 1/2$). **Figure III-31** shows the EPR signals of the triad in MeCN solution before and after irradiation.
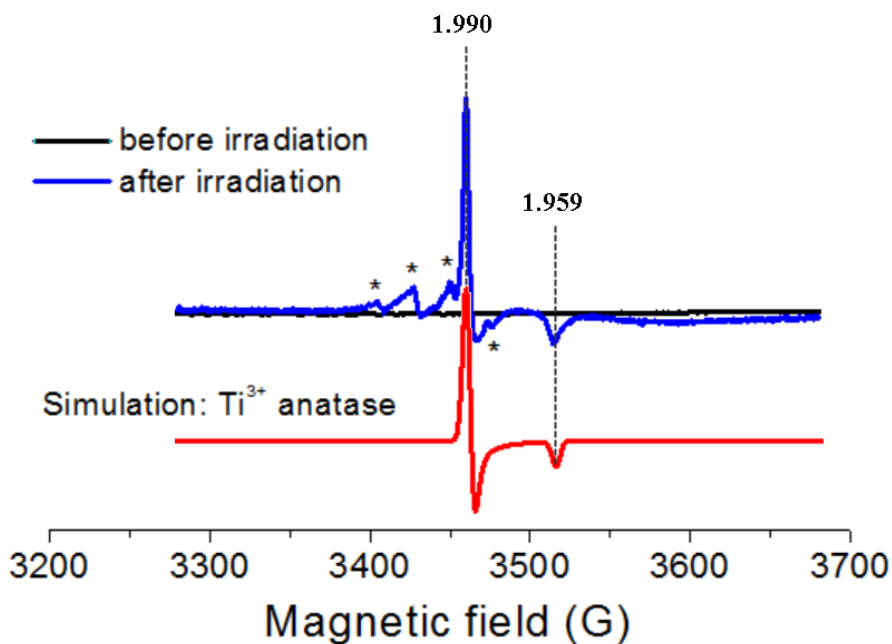
Figure III-31. EPR spectra of $Ru^{2+}/TiO_2/[Cr2P]^{3+}$ NPs (20% Ru, 2% Cr and 78 % BPA) before and after *in situ* irradiation by a 455 nm LED, together with simulation of trapped electrons in anatase TiO_2 NPs. The spectra were recorded with an X-band EPR spectrometer (f = 9.65 GHz, 20 mW) at 10 K. The asterisks mark peaks of $^{\bullet}CH_3$ radicals.

The spectrum before irradiation seems to suggest an EPR-silent system, although $[Cr2P]^{3+}$ molecules is expected to absorb in a wide range of magnetic field in a similar fashion as $[Cr(ttpy)_2]^{3+}$ free complex. However, the amount of grafted $[Cr2P]^{3+}$ in this study ($\sim 3.6 \times 10^{-5}$ M) is about two order of magnitude lower than in the experiment with Cr free complex ($\sim 10^{-3}$ M). Due to its very broad spectrum, the signal of grafted $[Cr2P]^{3+}$ on TiO_2 may be too small to record. With this degree of Cr complex dilution of only 2 %, the broad line centered at $g \sim 2$ due to high local concentration of paramagnetic Cr sites is also not observed.

Under continuous irradiation at 455 nm, the trapped electrons on TiO_2 are quickly created. They are characterized by EPR lines at $g_\perp$ = 1.990 and $g_{//}$ = 1.959.[46,47] No trapped holes (usually denoted as $O^{\bullet-}$ species in literature)[47] are detected in this triad, indicating that the trapped electrons are due to electron injection from Ru^{2+*} PS rather than direct bandgap excitation of TiO_2 semiconductor. Similar to the TiO_2/Ru^{2+} dyad, four small EPR lines (ratio = 1:3:3:1) separated by 23 G are also detected (marked with asterisks). They are ascribed to $^{\bullet}CH_3$ radicals[48] which have possibly been produced by the photo-degradation of remaining ethanol adsorbed on TiO_2.[49,50]

Meanwhile, the expected signal of $[Cr2P]^+$ (S = 1/2) at $g \sim 2$ is not detected. Even if the singly reduced $[Cr2P]^{2+}$ species is formed, it is not expected to be EPR-active in this X-band

129

frequency as the analogous $[Cr(ttpy)_2]^{2+}$ is EPR-silent despite its $S = 1$ spin state. Therefore, the EPR signal may correspond to either $Ru^{3+}/(e^-)TiO_2/[Cr2P]^{3+}$ or $Ru^{3+}/(e^-)TiO_2/[Cr2P]^{2+}$ transient species. Low temperature could inhibit the reduction of $[Cr2P]^{3+}$; however it allows for the detection of transient species. At room temperature the trapped electrons on TiO_2 will not be observable. The use of TEOA as sacrificial electron donor to compete with the back electron transfer pathways is vital for multi-electron accumulation on $[Cr2P]^{3+}$ sites.[16] Nevertheless, it may pose problems in this EPR experiment because its oxidized species, $TEOA^+$, may cause a high radical signal at $g \sim 2$ as well.

In summary, despite the possible formation of $[Cr(ttpy)_2]^+$ complex in solution by TiO_2/Ru^{II} NPs under visible irradiation and in the presence of TEOA, the quantitative photoreduction of grafted $[Cr2P]^{3+}$ in $Ru^{2+}/TiO_2/[Cr2P]^{3+}$ triad is not observed. It could be due to the difficulty to short-circuit the back electron transfer processes between photogenerated Ru^{3+} and $[Cr2P]^{2+}$ complexes on the TiO_2 surface by TEOA. Thermodynamic considerations have already shown that the back electron transfer between $[Cr(ttpy)_2]^{2+}$ and $[Ru(bpy)_2]^{3+}$ in solution is remarkably more favorable than the reduction of $[Ru(bpy)_3]^{3+}$ by TEOA (-1.41 eV compared with -0.52 eV), which is a necessary step to further reduce $[Cr(ttpy)_2]^{2+}$ species to $[Cr(ttpy)_2]^+$. When both $[RuP]^{2+}$ and $[Cr2P]^{3+}$ complexes are grafted on TiO_2 with a molar ratio of 10:1, the chance that a $[Cr2P]^{3+}$ site is surrounded by $[RuP]^{2+}$ sites is high than in homogeneous solution, thus this back electron transfer may be enhanced. Therefore, unfortunately we are not able to observe the electron accumulation in $[Cr2P]^{3+}$ sites.

III.5. Conclusion

In **Chapter 3** the electrochemical and photophysical behaviors of $[Cr(ttpy)_2]^{3+}$ complex have been extensively studied using electrochemistry, steady-state and transient absorption and emission spectroscopies. The complex shows rich electrochemical properties with five reversible redox states, $[Cr(ttpy)_2]^{n+}$ (n = 3, 2, 1, 0, -1). DFT calculations demonstrate that all the added electrons are localized on the ttpy ligands, thus the oxidation state of Cr always remains +3. The four complexes corresponding to n = 3, 2, 1, 0 exhibit different fingerprints in UV-vis absorption and EPR spectroscopy, which is convenient to identify them in a reaction mixture.

The $[Cr(ttpy)_2]^{3+}$ complex has found applications in photo-induced multiple electron storage and electrocatalysis in homogeneous environments. In the presence of another PS like $[Ru(bpy)_3]^{2+}$ and a sacrificial electron donor like TEOA, the $[Cr(ttpy)_2]^{3+}$ can be doubly reduced with 100 % conversion. In addition, the $[Cr(ttpy)_2]^{3+}$ complex also shows electrocatalytic activity towards H_2 production in non-aqueous solution. It is, however, not a very good electrocatalyst due to possible decoordination of ttpy ligands under a prolonged bias.

Immobilization of $[Cr(ttpy)_2]^{3+}$ on ITO electrode and TiO_2 NPs was achieved by functionalizing the complex with two phosphonic anchoring group, which is denoted as $[Cr2P]^{3+}$. The $ITO/[Cr2P]^{3+}$ electrode exhibits three successive reduction waves at potentials comparable to those of $[Cr(ttpy)_2]^{3+}$, proving that the Cr complex retains rich electrochemical properties after being grafted. In contrast to the $[Cr(ttpy)_2]^{3+}$ complex in solution, $TiO_2/[Cr2P]^{3+}$ NPs show no emission after being photo-excited. The evidence for successful grafting on TiO_2 is a broad EPR line centered at $g \sim 2$, which is characteristic of closely packed paramagnetic species. The broad EPR line can still be observed at lower $[Cr2P]^{3+}$ concentrations, suggesting that the $[Cr2P]^{3+}$ sites likely stay close to each other on the TiO_2 surface.

Finally, both $[RuP]^{2+}$ PS and $[Cr2P]^{3+}$ complex have been immobilized on ITO electrode and TiO_2 NPs to study photo-induced charge transfer events and the possibility of accumulating multiple electrons on $[Cr2P]^{3+}$ sites. The electrochemical behavior of $ITO/\{[RuP]^{2+}+[Cr2P]^{3+}\}$ electrode is a superimposition of $ITO/[RuP]^{2+}$ and $ITO/[Cr2P]^{3+}$ signals, thus proving the successful grafting process. A similar superimposition is also observed in the UV-vis absorption spectrum of $Ru^{2+}/TiO_2/[Cr2P]^{3+}$ triad, which comprises of TiO_2/Ru^{2+} and $TiO_2/[Cr2P]^{3+}$ spectra. However, the multiple charge storage on $[Cr2P]^{3+}$ sites is not achieved. It may be due to accelerated kinetics of the back electron transfer reaction

between grafted $[RuP]^{3+}$ and $[Cr2P]^{2+}$ transient species to regenerate $[RuP]^{2+}$ and $[Cr2P]^{3+}$ initial complexes, thus preventing the $[Cr2P]^{2+}$ complex to be further reduced.

In the next chapter we will present a study on another complex as an electron acceptor that undergoes a coupled chemical reaction after being reduced. The coupled reaction may reduce the back electron transfer kinetics.

References

1   L. A. Büldt and O. S. Wenger, *Chem. Sci.*, 2017, DOI: 10.1039/C7SC03372A.

2   N. A. P. Kane-Maguire, *Top. Curr. Chem.*, 2007, **280**.

3   P. S. Wagenknecht and P. C. Ford, *Coord. Chem. Rev.*, 2011, **255**, 591–616.

4   N. Serpone, M. A. Jamieson, M. S. Henry, M. Z. Hoffman, F. Bolletta and M. Maestri, *J. Am. Chem. Soc.*, 1979, **101**, 2907–2916.

5   C. C. Scarborough, K. M. Lancaster, S. DeBeer, T. Weyhermuller, S. Sproules and K. Wieghardt, *Inorg. Chem.*, 2012, **51**, 3718–3732.

6   W. A. Wickramasinghe, P. H. Bird and N. Serpone, *Inorg. Chem.*, 1982, **21**, 2694–2698.

7   J. Schonle, E. C. Constable, C. E. Housecroft, A. Prescimone and J. A. Zampese, *Polyhedron*, 2015, **89**, 182–188.

8   E. C. Constable, C. E. Housecroft, M. Neuburger, J. Schönle and J. A. Zampese, *Dalt. Trans.*, 2014, **43**, 7227–7235.

9   L. Hammarstrom, *Acc. Chem. Res.*, 2015, **48**, 840–850.

10   Y. Pellegrin and F. Odobel, *Coord. Chem. Rev.*, 2011, **255**, 2578–2593.

11   S. Karlsson, J. Boixel, Y. Pellegrin, E. Blart, H.-C. Becker, F. Odobel and L. Hammarstrom, *J. Am. Chem. Soc.*, 2010, **132**, 17977–17979.

12   W. Song, C. R. K. Glasson, H. Luo, K. Hanson, M. K. Brennaman, J. J. Concepcion and T. J. Meyer, *J. Phys. Chem. Lett.*, 2011, **2**, 1808–1813.

13   Z. Chen, J. J. Concepcion, H. Luo, J. F. Hull, A. Paul and T. J. Meyer, *J. Am. Chem. Soc.*, 2010, **132**, 17670–17673.

14   W. Song, A. Ito, R. A. Binstead, K. Hanson, H. Luo, M. K. Brennaman, J. J. Concepcion and T. J. Meyer, *J. Am. Chem. Soc.*, 2013, **135**, 11587–11594.

15   M. P. O'Neil, M. P. Niemczyk, W. A. Svec, D. Gosztola, G. L. 3rd Gaines and M. R. Wasielewski, *Science (80-.).*, 1992, **257**, 63–65.

16   M. Kuss-Petermann, M. Orazietti, M. Neuburger, P. Hamm and O. S. Wenger, *J. Am. Chem. Soc.*, 2017, **139**, 5225–5232.

17   M. Skaisgirski, X. Guo and O. S. Wenger, *Inorg. Chem.*, 2017, **56**, 2432–2439.

18   F. Lakadamyali, A. Reynal, M. Kato, J. R. Durrant and E. Reisner, *Chem. Eur. J.*, 2012,

18, 15464–15475.

19   R. Farran, "Transfert d'électron photoinduit au sein d'assemblages hétérométalliques associant le [Ru(bpy)₃]²⁺ à des complexes bisterpyridine du Fe(II), Co(III) et Cr(III)", *PhD Dissertation,* Université Grenoble-Alpes, 2015.

20   M. C. Hughes and D. J. Macero, *Inorg. Chem.*, 1976, **15**, 2040–2044.

21   O. V. Gritsenko, P. R. T. Schipper and E. J. Baerends, *Chem. Phys. Lett.*, 1999, **302**, 199–207.

22   J. C. Barbour, A. J. I. Kim, E. DeVries, S. E. Shaner and B. M. Lovaasen, *Inorg. Chem.*, 2017, **56**, 8212–8222.

23   U. Casellato, R. Graziani, R. P. Bonomo and A. J. Di Bilio, *J. Chem. Soc. Dalt. Trans.*, 1991, 23–31.

24   K. Kasuga, H. Miyasaka, M. Handa and M. Dairaku, *Polyhedron*, 1995, **14**, 1675–1679.

25   O. Stern and M. Volmer, *Z. Phys.*, 1919, **20**, 183–188.

26   V. G. Vaidyanathan and B. U. Nair, *Eur. J. Inorg. Chem.*, 2004, 1840–1846.

27   A. Juris, V. Balzani, F. Barigelletti, S. Campagna, P. Belser and A. von Zelewsky, *Coord. Chem. Rev.*, 1988, **84**, 85–277.

28   S. Yasui, K. Itoh, M. Tsujimoto and A. Ohno, *Bull. Chem. Soc. Jpn.*, 2002, **75**, 1311–1318.

29   F. Bolletta, M. Maestri, L. Moggi and V. Balzani, *J. Chem. Soc. Chem. Commun.*, 1975, 901–902.

30   M. von Smoluchowski, *Z. Phys. Chem., 1917, 92,129.*, 1917, **92**, 129–168.

31   J. H. Dymond, M. A. Awan, N. F. Glen and J. D. Isdale, *Int. J. Thermophys.*, 1991, **12**, 433–447.

32   H. Sun and M. Z. Hoffman, *J. Phys. Chem.*, 1994, **98**, 11719–11726.

33   K. Kalyanasundaram, J. Kiwi and M. Gratzel, *Helv. Chim. Acta*, 1978, **61**, 2720–2730.

34   S.-F. Chan, M. Chou, C. Creutz, T. Matsubara and N. Sutin, *J. Am. Chem. Soc.*, 1981, **103**, 379–384.

35   N. Elgrishi, M. B. Chambers and M. Fontecave, *Chem. Sci.*, 2015, **6**, 2522–2531.

36   N. Elgrishi, M. B. Chambers, V. Artero and M. Fontecave, *Phys. Chem. Chem. Phys.*, 2014, **16**, 13635–13644.

37   C. Arana, S. Yan, M. Keshavarz-K., K. T. Potts and H. D. Abruna, *Inorg. Chem.*, 1992, **31**, 3680–3682.

38   B. D. McCarthy, D. J. Martin, E. S. Rountree, A. C. Ullman and J. L. Dempsey, *Inorg. Chem.*, 2014, **53**, 8350–8361.

39   R. Farran, D. Jouvenot, F. Loiseau, J. Chauvin and A. Deronzier, *Dalt. Trans.*, 2014, **43**, 12156–12159.

40   R. Farran, L. Le Quang, D. Jouvenot, F. Loiseau, R. Pansu, A. Deronzier and J. Chauvin, *Inorganica Chim. Acta*, 2017, **454**, 197–207.

41   R. Farran, D. Jouvenot, B. Gennaro, F. Loiseau, J. Chauvin and A. Deronzier, *ACS Appl. Mater. Interfaces*, 2016, **8**, 16136–16146.

42   F. Liu, T. Cardolaccia, B. J. Hornstein, J. R. Schoonover and T. J. Meyer, *J. Am. Chem. Soc.*, 2007, **129**, 2446–2447.

43   A. J. Bard and L. R. Faulkner, *Electrochemical methods: Fundamentals and Applications (2nd edition)*, John Wiley & Sons, 2001.

44   S. Ardo and G. J. Meyer, *J. Am. Chem. Soc.*, 2011, **133**, 15384–15396.

45   R. N. Sampaio, A. V. Muller, A. S. Polo and G. J. Meyer, *ACS Appl. Mater. Interfaces*, 2017, **9**, 33446–33454.

46   R. F. Howe and M. Gratzel, *J. Phys. Chem.*, 1987, **91**, 3906–3909.

47   C. P. Kumar, N. O. Gopal, T. C. Wang, M.-S. Wong and S. C. Ke, *J. Phys. Chem. B*, 2006, **110**, 5223–5229.

48   M. Kaise, H. Nagai, K. Tokuhashi, S. Kondo, S. Nimura and O. Kikuchi, *Langmuir*, 1994, **10**, 1345–1347.

49   V. Brezova, P. Tarabek, D. Dvoranova, A. Stasko and S. Biskupic, *J. Photochem. Photobiol. A Chem.*, 2003, **155**, 179–198.

50   D. Dvoranova, Z. Barbierikova and V. Brezova, *Molecules*, 2014, **19**, 17279–17304.

51   H. A. Asiri and A. B. Anderson, *J. Electrochem. Soc.*, 2015, **162**, F115–F122.

CHAPTER IV

Ru(II)/TiO$_2$/Mn(I) TRIAD FOR PHOTOCATALYTIC CO$_2$ REDUCTION

Abstract

Herein we present the electrocatalytic and photocatalytic reduction of CO$_2$ to CO and HCOOH using a Mn(I) tricarbonyl complex, [Mn(ttpy)(CO)$_3$Br] (ttpy = 4'-(p-tolyl)-2,2':6',2''-terpyridine), as pre-catalyst and [Ru(bpy)$_3$]$^{2+}$ (bpy = 2,2'-bipyridine) as photosensitizer. The photocatalytic CO$_2$ reduction experiments were performed under irradiation at 470 ± 40 nm in DMF/TEOA (TEOA: triethanolamine, C_{TEOA} = 1 M) solution mixture containing 1-benzyl-1,4-dihydronicotinamide (BNAH, 0.1 M) as sacrificial electron donor and different ratios of [Mn(ttpy)(CO)$_3$Br]:[Ru(bpy)$_3$]$^{2+}$ (Mn:Ru). The optimization of the Mn:Ru ratio shows that the 1:10 ratio offers the best performance in terms of total turnover number (TON$_{max}$ (CO) = 19, TON$_{max}$ (HCOOH) = 31) after 16 hours of irradiation. Afterwards, both complexes are grafted on TiO$_2$ nanoparticles via phosphonic acid anchoring groups to form a triad structure (denoted as Ru^{II}/TiO$_2$/Mn^I) with a Mn:Ru ratio estimated around 1:10. Under similar experimental conditions, the Ru^{II}/TiO$_2$/Mn^I nanoparticles produce HCOOH as the only product with TON$_{max}$ (HCOOH) = 27. The enhanced selectivity towards HCOOH when using grafted complexes compared with the mixture of homogeneous complexes in solution could be related to the mechanism of the first reduction process of [Mn(ttpy)(CO)$_3$Br] and hence the catalytically active species. We propose that a doubly reduced Mn^{-I} complex is the active species in homogeneous solution, whereas a singly reduced Mn^0 complex is the active species in Ru^{II}/TiO$_2$/Mn^I nanoparticles.

Résumé

Dans ce chapitre, nous présentons les résultats de la réduction électrocatalytique et photocatalytique du CO$_2$ en CO et HCOOH en utilisant un complexe du Mn(I) tricarbonyl [Mn(ttpy)(CO)$_3$Br] (ttpy = 4'-(p-tolyl)-2,2':6',2''-terpyridine) comme pré-catalyseur et le complexe [Ru(bpy)$_3$]$^{2+}$ (bpy = 2,2'-bipyridine) comme photosensibilisateur. La réduction photocatalytique du CO$_2$ sous irradiation à 470 ± 40 nm dans le DMF/TEOA (TEOA: triethanolamine, C_{TEOA} = 1 M) et contenant le 1-benzyl-1,4-dihydronicotinamide (BNAH, 0,1 M) en tant que donneur d'électrons sacrificiel a été menée en variant le rapport de concentration [Mn(ttpy)(CO)$_3$Br] : [Ru(bpy)$_3$]$^{2+}$ (Mn:Ru). Les résultats montrent qu'un rapport Mn:Ru de 1:10 offre les meilleures performances en termes de TON total: TON$_{max}$ (CO) = 19, TON$_{max}$ (HCOOH) = 31 après 16 heures d'irradiation. Les deux complexes [Mn(ttpy)(CO)$_3$Br] et [Ru(bpy)$_3$]$^{2+}$ ont été greffés sur des nanoparticules de TiO$_2$ via des groupements d'ancrage du type acide phosphonique portés par les ligands polypyridiniques pour former une structure triade (Ru^{II}/TiO$_2$/Mn^I). Le ratio Mn:Ru a été fixé sur les nanoparticules, proche de 1:10. Dans des conditions similaires à celles de la réduction photocatalytique du CO$_2$ en utilisant des complexes homogènes [Ru(bpy)$_3$]$^{2+}$ et [Mn(ttpy)(CO)$_3$Br] en solution, les nanoparticules hybrides Ru^{II}/TiO$_2$/Mn^I produisent HCOOH comme seul produit avec un TON$_{max}$ (HCOOH) = 27. La sélectivité accrue vers HCOOH lors de l'utilisation de Ru^{II}/TiO$_2$/Mn^I par rapport au mélange des complexes en solution pourraient être liés au mécanisme du premier processus de réduction de [Mn(ttpy)(CO)$_3$Br] et donc à l'espèce catalytiquement active. Nous proposons que le complexe Mn^{-I} doublement réduit soit l'espèce active en solution homogène, alors qu'un complexe Mn^0 mono réduit pourrait être l'espèce active sur les nanoparticules Ru^{II}/TiO$_2$/Mn^I.

IV.1. Introduction

In recent decades, the rise of the CO_2 content in the Earth atmosphere has become a major concern for human beings. As a greenhouse gas, it has been identified as a main factor contributing to the global warming[1] and sea level rise[2]. Chemical conversion of CO_2 into more value-added products such as CO and HCOOH provides a means to reduce its atmospheric content and to recycle CO_2 emitted from coal burning factories. However, the process is energy consuming as the O=C=O bonds are quite stable (around 800 kJ.mol^{-1}). **Table IV-1** shows the standard reduction potentials for several important products.[3] The potentials represent equilibrium potentials that are required for the reaction to occur, but usually a higher potential is necessary to achieve a significant reaction rate.

Table IV-1. CO₂ reduction potentials *vs* NHE in aqueous solution, 1 atm gas pressure and 1 M solutes[3]

Reactions	E^0 (V) vs SHE	E^0 (V) vs Ag/AgNO₃ 0.01 M[*]
$CO_2 + e^- \rightarrow CO_2^{\bullet-}$	-1.90	-2.44
$CO_2 + 2H^+ + 2e^- \rightarrow HCOOH$	-0.61	-1.15
$CO_2 + 2H^+ + 2e^- \rightarrow CO + H_2O$	-0.53	-1.07
$2CO_2 + 2H^+ + 2e^- \rightarrow H_2C_2O_4$	-0.49	-1.03

[*] Calculated by subtracting 0.54 V from E^0 vs SHE[4]

In this chapter we will mainly focus on the photocatalytic CO_2 reduction, with an emphasis on molecular and hybrid systems to tackle the issue. The reader is kindly referred to recent reviews by Perutz et al.[1], Ishitani et al.[5,6], Rieger et al.[7] and Fontecave et al.[8] for more information about homogeneous and hybrid systems for the electro- and photo-catalytic CO_2 reduction.

Since the pioneering works by Lehn and co-workers on the photocatalytic[9] and electrocatalytic[10] CO_2 reduction using [Re(bpy)(CO)₃Cl] catalyst, numerous publications on homogeneous catalysts have been made. The general strategy is to covalently link a photosensitizer (PS) and a molecular catalyst together for CO_2 reduction under visible light. This approach has been extensively summarized in the aforementioned reviews. It, however, often requires challenging multi-step synthesis to reach the desired supramolecules.

In recent years, an emergent approach is to immobilize the molecular PS and catalyst onto the surface of another material such as semiconductors, nanoparticles (NPs), electrodes and metal-organic framework (MOF)[5] to form a new hybrid system. We are interested in the systems containing NPs as they provide a good scaffold with a great surface area to accommodate the molecular PS and catalyst. Furthermore, semiconducting NPs such as TiO_2

can also act as an electronic component for the electron transfer reaction between the PS and the catalyst centers. Finally, this approach usually requires significantly less complicated synthesis than the supramolecular approach. This introduction section will highlight recent developments in this class of hybrid materials.

Cowan and co-workers[11] immobilized $[Ru(bpy)_3]^{2+}$ PS and $Ni(cyclam)^{2+}$ (cyclam = 1,4,8,11-tetraazacyclotetradecane) catalyst on ZrO_2 for photocatalytic CO_2 reduction to CO (**Scheme IV-1**). The system $Ru^{2+}/ZrO_2/Ni^{2+}$ (Ru:Ni = 2.6:1 % mol) produceed both CO (14.0 ± 1.4 µmol.g⁻¹) and H_2 (58.1 ± 9.1 µmol.g⁻¹) after 7 hours of visible irradiation in the presence of ascorbic acid as a sacrificial electron donor. It corresponded to the maximum turnover number (TON_{max}) for CO equal to 4.8, while the selectivity of CO_2 over H_2 was still poor. Increasing the irradiation time lead to decrease in activity, possibly due to deactivation pathway via the formation of $Ni^I(cyclam)$-CO species. Under the same conditions, a mixture of the two complexes in solution exhibited negligible CO production (TON_{max} (CO) ~ 0.2 after 7 hours). After excitation of the Ru^{2+} complex, transient absorption spectroscopy (TAS) showed that Ru^{2+*} excited state was partly reductively quenched by ascorbic acid to form Ru^+ species, which then transferred an electron to the Ni^{2+} sites. The rate of electron transfer between Ru^+ and Ni^{2+} immobilized on TiO_2 was estimated as 7.7×10^3 s⁻¹, whereas the rate between the two complexes in solution was significantly slower (10 s⁻¹). This enhanced electron transfer rate in the $Ru^{2+}/TiO_2/Ni^{2+}$ triad was proposed to be critical for the higher photocatalytic activity of the triad than the complex mixture in solution. Since ZrO_2 is redox-inactive, the charge transfer events in $Ru^{2+}/ZrO_2/Ni^{2+}$ could only occur via electron transfer between neighboring Ru^{2+} and Ni^{2+} species on surface, called "on particle" mechanism. This study proved that the immobilization of the PS and catalyst on surface increased the electron transfer kinetics by eliminating the complex diffusion in solution.
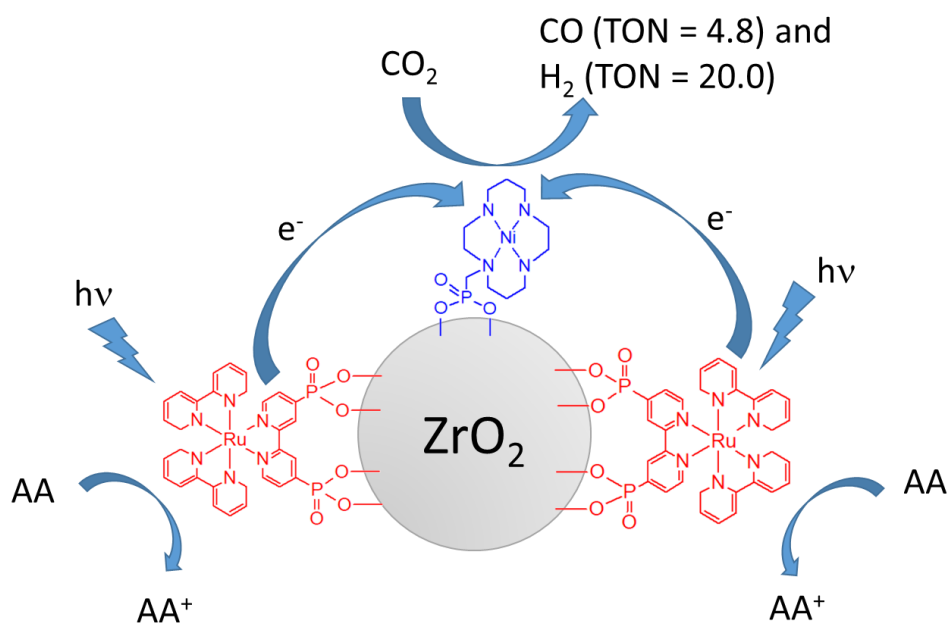
Scheme IV-1. Photocatalytic CO_2 reduction using $Ru^{2+}/ZrO_2/Ni^{2+}$ NPs mentioned in reference 11. AA = ascorbic acid

Since [Re(bpy)(CO)$_3$Cl] complex can act as both PS and catalyst, Reisner and co-workers have studied the photocatalytic CO_2 reduction using a related complex [Re(bpy)(CO)$_3$(3-picoline)]$^+$ bearing two phosphonic acid groups (denoted as [ReP]$^+$) which was immobilized on TiO$_2$ NPs.[12] The chemical structure of TiO$_2$/[ReP]$^+$ NPs and the proposed catalytic mechanism are shown in **Scheme IV-2**. Under irradiation the [ReP]$^+$ photocatalyst was reduced by triethanolamine (TEOA), a sacrificial electron donor, to form [ReP] which could react with CO_2. Optimal loading of the Re complexes on TiO$_2$ NPs was found to be 0.02 mmol.g^{-1}. In DMF/TEOA mixed solvent, TiO$_2$/[ReP]$^+$ NPs showed TON$_{max}$ (CO) ~ 50 after 24 hours of visible irradiation. In comparison, in the absence of TiO$_2$, the [Re(bpy)(CO)$_3$(3-picoline)]$^+$ homogeneous complex could only produce a small amount of CO (TON$_{max}$ ~ 6) during the same period. The mixture of TiO$_2$ and [Re(bpy)(CO)$_3$Cl] catalyst without phosphonic acid groups in solution also produced the same amount of CO as the Re catalyst alone. By transient absorption measurements, the authors attributed the enhanced photocatalytic activity of TiO$_2$/[ReP]$^+$ to the better stabilization of the catalytically active species [ReP] by TiO$_2$ surface: the lifetime of TiO$_2$/[ReP] was estimated to be more than 1 s while that of reduced [Re(bpy)(CO)$_3$(3-picoline)] in solution was around 60 ms. The longer lifetime of this intermediate species allowed for higher chances to react with CO_2 and to undergo the required second reduction step to release CO. However, the second reduction step was not observed by TAS. In this study, TiO$_2$ was considered inactive in the electron transfer mechanism; it only acted as a scaffold to stabilize the intermediate.

However, when redox-inert NPs such as ZrO_2 were used, the photocatalytic activity is reduced. If TiO_2 was inactive, it cannot fully explain the higher activity for the $TiO_2/[ReP]^+$ system towards CO_2 reduction. The same research group of Reisner later published another article to address the role of TiO_2 associated to $[Re(bpy)(CO)_3(DMF)]$ complex bearing two phosphonic acid groups (denoted as $[Re(DMF)P]^+$) using time-resolved IR spectroscopy.[13] They proposed that the mechanistic difference between $TiO_2/[Re^I(DMF)P]^+$ and $ZrO_2/[Re^I(DMF)P]^+$ or other homogeneous systems was the first step of photo-induced electron injection from Re^{I*} excited state to TiO_2 to form $(e^-)TiO_2/[Re^{II}P]^{2+}$ species, which had a long lifetime and high oxidative power as compared to the MLCT excited state Re^{I*} in solution. Consequently, the higher oxidative power of $(e^-)TiO_2/[Re^{II}P]^{2+}$ than Re^{I*} resulted in a more efficient reaction with TEOA. This step may be critical for the enhanced photocatalytic activity observed in the publication mentioned above. In this study TiO_2 was shown to act as an electron reservoir that could accept, save and give back the electrons to the Re catalyst to complete the catalytic cycle.
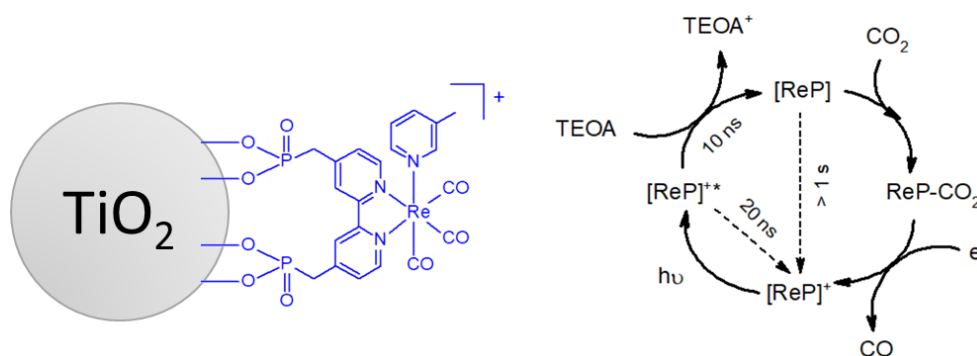
Scheme IV-2. Structure of TiO_2/Re^I NPs and the proposed catalytic mechanism mentioned in reference 12

In order to improve the photocatalytic efficiency of TiO_2/Re^I system, Kang and co-workers[14] immobilized an organic dye and $[Re(bpy)(CO)_3Cl]$ catalyst on TiO_2 NPs (**Scheme IV-3**). In contrast to the Reisner's work on TiO_2/Re^I where Re complex acted as both PS and catalyst, the Re species in this study only operated as a catalyst. Since photocatalytic CO_2 reduction in homogeneous solution using the $[Re(bpy)(CO)_3Cl]$ suffers from short durability due to the catalyst degradation, fixing it on a surface was expected to reveal its intrinsic photocatalytic activity. Under visible irradiation ($\lambda > 420$ nm), the hybrid system exhibited remarkable TON_{max} (CO) > 435 *versus* the Re catalyst in DMF solution and in the presence of 1,3-dimethyl-2-phenyl-2,3-dihydro-1H-benzo[d]imidazole (BIH) as sacrificial electron donor. The system also reached good selectivity for CO, since H_2 content was less than 5 % of CO content, and no formic acid was detected with the HPLC analysis of the liquid phase. Kang et al. later published another article[15] proving that the charge transfer mechanism occured through the conduction band (CB) of TiO_2 (called "through particle" mechanism) by Mott-

Schottky analysis. The addition of a small amount of H_2O (up to 3 %) and $LiClO_4$ electrolyte (~ 0.6 mM) was found to significantly improve the CO_2 reduction to CO ($TON_{max} > 570$ after 30 hours, no leveling-off tendency in the TON *vs* time plot). The Mott-Schottky analysis showed that water and Li^+ cations can tune the flat-band potential (E_{fb}) of TiO_2 to better align the energy levels of the three components in such a way that $-E(Dye^*/Dye) > -E_{fb} > -E(Re^I/Re^0)$.
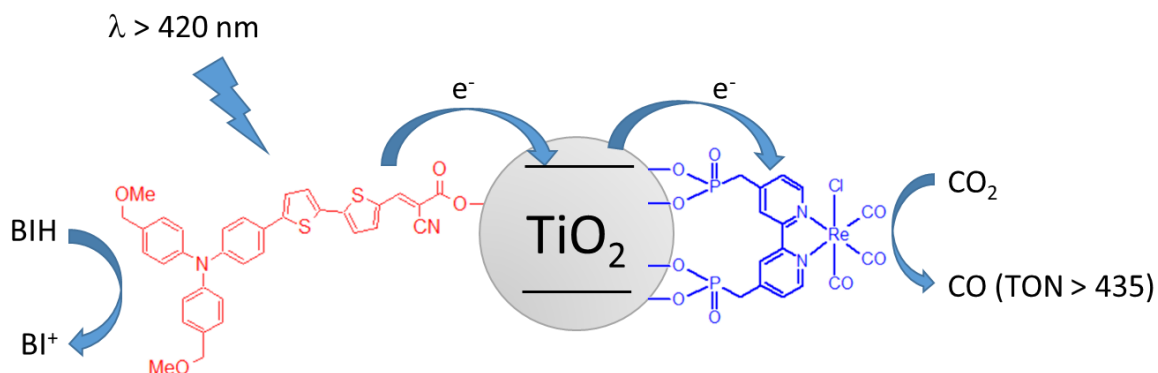

Scheme IV-3. Photocatalytic CO_2 reduction using $Dye/TiO_2/Re^I$ NPs mentioned in references 14 and 15

The search for other complexes that can replace the prototypical but expensive $[Re(bpy)(CO)_3Cl]$ complex is of great interest. Analogous complexes, $[Mn(bpy)(CO)_3Br]$ and $[Mn(dmbpy)(CO)_3Br]$ (dmbpy = 4,4'-dimethyl-2,2'-bipyridine) (**Scheme IV-4a** and **b**), were first reported by Chardon-Noblat, Deronzier and co-workers in our ClRe group for electrocatalytic CO_2 reduction.[16] In MeCN solution and 5 % H_2O as proton source, the complexes produced CO as the only reduction product with $TON_{max} = 13$ for $[Mn(bpy)(CO)_3Br]$ and $TON_{max} = 34$ for $[Mn(dmbpy)(CO)_3Br]$. Recently, Ishitani et al.[17] reported the photocatalytic CO_2 reduction using $[Mn(bpy)(CO)_3Br]$ as catalyst, $[Ru(dmbpy)_3]^{2+}$ as PS and 1-benzyl-1,4-dihydronicotinamide (BNAH) as sacrificial electron donor in DMF/TEOA (4/1, v/v) mixed solvent. Under continuous irradiation at 480 nm to selectively excite the PS, HCOOH was produced with high TON_{max} (149) and selectivity (85 %) over CO and H_2. The activation pathways of the catalyst in the electrocatalytic or photocatalytic studies seem to have a great influence on the selectivity of the CO_2 reduction reaction.

A related complex $[Mn(phen)(CO)_3Br]$ (phen = 1,10-phenanthroline, **Scheme IV-4c**) has also been used as a CO_2 reduction photocatalyst in association with Zn(II) tetraphenylporphyrin (ZnTPP) as a PS and TEOA as an electron donor.[18] The mixture comprised only abundant metal complexes. Under visible light, the mixture favored the production of CO over HCOOH. Moreover, TON of CO was shown to depend on the ratio $[Mn(phen)(CO)_3Br]/ZnTPP$: when the ratio increased, TON of the products also increased

and the selectivity was also enhanced. For instance, when the ratio was equal to 4/1, TON_{max} reached 119 for CO and 19 for HCOOH.
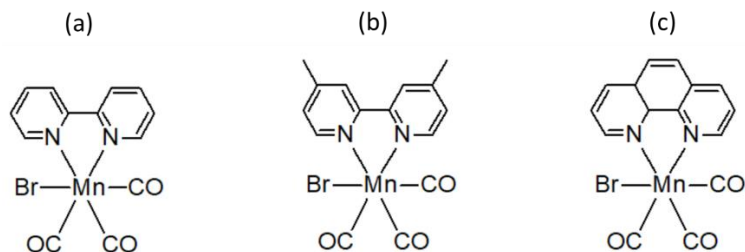
Scheme IV-4. Molecular structure of (a) [Mn(bpy)(CO)₃Br], (b) [Mn(dmbpy)(CO)₃Br] and (c) [Mn(phen)(CO)₃Br] complexes

Mechanistic studies have also been discussed in the three publications mentioned above. After the first monoelectronic reduction step on the metal center, the Br^- leaves and a Mn^0-Mn^0 dimer is formed. Reduction of the dimer generates the catalytic active species [Mn(bpy)(CO)₃]⁻ where the pentacoordinated Mn^{-I} center offers a vacancy for a CO_2 adduct. The reduction steps can be summarized as follows:

$$[Mn^I(bpy)(CO)_3Br] + e^- \rightarrow [Mn^I(bpy^{\bullet-})(CO)_3Br]^-$$

$$[Mn^I(bpy^{\bullet-})(CO)_3Br]^- \rightarrow [Mn^0(bpy)(CO)_3] + Br^-$$

$$[Mn^0(bpy)(CO)_3] \rightarrow 1/2 \ [Mn^0(bpy)(CO)_3]_2$$

$$1/2 \ [Mn^0(bpy)(CO)_3]_2 + e^- \rightarrow [Mn^{-I}(bpy)(CO)_3]^-$$
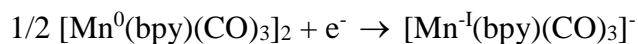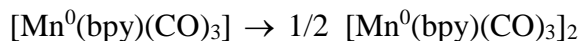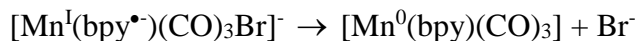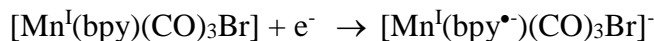
The first example concerning [Mn(bpy)(CO)₃Br] complex immobilized on TiO₂ thin film electrode has been reported by Reisner and co-workers.[19] They functionalized the bpy ligand with two phosphonic acid groups (called [MnP]) to anchor on the TiO₂ surface. The TiO₂/[MnP] modified electrode was used for the electrocatalytic CO₂ reduction in MeCN/H₂O (95/5, v/v) solution. The reason to deposit the complex on a mesoporous TiO₂ thin film was to achieve higher loading and better electrical conductivity between the electrode and the catalyst than the free complex in solution. Under an applied potential at -1.7 V *vs* Fc⁺/Fc (-1.6 V *vs* Ag/AgNO₃ 0.01 M) during 2 hours, the modified electrode produced CO as the main product with TON_{max} = 112. H₂ was also detected at ~ 20 % yield of CO, while HCOOH was not detected. The intermediate [Mn⁰(bpy)(CO)₃]₂ dimer was observed with UV-vis absorption spectroscopy although the Mn complex has been fixed on the surface. The authors attributed this observation to two possible mechanisms: (i) the lability of the phosphonic acid anchoring groups that the complex could be temporarily desorbed, forming a dimer then being re-adsorbed, and/or (ii) the local concentration of the Mn complex was high enough to be dimerized.

Recent works by Marc Bourrez[20] and Matthew Stanbury[21], former PhD students in our CIRe laboratory have focused on a novel catalyst $[Mn(\kappa^2\text{-ttpy})(CO)_3(MeCN)]^+$ (ttpy = 4'-(p-tolyl)-2,2':6',2''-terpyridine) for CO_2 reduction to CO and/or HCOOH. The complex showed better electrocatalytic CO_2 reduction efficiency (TON_{max} (CO) = 13) than the previously reported $[Mn(\kappa^2\text{-tpy})(CO)_3(MeCN)]^+$ (tpy = 2,2':6',2''-terpyridine) complex by Kubiak et al.[22] (TON_{max} (CO) ~ 4). In this chapter we will briefly present the characterization, electro- and photo-catalytic CO_2 reduction using a similar complex, $[Mn(\kappa^2\text{-ttpy})(CO)_3Br]$, in homogeneous solution. This chapter focuses on the immobilization of this Mn complex on TiO_2 NPs via a phosphonic acid anchoring group to form TiO_2/Mn^I dyad, and subsequently the co-immobilization of a $[Ru(bpy)_3]^{2+}$-based PS and Mn complex onto TiO_2 to yield $Ru^{II}/TiO_2/Mn^I$ triad. **Scheme IV-5** shows the structures of the dyad and triad that will be presented in this chapter. The photocatalytic CO_2 reduction using the triad will also be described.
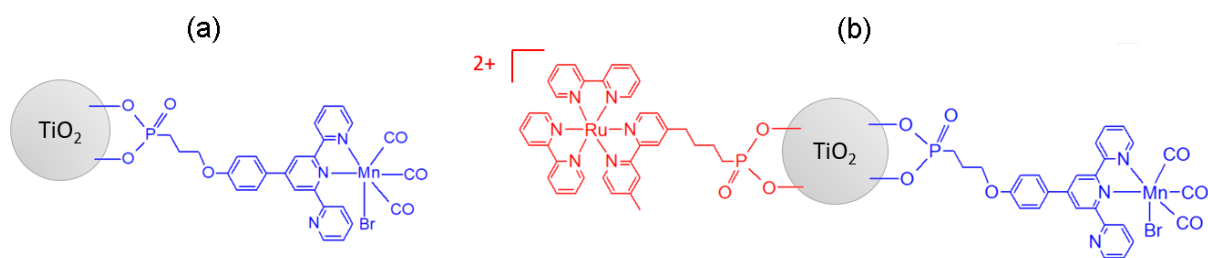

Scheme IV-5. Structure of (a) TiO_2/Mn^I dyad and (b) $Ru^{II}/TiO_2/Mn^I$ triad

IV.2.   Mn(I) tolylterpyridine tricarbonyl complex in solution

IV.2.1. Synthesis

The synthesis of [Mn(κ^2-ttpy)(CO)$_3$Br] complex was performed following a previous publication by our CIRe group.[23] A simple one-step synthesis was carried out between Mn(CO)$_5$Br and ttpy ligand in diethyl ether to yield [Mn(κ^2-ttpy)(CO)$_3$Br] as the only product (**Scheme IV-6**). The bidentate coordination was confirmed in the aforementioned study. The presence of three C≡O groups is proved by infrared (IR) spectroscopy in solid state showing three intense peaks at 2022, 1948, 1916 cm^{-1}. They correspond to symmetric (2022 cm^{-1}) and antisymmetric (1948 and 1916 cm^{-1}) C≡O stretching bands. The peaks are slightly blue-shifted compared with the analogous complex [Mn(κ^2-ttpy)(CO)$_3$(MeCN)]$^+$ (ν (C≡O) = 2043, 1962, 1939 cm^{-1})[23] where Br$^-$ is replaced by MeCN solvent molecule. The peak positions and the blue-shift tendency when Br$^-$ is substituted by MeCN have also been reported for the analogous [Mn(κ^2-tpy)(CO)$_3$Br][22] and [Mn(phen-dione)(CO)$_3$Br][24] (phen-dione = 1,10-phenanthroline-5,6-dione) complexes.
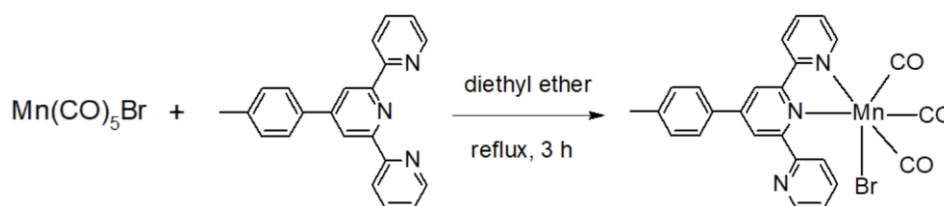
Scheme IV-6. Synthesis route to [Mn(κ^2-ttpy)(CO)$_3$Br] complex

IV.2.2. Electrochemical properties

The electrochemical properties of [Mn(κ^2-ttpy)(CO)$_3$Br] complex has been studied by cyclic voltammetry in MeCN + 0.1 M TBAPF$_6$ solution under Ar, using a carbon disk electrode as working electrode (WE). **Figure IV-1** shows its cyclic voltammograms (CVs) when the potential is first swept to positive values (**Figure a**) or negative values (**Figure b**). Since the CVs are similar to those of [Mn(κ^2-ttpy)(CO)$_3$(MeCN)][20,21], [Mn(bpy)(CO)$_3$Br][20] and [Mn(phen)(CO)$_3$Br][18] complexes, our CV interpretation is based on the explanations in these previous works without further investigation.

In the anodic scanning (**Figure IV-1a**), two irreversible oxidation peaks are detected at 0.62 V and 0.78 V, which is in accordance with Marc Bourrez's study on the same complex.[20] The author attributed the two peaks to two oxidation steps as follows:

(1)   *fac* [Mn^I(κ^2-ttpy)(CO)$_3$Br] → *fac* [Mn^{II}(κ^2-ttpy)(CO)$_3$Br]$^+$ + e$^-$ E_{pa1} = 0.62 V

(2)   *fac* [Mn^{II}(κ^2-ttpy)(CO)$_3$Br]$^+$ → *mer* [Mn^{II}(κ^2-ttpy)(CO)$_3$Br]$^+$

(3)   *mer* $[Mn^{II}(\kappa^2\text{-ttpy})(CO)_3Br]^+ + MeCN \rightarrow$ *mer* $[Mn^I(\kappa^2\text{-ttpy})(CO)_3(MeCN)]^+ + Br^\bullet$

(4)   *mer* $[Mn^I(\kappa^2\text{-ttpy})(CO)_3(MeCN)]^+ \rightarrow$ *mer* $[Mn^{II}(\kappa^2\text{-ttpy})(CO)_3(MeCN)]^{2+} + e^-$
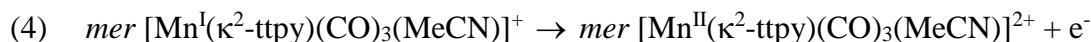
$$E_{pa2} = 0.78 \text{ V}$$

In the cathodic scanning (**Figure IV-1b**), the first irreversible cathodic peak at E_{pc1} = -1.44 V is assigned to the leaving of Br⁻ and pyridyl coordination to form a tridentate linkage between the ttpy ligand and Mn metal ion (reactions 5 and 6). It is followed by the release of a CO group and the formation of a dimer through metal-metal bonding (reaction 7). On the reverse scanning, the cathodic peak at -1.44 V is associated with an anodic peak at -0.89 V which corresponds to the oxidation of the Mn⁰-Mn⁰ dimer (reaction 8). Another irreversible oxidation peak is observed at 0.27 V due to the oxidation of the metal center in the tridentate complex (reaction 9). This peak is not observed if the CV is first swept in oxidation (**Figure IV-1a**).

(5) $[Mn^I(\kappa^2\text{-ttpy})(CO)_3Br] + e^- \rightarrow [Mn^I(\kappa^2\text{-ttpy}^{\bullet-})(CO)_3] + Br^-$ E_{pc1} = -1.44 V

(6) $[Mn^I(\kappa^2\text{-ttpy}^{\bullet-})(CO)_3]^+ \rightarrow [Mn^0(\text{ttpy})(CO)_3]$

(7) $[Mn^0(\text{ttpy})(CO)_3] \rightarrow 1/2\ [Mn^0(\text{ttpy})(CO)_2]_2 + CO$

(8) $1/2\ [Mn^0(\text{ttpy})(CO)_2]_2 + MeCN \rightarrow [Mn^I((\text{ttpy})(CO)_2(MeCN)]^+ + e^-$ E = -0.89 V

(9) $[Mn^I(\text{ttpy})(CO)_2(MeCN)]^+ \rightarrow [Mn^{II}(\text{ttpy})(CO)_2(MeCN)]^{2+} + e^-$ E = 0.27 V
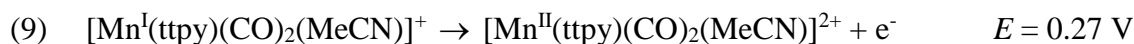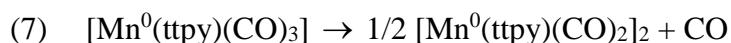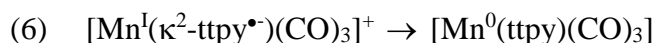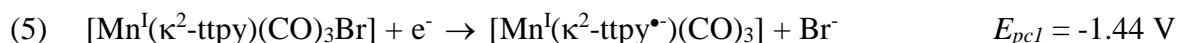
Further sweeping to more negative potentials leads to a second one-electron irreversible peak at E_{pc2} = -1.67 V which is ascribed to the reduction of the Mn⁰-Mn⁰ dimer to form $[Mn^{-I}(\text{ttpy})(CO)_2]^-$ species (reaction 10). The unsaturated coordination of the Mn⁻I center can slowly interact with MeCN solvent (reaction 11). The peak at -1.67 V is associated with a small oxidation peak at -1.45 V corresponding to the re-oxidation of the newly formed $[Mn^{-I}(\text{ttpy})(CO)_2]^-$ to come back to the previous dimer species (reactions 12 and 13). The chemical structures of these intermediate complexes are shown in **Scheme IV-7**.

(10) $1/2\ [Mn^0(\text{ttpy})(CO)_2]_2 + e^- \rightarrow [Mn^{-I}(\text{ttpy})(CO)_2]^-$ E_{pc2} = -1.67 V

(11) $[Mn^{-I}(\text{ttpy})(CO)_2]^- + MeCN \rightarrow [Mn^{-I}(\text{ttpy})(CO)_2(MeCN)]^-$

(12) $[Mn^{-I}(\text{ttpy})(CO)_2]^- \rightarrow [Mn^0(\text{ttpy})(CO)_2] + e^-$ E = -1.45 V

(13) $[Mn^0(\text{ttpy})(CO)_2] \rightarrow 1/2\ [Mn^0(\text{ttpy})(CO)_2]_2$
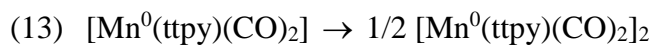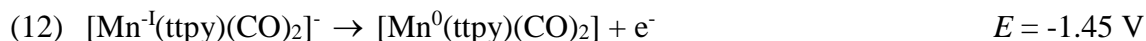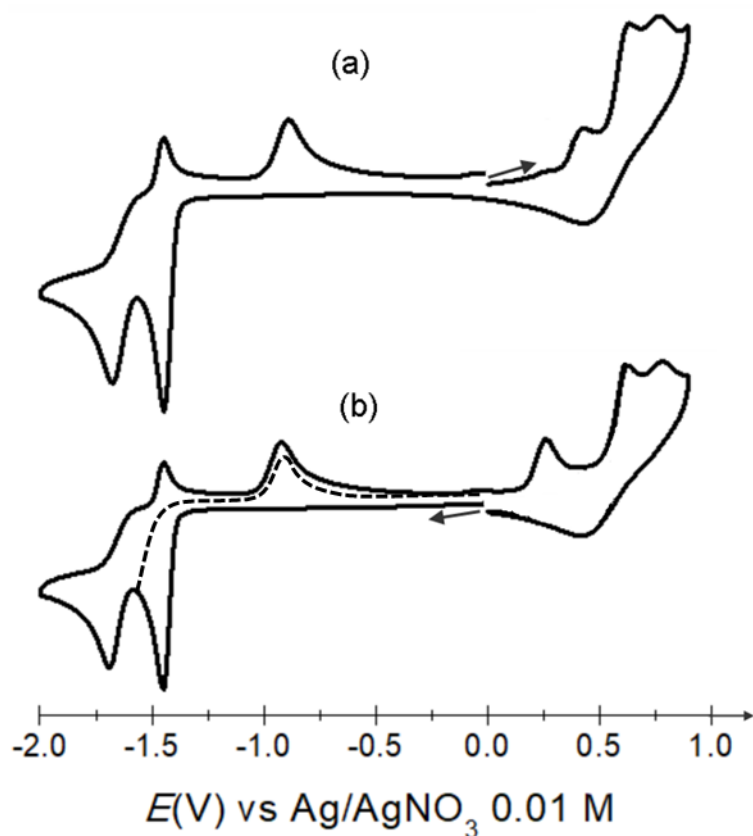
Figure IV-1. CVs of [Mn(ttpy)(CO)₃Br] complex (C = 1 mM) recorded with C disk electrode (d = 3 mm) in MeCN + 0.1 M TBAPF₆ under Ar, v = 100 mV.s^{-1}: (a) reductive scanning first, (b) oxidative scanning first

[Mn^I(κ^2-ttpy)(CO)₃Br]   [Mn^0(ttpy)(CO)₃]   [Mn^0(ttpy)(CO)₂]₂

[Mn^I(ttpy)(CO)₂(MeCN)]$^+$ [Mn^{II}(ttpy)(CO)₂(MeCN)]$^{2+}$ [Mn^{-I}(ttpy)(CO)₂]$^-$
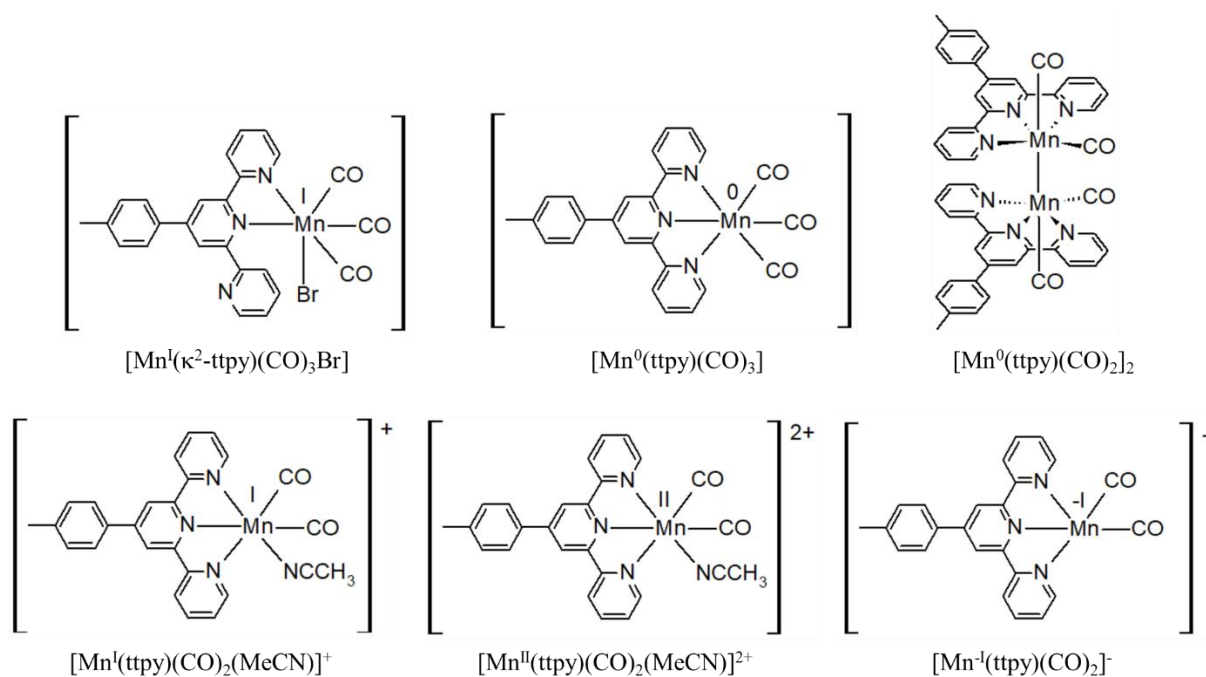
Scheme IV-7. Chemical structures of the species generated following the mechanism mentioned above

148

IV.2.3. UV-vis absorption spectroscopy

Figure IV-2 presents the UV-vis absorption spectrum of [Mn(ttpy)(CO)₃Br] complex in MeCN under air. The absorption maximum is at 420 nm, which is red-shifted compared with [Mn(ttpy)(CO)₃(MeCN)] complex (λ_{max} = 368 nm)[23]. The absorption band is attributed to a metal-to-ligand charge transfer (MLCT)[23] mixed with a halide-to-ligand charge transfer[25] transitions.
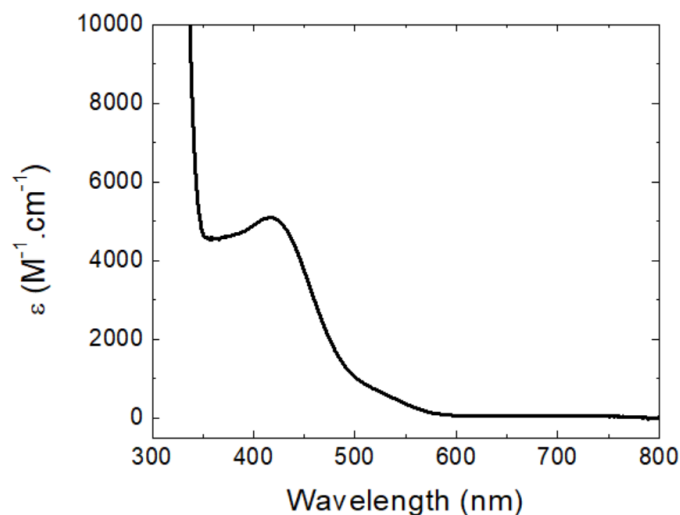
Figure IV-2. UV-vis absorption spectra of [Mn(ttpy)(CO)₃Br] complex in MeCN solution in air.

IV.2.4. Electrocatalytic CO₂ reduction

The electrocatalytic CO₂ reduction experiment has been conducted using [Mn(ttpy)(CO)₃Br] catalyst and H₂O as proton source. First, the CVs of the complex recorded in neat MeCN + 0.1 M TBAPF₆ under Ar (black line) and in MeCN + 5 % H₂O under CO₂ (red line) are shown in **Figure IV-3**. We can see that the current is improved at both reduction peak, with the catalytic current occurring on the second reduction. It suggests that the electrocatalytic CO₂ reduction may occur at both potentials, i.e. a mix of one-electron and two-electron mechanisms. A similar tendency has already been observed for [Mn(bpy)(CO)₃Br][22], [Mn(bpy)(CO)₃(MeCN)][21] and [Mn(phen)(CO)₃Br][18] complexes. However, when [Mn(ttpy)(CO)₃(MeCN)] was used, only increase in the current magnitude at the second reduction peak (-1.62 V) was reported.[21]

In order to study the reduction products of CO₂, a potential of -1.7 V was applied for comparison with previous studies. CO gas is produced as the only reduction product with TON$_{max}$ (CO) = 12 after 4 hours and 100 % Faradaic yield while no H₂ or HCOOH is formed. The numbers are in line with the previous work on [Mn(ttpy)(CO)₃(MeCN)] electrocatalyst (TON$_{max}$ (CO) = 13, 100 % Faradaic yield)[21], and is significantly improved in comparison with [Mn(tpy)(CO)₃Br] catalyst (TON$_{max}$ (CO) ~ 4)[22] and [Mn(tpy)(CO)₃(MeCN)](PF₆)

catalyst (TON_{max} (CO) = 1, 20 % Faradaic yield)[21] where the 4-tolyl substituent is absent. The reason for this enhanced efficiency and selectivity could be related to the increased stability and solubility of the Mn catalyst bearing a tolyl substituent.[21]
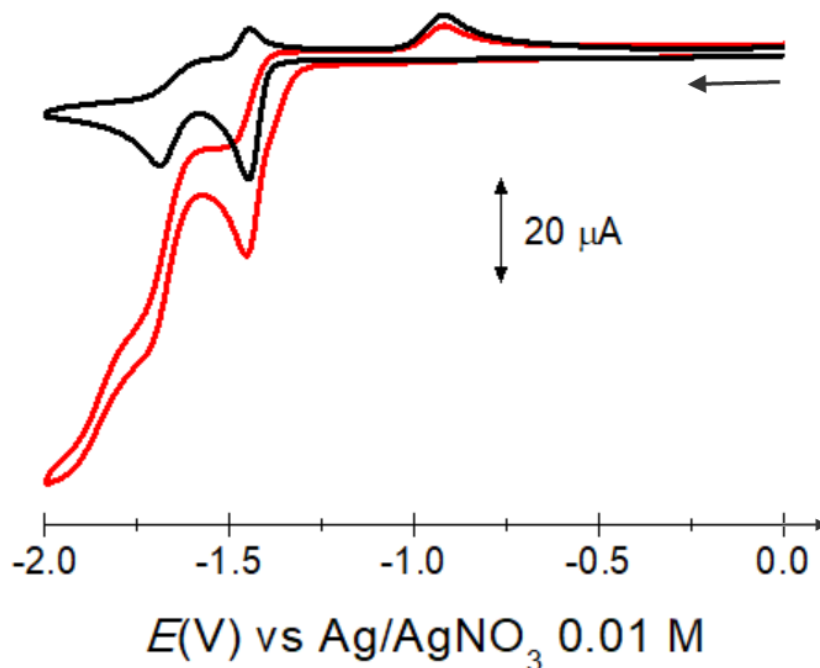
Figure IV-3. CV of [Mn(ttpy)(CO)₃Br] complex (C = 1 mM) in MeCN + 0.1 M TBAPF₆ + H₂O (5 %, v/v) under CO_2 (red line), in comparison with the CV recorded under Ar in neat MeCN (black line), v = 100 mV.s⁻¹, WE = C disk (d = 3 mm)

IV.2.5. Photocatalytic CO₂ reduction in presence of [Ru(bpy)₃]²⁺

Photocatalytic CO_2 reduction experiments have been carried out in DMF/TEOA (C_{TEOA} = 1 M) solution mixture in the presence of [Ru(bpy)₃]²⁺ as PS, [Mn(ttpy)(CO)₃Br] as catalyst and BNAH as sacrificial electron donor. A mechanism has been proposed in previous works[17,21], which is summarized in **Scheme IV-8**.
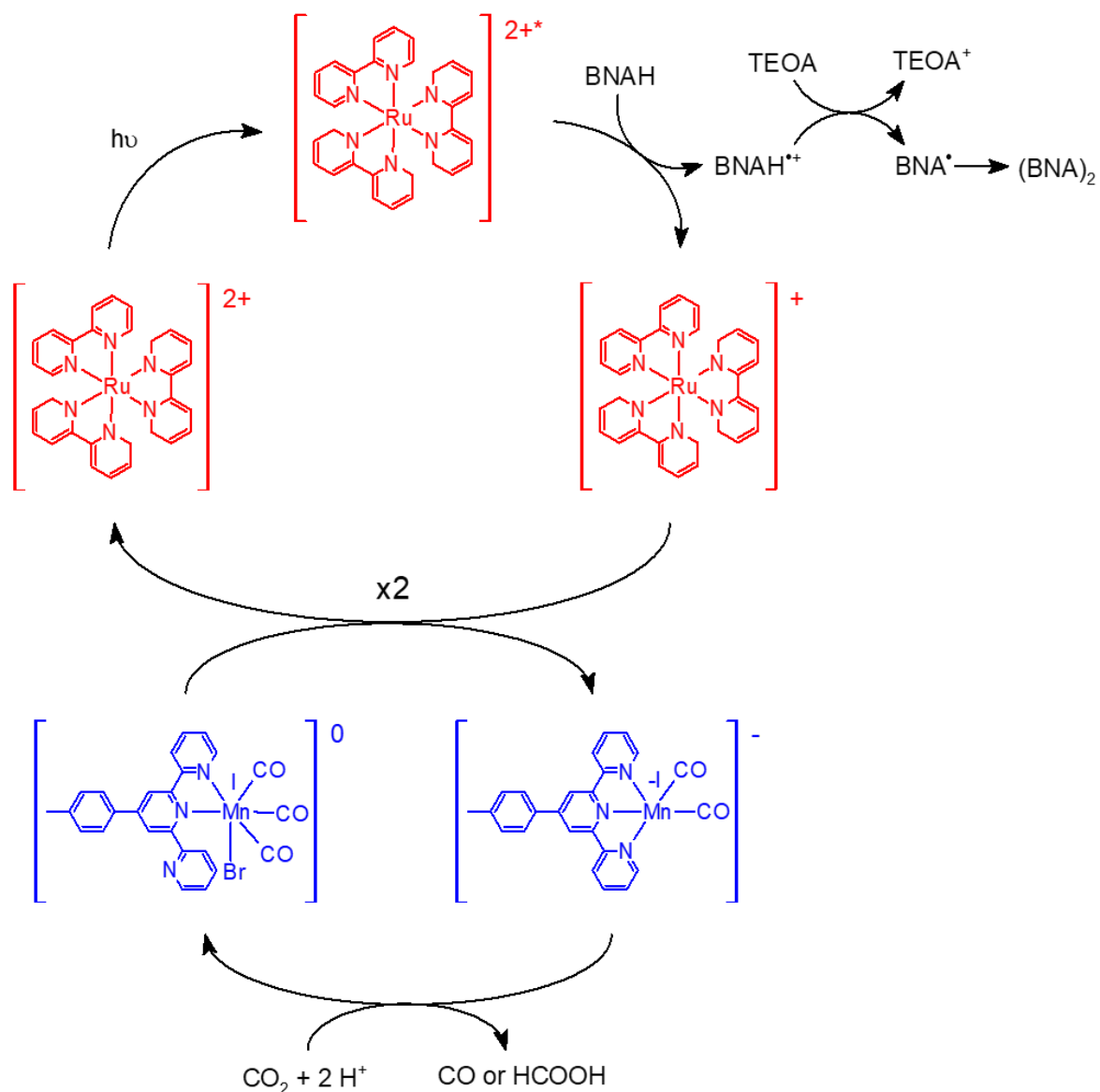
Scheme IV-8. Proposed mechanism for the photocatalytic CO_2 reduction using [Mn(ttpy)(CO)₃Br] catalyst. Adapted from reference 21

Upon the excitation at 450 nm, [Ru(bpy)₃]$^{2+}$ PS is selectively excited and singly reduced by the sacrificial electron donor BNAH. Since the reduction power of BNAH, E_{ox} = 0.27 V *vs* Ag/AgNO₃ 0.01 M (converted from E_{ox} = 0.57 V *vs* SCE in MeCN[5]) is stronger than that of TEOA (E_{ox} = 0.42 V[26]), BNAH can reductively quench the Ru^{2+*} excited state (E(Ru^{II*}/Ru^{I}) = 0.31 V). The [Ru(bpy)₃]$^{+}$, in turn, can reduce [Mn(ttpy)(CO)₃Br] twice to form the catalytically active species [Mn^{-I}(ttpy)(CO)₂]$^{-}$. In terms of energy, since the reduction power of Ru^{+} is E(Ru^{II}/Ru^{I}) = -1.67 V while the two reduction steps of the Mn complex occur at -1.44 V and -1.67 V, the Ru^{+} complex can reduce the Mn complex twice. The doubly reduced species [Mn^{-I}(ttpy)(CO)₂]$^{-}$ has a free coordination site to form an adduct with CO_2. It has been proposed that TEOA also participated to the formation of the Re-CO_2-TEOA intermediate complex when a similar catalyst, [Re(bpy)(CO)₃Cl], was used.[5] Finally,

reduction products like CO or HCOOH are formed via a two-electron, two-proton reduction process.

In our series of photocatalytic CO$_2$ reduction experiments, the molar ratio of Mn:Ru was varied to determine the optimal value, which will be used to graft the complexes on TiO$_2$ NPs. It is an advantage to work with NPs as the PS/catalyst ratio can be easily controlled, in comparison with supramolecules where PS and catalyst molecules are linked to each other, usually, at 1:1 ratio. **Table IV-2** presents the results obtained with different Mn:Ru ratio. For the experiments to be comparable, we only changed the catalyst amount while keeping the Ru PS amount fixed so that light absorbance by the PS remains the same in all the series. The results were obtained after 16 hours of irradiation at 470 ± 40 nm and corresponded to the maximum of production.

Table IV-2. Results of photocatalytic CO$_2$ reduction using a mixture of [Mn(ttpy)(CO)$_3$Br] catalyst and [Ru(bpy)$_3$](PF$_6$)$_2$ PS in 5 ml DMF solution containing TEOA (1 M) and BNAH (0.1 M) under CO$_2$. Irradiation was achieved by using a Xe lamp (0.3 mW.cm^{-2}, 5 cm apart), a UV-hot filter and a 470 ± 40 nm bandpass filter. The results were obtained after 16 hours of irradiation.

Ratio of Mn:Ru [a]	HCOOH		CO		TON$_{total}$ [c]
	n (µmol)	TON$_{max}$ [b]	n (µmol)	TON$_{max}$ [b]	
1:1	9.8	14	5.6	8	22
1:5	3.9	28	1.4	10	38
1:10	2.2	31	1.3	19	50
5:1	71.4	20	18.9	5	25
10:1	88.9	13	35.0	5	17

[a] Ratio of [Mn(ttpy)(CO)$_3$Br] : [Ru(bpy)$_3$]$^{2+}$ where Ru(II) concentration is unchanged (0.14 mM)

[b] Turnover number (TON) *versus* Mn catalyst

[c] TON$_{total}$ = TON$_{max}$ (HCOOH) + TON$_{max}$ (CO)

It is noted that the excitation wavelength has to be carefully chosen to minimize the photo-induced decarbonylation of the [Mn(ttpy)(CO)$_3$Br] complex as this side reaction can occur under room light.[27] In our study, the result obtained with the ratio of Mn:Ru = 1:1 is in agreement with a previous work[21] (TON$_{max}$ (HCOOH) = 11, TON$_{max}$ (CO) = 8) where the sample was monochromatically irradiated at 480 nm instead of 470 ± 40 nm. We thus conclude that irradiation at 470 ± 40 nm can selectively excite Ru^{2+} PS in the same way as the monochromatic irradiation at 480 nm. Interestingly, this photocatalytic reduction process in DMF/TEOA mixed solvent produces a mixture of CO and HCOOH while the electrocatalytic reduction using [Mn(ttpy)(CO)$_3$Br] in MeCN only produces CO. This observation is in

accordance with literature for the electrocatalytic and photocatalytic CO_2 reduction using [Mn(bpy)(CO)$_3$Br] complex in MeCN and DMF/TEOA solvent, respectively.[17]

The table also shows that decreasing the Mn:Ru ratio leads to higher total TON as expected due to higher chance for each Mn^I molecule being reduced twice by two Ru^I molecules. The best Mn:Ru ratio is determined at 1:10 where the total TON reaches the highest value of 50 in this series, although the selectivity of HCOOH over CO at about 1.6:1 is not high.

IV.3. TiO$_2$/Mn^I dyad and Ru^{II}/TiO$_2$/Mn^I triad nanoparticles

IV.3.1. Synthesis

❖ *Synthesis of ttpy-C$_3$-PO$_3$H$_2$ ligand*

To graft the [Mn(ttpy)(CO)$_3$Br] complex on TiO$_2$ NPs, we chose phosphonic acid as anchoring group. As presented in **Chapter 3** for the [Cr(ttpy)$_2$]$^{3+}$ complex bearing two phosphonic acid groups, the ttpy-PO$_3$H$_2$ ligand cannot be isolated from DMSO for characterization. Therefore, we employed a new synthesis route to ttpy-(CH$_2$)$_3$-PO$_3$H$_2$ (denoted as ttpy-C$_3$-PO$_3$H$_2$) ligand that has three methylene units as a bridge between the ttpy ligand and the phosphonic functionality (**Scheme IV-9**). In the last step, after the solvents were evaporated, there was still an unknown amount of HBr side product in the sample. This new ligand shows good solubility in DMSO. The ligand was characterized by mass spectroscopy and NMR (^{1}H, ^{31}P) spectroscopy before deposition on TiO$_2$ NPs. Further details can be found in the Experimental Section.
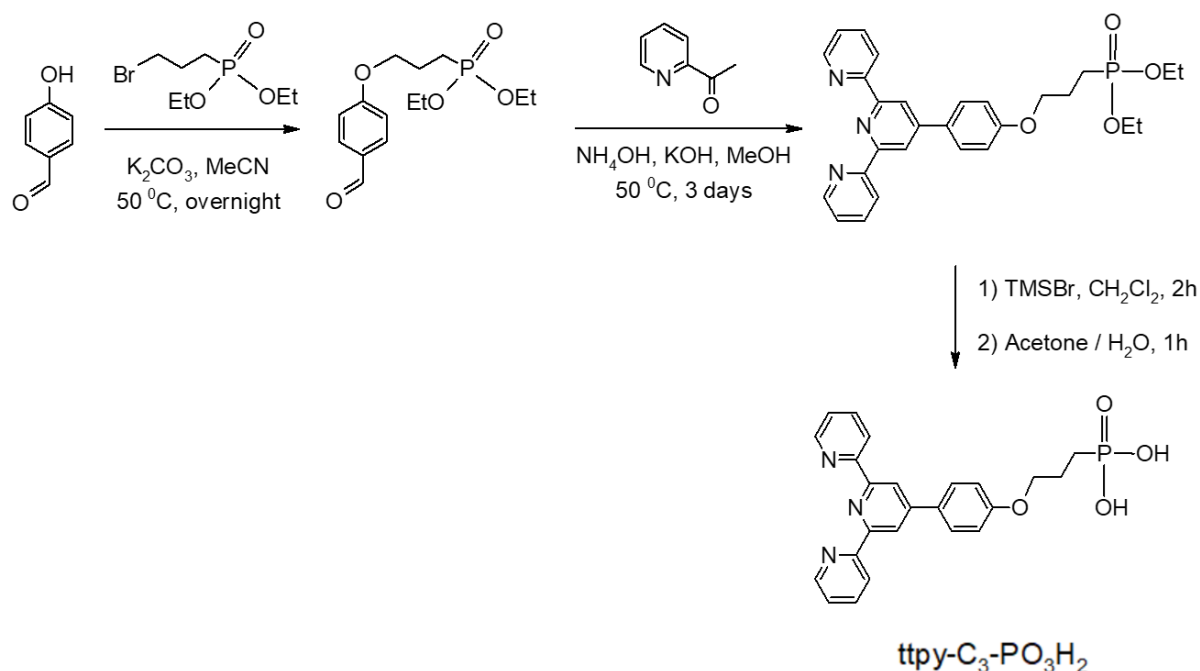
Scheme IV-9. Synthesis route to ttpy-C$_3$-PO$_3$H$_2$ ligand

❖ *Synthesis of TiO$_2$/Mn^I dyad NPs*

We first attempted to synthesize a new complex [Mn(ttpy-C$_3$-PO$_3$H$_2$)(CO)$_3$Br] by mixing Mn(CO)$_5$Br and the ttpy-C$_3$-PO$_3$H$_2$ together in the same way we synthesized the parent complex [Mn(ttpy)(CO)$_3$Br]. However, this approach was not successful due to the poor solubility of the metal precursor in DMSO, and the presence of HBr that may protonate the tpy ligand. Working with mixed solvent like DMSO/diethyl ether or DMSO/acetone did

not solve the issue. Therefore, we employed a two-step synthesis: first, the ligand was grafted on TiO$_2$ NPs in DMSO solution, followed by the complexation reaction between Mn(CO)$_5$Br and TiO$_2$/ttpy-C$_3$-PO$_3$H$_2$ NPs in acetone (**Scheme IV-10**). A similar "complexation on surface" strategy has been realized for the immobilization of [Re(bpy)(CO)$_3$Cl] on SiO$_2$ NPs via amide linkages[28], and the immobilization of [Mn(bpy)(CO)$_3$Br] on either a metal-organic framework (MOF)[29] or a periodic mesoporous organosilica (PMO)[30] substrate. After each step, modified TiO$_2$ NPs were washed with copious amounts of corresponding solvents to remove the excess amount of the ligand, metal precursor and HBr, prior to being dried under vacuum. Loading of Mn^I species on TiO$_2$ is estimated to be ~ 0.20 mmol.g^{-1} (around 3800 molecules per particle or 2 molecules per nm^2) by measuring the absorbance of washing solutions after each centrifugation step. It is important to note that in the second step of our procedure, acetone was used instead of diethyl ether because the ether was so volatile that it was completely evaporated during the necessary centrifugation steps after the grafting process.

Scheme IV-10. Synthesis route to TiO$_2$/Mn^I NPs

❖ *Synthesis of Ru^{II}/TiO$_2$/Mn^I (Mn:Ru = 1:10) triad NPs*

We prepared the Ru^{II}/TiO$_2$/Mn^I triad with the ratio of Mn:Ru = 1:10 based on the optimization of the Mn:Ru molar ratio in the photocatalytic CO$_2$ reduction described above. The complex ratio was roughly controlled by using an amount of [RuP]$^{2+}$ that was 10 times greater than the amount of Mn(CO)$_5$Br precursor. Further detail can be found in the **Experimental Section**. Since there are much less Mn species, grafting Mn first ensures that they can be better distributed on the TiO$_2$ NPs. After the two-step synthesis of TiO$_2$/Mn^I NPs, Ru^{2+} PS was then grafted as shown in **Scheme IV-11**. Loading of Mn^I and Ru^{II} complexes are roughly estimated to be 14 µmol.g^{-1} and 140 µmol.g^{-1}, respectively, by measuring the absorbance of washing solutions after each centrifugation step. The loading correspond to: (i) for Mn^I: 270 molecules per NP or 0.14 molecules per nm^2, (ii) for Ru^{II}: 2700 molecules per NP or 1.4 molecules per nm^2.
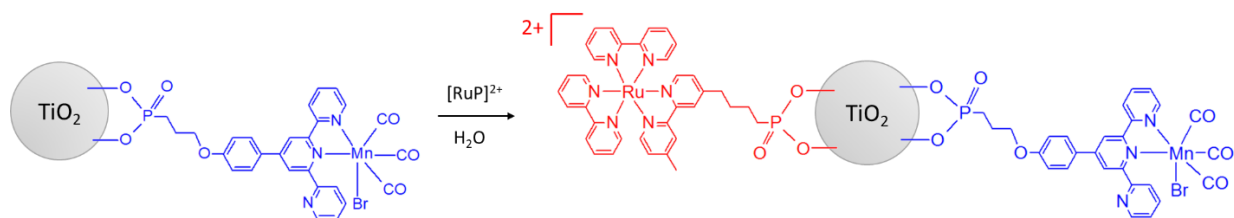
Scheme IV-11. Synthesis route to $Ru^{II}/TiO_2/Mn^I$ NPs

IV.3.2. Infrared spectroscopy

IR characterization has been employed to prove that the Mn complex was successfully anchored on TiO_2 by focusing on the C≡O stretching bands. **Figure IV-4** shows the IR spectra of the parent complex $[Mn(ttpy)(CO)_3Br]$ (black line), bare TiO_2 NPs (blue line) and TiO_2/Mn^I dyad (red line) in solid state in the C≡O vibration region. It can be seen that the peak at 2022 cm⁻¹ due to symmetric C≡O vibration remains unchanged, while the two other peaks seem to merge with each other to form a broad band centered at ~ 1930 cm⁻¹. The merging of two antisymmetric C≡O stretching bands after the Mn^I complex has been grafted on TiO_2 surface is consistent with literature for Re^{12}- and Mn^{19}-tricarbonyl bipyridine complexes immobilized on TiO_2 NPs. The experiments prove that the Mn complex has been successfully grafted.

It is important to note that the mode of coordination of the ttpy ligand to the Mn^I metal ion depends on the solvent used in the complexation reaction. Acetone has been shown to form a tridentate homogeneous complex, $[Mn(\kappa^3\text{-ttpy})(CO)_2Br]$,[23] which can be distinguished from the bidentate one based on the missing of the peak at ~ 2040 cm⁻¹. In our case, since the peak at 2022 cm⁻¹ is identical to the parent bidentate complex $[Mn(\kappa^2\text{-ttpy})(CO)_3Br]$, we conclude that the immobilized Mn^I complex retains the bidentate linkage even though the "complexation on surface" step has been carried out in acetone.
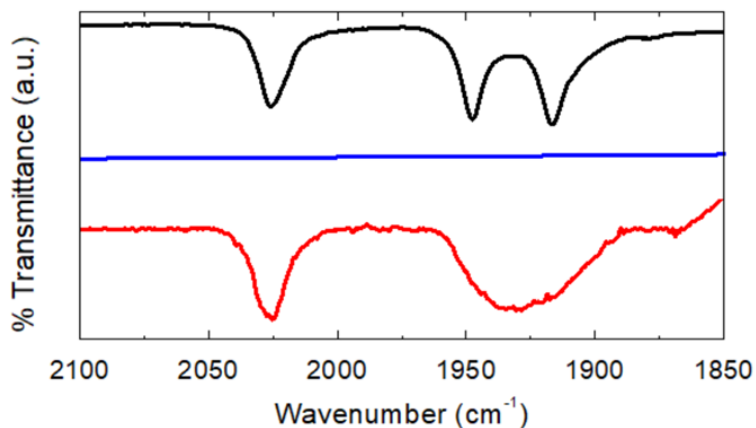

Figure IV-4. Solid state FT-IR spectra of $[Mn(ttpy)(CO)_3Br]$ complex (black line), bare TiO_2 NPs (blue line) and TiO_2/Mn^I NPs (red line) in the C≡O stretching region.
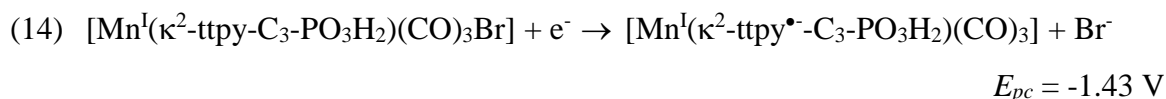
IV.3.3. Electrochemical properties

a) Mn^I complex grafted on FTO electrode

Before studying the electrochemical properties of TiO$_2$/Mn^I NPs, we first examined the electrical communication between the grafted Mn^I complex and a metal oxide electrode. FTO was chosen for this study because ITO showed significant degradation when the potential was swept to -2 V. The Mn^I complex was deposited onto the FTO electrode following the same procedure as for TiO$_2$/Mn^I NPs synthesis. The CV of FTO/Mn^I modified electrode is presented in **Figure IV-5a**.
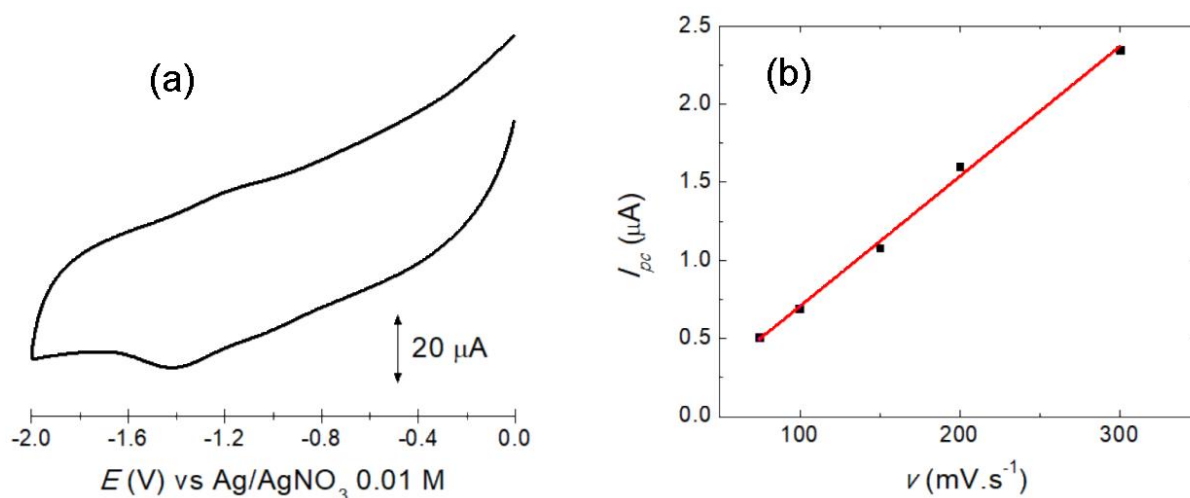
Figure IV-5. (a) CV of FTO/[MnP] electrode recorded in MeCN + 0.1 M TBAPF$_6$ under Ar, v = 100 mV.s^{-1}. (b) $I_{pc} - v$ plot based on the first reduction peak (black dots) and the linear fitting (red line, R^2 = 0.996)

The first cathodic peak appears at E_{pc} = -1.43 V, which is at the same potential as the first cathodic peak of the free complex in solution. However, on the reverse scan the associated anodic peak appears at a very different potential (E_{pa} = -1.16 V) than the peak recorded for the homogeneous complex in solution (-0.89 V, **Section IV.2.2**), which has been assigned to the oxidation of the Mn^0-Mn^0 dimer formed after the first reduction step. Since the Mn^I complex is immobilized onto the FTO surface, the formation of Mn^0-Mn^0 dimer should be prohibited. This assumption is supported by the lack of a second reduction process which is assigned to the reduction of the Mn^0-Mn^0 dimer in solution at -1.67 V. Scanning to potentials more negative than -2 V leads to the degradation of the FTO surface itself. Therefore, we tend to attribute the redox waves for FTO/Mn^I electrode to the following processes:

(14) $[Mn^I(\kappa^2\text{-ttpy-C}_3\text{-PO}_3H_2)(CO)_3Br] + e^- \rightarrow [Mn^I(\kappa^2\text{-ttpy}^{\bullet-}\text{-C}_3\text{-PO}_3H_2)(CO)_3] + Br^-$

$$E_{pc} = -1.43 \text{ V}$$

(15) $[Mn^I(\kappa^2\text{-ttpy}^{\bullet-}\text{-C}_3\text{-PO}_3H_2)(CO)_3] + MeCN \rightarrow [Mn^0(\text{ttpy-C}_3\text{-PO}_3H_2)(CO)_2(MeCN)] + CO$

(16) $[Mn^0(ttpy-C_3-PO_3H_2)(CO)_2(MeCN)] \rightarrow [Mn^I(ttpy-C_3-PO_3H_2)(CO)_2(MeCN)] + e^-$

$$E_{pa} = -1.16 \text{ V}$$
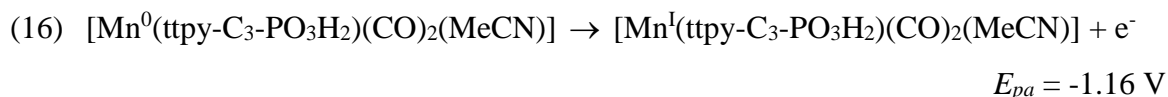
The first reduction process is centered on the ligand as for the complex in solution, and should lead to the release of Br$^-$ (reaction 14). Subsequently, an intramolecular charge transfer process induces the formation of Mn^0 complex (reaction 15). While the Mn^0 complex in solution undergoes dimerization after releasing CO (equation 7), we suppose that the immobilized Mn^0 complex on FTO stays on a monomeric form (equation 15). We have no experimental evidence for the release of CO when the complex is grafted on FTO. On the reverse scan, the oxidation peak at -1.16 V is attributed to the oxidation of the Mn^0 complex (equation 16).

Based on the first reduction peak at -1.43 V, a linear relationship between the cathodic peak current I_{pc} and scan rate v has been obtained (**Figure IV-5b**), proving the successful grafting of the Mn^I complex onto the electrode. The surface coverage Γ of Mn^I complex can be estimated to be $\Gamma_{Mn} = 1.9 \times 10^{-10}$ mol.cm^{-2} (see **Experimental Section** for the calculation) or about 1.1 molecules per nm^2. This number is in line with the loading of Mn^I on TiO$_2$ NPs (2 molecules per nm^2) shown in **Section IV.3.1**. The Γ value also suggests that the Mn^I complex molecules stay sufficiently far from each other on the FTO surface, supporting our assumption that the dimerization should be prohibited.

b) Mn^I complex grafted on TiO$_2$ NPs

Afterwards, we investigated the CV of TiO$_2$/Mn^I NPs in solid state using a microcavity Pt electrode. Due to different scale of current intensity, the CV is split into two parts corresponding to the anodic region (**Figure IV-6a**) and cathodic region (**Figure IV-6b**). For comparison, the CVs of TiO$_2$/ttpy-C$_3$-PO$_3$H$_2$ NPs are also shown in **Figure IV-7**.

(a) (b)
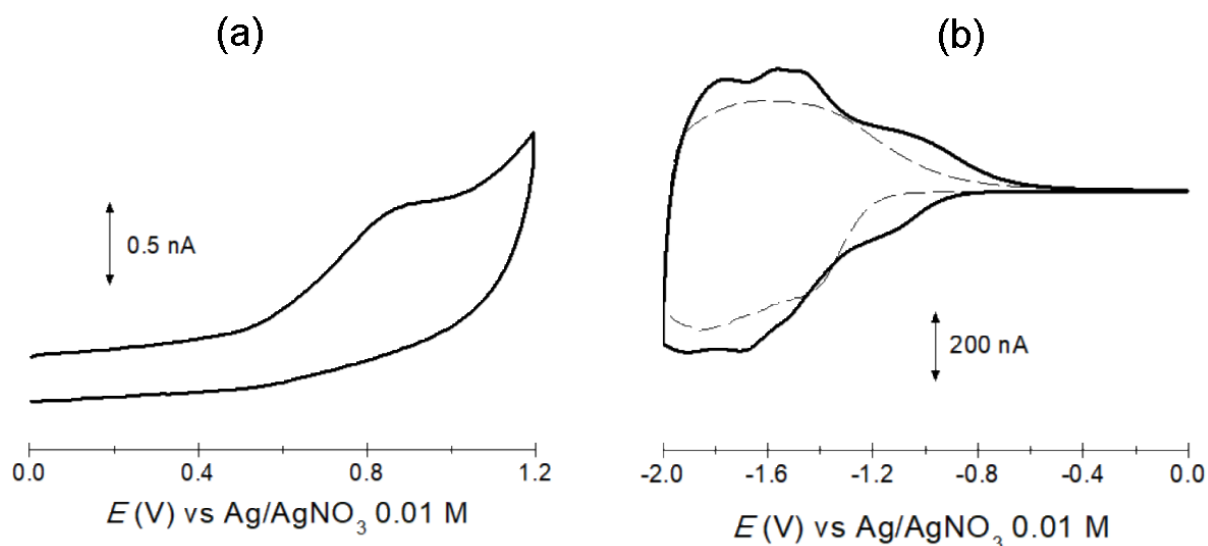
Figure IV-6. CVs of TiO₂/[MnP] NPs (solid lines) recorded in solid state using a microcavity Pt electrode in MeCN + 0.1 M TBAPF₆ under Ar, v = 100 mV.s⁻¹: (a) anodic region, (b) cathodic region. Dashed line shows the CV of bare TiO₂ NPs recorded under the same conditions.

(a) (b)
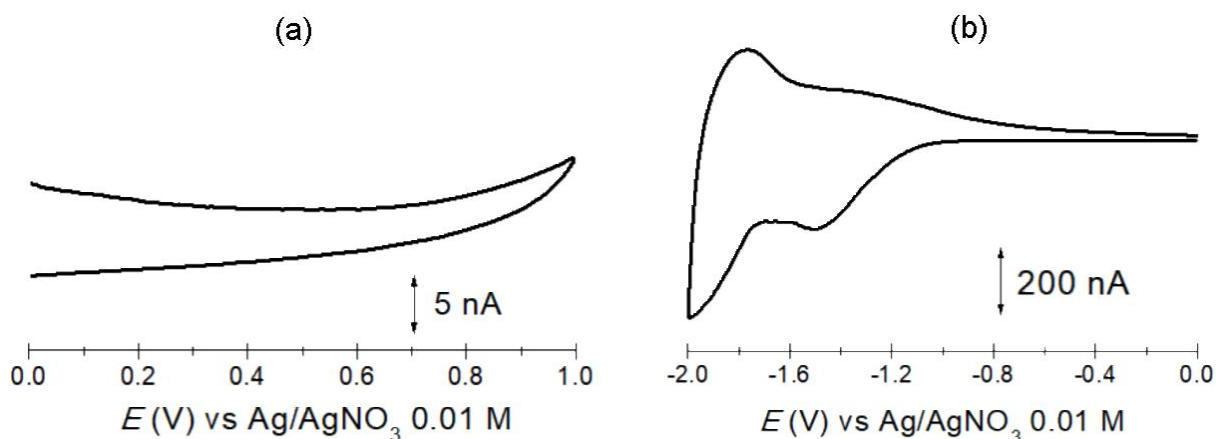
Figure IV-7. CVs of TiO₂/ttpy-(CH₂)₃-PO₃H₂ NPs recorded in solid state using a microcavity Pt electrode in MeCN + 0.1 M TBAPF₆ under Ar, v = 100 mV.s⁻¹: (a) anodic region, (b) cathodic region

In the anodic region of TiO₂/Mn^I (**Figure IV-6a**), only a broad, irreversible oxidation peak centered at E_{ox} = 0.86 V is observed. Bare TiO₂ NPs are not conductive in anodic potential scanning, and TiO₂/ttpy-C₃-PO₃H₂ NPs also do not show any oxidation peaks as expected (**Figure IV-7a**). Therefore, the anodic peak at 0.86 V is assigned to the oxidation of Mn^I metal center to Mn^{II} (reaction 17) in a similar way to the homogeneous complex in solution (E_{ox1} = 0.62 V, **Section IV.2.2**, reaction 1), although the potential has been shifted to a considerably higher value than that of the free complex [Mn^I(κ²-ttpy)(CO)₃Br] in solution. The oxidation process is irreversible since the electron transfer reaction may lead to a ligand exchange process between Br⁻ and MeCN solvent (reaction 18).

(17) *fac* [Mn^I(κ²-ttpy-C₃-PO₃H₂)(CO)₃Br] → *fac* [Mn^{II}(κ²-ttpy-C₃-PO₃H₂)(CO)₃Br]⁺ + e⁻

(18) *fac* [Mn^{II}(κ^2-ttpy-C$_3$-PO$_3$H$_2$)(CO)$_3$Br]$^+$ + MeCN $\rightarrow$

$$fac \text{ [Mn}^{II}(\kappa^2\text{-ttpy-C}_3\text{-PO}_3\text{H}_2)(CO)_3(MeCN)]^{2+} + Br^-$$
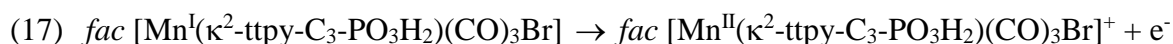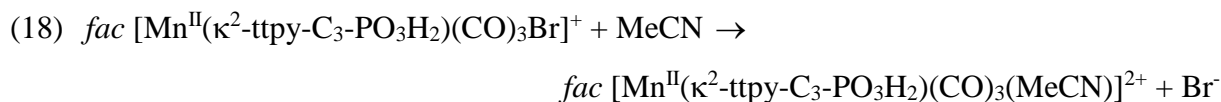
The second oxidation peak associated with the *fac* to *mer* configuration transformation of the Mn complex and subsequent oxidation of the *mer* Mn^I complex in solution are not observed for the FTO/Mn^I electrode. A reason for this phenomenon could be the geometric constraints of the immobilized Mn species precluding the *fac* to *mer* transformation.

In the cathodic region of TiO$_2$/Mn^I (**Figure IV-6b**), the first reduction peak appears at -1.11 V associated with an oxidation peak on the reverse scan at -1.01 V. These two redox peaks are not observed for TiO$_2$/ttpy-C$_3$-PO$_3$H$_2$ NPs (**Figure IV-7b**), thus it must be due to the reduction of the Mn^I complex. Similar to the FTO/Mn^I modified electrode, we also assume that the formation of dimer should be prohibited once the complex has been anchored on a surface. Therefore, we attribute the two peaks at -1.11 V and -1.01 V to the formation and re-oxidation of [Mn^0(ttpy-C$_3$-PO$_3$H$_2$)(CO)$_2$(MeCN)] species in the same way as FTO/Mn^I electrode (reactions 14-15 and reaction 16, respectively).

IV.3.4. Photophysical properties

a) UV-vis absorption spectroscopy

The UV-vis absorption spectra of TiO$_2$/Mn^I dyad and Ru^{II}/TiO$_2$/Mn^I triad are shown in **Figure IV-8**, in comparison with TiO$_2$ absorption spectrum. In solid state, TiO$_2$/Mn^I NPs do not exhibit the absorption maximum at 420 nm like the free Mn^I complex in solution. It only shows the extension of the absorption band into the visible region.

When both Ru^{II} and Mn^I complexes are grafted onto TiO$_2$ with molar ratio of Mn:Ru = 1:10, the absorption maximum at around 450 nm is attributed to the ^{1}MLCT absorption band of Ru^{II} PS. The absorption band of Mn^I overlaps to that of Ru^{II}, which is much more intense in the visible region. A small peak at around 575 nm has also been detected, which is not present in the UV-vis spectrum of TiO$_2$/Ru^{II} dyad (**Figure II-16**) or the [Mn(κ^2-ttpy)(CO)$_3$Br] complex (**Figure IV-2**).
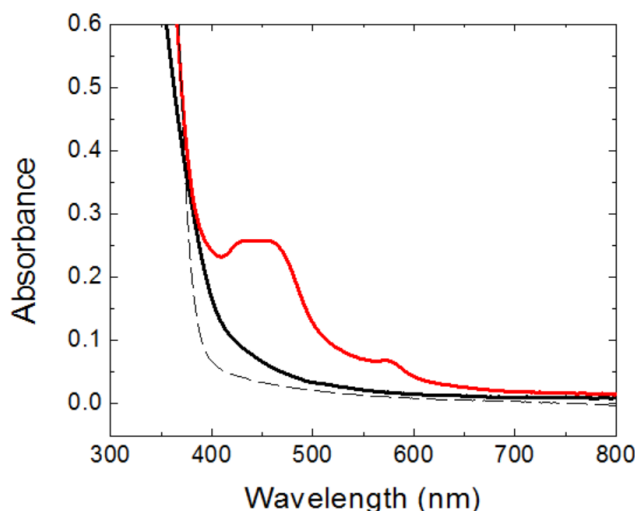
Figure IV-8. Solid state UV-vis spectra of TiO$_2$/Mn^I (black), Ru^{II}/TiO$_2$/Mn^I (Mn:Ru = 1:10, red) and TiO$_2$ (dotted line) NPs. Loadings of Mn^I complex on TiO$_2$/Mn^I and Ru^{II}/TiO$_2$/Mn^I are estimated to be ~ 0.20 mmol.g^{-1} and 14 µmol.g^{-1}, respectively.

b) Emission spectroscopy

The emission spectra of TiO$_2$/Mn^I dyad and Ru^{II}/TiO$_2$/Mn^I triad NPs have been recorded in colloidal solution following excitation at 450 nm. The TiO$_2$/Mn^I dyad does not show any emissions in the range between 500 and 850 nm. The emission spectrum of Ru^{II}/TiO$_2$/Mn^I triad is shown in **Figure IV-9** with a maximum of emission at 618 nm. It totally resembles the emission spectrum of TiO$_2$/Ru^{II} (**Figure II-16**), hence it is attributed to the ^{3}MLCT luminescence of Ru^{II*} complex.
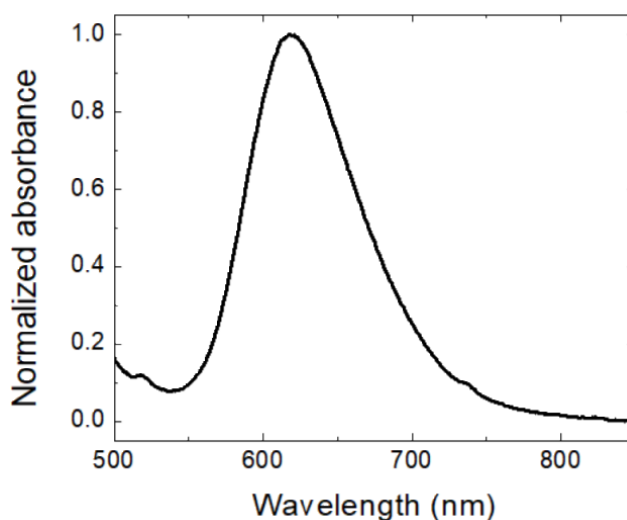
Figure IV-9. Emission spectrum of Ru^{II}/TiO$_2$/Mn^I colloidal solution after excitation at 450 nm.

c) Transient absorption spectroscopy

After light excitation, the charge separated state Ru^{III}/(e$^-$)TiO$_2$/Mn^I is created. Transient absorption (TA) experiments have been carried out to study the absorption spectra of these

transient species and the kinetics of charge recombination. Similar to **Chapter 3**, low concentration of the colloidal solution is required to avoid as much light scattering as possible. As a result, the full TA spectra from 400 nm to 700 nm need to be accumulated for at least 20 minutes to obtain a good signal-to-noise ratio. However, we encountered time-induced precipitation phenomenon, thus the result is not reliable. Therefore, we only focus on the signal decay at 450 nm to compare with the signal of TiO_2/Ru^{II} at the same wavelength (**Section II.3.6c**). The decay at 450 nm for the $Ru^{II}/TiO_2/Mn^{I}$ triad is shown in **Figure IV-10a**. The positive ΔOD has also been observed in the TiO_2/Ru^{II} case and ascribed to the transient absorption of $(e^-)TiO_2$. Hence, the decay corresponds to the charge recombination between Ru^{III} and $(e^-)TiO_2$.

Since the charge recombination between these species should take into account the diffusion of both trapped electrons and oxidized PS, the Kohlrausch – Williams – Watts (KWW)'s stretched exponential equation[31] is used to extract the kinetics of charge recombination, as previously described in **Section II.3.6**. **Figure IV-10b** shows the data fit by the KWW's equation. The KWW parameters (τ_{KWW} and β_{KWW}) are collected in **Table IV-3**.
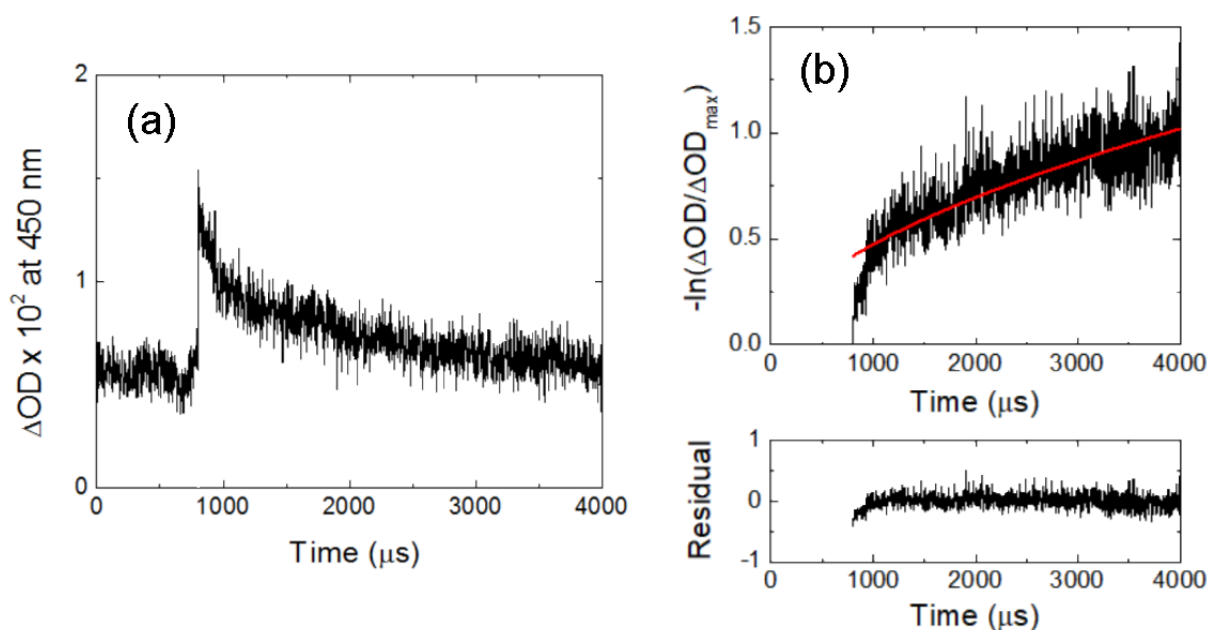
Figure IV-10. (a) TA decay at 450 nm for $Ru^{II}/TiO_2/Mn^{I}$ triad (Ru:Mn = 10:1); (b) $-ln(\Delta OD/\Delta OD_{max})$ *versus t* plot (black dots) obtained at 450 nm and fit with a power function (red line). The experiment was carried out in MeCN under Ar following excitation at 532 nm by a nanosecond pulsed laser.

Table IV-3. KWW fitting parameters (τ_{KWW} and β_{KWW}) and charge recombination rate k_{cr} between (e⁻)TiO₂ and Ru³⁺ species in Ru^{II}/TiO₂/Mn^I triad (Ru:Mn = 10:1 % mol), in comparison with TiO₂/Ru^{II} dyad

	τ$_{KWW}$ (µs)	β$_{KWW}$	k$_{cr}$ (s⁻¹)
Ru^{II}/TiO₂/Mn^I	3870 ± 460	0.55 ± 0.01	150 ± 15
TiO₂/Ru^{II}	3770 ± 800	0.51 ± 0.01	140 ± 30

It can be seen that both KWW parameters are very similar to those of TiO₂/Ru^{II} NPs. The β_{KWW} value is far from 1, justifying the use of the stretch exponential function. The charge recombination kinetics can be calculated as follows[32]:

$$k_{cr} = \left[\frac{1}{k_{KWW}\beta_{KWW}} \Gamma\left(\frac{1}{\beta_{KWW}}\right) \right]^{-1} = \left[\frac{\tau_{KWW}}{\beta_{KWW}} \Gamma\left(\frac{1}{\beta_{KWW}}\right) \right]^{-1} \qquad \text{(Eq IV-1)}$$

The rate of charge recombination is then estimated to be ~ 150 s⁻¹, which is identical to that of TiO₂/Ru^{II} (140 s⁻¹). This result suggests that the recombination of (e⁻)TiO₂ and Ru^{III} is not affected by the presence of Mn^I complex on the surface, implying that the Mn^I complex cannot be reduced by the electrons injected to TiO₂. It is in agreement with thermodynamic considerations where E(Ti⁴⁺/Ti³⁺ on TiO₂) = -1.0 V and E(Mn^I/Mn⁰) = -1.43 V. The electron transfer between (e⁻)TiO₂ and Mn^I, if occurs, would be endergonic by 0.43 eV.

IV.3.5. Photocatalytic CO₂ reduction

The photocatalytic CO₂ reduction using Ru^{II}/TiO₂/Mn^I triad NPs has been carried out in the same conditions as in **Section IV.2.5**. After 16 hours under irradiation at 450 nm, the triad photocatalyst produces HCOOH as the only product with the yield of 390 µmol.g⁻¹ NPs, corresponding to TON$_{max}$ (HCOOH) = 27 *vs* Mn^I catalyst. The experiment was reproduced twice to confirm the result. Increasing the irradiation time to 60 hours results in less formic acid (TON = 25) due to its degradation. Although the total TON is lower than that of the free [Ru(bpy)₃]²⁺ and [Mn(ttpy)(CO)₃Br] complexes in solution (TON$_{total}$ = 50), the selectivity of HCOOH over CO is significantly improved for the triad.

A control experiment using TiO₂/Ru^{II} instead of Ru^{II}/TiO₂/Mn^I does not produce CO or HCOOH, which confirms that the Mn^I complex acts as the catalyst. When TiO₂/Ru^{II} NPs and free Mn^I complex are used, we obtained the similar results as for the free complexes in homogeneous solution. When SiO₂/Ru^{II} and free Mn^I complex are used, the amounts of CO and HCOOH are significantly reduced. These experiments suggest that TiO₂ has an active role in the photocatalytic mechanism, and the immobilization of the Mn^I complex is related to

the enhanced selectivity of HCOOH over CO. **Table IV-4** summarizes the aforementioned results.

Table IV-4. Results of photocatalytic CO_2 reduction using $Ru^{II}/TiO_2/Mn^{I}$ triad, TiO_2/Ru^{II} dyad + free Mn^{I} in solution, and SiO_2/Ru^{II} dyad + free Mn^{I} complex in solution. The DMF solution contained TEOA (1 M) and BNAH (0.1 M). Irradiation was achieved by using a Xe lamp (0.3 mW.cm⁻², 5 cm apart), a UV-hot filter and a 470 ± 40 nm bandpass filter. The results were obtained after 16 hours of irradiation.

System	n_{Ru} (μmol)	n_{Mn} (μmol)	HCOOH		CO		Total TON
			n (μmol)	TON_{max}	n (μmol)	TON_{max}	
$Ru^{II}/TiO_2/Mn^{I}$	0.3	0.03	0.8	27	0	0	27
TiO_2/Ru^{II} + free Mn^{I}	0.3	0.03	1.1	38	0.2	6	44
SiO_2/Ru^{II} + free Mn^{I}	0.3	0.06	0.5	9	0.2	3	12
Ru^{II} + Mn^{I} in solution	0.7	0.07	2.2	31	1.3	19	50

Note: TON is calculated against the amount of Mn^{I} catalyst

Our photocatalytic CO_2 reduction results underline the importance of anchoring both PS and molecular catalyst on TiO_2 surface in terms of product selectivity. A previous study by Perutz, Reisner and co-workers[12] concerning the immobilization of [Re(bpy)(CO)₃(3-picoline)](PF₆) catalyst on TiO_2 NPs has also emphasized this importance in terms of the amount of the reduction product. The authors showed that the TiO_2/Re^{I} catalyst produces more CO than the free Re^{I} complex in solution with the same concentration: TON_{max} (CO) = 48 for TiO_2/Re^{I} compared with TON_{max} (CO) = 6 for the homogeneous Re^{I} in solution.

In a slightly different approach, another study by Kubiak, Cohen et al.[29] also showed enhanced selectivity towards HCOOH when [Mn(dcbpy)(CO)₃Br] (dcbpy = 5,5'-dicarboxylic-2,2'-bipyridine) complex was anchored on a metal-organic framework called UiO-67. In the presence of [Ru(dmb)₃]²⁺ (dmb = 4,4'-dimethyl-2,2'-bipyridine) as PS, BNAH as sacrificial electron donor and DMF/TEOA mixed solvent, the UiO-67/Mn^{I} photocatalyst produced TON_{max} (HCOOH) = 110 and TON_{max} (CO) = 5 after 18 hours of irradiation at 470 nm, corresponding to the selectivity of 95 % for HCOOH. Meanwhile, under the same conditions, the free [Mn(dcbpy)(CO)₃Br] catalyst mixed with [Ru(dmb)₃]²⁺ PS in solution only produced TON_{max} (HCOOH) = 57 and TON_{max} (CO) = 5 after 18 hours, corresponding to the selectivity of 92 % for HCOOH. A mechanism was proposed in this work to explain the formation of HCOOH as the main product (**Scheme IV-12**). It was based on the formation of singly reduced, coordinately unsaturated [Mn⁰(bpy)(CO)₃] and, subsequently, [(bpy)(CO)₃Mn^{I}-OC(O)H] adduct as intermediate species. It is important to note that the Mn⁰-

Mn^0 dimer, which has been proposed to be the photocatalytically active species for the [Mn(bpy)(CO)₃Br] complex in solution[17], was not able to formed when the Mn complex was anchored on the framework. The increased activity for UiO-67/Mn^I was attributed to the isolation of the Mn^I active sites on the framework, which stabilized the catalyst and prevented dimerization of the singly reduced Mn^0 species.
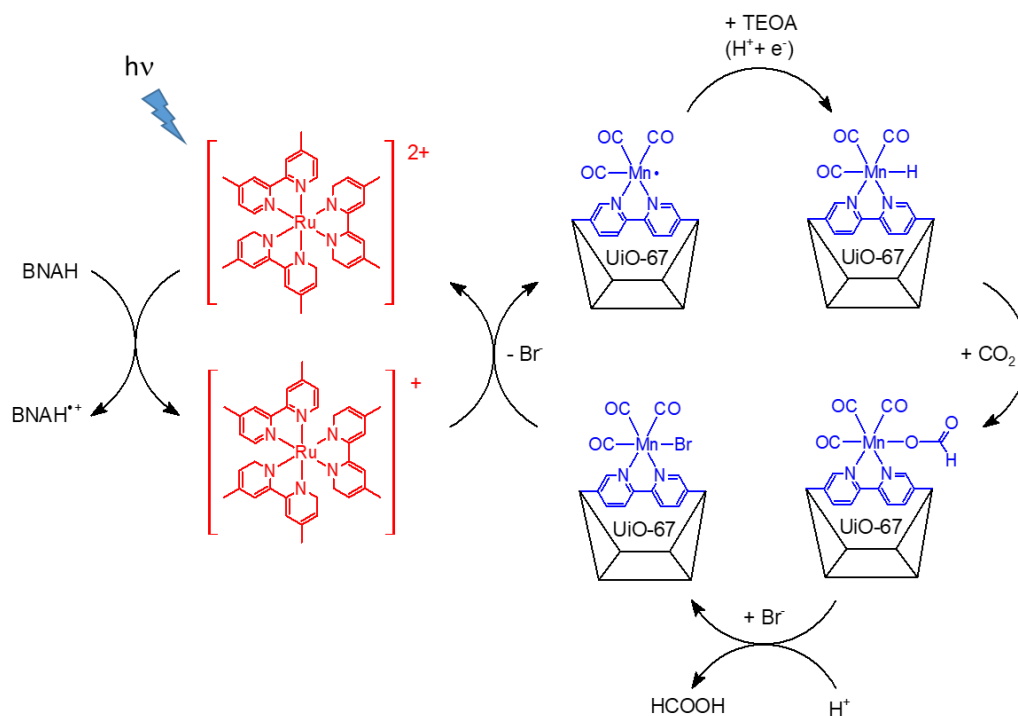
Scheme IV-12. Proposed mechanism for the photocatalytic CO₂ reduction using UiO-67/Mn^I catalyst in ref 29

Our results also highlight the role of semiconducting TiO₂ NPs as a substrate compared to SiO₂. In literature, Li and co-workers[28] immobilized [Re(bpy)(CO)₃Cl] catalyst on SiO₂ NPs via amide linkages for photocatalytic CO₂ reduction in the presence of [Ru(bpy)₃]²⁺ PS. The SiO₂/Re^I system only showed photocatalytic activity similar to the free complex in solution (TON_{max} (CO) ~ 12).

The proposed mechanism of the photocatalytic CO₂ reduction shown in **Scheme IV-8** requires that the Mn^I complex needs to be reduced twice to form the catalytically active species Mn^{-I}. For the mixture of [Ru(bpy)₃]²⁺ and [Mn(ttpy)(CO)₃Br] complexes in solution, the reduction of Ru^{2+*} excited state by BNAH occurs first to yield Ru^+ species, which can reduce the Mn complex twice. In the case of Ru^{II}/TiO₂/Mn^I triad, there are two reduction pathways to reduce Mn^I to Mn^0: (i) electron injection from Ru^{II*} to TiO₂ followed by electron transfer to Mn^I, then Ru^{III} is regenerated by BNAH (reactions 20, 21 and 22); or (ii) Ru^{II*} is reductively quenched by BNAH first to form Ru^I, then Ru^I transfers an electron to Mn^I via lateral transfer on surface and/or injects an electron to TiO₂ (reactions 23, 24 and 25).

(19) $Ru^{II}/TiO_2/Mn^I \xrightarrow{h\nu} Ru^{II*}/TiO_2/Mn^I$

(20) $Ru^{II*}/TiO_2/Mn^I \longrightarrow Ru^{III}/(e^-)TiO_2/Mn^I$ $\qquad\qquad \Delta G_{20} = -0.10 \text{ eV}$

(21) $Ru^{III}/(e^-)TiO_2/Mn^I \longrightarrow Ru^{III}/TiO_2/Mn^0$ $\qquad\qquad \Delta G_{21} = 0.11 \text{ eV}$

(22) $Ru^{III}/TiO_2/Mn^0 + BNAH \longrightarrow Ru^{II}/TiO_2/Mn^0 + BNAH^{\bullet+}$ $\quad \Delta G_{22} = -0.65 \text{ eV}$

(23) $Ru^{II*}/TiO_2/Mn^I + BNAH \longrightarrow Ru^I/TiO_2/Mn^I + BNAH^{\bullet+}$ $\quad \Delta G_{23} = -0.04 \text{ eV}$

(24) $Ru^I/TiO_2/Mn^I \longrightarrow Ru^{II}/TiO_2/Mn^0$ $\qquad\qquad\qquad \Delta G_{24} = -0.56 \text{ eV}$

(25) $Ru^I/TiO_2/Mn^I \longrightarrow Ru^{II}/(e^-)TiO_2/Mn^I$ $\qquad\qquad\quad \Delta G_{25} = -0.67 \text{ eV}$
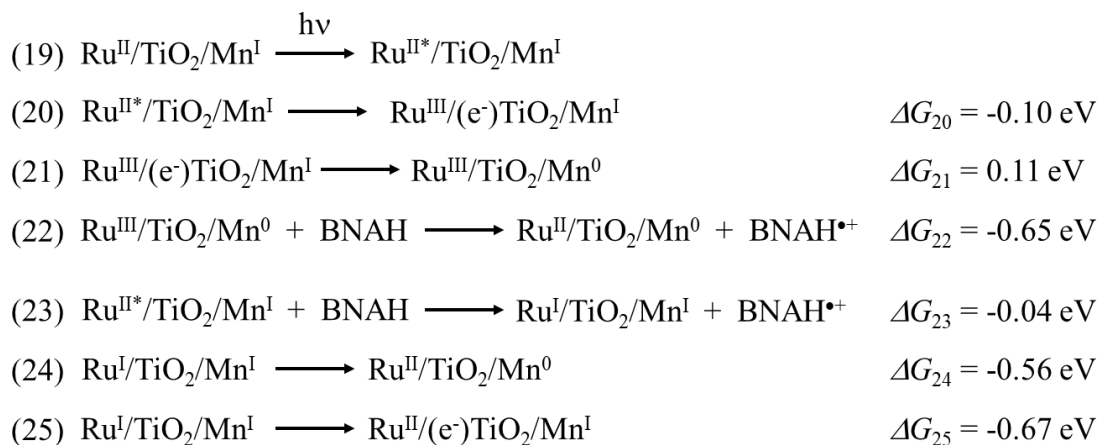
(*Note:* $E(Ru^{III}/Ru^{II}) = 0.92$ V; $E(Ru^{II}/Ru^I) = -1.67$ V; $E(Ru^{III}/Ru^{II*}) = -1.10$ V; $E(Ru^{II*}/Ru^I) = 0.31$ V; $E(Ti^{4+}/Ti^{3+}$ on $TiO_2) = -1.0$ V; $E(Mn^I/Mn^0$ grafted on $TiO_2) = -1.11$ V; $E_{ox}(BNAH^+/BNAH) = 0.27$ V *vs* Ag/AgNO₃ 0.01 M).

Thermodynamically, the electron transfer between $(e^-)TiO_2$ and Mn^I in the first pathway (reaction 21) is not favorable. The TAS results mentioned in **Section IV.3.4** also show that the injected electrons on TiO_2 CB are not consumed by Mn^I species. Therefore, the second pathway is more feasible to reduce the Mn^I complex. In this pathway, TiO_2 seems to be inactive, which is in accordance with a previous publication[12]. TiO_2 only acts as a substrate so that the Ru^{II} PS and Mn^I catalyst molecules are arranged sufficiently close to each other to enhance the charge transfer kinetics. Since the molar ratio of Mn:Ru is equal to 1:10, the chance that a Mn^I molecule is surrounded by several Ru^{II} molecules is expected to be high. However, our experiments using $(TiO_2/Ru^{II}$ + free $Mn^I)$ and $(SiO_2/Ru^{II}$ + free $Mn^I)$ photocatalytic systems resulted in significantly less products for the latter system (**Table IV-4**), suggesting that TiO_2 may have an active role but it is not well understood yet.

In contrast with the electrocatalytic CO_2 reduction experiment, the second reduction step to generate Mn^{-I} complex has not been observed for the grafted Mn complex on FTO by cyclic voltammetry. However, the photocatalytic active species can be the singly reduced complex $[Mn^0(ttpy\text{-}C_3\text{-}PO_3H_2)(CO)_2]$ anchored on TiO_2 NPs in a similar way to what has been proposed by Kubiak, Cohen et al.[29] for UiO-67/Mn^I system (**Scheme IV-12**).

IV.3.6. Electron paramagnetic resonance spectroscopy

a) Effect of BNAH

Before mimicking the conditions applied in the photocatalytic CO_2 reduction, we first investigated the magnetic behavior of the sacrificial electron donor BNAH alone in MeCN solution. As expected, the sample does not show any EPR signal when the measurement was

performed in dark. Under continuous irradiation at 455 nm, it shows a thin EPR line centered at $g \sim 2$ if the sample has been prepared under O_2 (**Figure IV-11**, red line). If the sample has been prepared under Ar, no EPR signals have been recorded (**Figure IV-11**, black line). Therefore, the organic radical $BNAH^{\bullet+}$ is obtained by photooxidation of BNAH under visible irradiation and in the presence of O_2. This experiment shows the importance of the complete removal of O_2, otherwise this $g \sim 2$ line may interfere with the desired signals of other transient species.
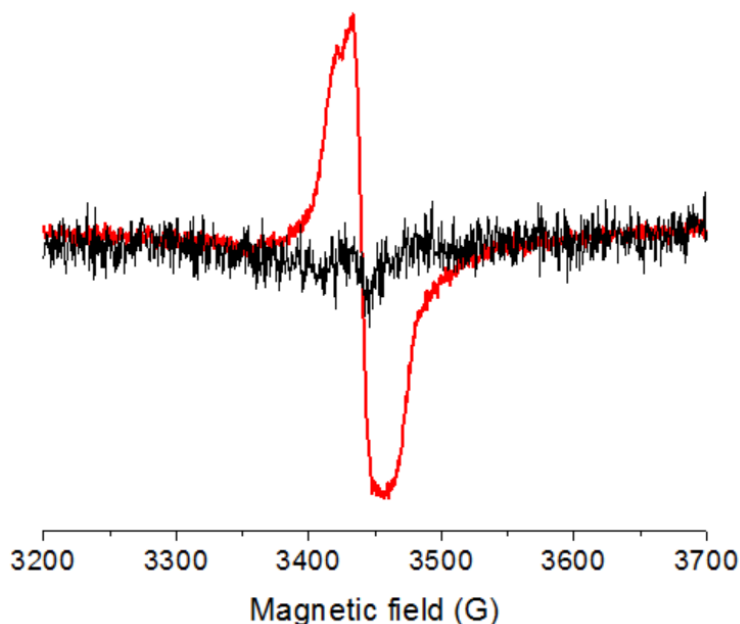
Figure IV-11. EPR spectra of BNAH (0.1 M) in MeCN prepared under O_2 (red line) and under Ar (black line), irradiated *in situ* by a 455 nm LED. The spectra were recorded with an X-band EPR spectrometer (f = 9.655 GHz, 2 mW, 5 G modulation) at 10 K, accumulated for 10 mins.

b) Ru^{II}/TiO₂/Mn^{I} triad and BNAH as electron donor

In a previous study[21] on homogeneous Mn^{I} complex, the first reduction step leads to Mn^0-Mn^0 dimer which is EPR-silent due to the antiferromagnetic coupling of two Mn^0 (S = 1/2) species. In this study, since the Mn^{I} complex has been anchored on TiO_2 surface, the dimerization cannot occur, hence the expected singly reduced Mn^0 complex (S = 1/2) may be detectable with the EPR technique.

We carried out the EPR investigation of the Ru^{II}/TiO₂/Mn^{I} triad in MeCN solution containing BNAH (0.1 M) in dark and under 455 nm irradiation. The EPR tube containing this sample has been carefully prepared in dark under Ar before being frozen in liquid nitrogen. As a comparison, we also prepared another tube containing TiO_2/Ru^{II} dyad instead of the triad, and the same amount of BNAH and MeCN as for the first tube. The Ru^{II} content in both samples is approximately equal. As expected, both samples are EPR-silent when they

are measured in dark since Mn^I ($3d^6$) and Ru^{II} ($4d^6$) are diamagnetic. Under 455 nm irradiation, photo-induced paramagnetic species can be detected by EPR. Their EPR signals under 455 nm irradiation (**Figure IV-12**) have been accumulated over the same time period.
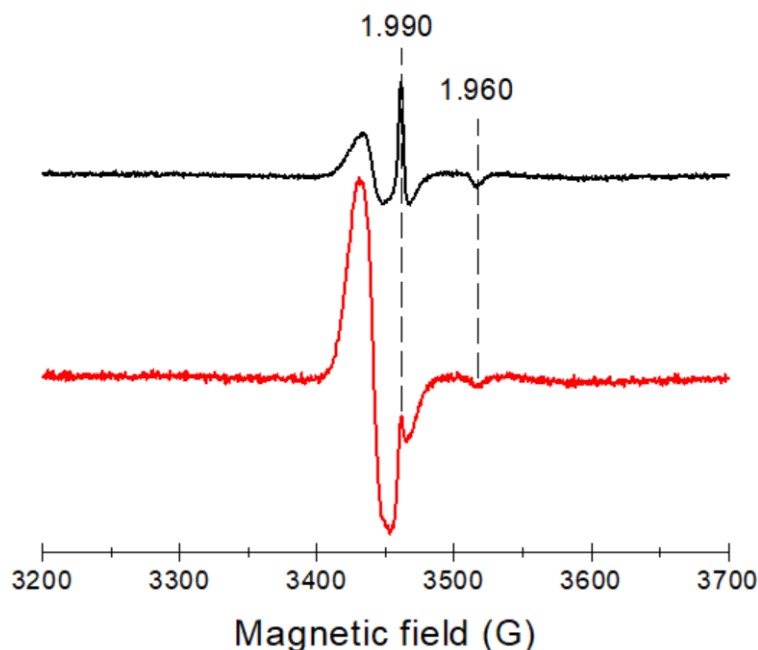

Figure IV-12. EPR spectra of TiO_2/Ru^{II} dyad (black) and $Ru^{II}/TiO_2/Mn^I$ triad (red) colloidal in MeCN ($C_{NPs} = 6$ g.L^{-1}) and 0.1 M BNAH, irradiated *in situ* by a 455 nm LED. The samples were prepared in an Ar glovebox. Both spectra were recorded with an X-band EPR spectrometer ($f = 9.654$ GHz, 2 mW, 5 G modulation) at 10 K, accumulated for 55 mins.

It can be seen that the two samples exhibit two EPR lines at $g_\perp = 1.990$ and $g_{//} = 1.960$ corresponding to trapped electrons in Ti^{3+} sites.[33,34] As shown in **Chapter 2**, they are attributed to the injected electrons from Ru^{2+*} to TiO_2. Based on the line at $g_{//} = 1.960$, the amount of trapped electrons in both samples is about equal, which is due to the same amount of Ru^{II} species and the same time of signal accumulation.

Beside the signal of Ti^{3+}, an intense signal at 3441 G has been detected in both samples. As it is similar in shape and position to the BNAH radical obtained under O_2, we also attribute this signal to the BNAH radical. However, since there are no O_2 in this case, the BNAH radical must be a consequence of photo-induced electron transfer reaction from BNAH to Ru^{II*} excited state to form $BNAH^{•+}$ and Ru^I species. If Mn^I is redox-inactive, the signal of BNAH radical should be identical in both cases due to the same amounts of Ru^{II} and TiO_2. In fact, the signal intensity for $Ru^{II}/TiO_2/Mn^I$ triad is significantly greater than for TiO_2/Ru^{II} dyad. Meanwhile, there are no reasons for the reductive quenching of Ru^{2+*} by BNAH to be accelerated in the triad. Therefore, the increase in intensity of the line at 3441 G may imply a superimposition of two paramagnetic species.

To further study the signal centered at 3441 G, pulsed EPR technique was employed. **Figure IV-13a** shows the field-swept spectra of BNAH$^{•+}$ radicals alone prepared under O_2 (red) and the radicals in the presence of Ru^{II}/TiO$_2$/Mn^{I} triad prepared under Ar (black). Both samples were irradiated *in situ* at 455 nm. The two spectra are very similar, indicating that most of the signal in the triad + BNAH sample is due to BNAH$^{•+}$ radicals. In addition, HYSCORE spectrum of the triad + BNAH sample was also recorded (**Figure IV-13b**). Spots on the diagonal line centered at 15 MHz are attributed to proton hyperfine coupling of the BNAH$^{•+}$ radicals, while a weak spot at 3.6 MHz is assigned to distant Mn atoms. No Mn hyperfine couplings were observed. It is however not in contradiction with the calculations of hyperfine interactions by Dr. Jean-Marie Mouesca (CEA Grenoble / INAC / SyMMES) for ^{55}Mn isotope ($I = 5/2$), which shows a quadrupolar interaction at 55 MHz. This interaction will spread the HYSCORE signal of Mn in Mn^0 complex on a very broad range, making it undetectable. Therefore, the presence of monomeric Mn^0 complex is not observed by the EPR technique.
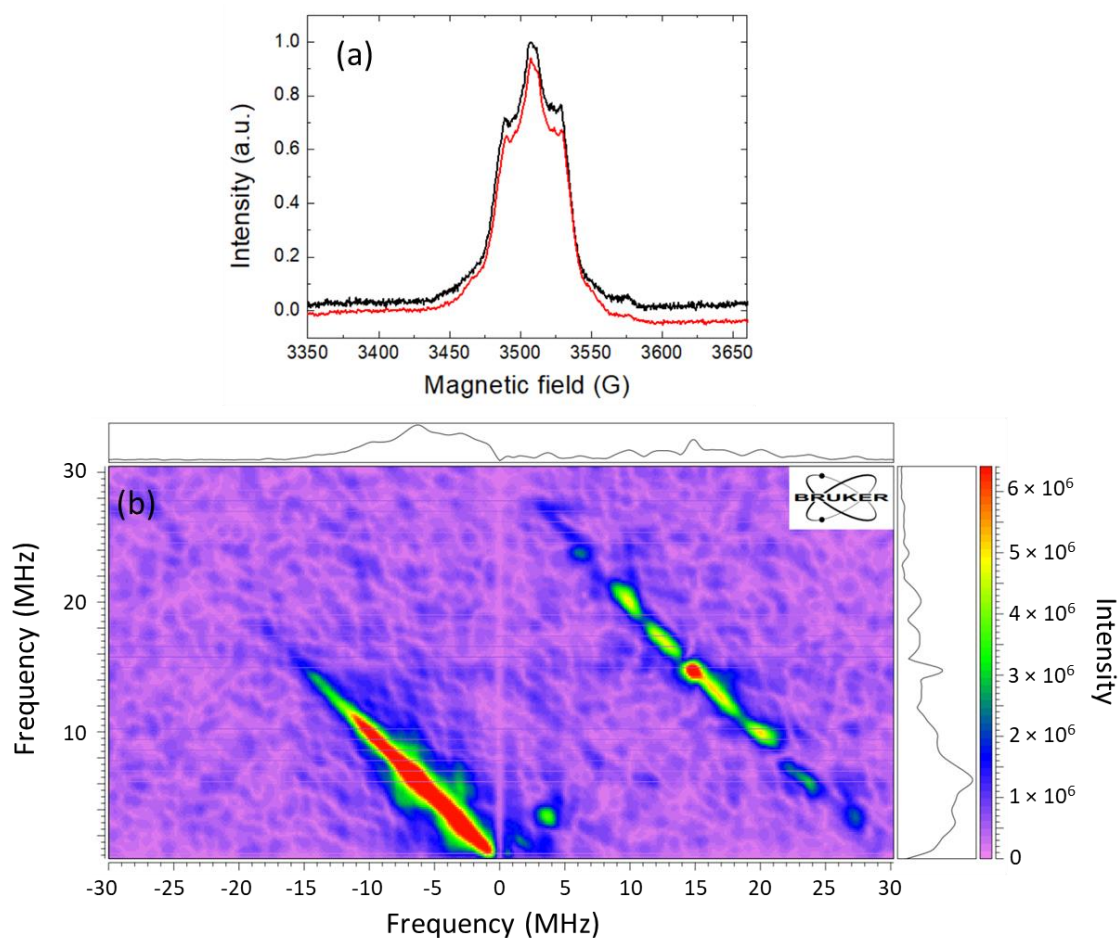
Figure IV-13. (a) Pulsed EPR field-swept spectra of BNAH$^{•+}$ radicals alone (red) and Ru^{II}/TiO$_2$/Mn^{I} triad + BNAH$^{•+}$ (black). (b) HYSCORE spectrum of Ru^{II}/TiO$_2$/Mn^{I} triad + BNAH$^{•+}$ mixture. The samples were irradiated in situ by a 455 nm LED.

It is also important to note that the doubly reduced species $[Mn^{-I}(ttpy)(CO)_2]^-$ in homogeneous solution has been shown to exhibit a broad EPR line spread over ~ 3000 G[21], which is characteristic of an unpaired electron on the metal center. However, this doubly reduced species is not observed in our study for $Ru^{II}/TiO_2/Mn^{I}$ triad. From the electrochemistry and EPR results, we propose that the grafted Mn^{I} in the triad undergoes the one-electron reduction pathway, which has been proved for the analogous $[Mn(bpy)(CO)_3Br]$ complex anchored on the MOF named UiO-67 (**Scheme IV-12**).[29] In this scenario the catalytically active species is thought to be $[Mn^{0}(ttpy-C_3-PO_3H_2)(CO)_2]$ (**Scheme IV-13**) where a coordination site is ready for the formation of a CO_2 adduct[5].
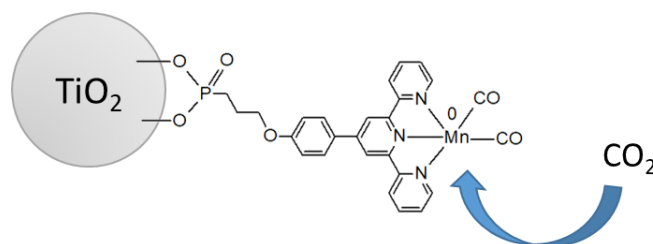
Scheme IV-13. Proposed catalytically active species $[Mn^{0}(ttpy-C_3-PO_3H_2)(CO)_2]$ for the $Ru^{II}/TiO_2/Mn^{I}$ triad

IV.4. Conclusion

In this chapter, firstly, the electrochemical properties of $[Mn^I(\kappa^2\text{-ttpy})(CO)_3Br]$ complex were investigated. The complex showed promising electrocatalytic activity for CO_2 reduction with TON_{max} (CO) = 12, which could occur via one- or two-electron pathway mechanism. In the presence of $[Ru(bpy)_3]^{2+}$ as a PS and BNAH as a sacrificial electron donor, the Mn complex could be reduced and the mixture showed photocatalytic activity for the CO_2 reduction to produce both CO and HCOOH under irradiation at 470 nm. These results are in accordance with the analogous $[Mn^I(\kappa^2\text{-ttpy})(CO)_3(MeCN)]^+$ complex which has been already studied by former PhD students in the CIRe group.

Afterwards, a terpyridine-based ligand bearing a phosphonic acid group was synthesized and adsorbed on TiO_2 NPs. The $[Mn^I(\kappa^2\text{-ttpy-}C_3\text{-PO}_3H_2)(CO)_3Br]$ complex on TiO_2 (called TiO_2/Mn^I) was obtained by coordination chemistry between $Mn(CO)_5Br$ precursor and TiO_2/ttpy modified NPs. The grafting process was proved by IR, UV-vis absorption as well as cyclic voltammetry. Subsequently, $[Ru(bpy)_3]^{2+}$ was also immobilized on TiO_2/Mn^I NPs to form a $Ru^{II}/TiO_2/Mn^I$ triad. The ratio of Mn:Ru was chosen to be 1:10 as it was the optimal condition for the photocatalytic CO_2 reduction using the two homogeneous complex in solution. The $Ru^{II}/TiO_2/Mn^I$ triad NPs showed good photocatalytic activity for the CO_2 reduction: TON_{max} (HCOOH) = 27 over 16 hours of irradiation with 100 % selectivity for HCOOH. Although the total TON was lower than that of the two homogeneous complexes in solution (TON_{total} = 50), the selectivity for HCOOH was greatly improved.

A reason for this improved photocatalytic behavior using the triad is thought to be related to the immobilization of Mn^I catalyst. In homogeneous solution, the reduction of Mn^I complex may follow the two-electron pathway: first, it undergoes monoelectronic reduction and dimerization to form $Mn^0\text{-}Mn^0$, which is subsequently reduced again to yield the catalytically active species Mn^{-I}. When the Mn^I complex is immobilized, the dimerization step is assumed to be prohibited, thus the monomeric paramagnetic Mn^0 species (S = 1/2) is expected. Unfortunately, its presence was not confirmed by EPR, possibly due to a very broad signal of the Mn^0 quadrupolar interaction in the HYSCORE spectrum. The Mn^{-I} species were not observed by X-band EPR technique. Based on the electrochemistry and EPR results, we propose that the reduction of the immobilized Mn^I complex in $Ru^{II}/TiO_2/Mn^I$ triad may follow the one-electron pathway without the formation of $Mn^0\text{-}Mn^0$ dimer, hence the catalytically active species is assumed to be $[Mn^0(\text{ttpy-}C_3\text{-PO}_3H_2)(CO)_2]$. Under visible light and in the presence of BNAH as an electron donor, Ru^{II} is reduced to Ru^I, followed by electron transfer from Ru^I to Mn^I to form the Mn^0 species. The electron transfer process probably occurs

between neighboring Ru^I and Mn^I species on the surface of TiO_2, and not through TiO_2 conduction band. The specific role of TiO_2 scaffold compared to SiO_2 is not yet fully understood.

References

1   C. D. Windle and R. N. Perutz, *Coord. Chem. Rev.*, 2012, **256**, 2562–2570.

2   R. M. DeConto and D. Pollard, *Nature*, 2016, **531**, 591–597.

3   E. E. Benson, C. P. Kubiak, A. J. Sathrum and J. M. Smieja, *Chem. Soc. Rev.*, 2009, **38**, 89–99.

4   V. V. Pavlishchuk and A. W. Addison, *Inorganica Chim. Acta*, 2000, **298**, 97–102.

5   Y. Yamazaki, H. Takeda and O. Ishitani, *J. Photochem. Photobiol. C Photochem. Rev.*, 2015, **25**, 106–137.

6   G. Sahara and O. Ishitani, *Inorg. Chem.*, 2015, **54**, 5096–5104.

7   R. Reithmeier, C. Bruckmeier and B. Rieger, *Catalysts*, 2012, **2**, 544–571.

8   N. Elgrishi, M. B. Chambers, X. Wang and M. Fontecave, *Chem. Soc. Rev.*, 2017, **46**, 761–796.

9   J. Hawecker, J.-M. Lehn and R. Ziessel, *J. Chem. Soc. Chem. Commun.*, 1983, 536–538.

10   J. Hawecker, J.-M. Lehn and R. Ziessel, *J. Chem. Soc. Chem. Commun.*, 1984, 328–330.

11   G. Neri, M. Forster, J. J. Walsh, C. M. Robertson, T. J. Whittles, P. Farras and A. J. Cowan, *Chem. Commun.*, 2016, **52**, 14200–14203.

12   C. D. Windle, E. Pastor, A. Reynal, A. C. Whitwood, Y. Vaynzof, J. R. Durrant, R. N. Perutz and E. Reisner, *Chem. Eur. J.*, 2015, **21**, 3746–3754.

13   M. Abdellah, A. M. El-Zohry, L. J. Antila, C. D. Windle, E. Reisner and L. Hammarstrom, *J. Am. Chem. Soc.*, 2017, **139**, 1226–1232.

14   E.-G. Ha, J.-A. Chang, S.-M. Byun, C. Pac, D.-M. Jang, J. Park and S. O. Kang, *Chem. Commun.*, 2014, **50**, 4462–4464.

15   D.-I. Won, J.-S. Lee, J.-M. Ji, W.-J. Jung, H.-J. Son, C. Pac and S. O. Kang, *J. Am. Chem. Soc.*, 2015, **137**, 13679–13690.

16   M. Bourrez, F. Molton, S. Chardon-Noblat and A. Deronzier, *Angew. Chemie, Int. Ed.*, 2011, **50**, 9903–9906.

17   H. Takeda, H. Koizumi, K. Okamoto and O. Ishitani, *Chem. Commun.*, 2014, **50**, 1491–1493.

18   J.-X. Zhang, C.-Y. Hu, W. Wang, H. Wang and Z.-Y. Bian, *Appl. Catal. A Gen.*, 2016,

522, 145–151.

19   T. E. Rosser, C. D. Windle and E. Reisner, *Angew. Chemie, Int. Ed.*, 2016, **55**, 7388–7392.

20   M. Bourrez, "Synthèse, étude et caractérisation de nouveaux catalyseurs moléculaires pour la réduction du CO_2 en vue de son utilisation comme source de carbone", *PhD Dissertation,* Université Grenoble-Alpes, 2012.

21   M. Stanbury, "Réduction photo et électro-assistée sélective du dioxyde de carbone sur des catalyseurs moléculaires", *PhD Dissertation,* University of Grenoble-Alpes, 2016.

22   C. W. Machan and C. P. Kubiak, *Dalt. Trans.*, 2016, **45**, 17179–17186.

23   J.-D. Compain, M. Stanbury, M. Trejo and S. Chardon-Noblat, *Eur. J. Inorg. Chem.*, 2015, 5757–5766.

24   M. Stanbury, J.-D. Compain, M. Trejo, P. Smith, E. Gouré and S. Chardon-Noblat, *Electrochim. Acta*, 2017, **240**, 288–299.

25   G. J. Stor, D. J. Stufkens, P. Vernooijs, E. J. Baerends, J. Fraanje and K. Goubitz, *Inorg. Chem.*, 1995, **34**, 1588–1594.

26   K. Kasuga, H. Miyasaka, M. Handa and M. Dairaku, *Polyhedron*, 1995, **14**, 1675–1679.

27   J.-D. Compain, M. Bourrez, M. Haukka, A. Deronzier and S. Chardon-Noblat, *Chem. Commun.*, 2014, **50**, 2539–2542.

28   C. Liu, K. D. Dubois, M. E. Louis, A. S. Vorushilov and G. Li, *ACS Catal.*, 2013, **3**, 655–662.

29   H. Fei, M. D. Sampson, Y. Lee, C. P. Kubiak and S. M. Cohen, *Inorg. Chem.*, 2015, **54**, 6821–6828.

30   X. Wang, I. Thiel, A. Fedorov, C. Coperet, V. Mougel and M. Fontecave, *Chem. Sci.*, 2017, Ahead of Print.

31   S. Ardo and G. J. Meyer, *J. Am. Chem. Soc.*, 2011, **133**, 15384–15396.

32   R. N. Sampaio, A. V. Muller, A. S. Polo and G. J. Meyer, *ACS Appl. Mater. Interfaces*, 2017, **9**, 33446–33454.

33   R. F. Howe and M. Gratzel, *J. Phys. Chem.*, 1987, **91**, 3906–3909.

34   C. P. Kumar, N. O. Gopal, T. C. Wang, M.-S. Wong and S. C. Ke, *J. Phys. Chem. B*, 2006, **110**, 5223–5229.

CHAPTER V

PHOTOACTIVE TiO$_2$/[Ru(bpy)$_2$(bpy-pyr)]$^{2+}$ HYBRID NANOCOMPOSITES

Abstract

In this chapter, $[Ru(bpy)_3]^{2+}$ photosensitizer has been functionalized with a pyrrole unit and a phosphonic acid group to anchor on TiO_2 NPs to form a hybrid system called $TiO_2/[Ru\text{-}pyr]^{2+}$. The electrochemical and photophysical properties of this system have been studied. Photo-induced electron injection from $[Ru(bpy)_3]^{2+*}$ unit to TiO_2 to yield $(e^-)TiO_2/[Ru^{III}\text{-}pyr]^{3+}$ occurs in nanosecond time scale, which is followed by the reduction of Ru^{III} by pyrrole moiety. A transient charge separated state $(e^-)TiO_2/[Ru^{II}\text{-}pyr^+]^{3+}$ is then formed. In the presence of O_2 as an electron scavenger for the injected electrons in TiO_2 NPs, the positively charged pyrrole moieties induce oxidative polymerization to yield $TiO_2/poly(Ru\text{-}pyr)$ nanocomposite. Afterwards, the nanocomposite has been deposited onto a FTO electrode using an electrophoretic deposition process. These electrodes behave as efficient photoanode under visible irradiation in the presence of triethanolamine as sacrificial electron donor. The nanostructuration of the polypyrrole network enhances both the homogeneity of surface deposition and photocurrent intensity compared to the results obtained with a $FTO/TiO_2/Ru^{II}$ electrode.

Résumé

Dans ce chapitre, le photosensibilisateur $[Ru(bpy)_3]^{2+}$ a été modifié par une unité pyrrole et un groupe acide phosphonique puis immobilisé sur les nanoparticules de TiO_2 pour former un système hybride $TiO_2/[Ru\text{-}pyr]^{2+}$. Les propriétés électrochimiques et photophysiques de ces systèmes ont été étudiées. L'injection d'électrons photoinduit à partir du $[Ru(bpy)_3]^{2+*}$ vers le TiO_2 pour former $(e^-)TiO_2/[Ru^{III}\text{-}pyr]^{3+}$ se produit à l'échelle de temps de la nanoseconde, et est suivie de la réduction de Ru^{III} par le pyrrole. Un état transitoire à charge séparé $(e^-)TiO_2/[Ru^{II}\text{-}pyr^+]^{3+}$ est ensuite formé. En présence d'O_2 comme agent piégeur des électrons injectés dans le TiO_2, les groupements pyrrole oxydé induisent une polymérisation pour former un nanocomposite $TiO_2/poly(Ru\text{-}pyr)$. Le nanocomposite $TiO_2/poly(Ru\text{-}pyr)$ a été déposé sur des électrodes FTO en utilisant une méthode d'électrophorèse. Ces électrodes se comportent comme des photocathodes en présence de TEOA comme donneur d'électron sacrificiel. La nanostructuration du réseau de polypyrrole permet d'améliorer l'homogénéité du dépôt et d'augmenter l'intensité du photocourant comparé à une électrode obtenue par immobilisation du système TiO_2/Ru^{II}.

V.1. Introduction

Photoactive hybrid nanocomposites are promising materials for a wide range of applications from photocatalysis to photoelectrodes. Engineering the interface between organic – inorganic components has important impact on the material properties, thus it is critical for every application. Notably, coating of an organic polymer on TiO$_2$ nanomaterials may change its hydrophobic / hydrophilic property, stability or electrical conductivity. In the latter case, the use of pyrrole, vinyl or styrene monomers offer an advantage to easily control the polymerization process, which can be initiated by TiO$_2$ band-gap excitation. The resulting material consists of TiO$_2$ nanoparticles (NPs) embedded in a conducting polymer network. This section is focused on the preparation methods of these materials, their characterization and applications after deposition on transparent electrodes in photo-to-current energy conversion.

Strandwitz et al.[1] studied the *in situ* photopolymerization of pyrrole in mesoporous TiO$_2$ thin film. First, a layer of TiO$_2$ (thickness ∼ 0.5 µm) was dip-coated onto a Fluorine-doped Tin Oxide (FTO) electrode. The electrode was then immersed into an aqueous solution of pyrrole and methyl viologen (MV^{2+}) under 365 nm irradiation. This TiO$_2$ band-gap excitation promotes electrons to the conduction band (CB) and leaving a hole on the valence band (VB). The electron is then transferred to MV^{2+}, while pyrrole is subsequently oxidized by the holes. In turn, the oxidized pyrrole initiates the oxidative polymerization of pyrrole to form polypyrrole. The photopolymerization process and mechanism of pyrrole oxidative polymerization are summarized in **Scheme V-1**. Pore size between TiO$_2$ NPs coated on FTO was monitored by N$_2$ adsorption isotherms. After 24 hours of irradiation the average pore diameter slightly decreases from 4.7 nm to 4.3 nm, which equals to ∼ 20 % pore filling by the polypyrrole film. This poorly efficient coverage is probably due to several reasons such as: (i) the competitive UV absorption of polypyrrole, thus blocking the light to reach TiO$_2$; (ii) polypyrrole acting as an energy barrier for other pyrrole monomers in solution to be in contact with the electrode and then be oxidized; and (iii) decomposition of polypyrrole due to photocatalytically active TiO$_2$ NPs.
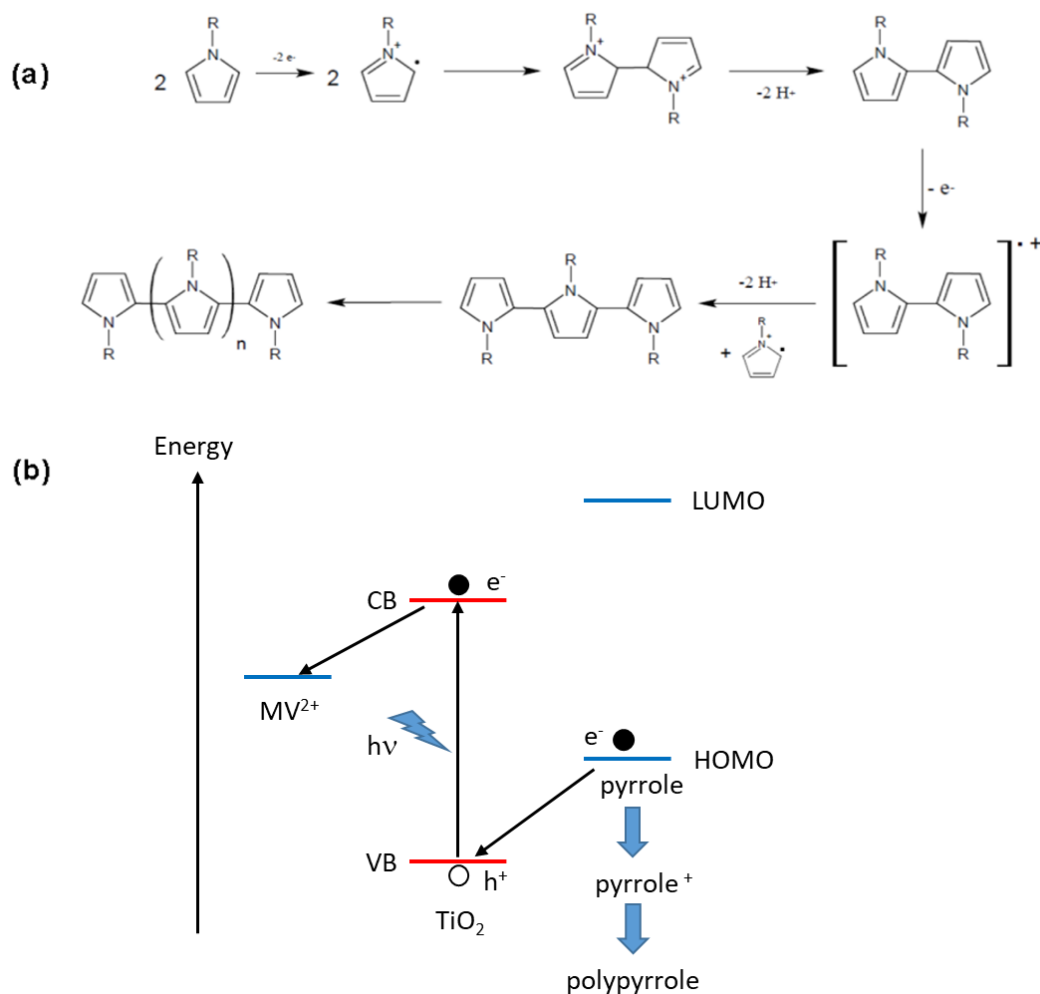
Scheme V-1. (a) Mechanism of pyrrole oxidative polymerization. (b) *In situ* photopolymerization of pyrrole on mesoporous TiO₂ film. Adapted from reference 1. The LUMO level of pyrrole cannot be determined electrochemically.

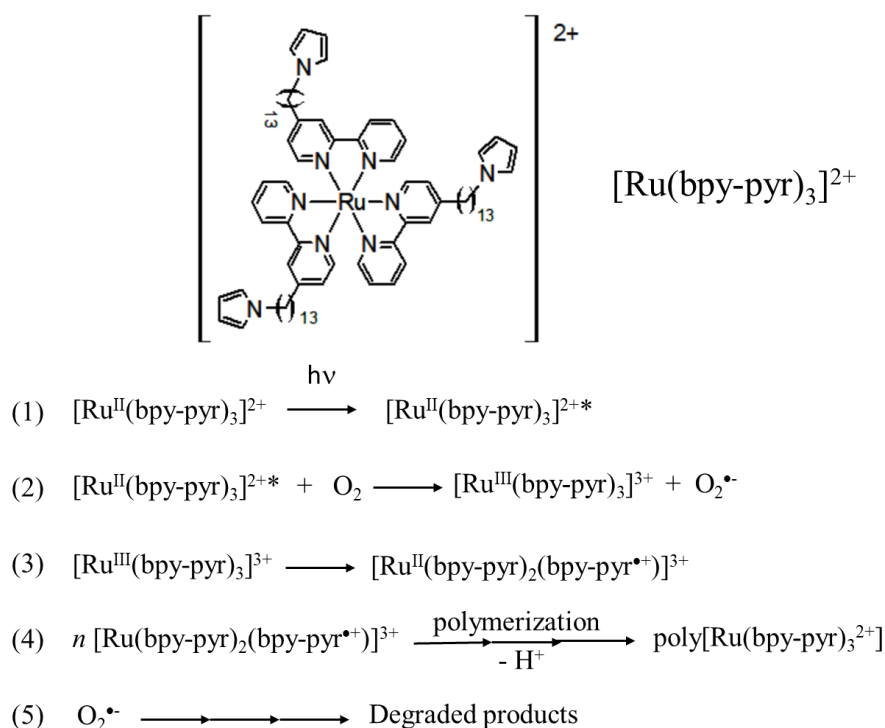Well-defined nanostructured composites of TiO₂ NPs and various polymers such as polystyrene (PS), poly(methyl methacrylate) (PMMA) and poly(*N*-isopropylacrylamide) (PNIPAM) have been reported by Wang et al.[2] following a surface-initiated photopolymerization method. TiO₂ NPs were first modified with 3-(trimethoxysilyl)propyl methacrylate (MPS) which not only formed Si-O-Ti linkages with TiO₂ but also possessed terminal C=C bonds. Under UV light electrons and holes are created on the CB and VB of TiO₂, respectively. The holes are then transferred to the C=C bonds to generate radicals which can initiate the oxidative polymerization process. The covalent bonding between MPS and TiO₂ ensures that the polymer is bound to the TiO₂ surface. However, the polymer degradation due to photocatalytically active TiO₂ under UV light has not been mentioned. **Scheme V-2** summarizes this mechanism. The TiO₂/polymer core/shell NPs with precise, tunable architecture are versatile building blocks for numerous potential applications in

sensing, analysis or textile engineering. For example, monodisperse TiO_2 spheres could be used as photonic crystals due to the high refractive index and transparency under visible light.
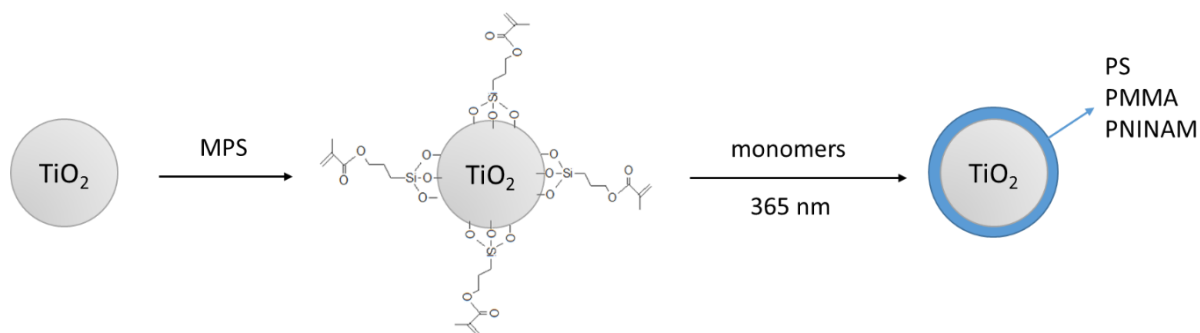
**Scheme V-2**. Surface-initiated photopolymerization of PS, PMMA and PNINAM on TiO_2 NPs. Adapted from reference 2

The aforementioned works requires UV light to initiate the photopolymerization process since TiO_2 does not absorb visible light. However, such condition may eventually lead to destruction of the polymer as TiO_2 can photodegrade organic materials under UV light.[3] Incorporating pyrrole and $[Ru(bpy)_3]^{2+}$ photosensitizer (PS) allows the polymerization to occur under visible irradiation. One of the pioneering works in this field has been done by Deronzier et al.[4] The authors covalently linked the PS and pyrrole via alkyl chains, named $[Ru(bpy\text{-}pyr)_3]^{2+}$ (**Scheme V-3**). The complex can be electropolymerized and deposited on a Pt electrode in either MeCN or H_2O solvent, although the polymerization kinetics is much slower in H_2O. In air-saturated aqueous solution, the complex can be photopolymerized under visible irradiation ($\lambda > 405$ nm), forming a film in less than 30 s. The film is electroactive in the anodic region in both MeCN and H_2O solvents (with suitable electrolytes); however, it is not in the cathodic region in aqueous solution due to its hydrophobicity. The authors later proposed a mechanism[5] for the photopolymerization process (**Scheme V-3**). The critical steps are the reductive quenching of $[Ru^{II}(bpy\text{-}pyr)_3]^{2+*}$ excited state by O_2 to generate Ru^{III} species (step 2), followed by an electron transfer between the pyrrole moiety and Ru^{II} leading to a radical cation on pyrrole moiety (step 3). This radical then initiates the polymerization (step 4).

$$[Ru(bpy\text{-}pyr)_3]^{2+}$$

(1) $[Ru^{II}(bpy\text{-}pyr)_3]^{2+} \xrightarrow{h\nu} [Ru^{II}(bpy\text{-}pyr)_3]^{2+*}$

(2) $[Ru^{II}(bpy\text{-}pyr)_3]^{2+*} + O_2 \longrightarrow [Ru^{III}(bpy\text{-}pyr)_3]^{3+} + O_2^{\bullet-}$

(3) $[Ru^{III}(bpy\text{-}pyr)_3]^{3+} \longrightarrow [Ru^{II}(bpy\text{-}pyr)_2(bpy\text{-}pyr^{\bullet+})]^{3+}$

(4) $n\ [Ru(bpy\text{-}pyr)_2(bpy\text{-}pyr^{\bullet+})]^{3+} \xrightarrow[-\ H^+]{\text{polymerization}} poly[Ru(bpy\text{-}pyr)_3{}^{2+}]$

(5) $O_2^{\bullet-} \longrightarrow \longrightarrow$ Degraded products

Scheme V-3. [Ru(bpy-pyr)$_3$]$^{2+}$ and its photopolymerization mechanism mentioned in references 4 and 5

Lattach et al.[6] studied the electrodeposition of MoS$_x$ NPs into a polymer containing [Ru(bpy)$_3$]$^{2+}$ PS covalently linked with pyrrole (**Scheme V-4**), resulting in an electrogenerated hybrid nanocomposite film on a carbon electrode, denoted as C/poly(Ru-pyr)/MoS$_x$. MoS$_x$ has been chosen as a low cost, efficient catalyst for the hydrogen evolution reaction in aqueous solution to replace Pt. First, pyrrole-containing [Ru(bpy)$_3$]$^{2+}$ complex was coated onto the carbon electrode by electropolymerization to form a poly(Ru-pyr) film. Subsequently, the modified electrode was immersed into a solution containing MoS$_4{}^{2-}$, which was trapped inside the polymer by ion exchange mechanism. The anion was then electroreduced to MoS$_x$ particles by cyclic voltammetry (CV). A well-structured nanocomposite film with grain size ~ 20 nm was proven by Atomic Force Microscopy (AFM). Under visible irradiation and at pH 3, the hydrogen evolution reaction occurred with quantitative yield to reach turnover number (TON) of 31 after 2 hours. The photocurrent remained stable at 15 µA.cm^{-2} during the process.
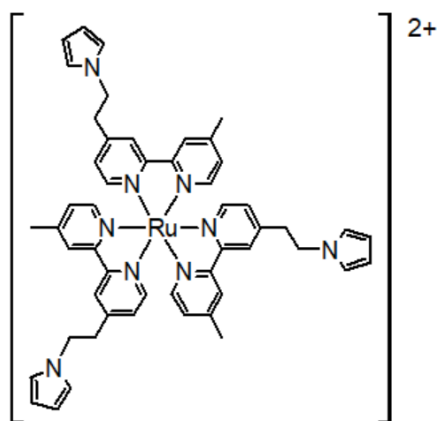
Scheme V-4. Pyrrole-containing [Ru(bpy)₃]²⁺ complex mentioned in reference 6.

In this chapter we will present the incorporation of a pyrrole-containing [Ru(bpy)₃]²⁺ complex covalently grafted on TiO₂ NPs. The aim of this design is to prepare a photoactive hybrid nanocomposite capable of polymerization under visible light, thus avoiding possible detrimental effects of TiO₂ on organic components under UV light. It is hence expected that the formation of polypyrrole will increase the conductivity of the resulting nanocomposite material after deposition on an electrode. The resulting hybrid system, called TiO₂/[Ru-pyr]²⁺ (**Scheme V-5**) has been designed following the Electron Acceptor – PS – Electron Donor architecture, in which the [Ru(bpy)₃]²⁺ PS is anchored on TiO₂ surface to facilitate the photo-induced electron transfer process as presented in **Chapter 2**. In this structure TiO₂ acts as the electron acceptor for [Ru(bpy)₃]²⁺* and pyrrole as electron donor to regenerate the PS by reducing the Ru^III species. First, the synthesis, electrochemical and photophysical properties of the complex in solution will be discussed. Afterwards, grafting of the complex onto TiO₂ NPs together with its properties will be presented. The photopolymerization process will be addressed in detail via various characterization techniques. Finally, deposition of the nanocomposite onto a FTO surface and its photo-to-current energy conversion will be shown, highlighting the role of polypyrrole.
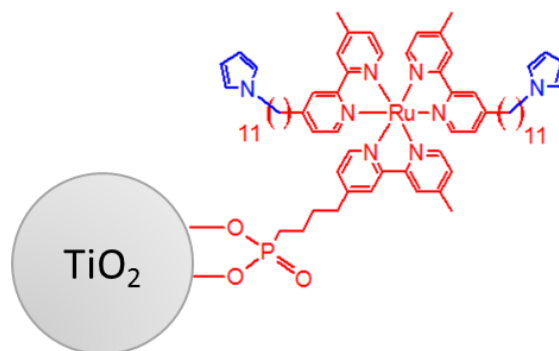

Scheme V-5. Structure of TiO₂/[Ru-pyr]²⁺ hybrid nanoparticles

V.2. Pyrrole-containing Ru(II) tris-bipyridine complex in solution

V.2.1. Synthesis

The synthesis of bpy-pyr ligand[4] and [Ru(bpy-pyr)₂Cl₂] complex[7] (bpy-pyr = 4-methyl-4'-[11-(1*H*-pyrrol-1-yl)undecyl]-2,2'-bipyridine) have been done in a similar manner reported in literature with some modifications (see **Experimental Section** for more details). Incorporating another bpy ligand was achieved by refluxing [Ru(bpy-pyr)₂Cl₂] and 4,4'-dimethyl-2,2'-bipyridine (dmbpy, 1 equiv) in H₂O/ethanol mixture (2/8 v/v) overnight under Ar. The as-synthesized product was allowed for anion exchange with excess amount of KPF₆ to yield [Ru(dmbpy)(bpy-pyr)₂](PF₆)₂ complex which is hereafter denoted as [Ru-pyr]²⁺ (**Scheme V-6**). We chose the dmbpy ligand because in the next step a phosphonic group will be incorporated into this ligand as anchoring group to TiO₂ NPs. Therefore the study on [Ru-pyr]²⁺ complex can be compared with that grafted on TiO₂ NPs.
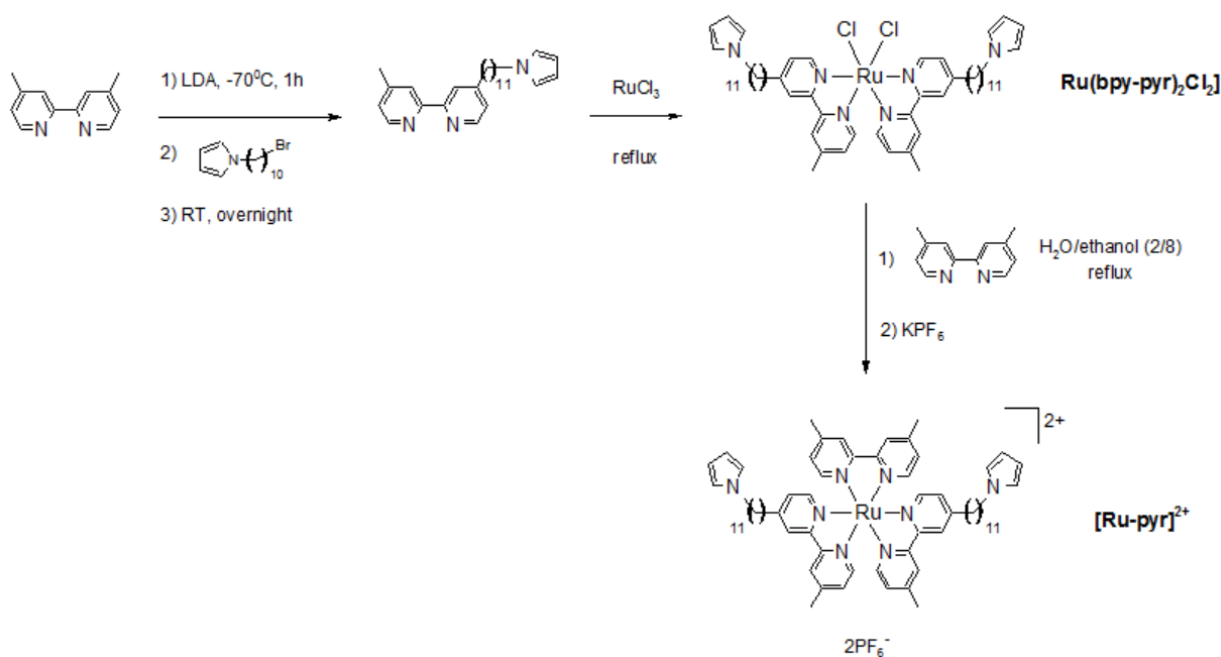

Scheme V-6. Synthesis procedure for [Ru-pyr]²⁺ complex

V.2.2. Electrochemical properties

Cyclic voltammetry was employed to studied the electrochemical properties of [Ru-pyr]²⁺ in solution. Its CV is shown in **Figure V-1**. A quasi-reversible wave at $E_{1/2} = 0.84$ V, which is shifted by 100 mV compared with [Ru(bpy)₃]²⁺,[8] is attributed to the oxidation of pyrrole and Ru^{III}/Ru^{II} couple, since their oxidation potentials are known to be indistinguisable.[4,6] The bpy-pyr ligand oxidation has been reported to be irreversible at potentials around 1 V.[9] In our case, the I_{pa}/I_{pc} ratio is larger than unity, showing that this oxidation is also not reversible. In the cathodic part, three reversible waves centered at $E_{1/2}$

= -1.73, -1.93 and -2.16 (V) are assigned to the reduction of the complex localized on its three bpy ligands since they are in accordance with the $[Ru(bpy)_3]^{2+}$ complex.[8] The weakly electron-donating -CH₂- group on a bpy ligand shifts all the potentials to more negative values than that of $[Ru(bpy)_3]^{2+}$. **Table V-1** collects the redox potentials of $[Ru-pyr]^{2+}$ and $[Ru(bpy)_3]^{2+}$ for comparison.
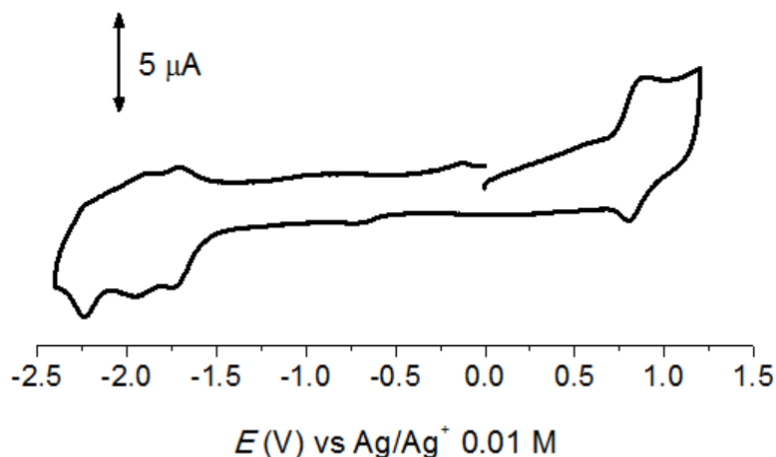

Figure V-1. CV of $[Ru-pyr]^{2+}$ (1 mM) in MeCN + 0.1 M TBAP under Ar. WE = C disk (3 mm), v = 100 mV/s

Table V-1. Summary of electrochemical properties of $[Ru-pyr]^{2+}$ compared with $[Ru(bpy)_3]^{2+}$

$E_{1/2}$ (ΔEp), V	E_{ox}	E_{red} (1)	E_{red} (2)	E_{red} (3)
$[Ru-pyr]^{2+}$	0.84 (0.08)	-1.73 (0.05)	-1.93 (0.06)	-2.16 (0.09)
$[Ru(bpy)_3]^{2+, a}$	0.94	-1.67	-1.83	-2.07

ᵃ From reference [8]

The electropolymerization and deposition of $[Ru-pyr]^{2+}$ on ITO electrode were achieved by scanning the potential between -2.4 V and 1.2 V in MeCN + 0.1 M TBAP solution under Ar (**Figure V-2a**). Such an electroreductive scanning is necessary to deposit a film onto an ITO electrode (denoted as ITO/poly(Ru-pyr)), as iteratively oxidative scanning between 0 and 1.2 V shows no CV signal for a deposition process. A similar behavior has been observed for related pyrrole-containing $[Ru(bpy)_3]^{2+}$ complexes.[4] The authors attributed the deposition of the polymer film to the strong adsorption of doubly reduced species $[Ru(bpy)(bpy^{\bullet-})_2-pyr]^0$. After 15 scanning cycles, the ITO/poly(Ru-pyr) electrode was transferred to a complex-free electrolyte solution to record its CV (**Figure V-2b**). Growths in the magnitude of all redox waves indicate the increase in the number of redox active species on the surface. Together with the formation of a noticeable conductive film on the electrode, these observations prove the successful electrodeposition of poly(Ru-pyr) film on ITO.
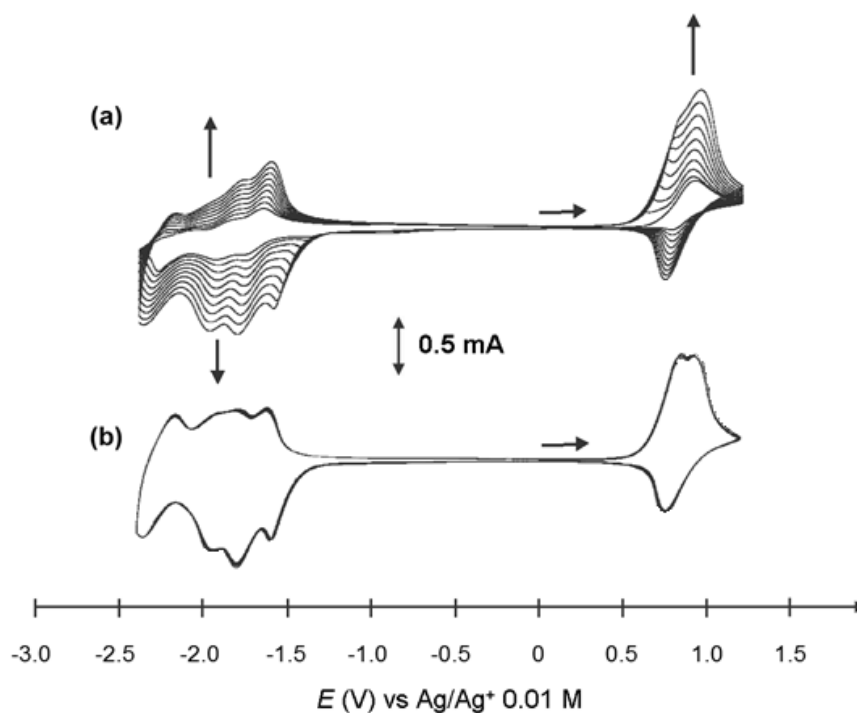
Figure V-2. Electropolymerization of [Ru-pyr]²⁺ (0.6 mM) on an ITO electrode (v = 100 mV/s, in MeCN + TBAP 0.1 M under Ar). (a) 15 CVs obtained during the polymerization, with vertical arrows indicating the changes in its CV. (b) CV of the ITO/poly(Ru-pyr) electrode after transferred to a complex-free solution.

V.2.3. Photophysical properties

Figure V-3 presents the UV-vis absorption and emission spectra of [Ru-pyr]²⁺ complex compared with those of [Ru(bpy)₃]²⁺ reference. The absorption maxima at 460 nm and 286 nm of [Ru-pyr]²⁺ are assigned to the singlet metal-to-ligand charge transfer (¹MLCT) and ligand-centered (LC) transition, respectively. The extinction coefficient of [Ru-pyr]²⁺ at 460 nm (ε = 13900 M⁻¹.cm⁻¹) is similar to that of [Ru(bpy)₃]²⁺ at 450 nm (ε = 13000 M⁻¹.cm⁻¹)[8].

After excitation at 450 nm, the [Ru-pyr]²⁺ complex exhibits a broad emission spectrum with a maximum at 621 nm, which is characteristic of Ru²⁺* ³MLCT state. Both visible absorption and emission wavelength maxima are only slightly red-shifted compared to those of [Ru(bpy)₃]²⁺. The shifts are in accordance with literature for a series of [Ru(bpy)₃]²⁺ linked to two or three pyrrole groups via alkyl chains[10] and show that the substitution only has a minor influence on the electronic structure of the ground state and excited state of the complex.
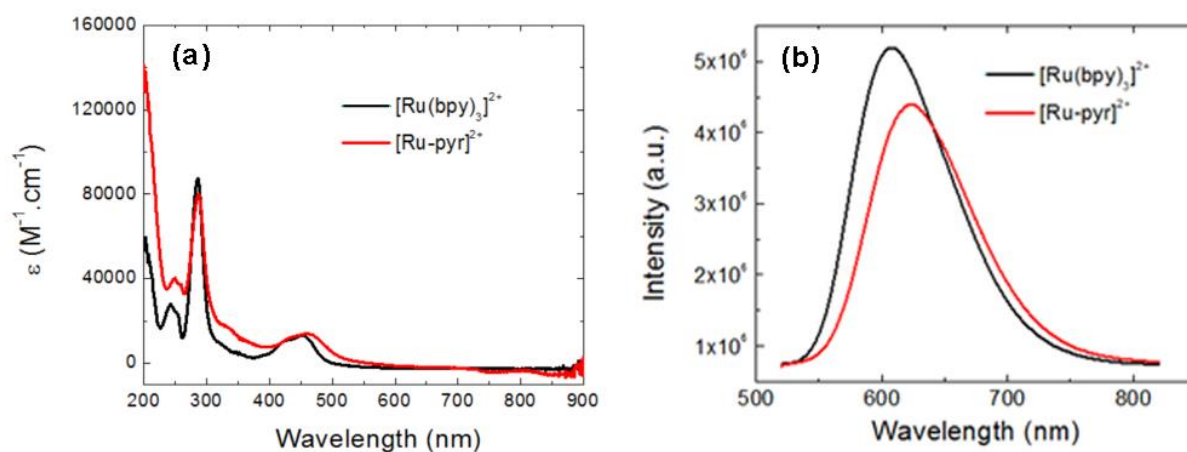
Figure V-3. (a) UV-vis absorption spectra and (b) emission spectra of [Ru(bpy)$_3$]$^{2+}$ (black) and [Ru-pyr]$^{2+}$ (red) complexes in MeCN under Ar. Emission spectra were recorded after 450 nm light excitation.

Similar to **Section II.2.2**, using [Ru(bpy)$_3$]$^{2+}$ as reference (Φ = 0.062)[11], the emission quantum yield Φ of [Ru-pyr]$^{2+}$ is calculated as 0.043 (see **Experimental Section** for the calculation), which is about 70 % of that of [Ru(bpy)$_3$]$^{2+}$.

Following light excitation by a 400 nm picosecond laser, time-resolved emission spectroscopy exhibits a monoexponential decay at 610 nm with a lifetime τ = 670 ns (**Figure V-4**), which is only slightly shorter than that of [Ru(bpy)$_3$]$^{2+*}$ (τ = 757 ns). **Table V-2** collects the essential photophysical data of [Ru-pyr]$^{2+}$ and [Ru(bpy)$_3$]$^{2+}$ for comparison. Both quantum yield and emission lifetime values suggest that no charge transfer or energy transfer reactions take place between [Ru(bpy)$_3$]$^{2+*}$ excited state and the pyrrole moieties. Both subunits behave independently.
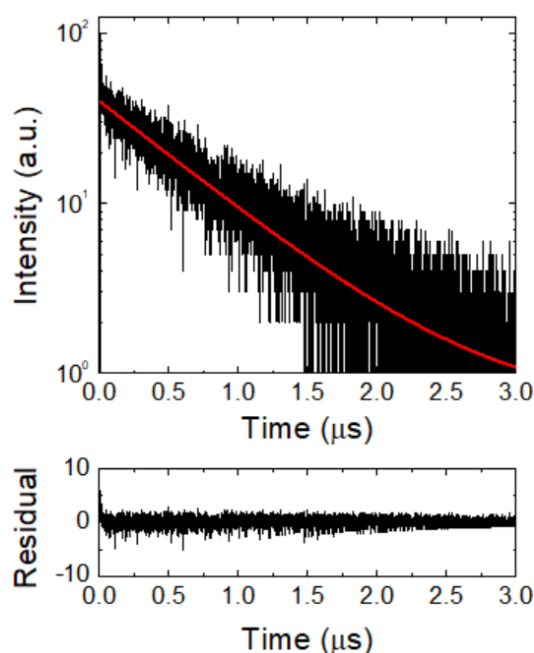
Figure V-4. Time-resolved emission decay of [Ru-pyr]²⁺* excited state in MeCN under Ar. The sample was excited at 400 nm using a picosecond pulsed laser, and the emitted photons were collected at 610 nm using a TCSPC photometer. The red curve represent the monoexponential fitting of the decays

Table V-2. Summary of the photophysical properties of [Ru-pyr]²⁺ and [Ru(bpy)₃]²⁺ complex

	¹MLCT λ_{abs} (nm) [ε, M⁻¹.cm⁻¹]	LCCT λ_{abs} (nm) [ε, M⁻¹.cm⁻¹]	λ_{em} (nm)	Φ	τ (ns) [a]
[Ru-pyr]²⁺	460 [13900]	286 [80000]	621	0.043	670 ± 32
[Ru(bpy)₃]²⁺	450 [13000]	285 [87000]	608	0.062[11]	757 ± 9

[a] *Excitation by a picosecond pulsed laser at 400 nm*
All measurements were conducted in MeCN solution under Ar at room temperature.

As mentioned in the previous chapter, the redox potential of Ru^{II*}/Ru^{I} can be calculated from the redox potential of Ru^{III}/Ru^{II} and the emission maximum of Ru^{II*} by the simplified Rehm-Weller equation (**Equation V-1**):

$$E(\text{Ru}^{II*}/\text{Ru}^{I}) = E(\text{Ru}^{II}/\text{Ru}^{I}) + \frac{hc}{\lambda_{em,77\,K}e} \approx E(\text{Ru}^{II}/\text{Ru}^{I}) + \frac{1240}{\lambda_{em,RT}} \qquad \text{(Eq V-1)}$$

It is hence estimated that E (Ru^{II*}/Ru^{I}) = 0.31 V *vs* Ag/Ag⁺ 0.01 M. Taking into account the oxidation potential of the pyrrole monomers ($E \sim 0.84$ V), the photo-induced electron transfer reaction between [Ru(bpy)₃]²⁺* and pyrrole moieties would be endergonic by around 0.52 eV.

V.3. Immobilization of [Ru-pyr]²⁺ on TiO₂ nanoparticles

V.3.1. Synthesis

The synthesis of TiO₂/[Ru-pyr]²⁺ NPs is schematically summarized in **Scheme V-7**. Similar to **Chapter 3**, a bpy ligand bearing a phosphonic group (denoted bpy-PO₃H₂) was prepared in the first step. The use of TMSBr as deprotecting agent of the –P(O)(OEt)₂ group lead to the formation of HBr by-product, which could not quantitatively separated from the desired product. Our attempts to use this ligand for the complexation with [Ru(bpy-pyr)₂]Cl₂ (where bpy-pyr = 4-methyl-4'-[11-(1*H*-pyrrol-1-yl)undecyl]-2,2'-bipyridine) to form [Ru(bpy-pyr)₂(bpy-PO₃H₂)]²⁺ were not successful due to the H⁺ in HBr initiating the oxidative polymerization of pyrrole moieties. The polypyrrole film could be easily observed in a NMR tube.

Therefore, we employed a stepwise approach as we did in **Chapter 3** for the synthesis of TiO₂/[Ru-pyr]²⁺ NPs. First, the bpy-PO₃H₂ ligand was chemically adsorbed onto anatase TiO₂ colloidal aqueous solution at room temperature, followed by alternate centrifugation – washing steps with copious amount of water to remove unadsorbed ligands and HBr from the solid phase. In the second step, [Ru(bpy-pyr)₂]Cl₂ was added to a suspension of TiO₂/bpy NPs in ethanol / acetone (8/2 v/v) solution under Ar, and the reaction mixture was refluxed overnight. The modified NPs were then separated and washed by alternate centrifugation – washing steps in ethanol / acetone mixture, and dried in an oven to yield a dark red powder. The complexation between TiO₂/bpy and [Ru(bpy-pyr)₂]Cl₂ was quantitatively achieved as the [Ru(bpy-pyr)₂]Cl₂ complex cannot be detected by UV-vis spectroscopy in the washing solution after the complexation. The loading of [Ru-pyr]²⁺ on anatase TiO₂ is estimated as 0.20 mmol.g⁻¹ (about 3800 molecules per NP or 2 molecules per nm²) by measuring the UV-vis absorbance of supernatant solution after each centrifugation step, which is similar to that obtained for TiO₂/Ru^{II} (see **Section II.3.3**).
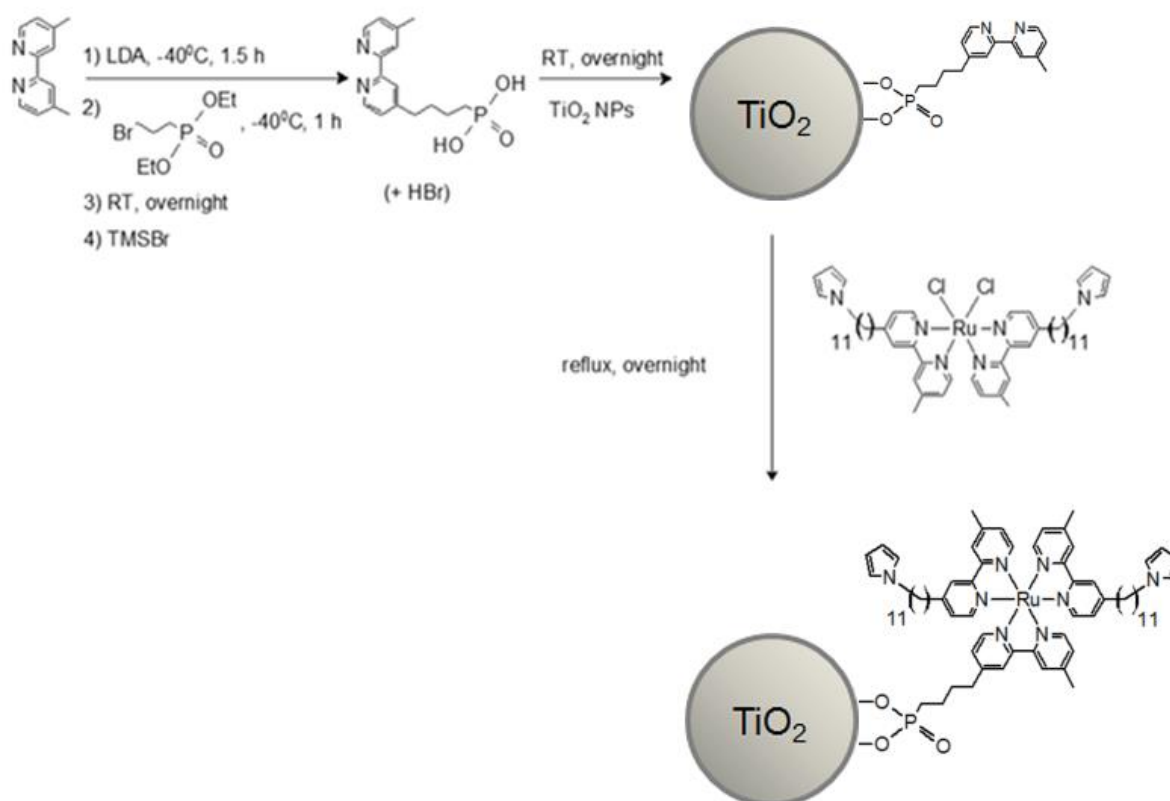
Scheme V-7. Synthesis procedure of TiO$_2$/[Ru-pyr]$^{2+}$ NPs.

V.3.2. Electrochemical properties

The electrochemical properties of TiO$_2$/[Ru-pyr]$^{2+}$ NPs were studied in solid state using a microcavity Pt electrode (d = 50 µm). **Figure V-5** presents the anodic CVs of TiO$_2$/[Ru-pyr]$^{2+}$ and TiO$_2$/Ru^{II} NPs. The former exhibits an intense, irreversible oxidation wave at E_{pa} = 0.82 V, while the latter showed a quasi-reversible redox system at $E_{1/2}$ = 0.98 V. The irreversibility is due to the oxidation of pyrrole to form polypyrrole superimposed on the reversible oxidation of [Ru(bpy)$_3$]$^{2+}$ subunit, as described in **Section V.2.2**. Cathodic scanning of the CV does not lead to any signals of reduced [Ru-pyr]$^+$ species due to the population of the CB of TiO$_2$ starting from ~ -1 V, while the first reduction of the complex may occur at ~ -1.7 V.

188
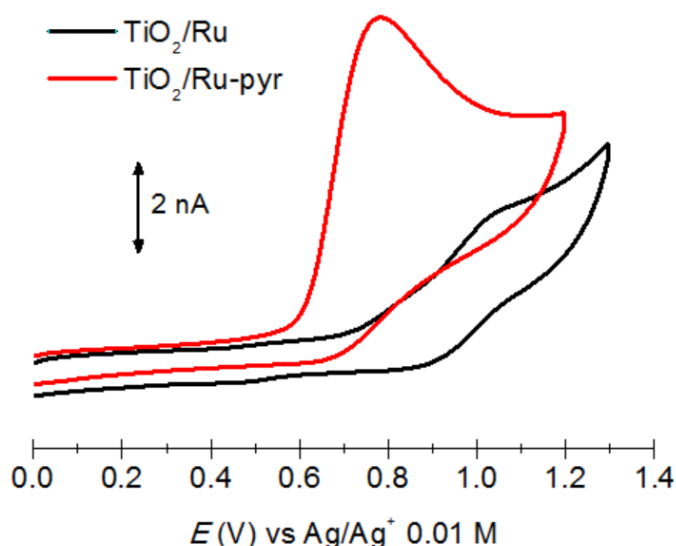
Figure V-5. CV of TiO₂/Ru^{II} (black) and TiO₂/[Ru-pyr]²⁺ (red) NPs recorded in solid state with a microcavity Pt electrode (d = 50 µm) in MeCN + TBAPF₆ 0.1 M under Ar, v = 100 mV/s.

V.3.3.   Photophysical properties

❖ *UV-vis-NIR spectroscopy*

Figure V-6a shows the UV-vis-NIR spectrum of TiO₂/[Ru-pyr]²⁺ NPs in solid state using an integrating sphere. A broad peak at ~ 460 nm was recorded, which is similar to the initial [Ru-pyr]²⁺ complex. The peak is attributed to the ^{1}MLCT absorption band of [Ru(bpy)₃]²⁺ core. The LC transition is not clearly observed due to the strong absorption of TiO₂ at wavelengths below 390 nm.

In colloidal solution of MeCN under Ar, TiO₂/[Ru-pyr]²⁺ NPs display a broad, featureless emission spectrum (**Figure V-6b**) after light excitation at 450 nm. The emission spectrum is similar in shape as those obtained with [Ru-pyr]²⁺ and TiO₂/Ru^{II} colloid, thus it can be reasonably assigned to the emission of the [Ru(bpy)₃]$^{2+*}$ excited state. The emission maximum at 625 nm is slightly red shifted compared to the initial complex [Ru-pyr]²⁺ (621 nm). A similar red shift after immobilizing the Ru complex on TiO₂ has been described for TiO₂/Ru^{II} (see **Section II.3.6**).

Using the simplified Rehm-Weller equation (**Equation V-2**), the redox potential of grafted Ru^{III}/Ru^{II*} in TiO₂/[Ru-pyr]²⁺ is estimated at -1.16 V *vs* Ag/Ag⁺ 0.01 M, which is equal to that of the free complex [Ru-pyr]²⁺ in solution. The result confirms that the complex reduction power has been retained on the NPs.
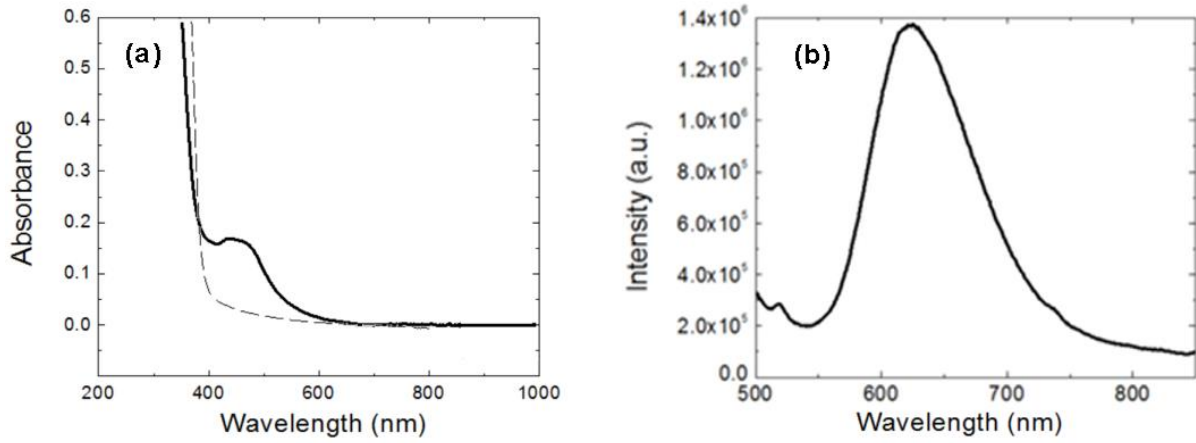
Figure V-6. (a) Solid state UV-vis-NIR spectrum of TiO₂/[Ru-pyr]²⁺ NPs (solid line) and TiO₂ NPs (dashed line) meaured in solid state. (b) Emission spectrum of TiO₂/[Ru-pyr]²⁺ colloid in MeCN under Ar, excited at 450 nm.

$$E(\text{Ru}^{\text{III}}/\text{Ru}^{\text{II}*}) = E(\text{Ru}^{\text{III}}/\text{Ru}^{\text{II}}) - \frac{hc}{\lambda_{em,77\,\text{K}}e} \approx E(\text{Ru}^{\text{III}}/\text{Ru}^{\text{II}}) - \frac{1240}{\lambda_{em,\text{RT}}} \qquad \text{(Eq V-2)}$$

❖ *Time-resolved emission spectroscopy*

The emission decay of TiO₂/[Ru-pyr]²⁺* excited state was recorded at 610 nm after excitation by a picosecond pulsed laser at 400 nm (**Figure V-7**). The decay was fit with a biexponential function to yield two lifetime values τ_1 = 365 ns and τ_2 = 40 ns with corresponding fractional amplitudes of 14 % and 86 %. Similar to **Chapter 2**, the short lifetime τ_1 is attributed to the charge injection to TiO₂ NPs while the long one τ_2 is due to a fraction of [Ru(bpy)₃]²⁺* species that are not able to inject electrons into the NPs. The lifetime of this class of [Ru(bpy)₃]²⁺* centers is shorter than that of [Ru-pyr]²⁺* in solution. It could be a consequence of an energy transfer process between close [Ru(bpy)₃]²⁺ centers anchored on the surface of the NPs.

The rates of energy transfer and electron injection processes in TiO₂/[Ru-pyr]²⁺ NPs have been calculated in a similar way as described in **Section II.3.6**. Applying the **Equation V-3** and using [Ru-pyr]²⁺ in solution as a reference, one can estimate the kinetics of this energy transfer process to be $k_q = 1.2 \times 10^6$ s⁻¹, which is similar to the same kinetics calculated with TiO₂/Ru^II NPs. The result suggests the average distance between Ru centers is almost the same in both modified NPs.

$$k_q = \frac{1}{\tau_1} - \frac{1}{\tau_{Ru-pyr}} \qquad \text{(Eq V-3)}$$

(τ_1 = 365 ns, τ_{Ru-pyr} = 670 ns)

190

Using the lifetime of [Ru-pyr]²⁺* free complex in solution as reference and **Equation V-4,** one can calculate the electron injection rate in TiO₂/[Ru-pyr]²⁺* NPs to be $k_{inj} = 2.4 \times 10^7$ s⁻¹, which is comparable to that of TiO₂/Ru^II NPs (3.0×10^7 s⁻¹). All the lifetimes and kinetic rates of TiO₂/[Ru-pyr]²⁺ are in line with those of TiO₂/Ru^II NPs (**Table V-3**) since the pyrrole moieties do not interact with [Ru(bpy)₃]²⁺* centers as previously observed.

$$k_{inj} = \frac{1}{\tau_2} - \frac{1}{\tau_{Ru-pyr}}$$ (Eq V-4)

($\tau_2 = 40$ ns, $\tau_{Ru-pyr} = 670$ ns)
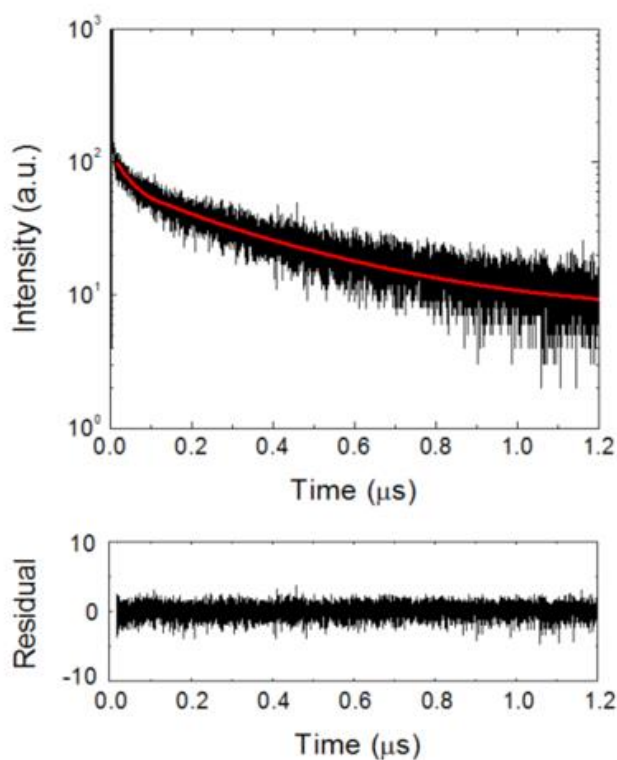
Figure V-7. Time-resolved emission decay of TiO₂/[Ru-pyr]²⁺* NPs in MeCN under Ar, excited at 400 nm by a picosecond pulse laser and recorded at 610 nm. Red line shows a biexponential fitting of the decay.

Table V-3. Summary of the photophysical properties of TiO₂/[Ru-pyr]²⁺ compared with [Ru-pyr]²⁺ and TiO₂/Ru^II

	¹MLCT λ_{abs} (nm)	λ_{em} (nm)	τ (ns)	k_{inj}, s⁻¹	k_q, s⁻¹
TiO₂/[Ru-pyr]²⁺	460[a]	625	365 ± 8 (14%)	2.4×10^7	1.2×10^6
			40 ± 1 (86%)		
[Ru-pyr]²⁺	460	621	670	-	-
TiO₂/Ru^II	450	627	366 ± 7 (12%)	3.0×10^7	1.6×10^6
			32 ± 0.6 (88%)		

V.4.   Polypyrrole nanocomposites

V.4.1.   Photopolymerization of TiO$_2$/[Ru-pyr]$^{2+}$ NPs in solution

TiO$_2$/[Ru-pyr]$^{2+}$ colloid (C = 1 g.L^{-1}) in air-saturated MeCN was irradiated at 450 nm during 2 hours for photo-induced polymerization of pyrrole moieties. The irradiation was achieved by a Xe lamp, a UV-hot bandpass (400-750 nm) filter coupled with a 450 nm bandpass filter. In these conditions, [Ru(bpy)$_3$]$^{2+}$-like PS is excited, then injects an electron to TiO$_2$ within 40 ns (see **Section V.3.4**). The resulting Ru^{3+} species are reduced by pyrrole units to regenerate Ru^{2+} state. Positively charged pyrrole units can initiate an oxidative polymerization of pyrrole, leading to a polypyrrole network wrapping around each NP and/or electronically connecting the particles together. The trapped electrons in TiO$_2$ are efficiently scavenged by O$_2$ as already reported in literature.[4,10] Finally a nanocomposite is formed, denoted as TiO$_2$/poly(Ru-pyr). **Scheme V-8** illustrates the photopolymerization process.

$$(1) \quad TiO_2/[Ru^{II}\text{-pyr}]^{2+} \quad \xrightarrow{h\nu} \quad TiO_2/[Ru^{II*}\text{-pyr}]^{2+}$$

$$(2) \quad TiO_2/[Ru^{II*}\text{-pyr}]^{2+} \quad \xrightarrow{k_{inj}} \quad (e^-)TiO_2/[Ru^{III}\text{-pyr}]^{3+}$$

$$(3) \quad (e^-)TiO_2/[Ru^{III}\text{-pyr}]^{3+} \quad \longrightarrow \quad (e^-)TiO_2/[Ru^{II}\text{-pyr}^+]^{3+}$$

$$(4) \quad (e^-)TiO_2/[Ru^{II}\text{-pyr}^+]^{3+} \quad + \quad O_2 \quad \longrightarrow \quad TiO_2/[Ru^{II}\text{-pyr}^+]^{3+} \quad + \quad O_2^{\bullet-}$$

$$(5) \quad n\ TiO_2/[Ru^{II}\text{-pyr}^+]^{3+} \quad \xrightarrow[-H^+]{\text{polymerization}} \quad TiO_2/poly[Ru^{II}\text{-pyr}]^{2+}$$
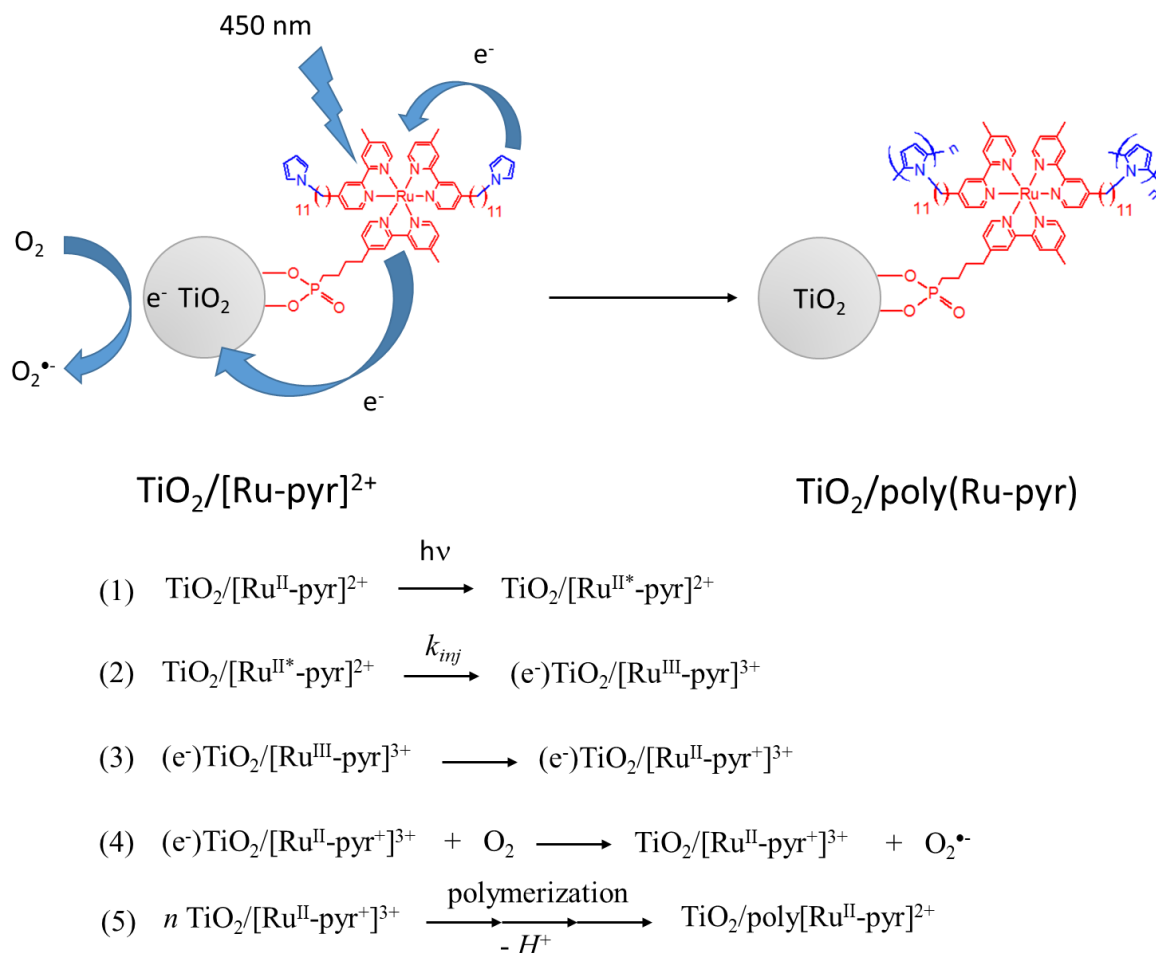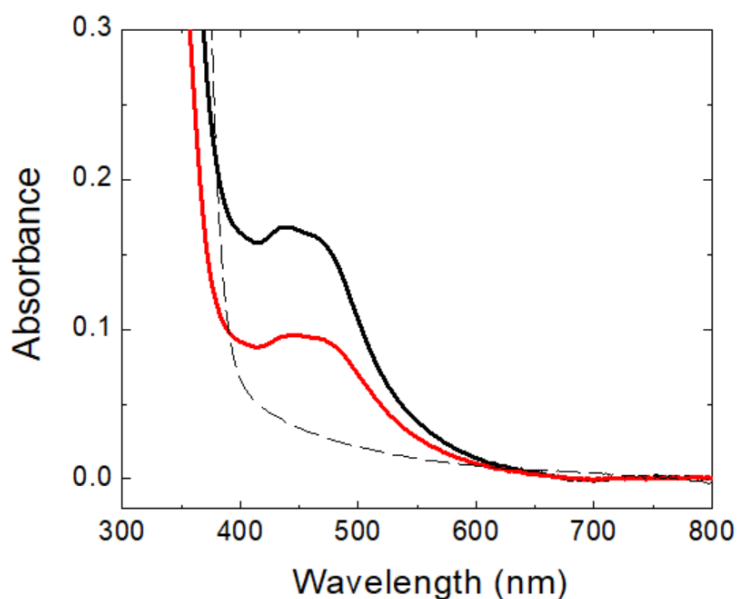
Scheme V-8. Schematic illustration of the photopolymerization process

### V.4.2. Photophysical properties

a) UV-vis absorption spectroscopy

Solid state UV-vis absorption spectra of TiO_2/[Ru-pyr]$^{2+}$ and TiO_2/poly(Ru-pyr) NPs have been studied for the samples before and after photopolymerization. The TiO_2/poly(Ru-pyr) NPs, after 2 hours of photopolymerization by 450 nm irradiation, were centrifuged and washed several times with acetone, dried under vacuum prior to the measurement. The spectra are shown in **Figure V-8**. The broad peak at 460 nm due to the ^{1}MLCT absorption band of [Ru(bpy)₃]$^{2+}$ unit remains unchanged in shape and position, indicating that the [Ru(bpy)₃]$^{2+}$ core PS is probably not significantly degraded. The LCCT absorption peak of the PS is not observable due to large absorption of TiO_2 NPs in the UV region.

Figure V-8. Solid state UV-vis absorption spectra of TiO_2/[Ru-pyr]$^{2+}$ (black line), TiO_2/poly(Ru-pyr) (red line) and naked TiO_2 NPs (dashed line)

b) Emission spectroscopy

The changes in emission spectrum of TiO_2/[Ru-pyr]$^{2+}$ during the photopolymerization process are shown in **Figure V-9**. After light excitation at 450 nm, all the samples after 0 h, 1 h and 2 h of irradiation exhibit a similarly broad signal indicative of [Ru(bpy)₃]$^{2+*}$ state. Emission intensity of the nanocomposite decreases by around 50 % after 1 hour and 60 % after 2 hours of photopolymerization. The emission maximum is slightly red-shifted from 625 nm to 631 nm after the two hours.
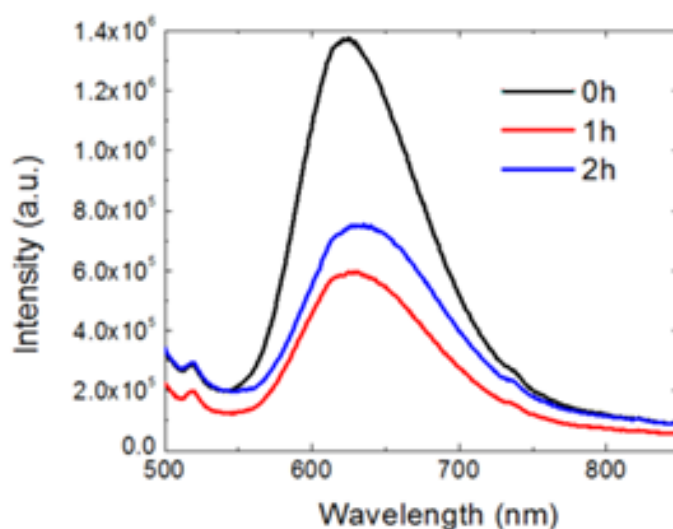
Figure V-9. Steady-state emission spectra of TiO₂/[Ru-pyr]²⁺ colloid (C = 0.05 g.L⁻¹) in MeCN after 0h, 1h and 2h irradiation at 450 nm (black, red and blue lines respectively). Signals were recorded under an Ar atmosphere.

### c) Time-resolved emission spectroscopy

Lifetimes of [Ru(bpy)₃]²⁺* state in the nanocomposite have also been recorded with a time-resolved emission spectrometer after 1 and 2 hours of photopolymerization. Following excitation at 400 nm, the samples show a decay at 610 nm which is fit with a biexponential function (**Figure V-10**). Similar to **Section V.3.4**, the shorter component of the decay is attributed to the photo-induced electron injection from Ru²⁺* to TiO₂, while the longer one is assigned to the energy transfer between close Ru²⁺* species on the surface. Using **Equations V-3** and **V-4**, one can estimate the rates of the two quenching pathways (**Table V-4**). As the irradiation time is increased, both rates are enhanced but the injection rate increases faster than the energy transfer rate (6 times compared with 3 times after 2 hours).

By assuming Forster resonance energy transfer (FRET) model and applying **Equations V-5, 6** and **7** (see **Section II.3.6** for more detail), the FRET efficiency and the average distance between Ru²⁺ species, r(Ru-Ru), on surface was estimated. In this calculation the orientational factor κ was assumed to be 2/3, which is generally accepted for a species in solution able to rotate freely. Before irradiation, the distance is about 2.0 nm, which is in accordance with the estimated loading of ~ 2 [Ru-pyr]²⁺ molecules per nm² of TiO₂ surface mentioned above. During the irradiation, the distance is gradually reduced. All the relevant photophysical properties of the nanocomposite are summarized in **Table V-4**.

$$Efficiency = \frac{R_0^6}{R_0^6 + r^6} = 1 - \frac{\tau_{DA}}{\tau_D} \qquad \text{(Eq V-5)}$$

$$R_0^6 = 8.8 \times 10^{17} \left(\kappa^2 n^{-4} \phi_D J \right) \qquad \text{(Eq V-6)}$$

$$J = \frac{\int F_D(\lambda)\varepsilon_A(\lambda)\lambda^4 d\lambda}{\int F_D(\lambda)d\lambda} \qquad \text{(Eq V-7)}$$
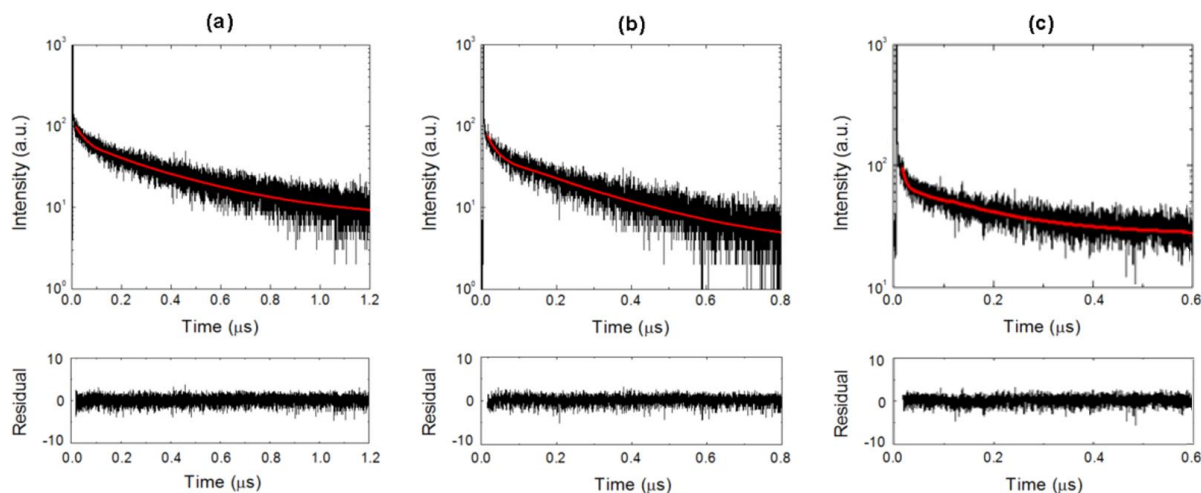
Figure V-10. Time-resolved emission decays of TiO₂/[Ru-pyr]²⁺* after (a) 0h, (b) 1h and (c) 2h irradiation at 450 nm. Red curves represent the biexponential fitting of the decays.

**Table V-4**. Summary of the photophysical properties of TiO₂/poly(Ru-pyr) after 0h, 1h and 2h irradiation at 450 nm

	λ_{em}, nm	τ, ns (%)	k_{inj}, s⁻¹	k_q, s⁻¹	FRET efficiency	r (Ru-Ru), nm
0 h	625	365 ± 8 (14 %) 40 ± 1 (86 %)	2.4×10^7	1.2×10^6	0.46	2.0
1 h	625	251 ± 6 (9 %) 21 ± 0.4 (91 %)	4.6×10^7	2.5×10^6	0.63	1.8
2 h	631	178 ± 6 (2 %) 7 ± 0.1 (98 %)	1.4×10^8	4.1×10^6	0.73	1.6

From the **Table V-4**, one can notice that the electron injection from Ru²⁺* to TiO₂ is enhanced in both kinetics and efficiency as the irradiation time is prolonged. After 2 hours of photopolymerization, the rate is increased by 6 times and efficiency reaches 98 %. Since the distance between [Ru-pyr]²⁺ and TiO₂ surface is fixed during the irradiation time and the electron injection follows a tunneling mechanism, this rate increase suggests a more conducting environment around the nanocomposite. Therefore the polypyrrole proves to be useful to ameliorate the conductivity.

In the meantime, the rate of energy transfer process is only increased by 3 times, thus making it two order of magnitude lower than the injection rate in the nanocomposite obtained

after 2 hours of irradiation. Applying the FRET model to this quenching pathway allows for the determination of FRET efficiency and average Ru-Ru distance. It is evident that the FRET efficiency rises and the distance declines during the time of irradiation. The observations can be due to the polypyrrole network pushing the $[Ru(bpy)_3]^{2+}$ molecules closer to each other, and/or connecting neighboring NPs in order to reduce this average distance. After the photopolymerization, the $[Ru(bpy)_3]^{2+}$ centers may also appear closer to TiO₂ surface as suggested by the increased k_{inj} values. Therefore, the photopolymerization may lead to the densification of the $[Ru(bpy)_3]^{2+}$ centers covering the TiO₂ NPs as illustrated in **Scheme V-9**.
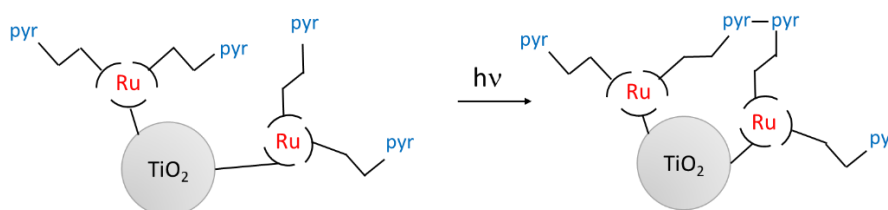
**Scheme V-9**. Illustration of the densification of $[Ru(bpy)_3]^{2+}$ centers on TiO₂ NPs following the photopolymerization process.

V.4.3.   Electron paramagnetic resonance spectroscopy

EPR spectroscopy coupled with an *in situ* LED irradiation may allow for the detection of photo-induced paramagnetic species in this nanocomposite. The spectrum of TiO₂/[Ru-pyr]²⁺ colloid in MeCN glass irradiated at 455 nm under O₂ has been recorded at cryogenic temperature and shown in **Figure V-11**. The presence of O₂ allows this experiment to be consistent with the photopolymerization study mentioned above, although at 20 K it is not expected to react with other species. For *g*-value calculations, 2,2-diphenyl-1-picrylhydrazyl (DPPH) ($g = 2.0036$) has been used as reference. Simulations of (e⁻)TiO₂ and conducting species in polypyrrole are also shown in red and blue lines respectively. The simulation of trapped electrons in anatase TiO₂ has been done according to published *g*-values: $g_{\perp} = 1.990$ and $g_{//} = 1.960$.[12] It should be noted that only the trapped electrons are observable by EPR spectroscopy, while CB electrons are EPR silent.[13] Similarly, the simulation of conducting species in polypyrrole chain (polarons) has been performed by $g = 2.0037$ (line width $\Delta H_{p-p} = 9$ G). It should be noted that this *g*-value is higher than those recorded by electrochemical or chemical synthesized polypyrrole films ($g \sim 2.0025$).[14,15]

Comparing the signal and the simulations, we suggest the formation of a charge separated state (e⁻)TiO₂/Ru^{II}-pyr$^{•+}$. Under He atmosphere and at such a low temperature, there is no oxidative quencher for the electrons in TiO₂, thus they are trapped at defect sites on TiO₂ surface and detectable by EPR. The resulting $[Ru(bpy)_3]^{3+}$ species is probably undetectable

due to its broad EPR signal (see **Section II.3.7**). However, a radical is detected for pyrrole which suggests an efficient reduction of Ru^{3+} by pyrrole moieties even at 20 K. EPR line width ΔH_{p-p} has been shown to decline with temperature for an electrochemically synthesized film, staying at less than 0.15 G at 100 K.[14] In this case the large line broadening value (ΔH_{p-p} = 9 G) suggests a decrease in polaron mobility due to polypyrrole immobilization.[15]
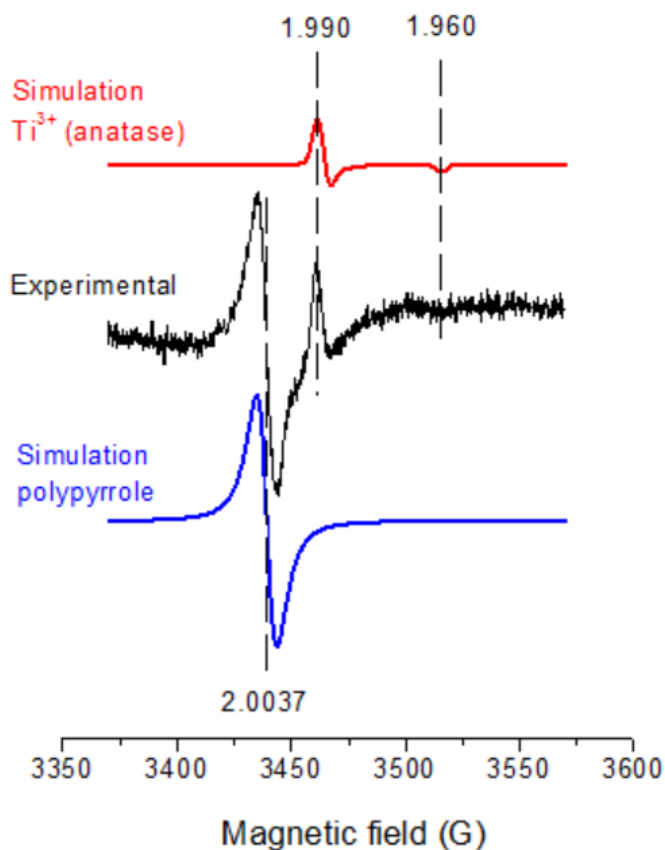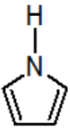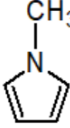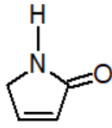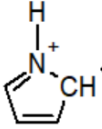

Figure V-11. EPR signal of the photo-induced polymerization of TiO₂/[Ru-pyr]²⁺ colloid (6 g.L⁻¹) in MeCN glass (black line), together with the simulation of trapped electrons on Ti³⁺ sites of anatase TiO₂ (red line) and the simulation of polypyrrole (blue line). The sample was irradiated *in situ* by a 455 nm LED from the cavity window. The spectrum was accumulated for 1 hour at 20 K with an X-band EPR spectrometer (f = 9.6532 GHz, 0.2 mW, 5 G modulation)

In order to get more insight into the isotropic g value of 2.0037, DFT calculations have been conducted by Dr. Jean-Marie Mouesca (INAC/SyMMES) using the SAOP (Statistical Average of Orbital Potentials) exchange-correlation potential.[16] First, as in our system there is a long alkyl chain attached to the nitrogen atom of pyrrole, we performed g-value calculations for pyrrole and pyrrole-CH₃ radical cations (**Table V-5**) to study the effect of the electron-donating methyl group. To simplify the task, we only examined monomer, dimer and trimer radical cations. The calculated g-values are presented in **Table V-6**. In both pyrrole and pyrrole-CH₃ cases, the g-values of all the cations slightly increase as the polymer chain propagates. In literature, an electrochemically synthesized polypyrrole film also exhibits a

slight increase in the *g*-value when the synthesis time is prolonged.[17] Nevertheless, the differences between pyrrole and pyrrole-CH₃ cations are insignificant. It can be concluded that the introduction of the methylene group has negligible effects on the isotropic *g*-values of the cations.

Table V-5. Chemical structures of monomer, dimer and trimer radical cations of pyrrole, pyrrole-CH₃ and pyrrole=O species

	Pyrrole	**Pyrrole-CH₃**	**Pyrrole=O**
Monomer cation			
Dimer cation			
Trimer cation			
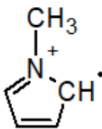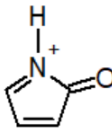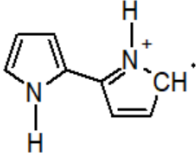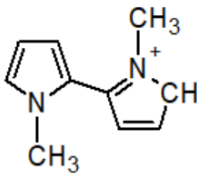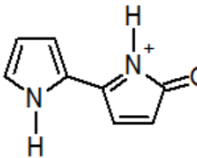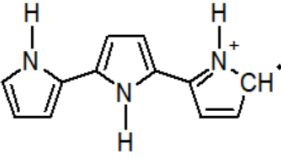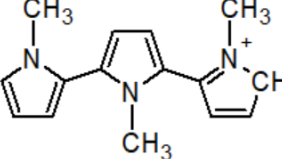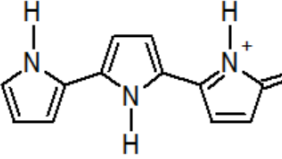
Table V-6. *g*-values of monomer, dimer and trimer radical cations of pyrrole calculated with DFT
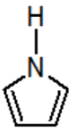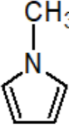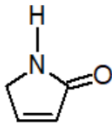
***g*-value**			
Monomer cation	2.00242	2.00239	2.01124
Dimer cation	2.00254	2.00251	2.00399
Trimer cation	2.00257	2.00251	2.00294

Since these *g*-values of pyrrole and pyrrole-CH₃ cations cannot explain the experimental *g* = 2.0037, we attempted to investigate the pyrrole=O species (**Table V-5**). This species is a side product between oxygen and corresponding radical cations[17] (**Scheme V-10**). As the

methylene group has almost no effects on the *g*-values of the cations, we chose the pyrrole=O molecule without the methylene group to study in order to reduce the calculation complication. Interesting, the *g*-value of the dimer cation of this species (2.00399, **Table V-6**) is very close to the experimental value. The result suggests that the EPR line centered at *g* = 2.0037 may be due to the formation of the pyrrole=O dimer as a side product.
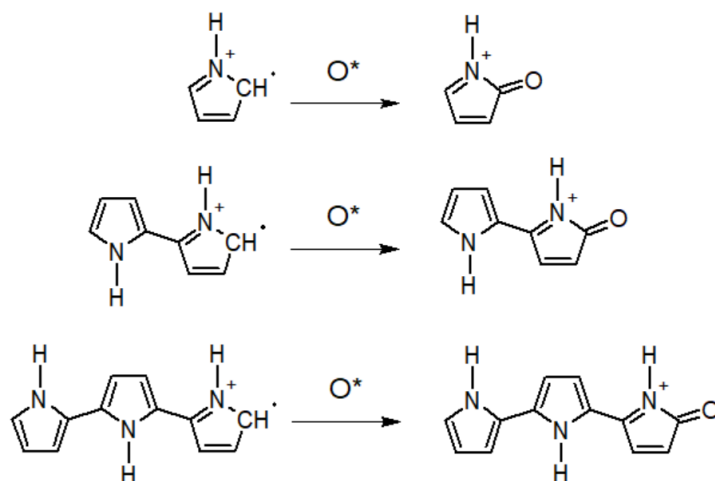
Scheme V-10. Formation of pyrrole=O cations

V.4.4. Dynamic light scattering

In collaboration with Dr. Denis Roux (Laboratoire Rhéologie et Procédés, UGA), we employed dynamic light scattering (DLS) technique to study size evolution of TiO₂/poly(Ru-pyr) nanocomposite during the photopolymerization process. Hydrodynamic diameter, which consists of the particle diameter and its electrical double layer, can be estimated with the DLS technique. Since the overall charges are only localized on [Ru(bpy)₃]²⁺ units and expected to be unchanged during the photopolymerization process, the associated electrical double layer thickness should be unchanged as well. Therefore, the changes in the hydrodynamic diameter is related to the changes in the NPs size. The hydrodynamic diameter *d(H)* can be estimated from the translational diffusion coefficient *D* using the Stokes-Einstein equation:

$$d(H) = \frac{kT}{3\pi\eta D}$$
(Eq V-8)

where *k* is the Boltzmann's constant, *T* the absolute temperature and η the solvent viscosity (0.341 mPa.s for MeCN at RT)[18]. The diffusion coefficient *D* can be calculated from the correlation function *g(τ)*. For a monodisperse colloid this correlation function is given by:

$$g(\tau) = A\left[1 + B\exp\left(-2\Gamma\tau\right)\right]$$
(Eq V-9)

$$\Gamma = Dq^2 \qquad\qquad \text{(Eq V-10)}$$

$$q = \left(\frac{4\pi n}{\lambda_0}\right)\sin\left(\frac{\phi}{2}\right) \qquad\qquad \text{(Eq V-11)}$$

where *A* and *B* are constants in the monoexponential model, *n* the refractive index of dispersant, λ_0 the laser wavelength used in the DLS measurement and θ the scattering angle.

The DLS measurements have been conducted at 23 ^{0}C in MeCN solution for samples before and after 1 or 2 hours of photopolymerization. Their correlograms are shown **Figure V-12**. All the signals are well fit with a monoexponential function indicating monodisperse colloids. The hydrodynamic diameter is thus determined to be 354 nm, 537 nm and 437 nm for the colloids after 0, 1 and 2 hours of irradiation, respectively. The result corresponds to a 50 % increase in size after 1 hour and 25 % increase in size after 2 hours of irradiation compared to the initial size. It is expected that the size of NPs also undergoes a similar change as the hydrodynamic diameter. Such large increases are expected to be significantly higher than the experimental uncertainties. It is a bit surprising that the average size of the NPs increases during the first hour of irradiation and decreases after. In any cases, the result suggests that pyrrole polymerization may mainly occur between the [Ru-pyr]²⁺ species on the same particle rather than connecting the particles together, since in the latter case the diameter should be increased much more significantly.
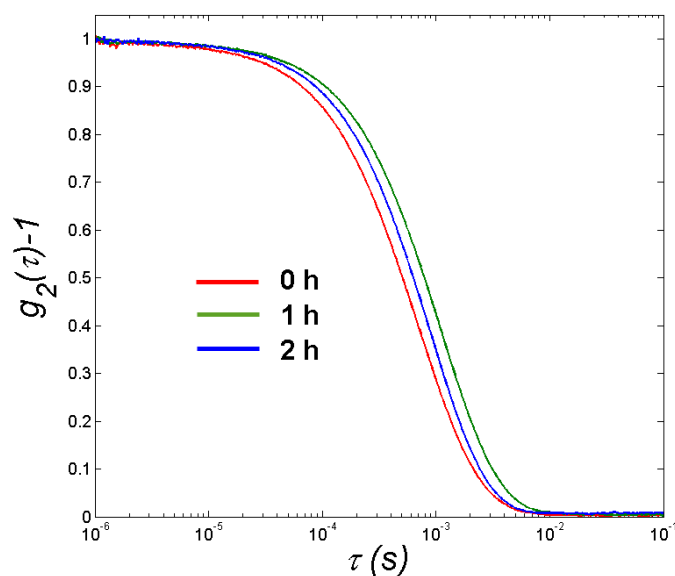
Figure V-12. DLS correlograms of TiO₂/poly(Ru-pyr) colloids in MeCN after 0 h (red), 1h (green) and 2 h (blue) of photopolymerization.

V.4.5. X-ray photoelectron spectroscopy

X-ray photoelectron spectroscopy (XPS) is a surface sensitive technique which allows for qualitative and quantitative determination of elemental compositions on the surface. In principle it can detect all the elements with $Z = 3$ (Li) and above. The chemical state of an element, which depends on its oxidation state and its bonding with surrounding atoms, can be distinguished by change in binding energy.

In collaboration with Dr. Anass Benayad (LITEN, CEA-Grenoble), we have conducted a comparative XPS study for TiO$_2$/Ru^{II}, TiO$_2$/[Ru-pyr]$^{2+}$ and TiO$_2$/poly(Ru-pyr) NPs. The main purpose was to record any changes in N, Ru and P peaks before and after the photopolymerization and to quantitatively determine the atomic concentration of the elements of interest. TiO$_2$/Ru^{II} was used as reference to monitor spectral changes associated with the incorporation of the pyrrole function. Spectral calibration was based on the Ti2p$_{3/2}$ peak at 457.9 eV, as this peak of TiO$_2$ support remains unchanged for all the samples.

Firstly, XPS survey spectra have been recorded for the three samples (**Figure V-13**). The presences of Ti, O, N, C, and P elements are clearly observed. The Ru3d signal appears at the binding energy very close to that of C1s signal. Other elements are not detected.
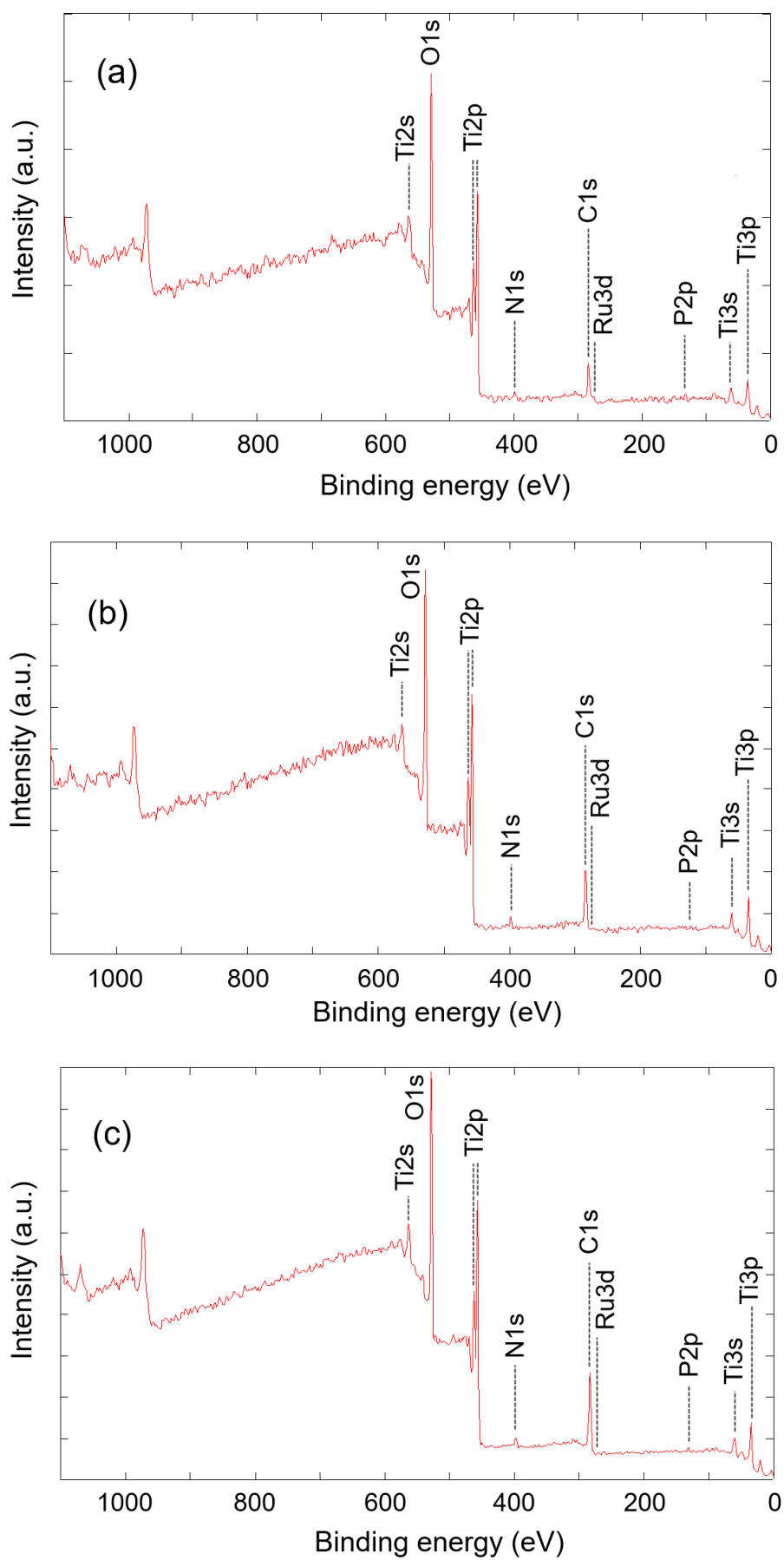
Figure V-13. XPS survey spectra of (a) TiO₂/Ru^{II}, (b) TiO₂/[Ru-pyr]²⁺ and (c) TiO₂/poly(Ru-pyr) NPs

High resolution XPS characterizations are then focused on the regions corresponding to the elements of interest. The $Ti2p_{3/2}$ and $Ti2p_{1/2}$ XPS core level spectra of the three samples are shown in **Figure V-14**. They are well fit by two Gaussian lines which peaked at 457.9 and 463.7 eV corresponding to the 3/2 and 1/2 states, respectively.[19] The peaks are ascribed to Ti^{4+} atoms in TiO_2 molecules on the particle surface. The similar peak position and FWHM show that Ti^{4+} is unchanged after the photopolymerization.
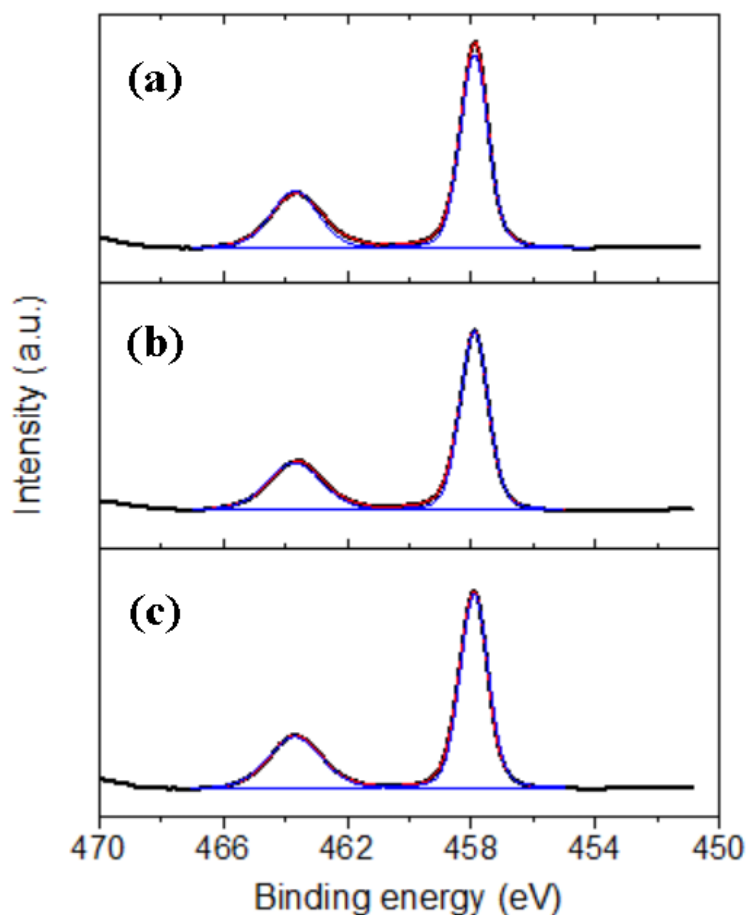
Figure V-14. Ti2p XPS core level spectra of (a) TiO_2/Ru^{II}, (b) $TiO_2/[Ru-pyr]^{2+}$ and (c) $TiO_2/poly(Ru-pyr)$. The red lines represent the fitting obtained by the sum of the Gaussian peaks in blue lines

Figure V-15 presents the Ru3d and C1s spectra of the three samples. The Ru3d spectra are fit with two Gaussian lines which peak at 280.7 eV and 284.8 eV corresponding to the 5/2 and 3/2 states, respectively.[19] The part of the $Ru3d_{3/2}$ spectrum that overlaps with the C1s spectrum has been subtracted prior to C1s peak fitting. The C1s spectra are not symmetric, which are then decomposed into three Gaussian lines at around 284.4 eV, 285.7 eV and 287.5 eV. The three component lines are assigned to C1s core signal in C-C, C-N and contaminated C=O/COO bonds, respectively. They remain almost unchanged in both peak position and FWHM during the photopolymerization.

In an XPS study of polypyrrole, Joo et al.[14] have also shown that the C1s core level signal could be decomposed into three Gaussian lines. The line due to C-N linkages appeared at the binding energy higher than the line due to C-C linkages. The line at the highest binding energy was characterized by a vastly greater FWHM compared to the other two lines due to C-C and C-N linkages. It was attributed to disorders in the polypyrrole chains such as interchain connections and chain terminations. In our study, the line at ~ 287.5 eV remains almost similar in all three samples and its FWHM is comparable to the other peaks, it is not expected to be a consequence of the polymer chain disorders since the amount of the disorders should increase with respect to the irradiation time. Therefore, we attribute this line to the contaminated –C=O/COO containing species on the particle surface.
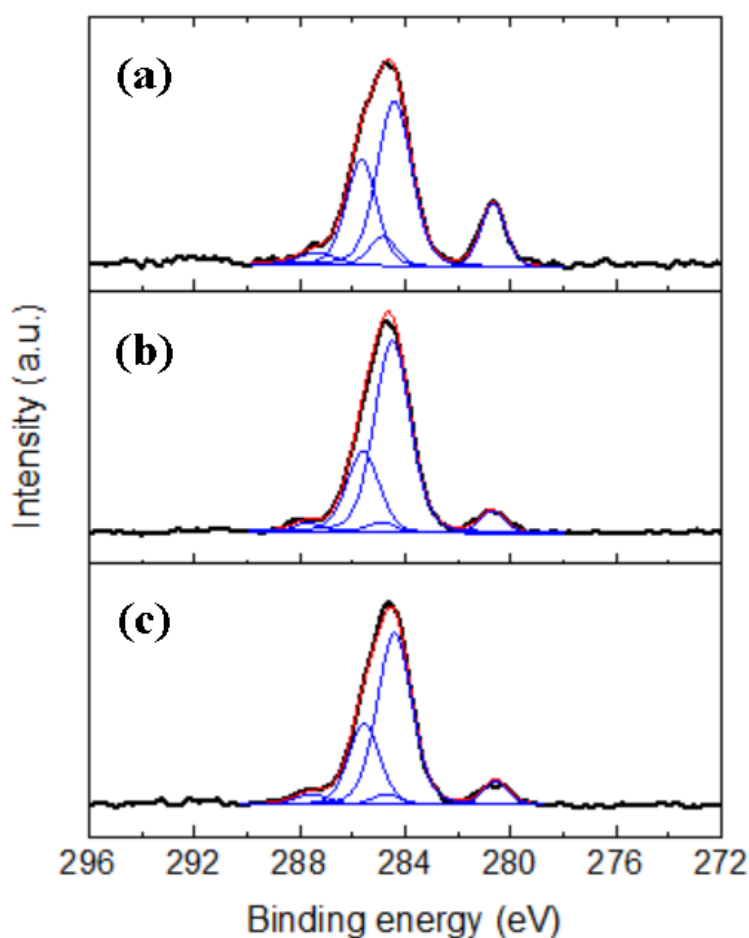
Figure V-15. C1s and Ru3d (5/2 and 3/2) XPS core level spectra of (a) TiO₂/Ru^{II}, (b) TiO₂/[Ru-pyr]²⁺ and (c) TiO₂/poly(Ru-pyr). The red lines represent the fitting obtained by the sum of the Gaussian peaks in blue lines

Figure V-16 presents the N1s XPS spectra of the three samples. In TiO₂/Ru^{II}, the spectrum is clearly fit with one Gaussian line peaked at 399.8 eV and FWHM = 1.62 eV. It is reasonably assigned to the =N- group in bpy ligands as they are all alike. The peak is in accordance with literature concerning the N atoms in bpy ligands being coordinated with Rh(I) metal center.[20] Deconvoluting the N1s spectra of TiO₂/[Ru-pyr]²⁺ and TiO₂/poly(Ru-

pyr) while keeping the 399.8 eV peak fixed gives rise to another line at 398.8 eV (FWHM = 1.53 eV). The new peak is ascribed to the uncoordinated N(R$_3$) pyrrolic group. After photopolymerization, no new Gaussian lines can be detected but the atomic concentration ratio of N(pyrrole) / N(bpy) increases from 0.9 to 1.3. It is probably due to the formation of a polypyrrole layer covering the surface while the bpy groups seem to be buried inside and thus exhibiting a less intense XPS signal. An overall consideration for the changes in atomic concentration will be discussed below (see **Figure V-19**).
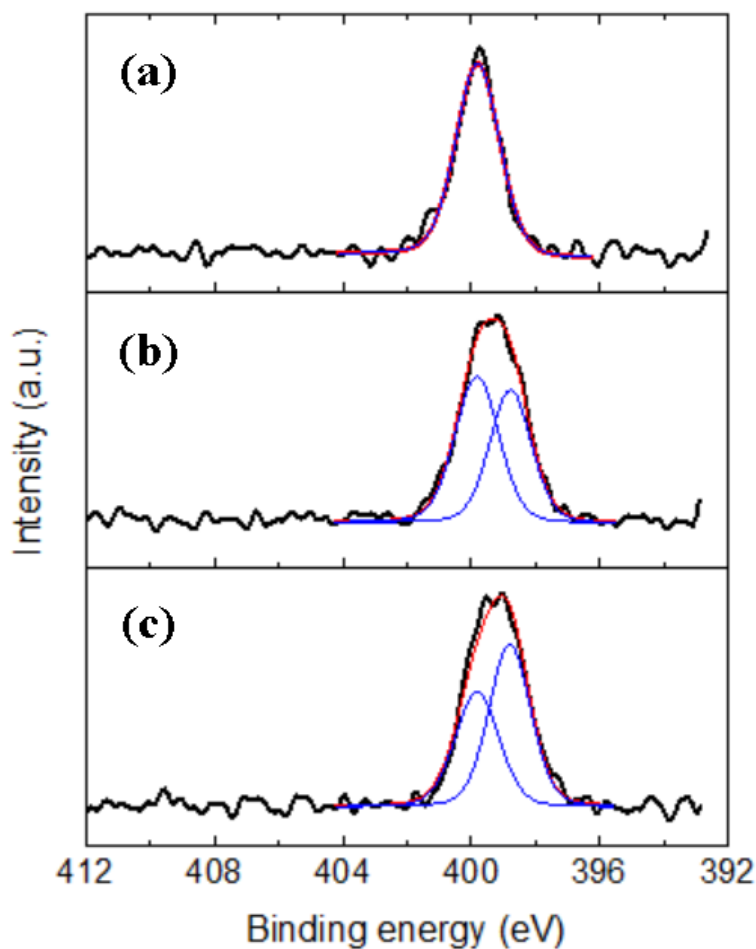
Figure V-16. N1s XPS core level spectra of (a) TiO$_2$/Ru^{II}, (b) TiO$_2$/[Ru-pyr]$^{2+}$ and (c) TiO$_2$/poly(Ru-pyr). The red lines represent the fitting obtained by the sum of the Gaussian peaks in blue lines

The P2p XPS spectra of the three samples are shown in **Figure V-17**. The spectrum of TiO$_2$/Ru^{II} is deconvoluted into two lines which peak at 132.4 eV and 133.3 eV, which are assigned to the P2p$_{3/2}$ and P2p$_{1/2}$ states, respectively. Introduction of the pyrrole moieties has minor influence on the peak positions (132.2 and 133.1 eV) while the FWHM remains the same. The peak position and FWHM of both P2p$_{3/2}$ and P2p$_{1/2}$ states are unchanged during the photopolymerization. It is hence concluded that the phosphonate anchoring groups are unaffected by the photopolymerization.

Figure V-17. P2p XPS core level spectra of (a) TiO_2/Ru^{II}, (b) $TiO_2/[Ru-pyr]^{2+}$ and (c) $TiO_2/poly(Ru-pyr)$. The red lines represent the fitting obtained by the sum of the Gaussian peaks in blue lines

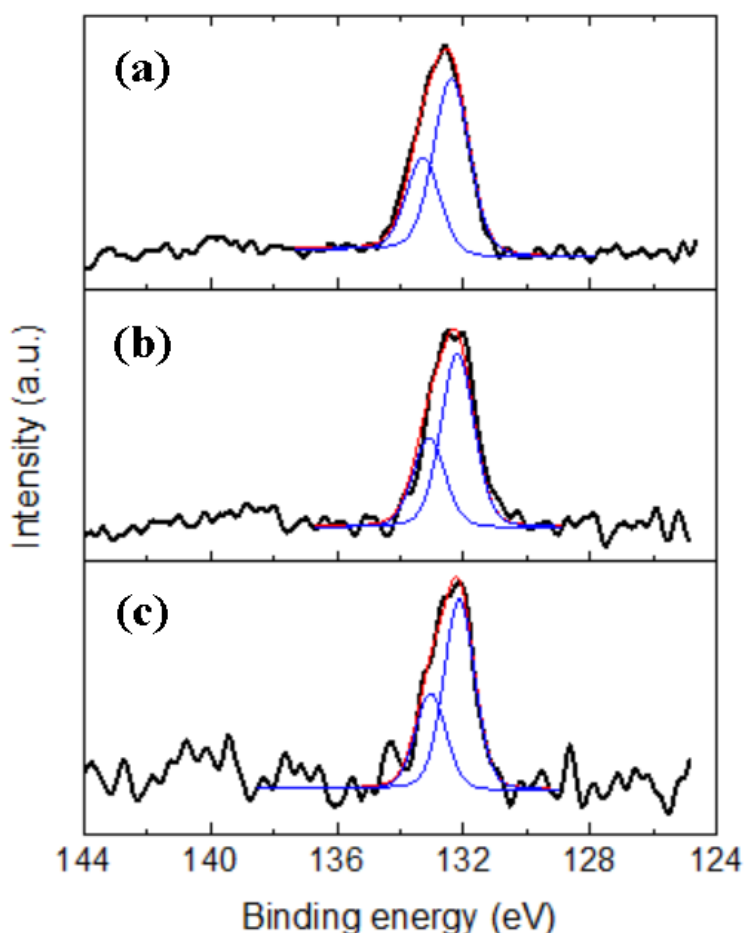**Figure V-18** shows the O1s XPS spectra of the three samples. The spectrum of TiO_2/Ru^{II} can be decomposed into three Gaussian lines which peak at 529.1 eV, 530.3 eV and 531.6 eV. The most intense line at the lowest binding energy is assigned to O^{2-} anions in TiO_2 molecules, while the one at 530.3 eV can be attributed to the oxygen atoms in phosphonate groups. The line at highest binding energy shows a very small contribution to the O1s signal and could be ascribed to hydroxyl groups on the TiO_2 particle surface.[21] $TiO_2/[Ru-pyr]^{2+}$ spectrum displays the same Gaussian lines after deconvolution. However, after photopolymerization only two lines at lower binding energies remain. The disappearance of the sub-oxides is explained by the coating polypyrrole network on the particle surface.
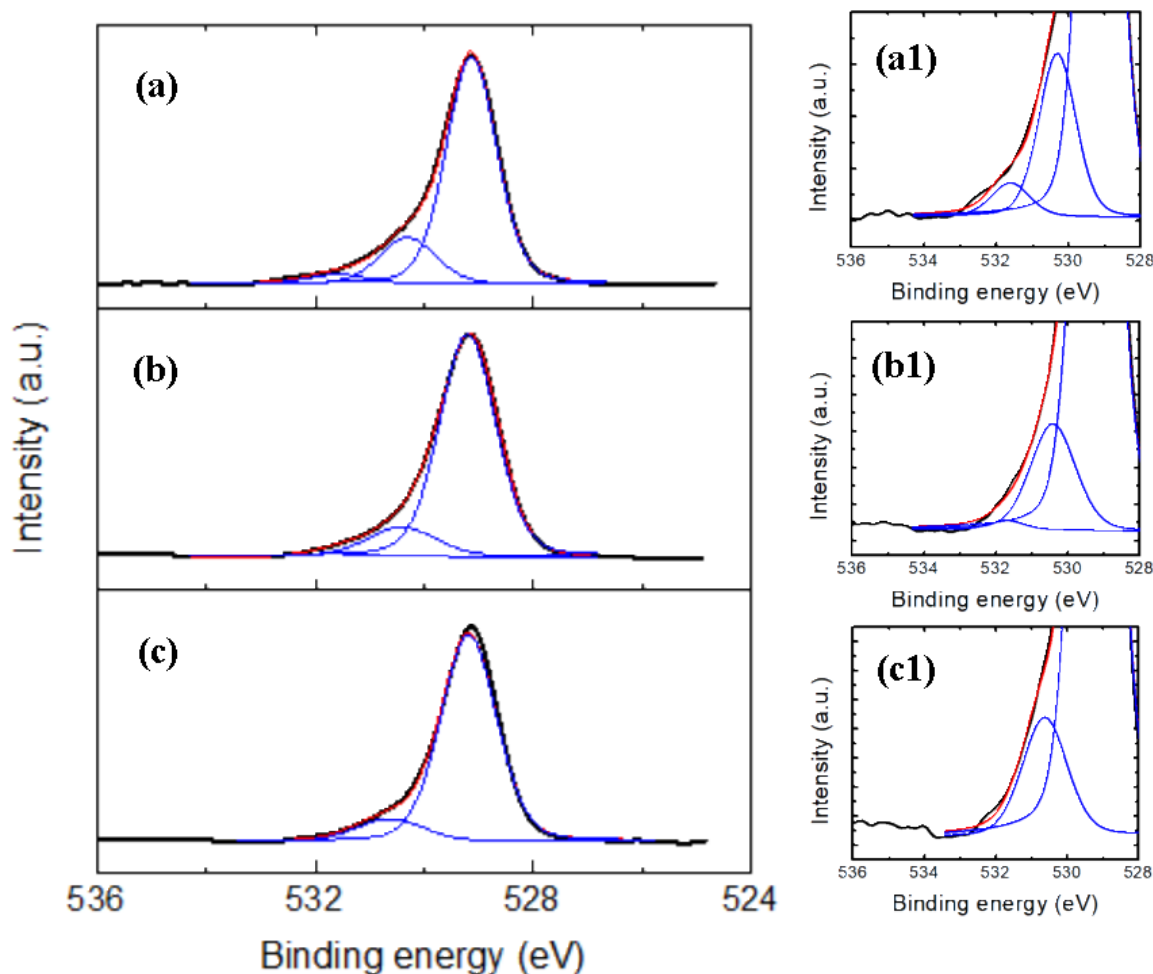
Figure V-18. O1s XPS core level spectra of (a) TiO$_2$/Ru^{II}, (b) TiO$_2$/[Ru-pyr]$^{2+}$ and (c) TiO$_2$/poly(Ru-pyr). *Right column*: (a1), (b1) and (c1) are zoom-in spectra in the 534 – 528 eV range of the spectra (a), (b) and (c), respectively. The red lines represent the fitting obtained by the sum of the Gaussian peaks in blue lines

Quantification of percentage atomic concentrations was achieved by integrating the areas under corresponding XPS peaks and correcting the areas with relative sensitivity factors. The result for relevant elements is shown in **Figure V-19**. Firstly, it is noted that the Ru and P contents remain the same after photopolymerization (0.2 % and 0.9 % respectively), indicating the PS is stable in the experimental conditions. Ti content is also kept unchanged at ~ 19 %. Slight decreases in contents of N (bpy) from 1.6 % to 1.2 % and C (C-N) from 8.0 % to 6.4 % may suggest a small degree of decoordination of the bpy ligands and/or a buried photosensitizer inside polypyrrole. The decoordination of the bpy ligands from [Ru(bpy)$_3$]$^{2+}$ has been known to occur under prolonged irradiation time.[22] However, taken into account the small growth in N (pyrrole) from 1.4 % to 1.6 % while the shape of Ru3d spectra is the same, the buried PS inside the polymer chains is probably the main reason for the declines in N (bpy) and C(C-C) contents during the photopolymerization.
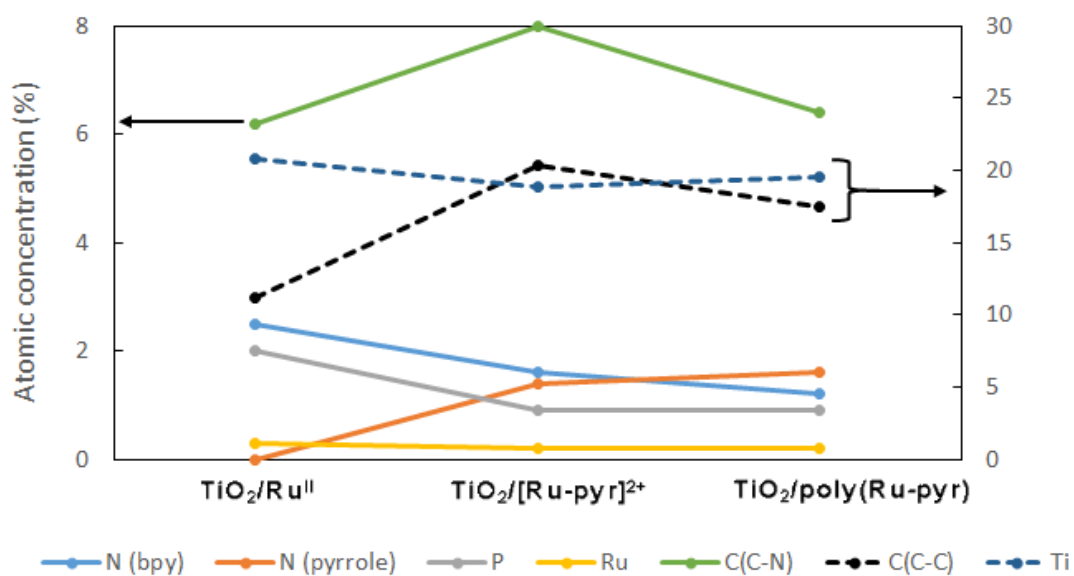
Figure V-19. Atomic concentration of the elements in TiO$_2$/Ru^{II}, TiO$_2$/[Ru-pyr]$^{2+}$ and TiO$_2$/poly(Ru-pyr) NPs. Solid lines are associated with the left y-axis while dashed lines are linked to the right y-axis. Error = ± 0.1 %

V.5. TiO$_2$/Ru^{II}-pyrrole nanocomposite immobilized on FTO electrode

V.5.1 Electrode fabrication methods
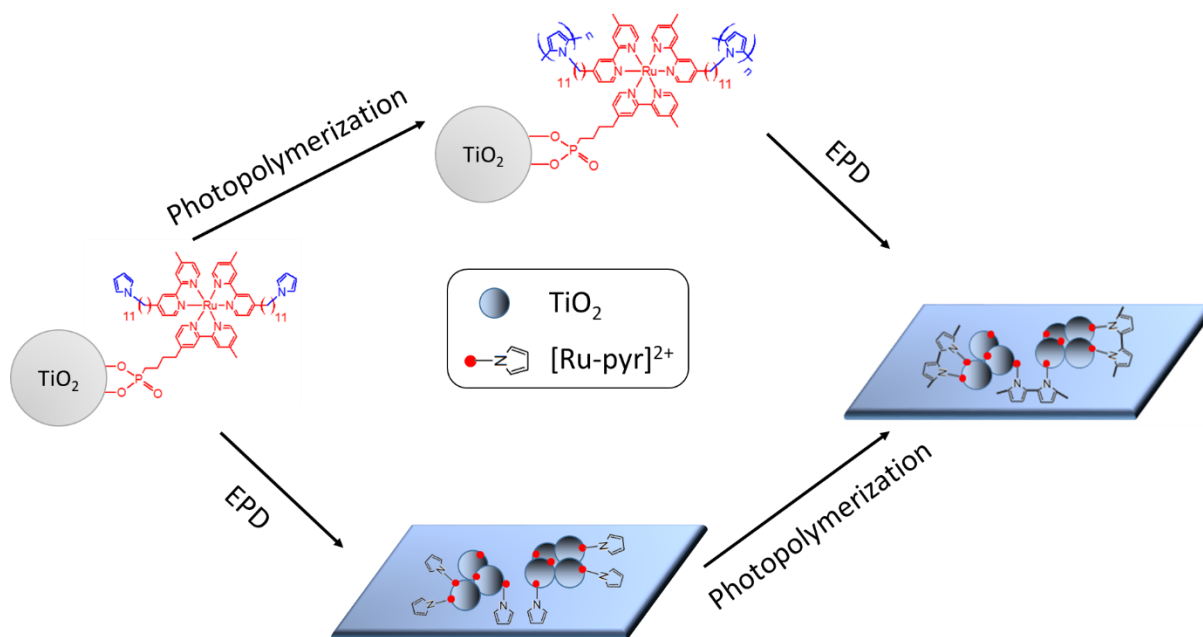
Deposition of TiO$_2$/poly(Ru-pyr) nanocomposite on FTO-coated glass substrate (herein called FTO electrode) has been realized by electrophoretic deposition (EPD) technique. It is achieved by applying a bias between the cathode and anode immersed in a solution of charged particles in a polar solvent. Under the bias the positively charged particles migrate to the cathode while negatively charged ones are drifted to the anode. The method has found various applications in depositing charged particles onto a conducting substrate[23] or metal organic framework (MOF) thin films[24] for electronic component fabrication or surface coating. The deposition process can be conveniently controlled and reproducible by manipulating the electric field between the electrodes, the colloid concentration and the time of deposition.[23] In this study we found this method suitable for our positively charged nanoparticles / nanocomposites which could be coated on the cathode. Acetonitrile was chosen as solvent due to its rather large electrochemical active window, which makes it chemically inert in the presence of strong oxidants or reductants such as [Ru(bpy)$_3$]$^{2+*}$, ppyr^{n+} and (e$^-$)TiO$_2$ species. Moreover, the solvent should not have too high or too low dielectric constant to favor the EPD process.[23] The solvent should also be sufficiently polar to well suspend the NPs. The deposition was performed under Ar to avoid any undesired side reactions.

To prepare the TiO$_2$/poly(Ru-pyr) nanocomposite-coated FTO electrode, we employed two strategies which are named after the sequential steps for a comparative study:

(i) *Photo-EPD strategy*: TiO$_2$/[Ru-pyr]$^{2+}$ precursor was suspended in air-saturated MeCN solution (C = 0.75 g.L^{-1}) and irradiated at 450 nm during 2 hours. The photopolymerization lead to TiO$_2$/poly(Ru-pyr) nanocomposite. Afterwards it was transferred to an Ar-saturated MeCN solution (C = 0.3 g.L^{-1}) where a potential of 120 V was applied between two FTO electrodes placed 0.5 cm apart in 1 hour for the EPD. This EPD bias is equivalent to an electric field of 24×10^3 V.m^{-1}.

(ii) *EPD-Photo strategy*: TiO$_2$/[Ru-pyr]$^{2+}$ precursor was first deposited on a FTO electrode by EPD ($E_{applied}$ = 24×10^3 V/m) in 1 hour. All the parameters and deposition conditions were kept the same as in the *Photo-EPD strategy*. The electrode was then washed and immersed into an air-saturated MeCN solution. Surface photopolymerization was achieved by irradiating the electrode at 450 nm. After certain irradiation time intervals the electrode was transferred to an electrochemical cell containing MeCN + 0.1 M TBAPF$_6$ in order to characterize the photopolymerization process by cyclic voltammetry.

The two strategies are schematically depicted in **Scheme V-11**. The characterization of the photopolymerization of TiO₂/poly(Ru-pyr) nanocomposite has been thoroughly discussed in **Section V.4**. This section focuses on the photopolymerization on FTO/TiO₂/[Ru-pyr]²⁺ surface following the *EPD-Photo* strategy. Comparative studies for the two strategies will also be mentioned in terms of the film characterization and their application as photoanode under visible irradiation.

Scheme V-11. Schematic illustration of *Photo-EPD* strategy and *EPD-Photo* strategy. The graph is not to scale.

V.5.2   Photopolymerization of TiO₂/[Ru-pyr]²⁺ nanocomposite on electrode

Before studying the photopolymerization on the FTO/TiO₂/[Ru-pyr]²⁺ electrode, we attempted the electropolymerization in 0.1 M TBAPF₆ in MeCN solution. **Figure V-20** presents the CVs during multiple oxidative cycles of TiO₂/[Ru-pyr]²⁺ NPs deposited on FTO electrode by EPD (denoted as FTO/TiO₂/[Ru-pyr]²⁺). The wave at ~ 0.9 V, which is assigned to the oxidation of Ru^{II} and pyrrole, is not completely reversible ($I_{pa}/I_{pc} \gg 1$). It is similar to the [Ru-pyr]²⁺ complex without phosphonic groups in solution (see Section V.2.2). If the electropolymerization occurred on the FTO/TiO₂/[Ru-pyr]²⁺ modified electrode, we would expect the emergence of a new oxidative peak around 0.5 V corresponding to the polypyrrole moieties,[25] and an increase in the peak intensity due to higher conductivity. The CVs in **Figure V-20** do not exhibit the typical signals for the electropolymerization process of pyrrole on electrode. In contrast, the electrochemical responses become less intense upon iterative scanning showing the passivation of the electrode. TiO₂ NPs are not conductive enough to allow for the efficient charge transfer and electropolymerization of the pyrrole units on the electrode. This experiment emphasizes the interest of a photochemical approach.
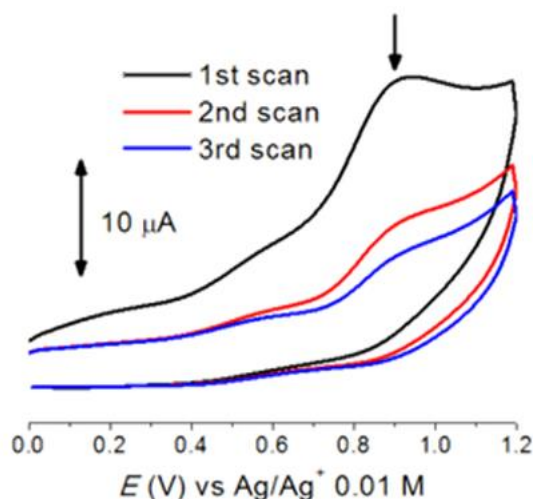
Figure V-20. CVs of FTO/TiO$_2$/[Ru-pyr]$^{2+}$ electrode recorded in MeCN + 0.1 M TBAPF$_6$ under Ar.

The FTO/TiO$_2$/[Ru-pyr]$^{2+}$ modified electrode was therefore subjected to a photopolymerization experiment. It was irradiated at 450 nm in an air-saturated MeCN solution. After certain irradiation time, it was transferred to another electrochemical cell containing 0.1 M TBAPF$_6$ electrolyte in MeCN to record CVs (**Figure V-21**). After 3 minutes of irradiation, the oxidation peak at ~ 0.9 V due to Ru^{III}/Ru^{II} and pyrrole monomers already decreases in intensity, suggesting the consumption of pyrrole monomers. The emergence of a new oxidative peak at 0.43 V is ascribable to polypyrrole oxidation, which is in accordance with literature.[25] Increasing the irradiation time shows almost no changes in the CVs.
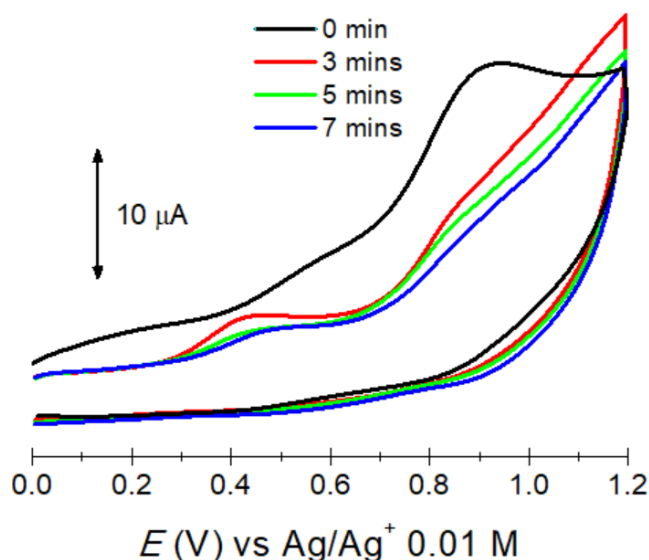
Figure V-21. CV of a FTO/TiO$_2$/[Ru-pyr]$^{2+}$ electrode under 450 nm irradiation, recorded in MeCN + 0.1 M TBAPF$_6$. Irradiation was performed with a Xe lamp + UV filter + 450-nm bandpass filter. Light power was estimated to be 0.2 W.cm^{-2}.

The UV-vis-NIR spectrum of FTO/TiO$_2$/poly(Ru-pyr) surface is shown in **Figure V-22**. The absorption of FTO substrate has been subtracted. The broad peak at 420 nm, assigned to

the [1]MLCT absorption band of [Ru(bpy)$_3$]$^{2+}$, is blue shifted compared to the initial TiO$_2$/[Ru-pyr]$^{2+}$ NPs (460 nm). The LCCT peak in the UV region cannot be observed due to intense absorption of TiO$_2$ NPs and FTO surface. A very broad band centered at around 1100 nm indicates the formation of polypyrrole.[15]
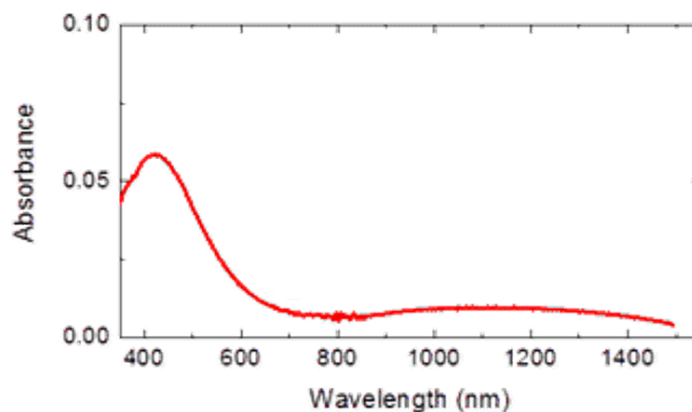
Figure V-22. UV-vis-NIR absorption spectrum of FTO/TiO$_2$/poly(Ru-pyr) modified electrode after photopolymerization. Absorption of FTO bare electrode has been subtracted.

V.5.3   X-ray photoelectron spectroscopy of FTO/TiO$_2$/poly(Ru-pyr) electrode

In collaboration with Dr. Anass Benayad (LITEN/CEA Grenoble), we have conducted XPS experiments for the nanocomposite TiO$_2$/poly(Ru-pyr) and the electrode FTO/TiO$_2$/poly(Ru-pyr) to study the effect of EPD process on the nanocomposite, especially the [Ru(bpy)$_3$]$^{2+}$-based PS and polypyrrole. The electrode has been fabricated following the *Photo-EPD* method. First, a survey spectrum of this electrode is shown in **Figure V-23**. It was calibrated by the Ti2p$_{3/2}$ peak at 457.9 eV as for the previous XPS study of the photopolymerization in solution (see **Section V.4.5**). The presences of Ti, O, N, C, and P elements are clearly observed as in the TiO$_2$/poly(Ru-pyr) sample. Besides these elements, Sn is also present due to the FTO substrate. The intensities of Sn and O signals are significantly higher than Ti signal, suggesting the SnO$_2$ is the principal component. Since the XPS technique is only sensitive to a few nm below the surface, this result indicates that the surface is not completely covered by the nanocomposite.
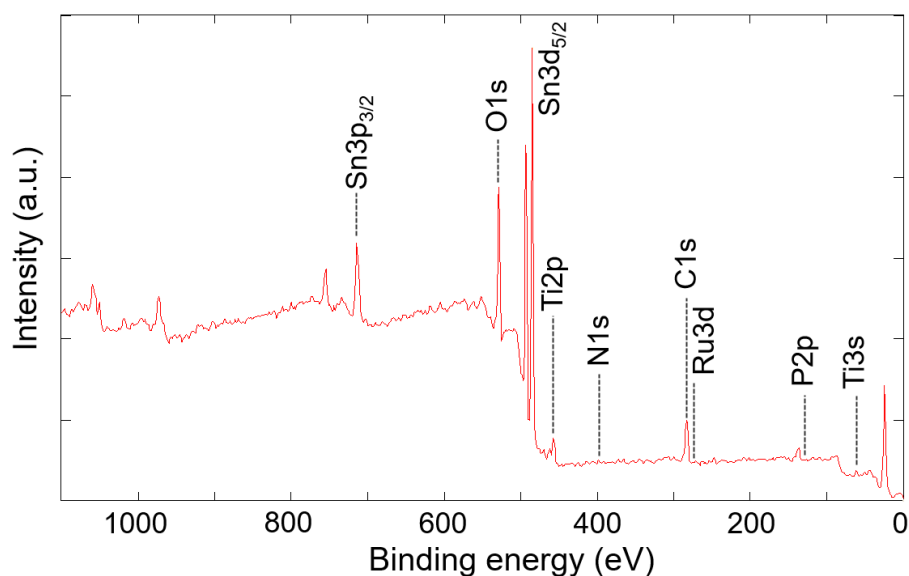
Figure V-23. XPS survey spectrum of FTO/TiO₂/poly(Ru-pyr) electrode fabricated with the *Photo-EPD* method

High resolution XPS characterizations are then focused on the regions corresponding to the elements of interest. **Figure V-24** presents their Ti2p spectra. They are well fit with two Gaussian lines which peak at 457.9 eV and 463.7 eV. The lines are assigned to Ti2p$_{3/2}$ and Ti2p$_{1/2}$ states,[19] respectively, of surface Ti^{4+} ions. Similar peak position and shape for the two samples shows that Ti^{4+} remains intact after the EPD process.
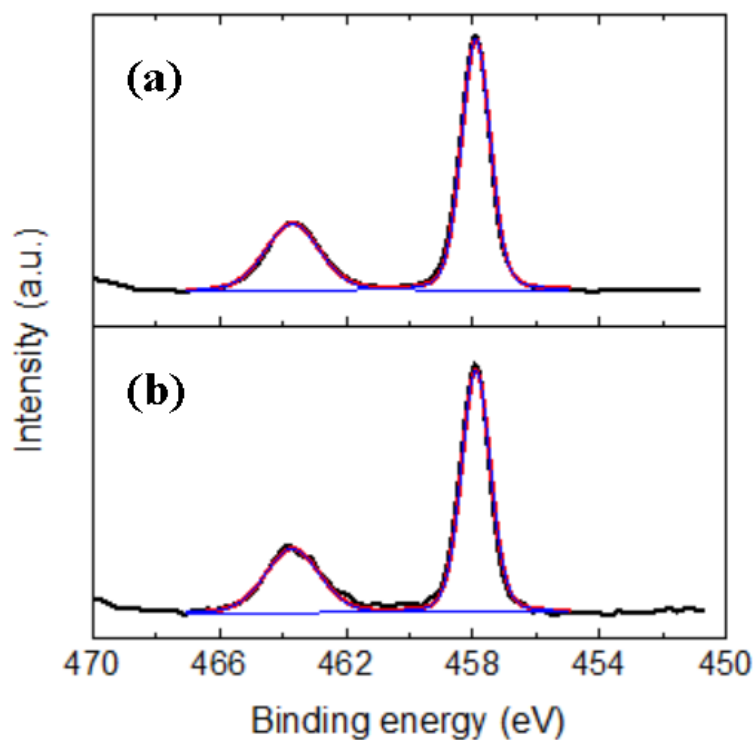
Figure V-24. Ti2p XPS core level spectra of (a) TiO₂/poly(Ru-pyr) and (b) FTO/TiO₂/poly(Ru-pyr). The red lines represent the fitting obtained by the sum of the Gaussian peaks in blue lines

Figure V-25 presents the C1s and Ru3d XPS spectra of the nanocomposite and the film. The Ru3d peak of FTO/TiO$_2$/poly(Ru-pyr) can be deconvoluted into two Gaussian lines which peak at 280.1 eV and 284.3 eV. They are ascribed to the Ru3d$_{5/2}$ and Ru3d$_{3/2}$ states, respectively.[19] Both peak positions are shifted ~ 0.5 eV to lower binding energies compared to the Ru3d$_{5/2}$ and Ru3d$_{3/2}$ peaks of TiO$_2$/poly(Ru-pyr) NPs (280.7 and 284.8 eV). The line shape remains unchanged, indicating the coordination sphere of [Ru(bpy)$_3$]$^{2+}$ is conserved after the EPD process. The part of Ru3d$_{3/2}$ state at 284.3 eV that overlaps with the C1s signal has been subtracted before the deconvolution of the C1s peak. The C1s peak is then decomposed into three Gaussian lines at 284.2 eV, 285.6 eV and 287.5 eV, which are similar to the TiO$_2$/poly(Ru-pyr) nanocomposite. The three lines are thus assigned to C-C, C-N and COO bonds. The strong increase in COO species may stem from impurities on the FTO substrate.
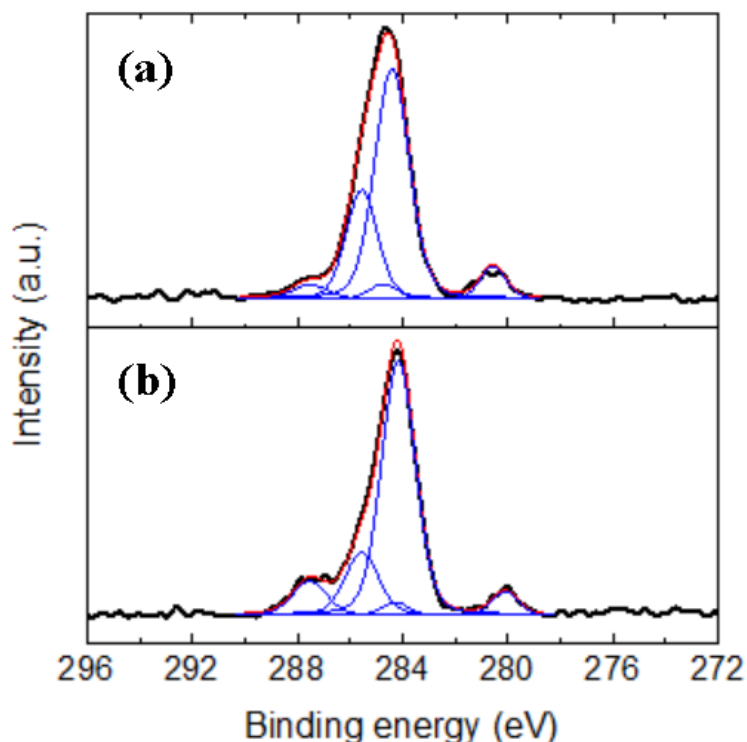
Figure V-25. C1s and Ru3d (5/2 and 3/2) XPS core level spectra of (a) TiO$_2$/poly(Ru-pyr) and (b) FTO/TiO$_2$/poly(Ru-pyr). The red lines represent the fitting obtained by the sum of the Gaussian peaks in blue lines

The N1s XPS spectra of both samples are shown in **Figure V-26**. Deconvolution of the N1s peak of FTO/TiO$_2$/poly(Ru-pyr) while keeping the peaks at 399.8 eV and 398.8 eV fixed gives rise to another peak at 397.3 eV with relatively small contribution in the signal magnitude. It could be due to impurities on the FTO surface. Similar to TiO$_2$/poly(Ru-pyr)

spectrum, the former two peaks are assigned to coordinated nitrogen atoms in bpy ligands and uncoordinated nitrogen in polypyrrole.
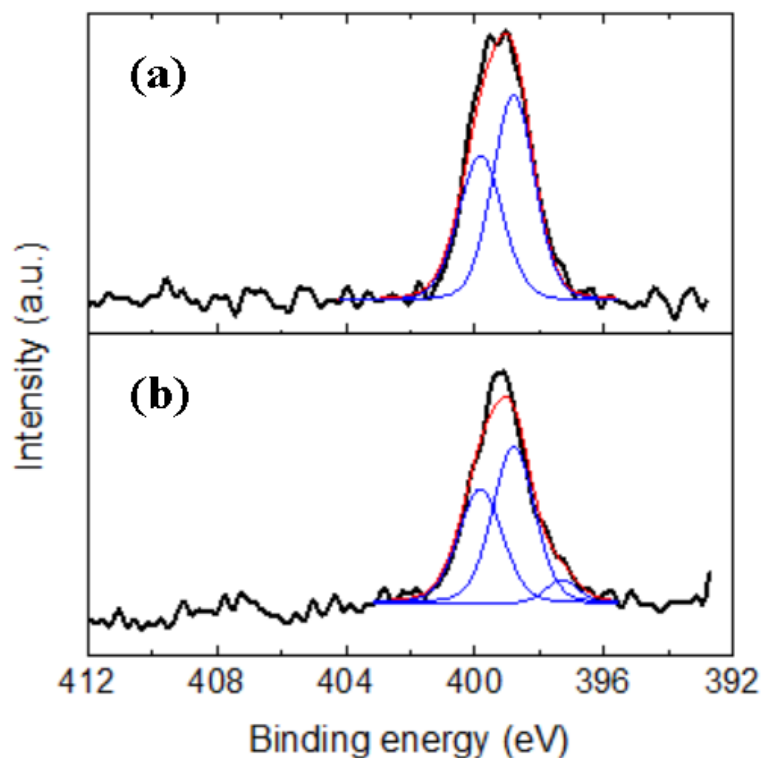
Figure V-26. N1s XPS core level spectra of (a) TiO₂/poly(Ru-pyr) and (b) FTO/TiO₂/poly(Ru-pyr). The red lines represent the fitting obtained by the sum of the Gaussian peaks in blue lines

Figure V-27 displays the O1s XPS spectra of the two samples. On FTO/TiO₂/poly(Ru-pyr) the O1s is evidently more asymmetric on the higher binding energy side. The spectrum is decomposed into three lines at 529.4 eV, 530.4 eV and 531.7 eV. Meanwhile the spectrum of TiO₂/poly(Ru-pyr) can only be deconvoluted into two lines at 529.2 eV and 530.6 eV, which are ascribed to O^{2-} in TiO_2 and O atoms in phosphonate group, respectively. Hence for the film, the two lines at lower binding energies is probably contributed by not only O^{2-} (TiO_2) and O (phosphonate) but also O^{2-} (SnO_2) which cannot be distinguished from the formers.
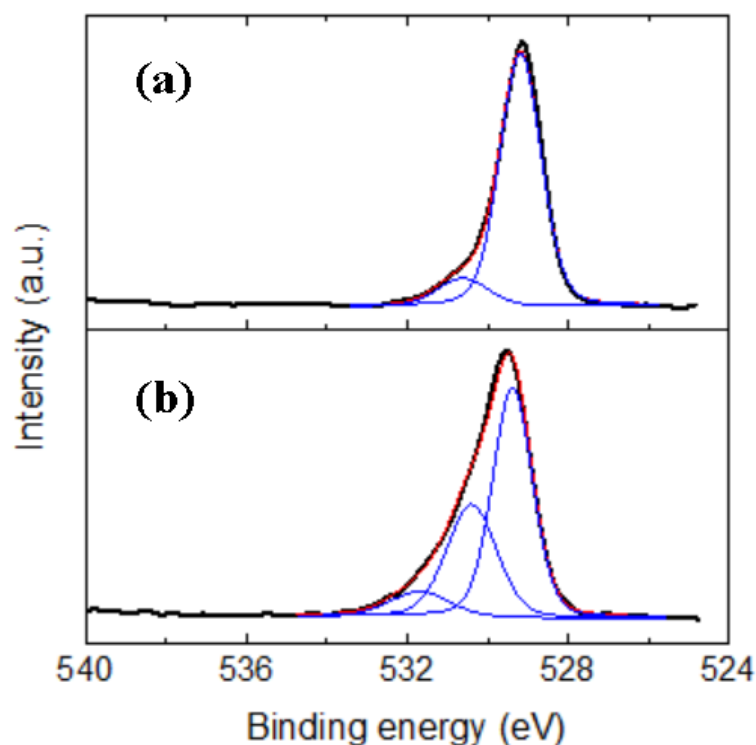
Figure V-27. O1s XPS core level spectra of (a) TiO$_2$/poly(Ru-pyr) and (b) FTO/TiO$_2$/poly(Ru-pyr). The red lines represent the fitting obtained by the sum of the Gaussian peaks in blue lines

Quantitative determination of percentage atomic concentration of some elements in TiO$_2$/poly(Ru-pyr) NPs and FTO/TiO$_2$/poly(Ru-pyr) thin film is collected in **Table V-7**. After the EPD of the nanocomposite onto FTO, Ru, N (bpy), N (pyrrole) and C (C-N bonds) contents remain almost the same while those of Ti and P markedly decrease. Since the XPS technique is highly surface sensitive to only a few nm depth while primary TiO$_2$ NPs are ~ 25 nm in diameter, the result suggests that TiO$_2$, together with the phosphonic anchoring group, may be buried inside the polypyrrole network. The increase in C (C-C bonds) content, which is present in the C$_{11}$ chain linking [Ru(bpy)$_3$]$^{2+}$ PS and pyrrole moiety, supports this explanation. Moreover, the EPD technique does not lead to the degradation of the complex despite a high applied electric field (2.4×10^3 V.m^{-1}) during 1 hour of the deposition process.

Table V-7. Atomic concentration of some elements in TiO$_2$/poly(Ru-pyr) NPs and FTO/TiO$_2$/poly(Ru-pyr) electrode. Error = ± 0.1 %

Atomic concentration (%)	N(bpy)	N(pyr)	P	Ru	C(C-C)	C(C-N)	Ti
TiO$_2$/poly(Ru-pyr)	1.2	1.6	0.9	0.2	17.5	6.4	19.6
FTO/ TiO$_2$/poly(Ru-pyr)	1.1	1.7	0.5	0.2	23.9	6.2	4.9

V.5.4   Scanning Electron Microscopy and Atomic Force Microscopy

In collaboration with Dr. Christine Lancelon-Pin (CERMAV, UPR CNRS 5301), we employed Scanning Electron Microscopy (SEM) to characterize the FTO/TiO₂/poly(Ru-pyr) electrode surfaces. Both electrodes made by the *Photo-EPD* method (**Figure V-28**) and *EPD-Photo* method (**Figure V-29**) were studied for comparison. Micrographs taken from a large scale (**Figures a**) show aggregates with several micrometers in diameter in both surfaces. *EPD-Photo* electrode shows additional much smaller particles surrounding the big aggregates. It should be noted that these small particles are also present on the *Photo-EPD* electrode but their amount is drastically reduced. In both electrodes, only a part of the FTO electrode is covered by the nanocomposite. This observation is in agreement with the XPS survey spectrum of FTO/TiO₂/poly(Ru-pyr) electrode which shows a significant signal of Sn^{4+} cations.

In a smaller scale (**Figures b**) on an aggregate, individual particles can be observed with diameter around 50-60 nm. Switching to CBS detector for probing the chemical contrast (**Figures c**) in the same area, we clearly observed a non-homogeneous distribution of white dots on the dark aggregate surface. The white dots are attributed to Ru^{2+} species as they are the heaviest element. The dark surface is assigned to Ti^{4+} ions while a slightly bright background is due to Sn^{4+} of the FTO support. Thanks to the chemical contrast mode, the small particles observed on both electrodes are identified as TiO₂ and not polypyrrole NPs.
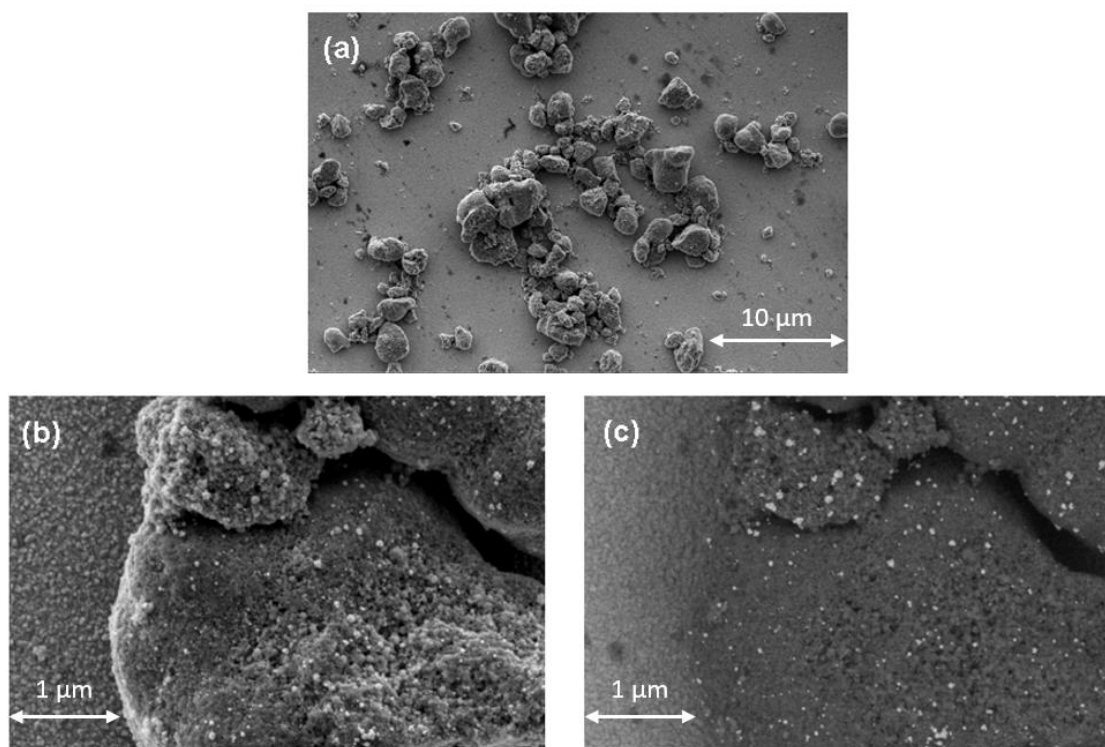
Figure V-28. SEM micrographs of FTO/TiO$_2$/poly(Ru-pyr) electrode prepared by the *Photo-EPD strategy*. (a) and (b) Topography of the surface recorded by an ETD detector. (c) Chemical contrast recorded by a CBS detector.
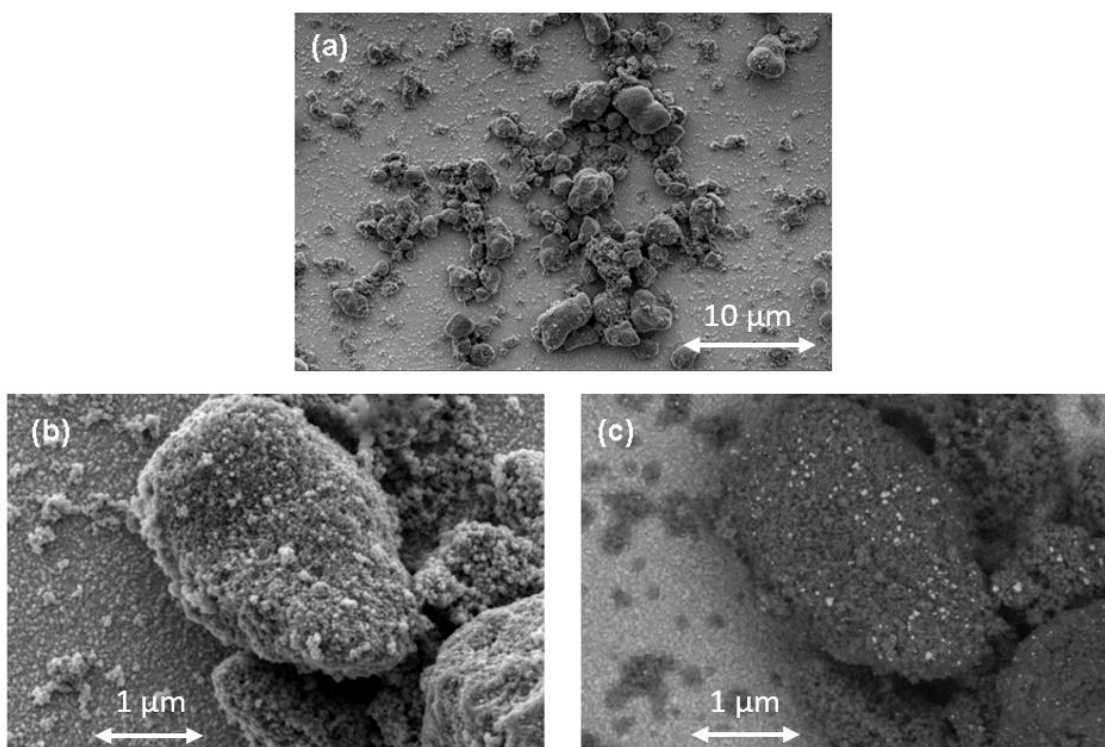
Figure V-29. SEM micrographs of FTO/TiO$_2$/poly(Ru-pyr) electrode prepared by the *EPD-Photo strategy*. (a) and (b) Topography of the surface recorded by an ETD detector. (c) Chemical contrast recorded by a CBS detector.

We also performed Atomic Force Microscopy (AFM) experiments to study the surface morphology at smaller scale (Collaborator: Mr. Hugues Bonnet, DCM). The two FTO/TiO$_2$/poly(Ru-pyr) electrodes made by the *Photo-EPD* and *EPD-Photo* methods are compared with the FTO/TiO$_2$/Ru^{II} electrode which has been made by the EPD of TiO$_2$/Ru^{II} NPs on FTO using the same protocol and parameters as for the nanocomposite electrodes. **Figure V-30** shows the AFM images of the electrodes.
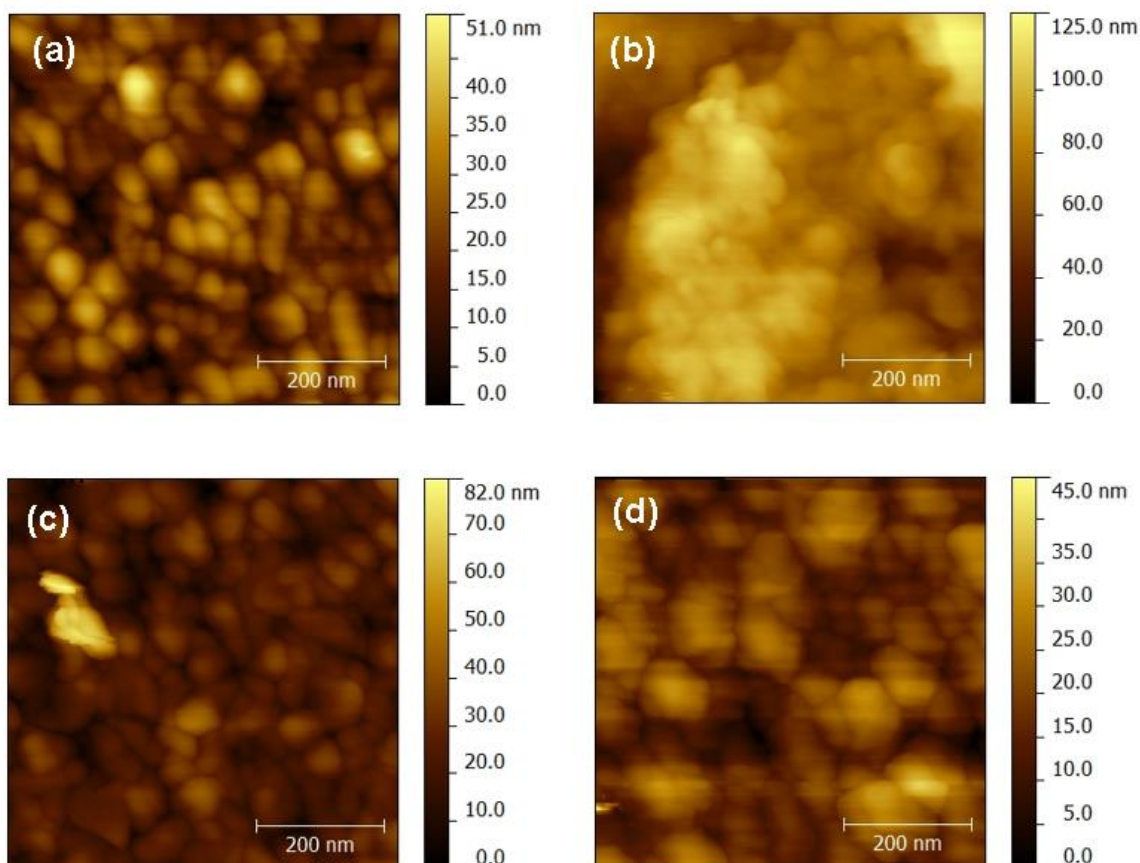
Figure V-30. AFM micrographs of (a) blank FTO, (b) FTO/TiO$_2$/Ru^{II}, (c) FTO/TiO$_2$/poly(Ru-pyr) prepared by the *Photo-EPD strategy*, and (d) FTO/TiO$_2$/poly(Ru-pyr) prepared by the *EPD-Photo strategy*. Surface RMS roughness are 7.4, 19, 8.8 and 5.5 nm, respectively.

In the absence of polypyrrole, the FTO/TiO$_2$/Ru^{II} electrode shows a very rough surface with large aggregates (**Figure V-30b**), where its root-mean-square (RMS) roughness strikingly increases from 7.4 nm for blank FTO (**Figure V-30a**) to 19 nm. In the presence of polypyrrole, both FTO/TiO$_2$/poly(Ru-pyr) electrodes made by the *Photo-EPD* and *EPD-Photo* methods exhibit RMS roughness comparable to the blank FTO (8.8 and 5.5 nm for the *Photo-EPD* electrode and *EPD-Photo* electrode, respectively). The *EPD-Photo* electrode also shows relatively uniform aggregates with diameter of ~ 100 nm and a more homogeneous surface than the *Photo-EPD* one. Therefore, the polypyrrole is proved to allow for better nanostructuration of the NPs as evidenced by smaller, more homogeneously distributed

aggregates. Such a nanostructuration effect of polypyrrole has been reported in literature for a polypyrrole network surrounding MoS_x NPs.[6]

V.5.5   Photocurrent generation

The FTO/nanocomposite electrodes fabricated by the *Photo-EPD* and *EPD-Photo* methods were employed as photoanode for light-to-electricity energy conversion. In order to study the role of polypyrrole film, we also deposit TiO_2/Ru^{II} NPs on FTO electrode using the same EPD protocol and parameters. For such energy conversion application, the modified electrode is dipped in MeCN solution in the presence of TEOA as a sacrificial electron donor, and a bias of 0.12 V is applied between this electrode and the counter electrode. Under visible irradiation, the $[Ru(bpy)_3]^{2+}$ PS unit is excited and injects an electron to the CB of TiO_2. The long lifetime of the charge-separated state $(e^-)TiO_2/Ru^{3+}$ prevents the charge recombination, allowing for this electron to be efficiently collected at the electrode under the applied bias. Afterwards, TEOA sacrificial agent reduces $[Ru(bpy)_3]^{3+}$ species to $[Ru(bpy)_3]^{2+}$ and the photon absorption – electron injection continues to yield a net anodic current. **Figure V-31** schematically summarizes this charge transfer mechanism.

Figure V-31. Electron transfer mechanism for the photocurrent generation using $FTO/TiO_2/Ru^{II}$ or $FTO/TiO_2/poly(Ru^{II}-pyr)$ electrodes under visible irradiation. CB and VB are conduction band and valence band of TiO_2, respectively

The photocurrent generation of the electrodes is presented in **Figure V-32a**. Both FTO/TiO₂/poly(Ru-pyr) electrodes show significantly enhanced photocurrents (*Photo-EPD*: 10.5 µA.cm⁻², *EPD-Photo*: 7.2 µA.cm⁻²) compared with FTO/TiO₂/Ru^II electrode (5.5 µA.cm⁻²). The result proves the importance of using conducting polypyrrole layer for this light-to-electricity energy conversion application. It is noted that the *Photo-EPD* strategy allows for a photocurrent 30 % greater than the *EPD-Photo* strategy.

Photocurrent stability has also been investigated under prolonged visible irradiation (**Figure V-32b**). After 16 minutes, the electrode fabricated by the *Photo-EPD* method shows ~ 60 % decrease in current magnitude, while that fabricated by the *EPD-Photo* method exhibits only 40 % decrease. The latter case is similar to the case of FTO/TiO₂/Ru^{II} electrode. Therefore, the *Photo-EPD* fabricated electrode allows for greater but less stable photocurrent than the *EPD-Photo* fabricated one. As the *Photo-EPD* method induces a less homogeneous surface, the aggregates may be desorbed more easily than the *EPD-Photo* electrode during the irradiation time.
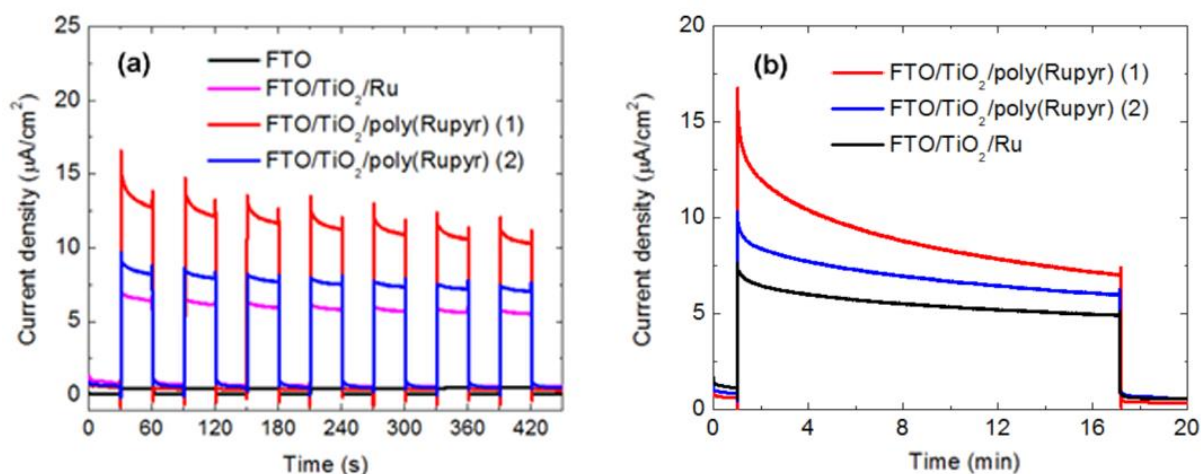
Figure V-32. (a) Photocurrent generation and (b) photocurrent stability of various electrodes. Experiments were conducted in MeCN + 0.1 M TBAPF₆ solution under visible irradiation, in the presence of 15 mM TEOA as sacrificial electron donor. $E_{applied}$ = 0.12 V vs Ag/Ag⁺ 0.01 M. Light power was estimated as 1.3 W.cm⁻². The notions (1) and (2) represent the *Photo-EPD strategy* and *EPD-Photo strategy* respectively.

V.6. Conclusion

The complex $[Ru\text{-}pyr]^{2+}$ where a $[Ru(bpy)_3]^{2+}$ PS is covalently linked to two pyrrole units has been systematically characterized in solution for its electrochemical and photophysical properties. The complex can be electropolymerized onto an ITO electrode.

Immobilization of the complex on TiO₂ NPs with phosphonic anchoring group has been achieved via a stepwise approach. First, bpy-PO₃H₂ ligand was allowed to chemically adsorbed on TiO₂, before surface complexation between TiO₂/bpy NPs and $[Ru(bpy\text{-}pyr)_2Cl_2]$ was conducted. The resulting hybrid system, called $TiO_2/[Ru\text{-}pyr]^{2+}$, has also been characterized by electrochemical and photophysical methods. Under visible irradiation the $[Ru(bpy)_3]^{2+}$ PS is excited and injects electrons to the CB of TiO₂ with the rate of 2.4×10^7 s^{-1}, which is comparable to the system without pyrrole function, i.e. TiO_2/Ru^{II}.

In air-saturated MeCN solution, the $TiO_2/[Ru\text{-}pyr]^{2+}$ hybrid NPs shows its ability to photopolymerize the pyrrole units under visible irradiation. The nanocomposite exhibits faster electron injection to TiO₂ and energy transfer between grafted neighboring Ru^{II*} species than $TiO_2/[Ru\text{-}pyr]^{2+}$ NPs. XPS spectroscopy reveals that the PS conserves its coordination sphere after the polymerization and a polypyrrole film covers the particle surface.

Film of TiO₂/poly(Ru-pyr) nanocomposite has been successfully deposited on FTO electrode by EPD via either direct deposition of the TiO₂/poly(Ru-pyr) nanocomposite prepared in solution (*Photo-EPD* method) or deposition of $TiO_2/[Ru\text{-}pyr]^{2+}$ NPs followed by photopolymerization on the surface (*EPD-Photo* method). The presence of non-homogeneous distribution of Ru^{II} species and micrometer-sized aggregates on the electrodes are confirmed by SEM images in both cases. AFM images show that the presence of polypyrrole allows for better nanostructuration of the NPs than without the polypyrrole. Both *Photo-EPD* and *EPD-Photo* electrodes exhibit enhanced photocurrent under visible irradiation compared with $FTO/TiO_2/Ru^{II}$ where polypyrrole is absent. This observation proves the importance of the polypyrrole coating layer to increase the conductivity and charge injection rate to TiO₂ semiconducting particles. The current magnitude produced by the *Photo-EPD* electrode is 30 % greater than that of the *EPD-Photo* electrode. It probably indicates a more efficient deposition process of the NPs already embedded in a polypyrrole network and/or faster charge injection kinetics of the electrode made by the *Photo-EPD* method. Meanwhile, the electrode made by the *EPD-Photo* may only have the polypyrrole occurring at the outermost layer. However, the *Photo-EPD* electrode exhibits a less stable photocurrent, which could be related to the desorption of the immobilized NPs from FTO substrate.

References

1   N. C. Strandwitz, Y. Nonoguchi, S. W. Boettcher and G. D. Stucky, *Langmuir*, 2010, **26**, 5319–5322.

2   X. Wang, Q. Lu, X. Wang, J. Joo, M. Dahl, B. Liu, C. Gao and Y. Yin, *ACS Appl. Mater. Interfaces*, 2016, **8**, 538–546.

3   A. Fujishima, X. Zhang and D. A. Tryk, *Surf. Sci. Rep.*, 2008, **63**, 515–582.

4   A. Deronzier, J.-C. Moutet and D. Zsoldos, *J. Phys. Chem.*, 1994, **98**, 3086–3089.

5   A. Deronzier, P. Jardon, A. Martre, J.-C. Moutet, C. Santato, V. Balzani, A. Credi, F. Paolucci and S. Roffia, *New J. Chem.*, 1998, 33–37.

6   Y. Lattach, J. Fortage, A. Deronzier and J.-C. Moutet, *ACS Appl. Mater. Interfaces*, 2015, **7**, 4476–4480.

7   W. F. De Giovani and A. Deronzier, *J. Chem. Soc. Chem. Commun.*, 1992, 1461–1463.

8   A. Juris, V. Balzani, F. Barigelletti, S. Campagna, P. Belser and A. von Zelewsky, *Coord. Chem. Rev.*, 1988, **84**, 85–277.

9   S. Cosnier, A. Deronzier and J.-C. Moutet, *J. Electroanal. Chem. Interfacial Electrochem.*, 1985, **193**, 193–204.

10   H. Laguitton-Pasquier, A. Martre and A. Deronzier, *J. Phys. Chem. B*, 2001, **105**, 4801–4809.

11   J. V Caspar and T. J. Meyer, *J. Am. Chem. Soc.*, 1983, **105**, 5583–5590.

12   C. P. Kumar, N. O. Gopal, T. C. Wang, M.-S. Wong and S. C. Ke, *J. Phys. Chem. B*, 2006, **110**, 5223–5229.

13   T. Berger, M. Sterrer, O. Diwald, E. Knozinger, D. Panayotov, T. L. Thompson and J. T. Yates, *J. Phys. Chem. B*, 2005, **109**, 6061–6068.

14   J. Joo, J. K. Lee, S. Y. Lee, K. S. Jang, E. J. Oh and A. J. Epstein, *Macromolecules*, 2000, **33**, 5131–5136.

15   T.-M. Wu, H.-L. Chang and Y.-W. Lin, *Polym. Int.*, 2009, **58**, 1065–1070.

16   O. V. Gritsenko, P. R. T. Schipper and E. J. Baerends, *Chem. Phys. Lett.*, 1999, **302**, 199–207.

17   S. Dong and J. Ding, *Synth. Met.*, 1987, **20**, 119–124.

18   J. H. Dymond, M. A. Awan, N. F. Glen and J. D. Isdale, *Int. J. Thermophys.*, 1991, **12**,

433–447.

19   J. F. Moulder, W. F. Stickle, P. E. Sobol and K. D. Bomben, *Handbook of X-ray Photoelectron Spectroscopy*, ULVAC-PHI, 1995.

20   S. Hamar-Thibault, J.-C. Moutet and S. Tingry, *J. Organomet. Chem.*, 1997, **532**, 31–37.

21   W. Gopel, J. A. Anderson, D. Frankel, M. Jaehnig, K. Phillips, J. A. Schafer and G. Rocker, *Surf. Sci.*, 1984, **139**, 333–346.

22   R. S. Khnayzer, C. E. McCusker, B. S. Olaiya and F. N. Castellano, *J. Am. Chem. Soc.*, 2013, **135**, 14068–14070.

23   L. Besra and M. Liu, *Prog. Mater. Sci.*, 2007, **52**, 1–61.

24   I. Hod, W. Bury, D. M. Karlin, P. Deria, C.-W. Kung, M. J. Katz, M. So, B. Klahr, D. Jin, Y.-W. Chung, T. W. Odom, O. K. Farha and J. T. Hupp, *Adv. Mater.*, 2014, **26**, 6295–6300.

25   S. Cosnier, A. Deronzier and J.-F. Roland, *J. Electroanal. Chem. Interfacial Electrochem.*, 1990, **285**, 133–147.

GENERAL CONCLUSIONS
AND PERSPECTIVES

General conclusions

In this thesis, we used TiO_2 nanoparticles (NPs) as a redox-active substrate to immobilize various complexes including $[Ru(bpy)_3]^{2+}$ (bpy = 2,2'-bipyridine) as a photosensitizer (PS) and $[Cr(ttpy)_2]^{3+}$ or $[Mn(ttpy)(CO)_3Br]$ (ttpy = 4'-(*p*-tolyl)-2,2':6',2"-terpyridine) as an electron acceptor. The phosphonic acid group was used to graft the complexes on TiO_2 NPs, thanks to the stability of the Ti-O-P linkages. The grafting process was notably followed by quartz crystal microbalance with energy dissipation. Under visible irradiation, $[Ru(bpy)_3]^{2+}$ is excited and injects an electron to the conduction band (CB) of TiO_2 to form a long-lived charge separated state $(e^-)TiO_2/Ru^{3+}$, which allows for the utilization of the charges in subsequent charge transfer reactions. For example, adding $[Cr(ttpy)_2]^{3+}$ complex in a solution containing the TiO_2/Ru^{2+} NPs and triethanolamine (TEOA) as a sacrificial electron donor generates the doubly reduced $[Cr(ttpy)_2]^+$ species under visible light. The reaction proceeds stepwise through the formation of $(e^-)TiO_2/Ru^{3+}$. However, when both $[Cr(ttpy)_2]^{3+}$ and $[Ru(bpy)_3]^{2+}$ complexes are grafted on TiO_2, the back electron transfer reaction between transient Ru^{3+} and Cr^{2+} to regenerate the initial species Ru^{2+} and Cr^{3+} may occur very fast, so that a further reduction to $[Cr(ttpy)_2]^+$ cannot be obtained, even in the presence of TEOA. In contrast, $(e^-)TiO_2$ can doubly reduce $[Cr(ttpy)_2]^{3+}$ in solution to $[Cr(ttpy)_2]^+$ in the presence of TEOA. The photoinduced electron transfer occurs through the CB of TiO_2. TiO_2 therefore acts as an electron relay between the Ru^{2+*} as an electron donor and Cr^{3+} as an electron acceptor.

We also aimed to utilize the positive charge on the oxidized Ru^{3+} in the photoinduced charge separated state $(e^-)TiO_2/Ru^{3+}$ for the oxidative polymerization of pyrrole. We synthesized a hybrid system containing TiO_2 NPs as a scaffold and an immobilized $[Ru(bpy)_3]^{2+}$-based PS bearing two pyrrole moieties. Under visible irradiation and in the presence of O_2, the $[Ru(bpy)_3]^{2+}$ PS in the $TiO_2/[Ru-pyr]^{2+}$ hybrid NPs is excited, injects an electron to TiO_2 to form a charge separated state $(e^-)TiO_2[Ru^{III}-pyr]^{3+}$. The Ru^{III} centers are then reduced by pyrrole to generate Ru^{II} and a pyrrole radical cation. This radical then initiates a photopolymerization process on TiO_2 surface to form a nanocomposite $TiO_2/poly(Ru-pyr)$ where a polypyrrole network surrounds the NPs. Meanwhile, the injected electrons on TiO_2 are efficiently scavenged by O_2. This polymerization process cannot occur

225

by exhaustive electrolysis since TiO_2 is not conductive enough. Therefore, in this photopolymerization process TiO_2 acts as an electron acceptor for Ru^{2+*} to form the transient Ru^{3+}, which has a lifetime long enough for the oxidation of pyrrole. After two hours of irradiation, the $[Ru(bpy)_3]^{2+}$ PS does not show any degradation. As an application, the nanocomposite deposited on a FTO electrode can generate an anodic photocurrent two times higher than the electrode covered with TiO_2/Ru^{II} NPs under visible light and in the presence of TEOA as a sacrificial electron donor. The enhanced photocurrent for the nanocomposite is attributed to the better conductivity and nanostructuration of the polypyrrole network.

In the case of $[Mn(ttpy)(CO)_3Br]$ anchored on TiO_2/Ru^{II} NPs, the injected electrons on TiO_2 by Ru^{2+*} cannot be transferred to the Mn^I sites because the reduction power of $(e^-)TiO_2$ is not sufficient to reduce Mn^I. In the presence of a sacrificial electron donor like 1-benzyl-1,4-dihydronicotinamide (BNAH) and under visible light, the Ru^{2+*} excited state is first reductively quenched by BNAH to form Ru^+, which has a stronger reduction power than Ru^{2+*}. Therefore, the Ru^+ can reduce Mn^I to Mn^0 by a lateral electron transfer on the surface of TiO_2 NPs and not through the CB of TiO_2. Therefore, TiO_2 may not participate in the electron transfer process leading to Mn^0. We propose that the singly reduced Mn^0 complex is the catalytically active species on the $Ru^{II}/TiO_2/Mn^I$ triad for the photoreduction of CO_2. Photocatalytic CO_2 reduction under visible light using the triad and BNAH as a sacrificial electron donor produces HCOOH as the only product with $TON_{max} = 27$ after 16 hours. The role of TiO_2 scaffold in this photoinduced electron transfer process is not yet fully understood, however it seems to have a more active role than just a redox-inert scaffold like SiO_2.

Perspectives

Different publications have emphasized the interest of using polypyridyl complexes of Cr(III) in photoredox catalysis. For instance, recent works have proved that $[Cr(bpy)_3]^{3+}$-based complexes can accelerate the Diels-Alder cycloaddition under visible irradiation and in the presence of O_2, due to its high photooxidation power.[1,2] In this case, $[Cr(ttpy)_2]^{3+}$ may be beneficial as the redox potential of its excited state (1.14 V *vs* Ag/AgNO$_3$ 0.01 M) is higher than that of $[Cr(bpy)_3]^{3+}$ (0.89 V[3]). Also, our work showed that the lifetime of $[Cr(ttpy)_2]^{3+*}$ excited state is long enough for electron transfer reactions. Moreover, with the phosphonic acid derivatization we can immobilize the complex on NPs for the easier separation of the catalyst after the reactions.

An older publication also reported the possible reduction of CO_2 to HCHO by a polyvinyl film bearing $[Cr(tpy)_2]^{3+}$ (tpy = 2,2':6',2''-terpyridine) units as an electrocatalyst.[4] In this thesis, we studied the electroreduction of H^+ to H_2 from trifluoroacetic acid (TFA) in

MeCN catalyzed by $[Cr(ttpy)_2]^{3+}$. It will be interesting to test the triad $Ru^{2+}/TiO_2/Cr^{3+}$ in the photocatalytic proton reduction as well. In order to regenerate the Ru^{2+} PS an electron donor like TEOA or ethylenediaminetetraacetic acid (EDTA) is usually used in non-aqueous and aqueous media, respectively. However, they only work in basic solutions. Meanwhile, TFA is a relatively strong acid (pK_a = 12.8 in MeCN[5]). Therefore, another electron donor and/or proton source should be employed to drive the photocatalytic proton reduction using this triad.

In the photocatalytic CO_2 reduction experiments using $Ru^{II}/TiO_2/Mn^{I}$ triad, the use of electron donor BNAH has several disadvantages as recently described.[6] Firstly, the reductive quenching of Ru^{II*} excited state by BNAH is not total. Secondly, after formation of Ru^{I} and $BNAH^{\bullet+}$, a fast back electron transfer between them occurs which prevents the utilization of the charge on Ru^{I} reduced species. Thirdly, $(BNA)_2$, the oxidation product of BNAH, is more efficient than BNAH to quench the Ru^{II*} excited state and can terminate the catalytic cycle. Therefore, the photocatalytic result may be enhanced if 1,3-dimethyl-2-phenyl-2,3-dihydro-1H-benzo[d]-imidazole (BIH) or 1,3-dimethyl-2-(o-hydroxyphenyl)-2,3-dihydro-1H-benzo[d]imidazole (BI(OH)H) (**Scheme 1**) is used as an electron donor to replace BNAH. They are promising electron donors because: (i) BIH and BI(OH)H have stronger reducing power than BNAH (E_{pa} *vs* Ag/AgNO$_3$ 0.01 M = 0.03 V for BIH[7] and 0.01 V for BI(OH)H[6], while E_{pa} = 0.27 V for BNAH in MeCN[7]); (ii) they have been proved to almost quantitatively quench the Ru^{II*} excited state[6]; and (iii) BIH and BI(OH)H can act as a consecutive two-electron donor while BNAH is a one-electron donor.

Scheme 1: Structures of BIH and BI(OH)H electron donors

Another perspective from this thesis is the incorporation of the $[Mn(ttpy)(CO)_3Br]$ catalyst to the TiO_2/poly(Ru-pyr) nanocomposite, then this hybrid system can be deposited on a FTO electrode. This electrode can be employed for the photoelectrocatalytic reduction of CO_2. Similarly, $[Cr(ttpy)_2]^{3+}$ can also be incorporated in the TiO_2/poly(Ru-pyr) nanocomposite and deposited on an electrode for proton reduction. In this way, the loading of these catalysts on a geometrical electrode area should be higher than simply grafting them on a flat electrode surface.

References

1   S. M. Stevenson, M. P. Shores and E. M. Ferreira, *Angew. Chemie, Int. Ed.*, 2015, **54**, 6505–6510.

2   R. F. Higgins, S. M. Fatur, S. G. Shepard, S. M. Stevenson, D. J. Boston, E. M. Ferreira, N. H. Damrauer, A. K. Rappé and M. P. Shores, *J. Am. Chem. Soc.*, 2016, **138**, 5451–5464.

3   N. A. P. Kane-Maguire, *Top. Curr. Chem.*, 2007, **280**.

4   J. A. Ramos Sende, C. R. Arana, L. Hernandez, K. T. Potts, M. Keshevarz-K and H. D. Abruna, *Inorg. Chem.*, 1995, **34**, 3339–3348.

5   B. D. McCarthy, D. J. Martin, E. S. Rountree, A. C. Ullman and J. L. Dempsey, *Inorg. Chem.*, 2014, **53**, 8350–8361.

6   Y. Tamaki, K. Koike and O. Ishitani, *Chem. Sci.*, 2015, **6**, 7213–7221.

7   Y. Yamazaki, H. Takeda and O. Ishitani, *J. Photochem. Photobiol. C Photochem. Rev.*, 2015, **25**, 106–137.

EXPERIMENTAL SECTION

1.   Chemicals

Solvents: Acetonitrile (CH_3CN), dichloromethane (CH_2Cl_2) and ethanol (C_2H_5OH, all purchased from Fisher, HPLC grade), dimethyl sulfoxide (DMSO, Acros, anhydrous 99.7%), *N,N*-dimethylformamide (DMF, Acros, anhydrous 99.8%), ethylene glycol (Prolab), chloroform ($CHCl_3$, Carlo Erba, HPLC grade), diethyl ether (Aldrich, 99.8%), hexane (95%), pentane (Carlo Erba), methanol (SDS anhydrous, analytical grade) and acetone (Aldrich, 99.5%) were used as purchased without any further purifications. Dry solvents were obtained by distillation under Argon. Distilled water was prepared with a Milli-Q system.

Reagents: all reagents have been used without further purifications, unless otherwise stated.

Nanoparticles (NPs): commercially available TiO_2 (anatase, d < 25 nm, Aldrich), TiO_2 (Degussa P25) and SiO_2 (d < 20 nm, Aldrich) were used as received.

Others: Column chromatography was carried out on silica gel 60 (Merck, 70-230 mesh). Thin layer chromatography (TLC) was performed on plates coated with silica gel 60 F_{254}.

2.   Apparatus and techniques

Nuclear magnetic resonance (NMR): ^{1}H NMR, ^{13}C NMR and ^{31}P NMR spectra were recorded with a 400 or 300 MHz Bruker spectrometer at room temperature (RT). Chemical shifts in the ^{1}H NMR spectra were referenced to residual solvent peaks. Coupling constants (*J*) and the chemical shifts (δ) were shown in Hz and ppm, respectively. The abbreviation for the characterization of the peaks are as follows: s = singlet, d = doublet, t = triplet, q = quartet, m = multiplet, dd = doublet of doublet, dt = doublet of triplet.

UV-visible absorption spectroscopy (UV-vis): UV-vis spectra of a homogeneous solution or a colloid in a conventional quartz cell were recorded with a Varian Cary 300 or a MCS 500 UV-vis-NIR Zeiss spectrophotometer. To record spectra of a powder or a thin film on electrode, a Perkin Elmer Lambda 650 spectrometer and an integration sphere were used. The NPs of interest were mixed with KBr, then a hydraulic press was used to make a pellet for the experiments.

Luminescence: Emission spectra were recorded with a Fluoromax-4 (Horiba Scientific) in a quartz cuvette with 4 transparent faces. Samples were purged with Ar for 15 minutes prior to experiment. The luminescent quantum yield Φ was calculated as follows:

$$\phi = \phi_{ref} \times \frac{I}{I_{ref}} \times \frac{Abs_{ref}}{Abs} \times \left(\frac{n}{n_{ref}} \right)^2$$

where *I* is the integrated area under the emission peak, *Abs* is the absorbance at the excitation wavelength, *n* is the refractive index of the solvent, and the subscript *ref* indicates a reference with known luminescent quantum yield. The reference is chosen to be $[Ru(bpy)_3](PF_6)_2$ with $\Phi_{ref} = 0.062$ in MeCN under Ar.[1]

Time-resolved emission spectroscopy: Spectra were recorded with a time-correlated single photon counting (TCSPC) after the samples were excited at 400 nm by a picosecond Nd:YAG laser. The decay of $[Ru(bpy)_3]^{2+*}$ state at 610 nm was measured by a PicoHarp 300 TCSPC detector (PicoQuant). The fitting of the luminescent decays was performed with a FluoFit software (PicoQuant). In case of a colloid, light scattering was taken into account by subtracting the decay at 400 nm from the decay at 610 nm prior to the fitting.

Transient absorption spectroscopy: Spectra were acquired using a LP920K system (Edinburgh Instruments) equipped with a nanosecond Nd:YAG laser (Brilliant – Quantel). Pump excitation of the sample was achieved by a third harmonic (355 nm) or a second harmonic (532 nm) module. A Xe900 pulsed Xenon lamp was used to generate a probe light. The photons were dispersed using a monochromator, transcripted by a R928 (Hamamatsu) photo-multiplicator, and recorded on a TDS 3012C (Tektronix) oscilloscope. All samples were purged with Ar for 15 minutes prior to the measurement.

Electrochemistry: All electrochemical measurements were performed in a standard three-electrode cell at RT under a continuous Ar flow or in a glovebox. Electrolytes were used without further purifications: tetrabutylammonium perchlorate (TBAP, Fluka), tetrabutylammonium hexafluorophosphate (TBAPF$_6$, Aldrich). A silver/silver nitrate in CH_3CN (Ag/AgNO$_3$ 0.01 M) and a platinum (Pt) coil were used as reference electrode and counter electrode, respectively. A carbon disk electrode (CHI Instrument) or a home-made Pt microcavity electrode was used as working electrode. Before experiment, the C disk electrode was polished using diamond paste and cleaned with ethanol. Cyclic voltammograms (CV) were recorded with a CHI 630 potentiostat (CH Instrument), or a Biologic SP300 potentiostat (Science Instruments). All reported potentials are against the Ag/AgNO$_3$ 0.01 M reference electrode, unless otherwise stated. One should subtract 0.090 V from them to convert them

against Fc$^+$/Fc reference. Half-wave potential ($E_{1/2}$) and peak-to-peak splitting (ΔE_p) are calculated as follows:

$$E_{1/2} = \frac{E_{pa} + E_{pc}}{2}, \qquad \Delta E_p = E_{pa} - E_{pc}$$

where E_{pa} and E_{pc} are anodic and cathodic peak potentials respectively.

The surface coverage Γ (mol.cm^{-2}) of a redox complex grafted on an ITO or FTO electrode is calculated as follows:

$$\Gamma = \frac{Q}{nFA}$$

where Q (C) is the integrated area under the oxidation or reduction peak , n is the number of electron transfer, $F = 96500$ C.mol^{-1} the Faraday constant, and A (cm^2) the apparent electrode area.

Electrocatalysis: Experiments were carried out at RT under Ar (for proton reduction) or CO_2/CH_4 (95/5 v/v) mixture (for CO_2 reduction) in a sealed conventional three-electrode cell. The solvent was MeCN + TBAPF$_6$ (0.1 M), to which water may be added in some CO_2 reduction experiments. Reference and counter electrodes were Ag/AgNO$_3$ 0.01 M and Pt plate, respectively. Working electrode was a carbon plate (8 cm^2) which had been cleaned by diamond paste and washed with ethanol prior to experiment. In a normal setting with 3 electrodes and 10 mL solution, the headspace volume was measured to be 170 mL. During the experiments, at each time interval a 100 µL sample was taken from the headspace gas using a gas tight injection syringe. Gas products were analyzed with the gas chromatographs described below. At the end of the experiments, a liquid sample was taken for HCOOH analysis.

Quartz crystal microbalance with energy dissipation (QCM-D): All QCM-D experiments were run at a flow rate of 10 µL/min, using SiO$_2$- or Ti-coated quartz crystals (Q-Sense). All solutions were kept in a thermomixer (Ependorf) for a constant temperature of 21 ^{0}C during the experiment. A pretreatment of the surface before measurement is required to improve the surface cleanliness. The SiO$_2$-coated sensor was sonicated in a 2 % SDS aqueous solution for 20 minutes, washed with water, then exposed to UV-O$_3$ treatment for 30 minutes. The Ti-coated sensor was rinsed in Hellmanex 1 % solution for 30 minutes, washed with water, dried and rinsed in pure ethanol for 10 minutes, then exposed to UV-O$_3$ treatment for 2 hours to oxidize the surface to TiO$_2$. Finally, both sensors were rinsed again in ethanol for 20 minutes, dried under N$_2$ before a QCM experiment.

Contact angle measurements: Contact angle measurements were performed with an OCA35 measuring device (Dataphysics). Each sample was measured 5 times at various positions on its surface.

Electron paramagnetic resonance spectroscopy: All spectra were recorded on an Bruker EMX spectrometer operating at X-band frequency ($f \sim 9.65$ GHz) equipped with an ER-4116 dual mode cavity and an ESR-900 flow cryostat (Oxford Instrument). Continuous irradiation at desired wavelengths was achieved with a 455 nm or a 365 nm LED (Thorlabs) from a side window of the EPR cavity (see a typical experiment setup in Scheme VI-1). Determination of *g*-values was referenced to the signal of DPPH ($g = 2.0036$, $B_0 = 3440.6$ G) obtained at room conditions. Spectral simulations were performed with Matlab equipped with an EasySpin toolbox. All samples were either prepared in a glovebox or under air, sonicated if necessary, frozen in liquid nitrogen and then put under He atmosphere for measurements.
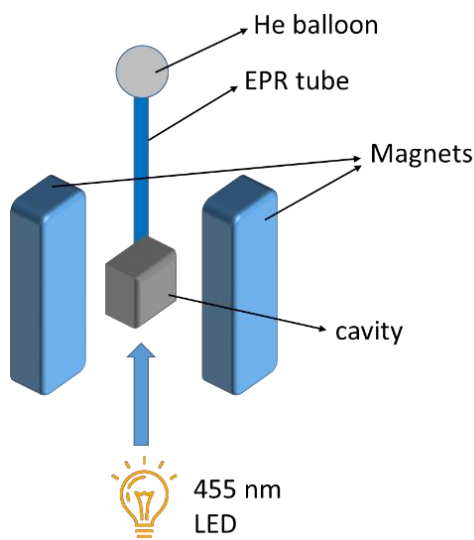
Scheme VI-1. EPR setup with in situ irradiation

Infra-red spectroscopy: The NPs or complexes of interest were well mixed with KBr and pressed into a pellet for measurement. Experiments were carried out at room conditions after subtracting the KBr signal with a Perkin Elmer Spectrum GX instrument.

Photocurrent measurement: A standard electrochemical cell with modified surfaces as working electrode were used. A 250 W Xenon lamp was employed to irradiate the electrode, with a fixed distance of 4 cm between the surface and the head of the optical fiber. A CHI 600 potentiostat was run in chronoamperometry mode to record the photocurrents. During the experiment, the light was alternatively switched on and off by placing a metallic plate over the source outlet. The energy of incident light is estimated to be 1.0 W.cm^{-2} (without filter), or 1.0 mW.cm^{-2} (UV hot filter).

Photocatalytic CO₂ reduction: A glass tube (12.5 mL) was charged with a $[Ru(bpy)_3]^{2+}$ photosensitizer complex and a catalyst in DMF/TEOA mixture (5 mL, $C_{TEOA} = 1$ M). The PS and catalyst can be homogeneous or anchored on TiO_2 NPs. The mixture was sonicated for a few minutes prior to be purged with Ar (20 mins) and then CO_2/CH_4 (95/5 v/v) mixture (20 mins). The dead volume was estimated at 7.5 mL. Afterwards, the tube was irradiated with a Xenon lamp (4 cm apart) in the presence of a UV filter and a 450 nm bandpass filter in order to selectively excite the PS. The light power is estimated to be 0.3 mW.cm^{-2}. During the experiment, at each time interval a 100 µL sample was taken from the headspace gas using a gas tight injection syringe. Gas contents were analyzed by GC which is described below. At the end of the experiment, a liquid sample was taken to analyze HCOOH content by HPLC.

Gas chromatography: Gas samples (100 µL) were taken from the headspace of the tube containing the reaction mixture. If the gas phase only contains H_2, the analysis was run with a Perkin Elmer Autosystem XL gas chromatograph equipped with a 5 Å molecular sieve column (oven temperature = 32 ^{0}C) and a thermal conductivity detector (TCD), using argon as the carrier gas. If the gas phase contains both CO and H_2, the analysis was conducted with a Perkin Elmer Clarus 500 gas chromatograph equipped with a PDID detector and a 30 m Carboplt 1010 column (Antelia) and 560S mass spectrometer using a TurboMass 5.4.2 program. The gas contents were calculated against 5 % CH_4 as internal reference in the gas phase. The results were compared to a standard gas mixture of CO, H_2 and CO_2 (Air Liquid). Helium was used as the carrier gas. If the gas phase only contains H_2, the analysis was run on

High performance liquid chromatography: Content of HCOOH produced by electrocatalysis was determined using a Perkin Elmer liquid chromatograph equipped with a Series 200 pump, 785 A UV-vis detector, Series 200 vacuum degasser and a SiELC primesep SB packed column (100 mm, 5 µm pore size, 20 µL injection volume), with the column eluent containing 46 mM methane sulphonic acid in H_2O. The HCOOH content produced by photocatalysis was analyzed using a Shimadzu liquid chromatograph LC-10AS equipped with an Alltech Select degassing system, a Perkin Elmer Series 200 UV-vis detector and a Perkin Elmer polypore H column (220 mm, 10 µm pore size, 20 µL injection volume), with the column eluent containing 10 mM H_2SO_4 in H_2O. Both chromatographs were checked by injecting an aqueous solution of HCOONa (0.01 M) prior to the experiments.

Atomic force microscopy: Experiments were conducted at the NanoBio platform of the Grenoble – Alpes University with the help of Mr. Hugues BONNET. Micrographs were obtained in oscillating mode with a PicoPlus AFM (Molecular Imaging) or in peakforce oscillating mode with a Dimension Icon AFM (Bruker) under ambient conditions. An AFM

cantilever with an aluminum coating (BudgetSensors Tap 150 al-G) was employed. Micrographs were processed using a Gwyddion software.

Scanning electron microscopy (SEM): Experiments were conducted in collaboration with Dr. Christine LANCELON PIN (CERMAV) for traditional SEM or CMTC team (Grenoble INP) for Field-Emission SEM (FE-SEM). Experiments of FE-SEM were carried out using a field emission gun (Zeiss Ultra 55) at low voltage (3 kV) to reduce the charging effect on non-conducting SiO_2 or weakly conducting TiO_2 surfaces. Imaging was done with secondary electrons using the In Lens detector. Normal SEM experiments were done using an ETD detector for topography imaging and a CBS detector for chemical contrast.

Transmission electron microscopy (TEM): Experiments were conducted in collaboration with Dr. Jean-Luc PUTAUX (CERMAV) using a Phillips CM200 Cryo-microscope operating at 80 kV under RT and high vacuum. A small volume of colloid was deposited onto a glow-discharged copper grid and the solvent was evaporated.

X-ray photoelectron spectroscopy (XPS): Experiments were conducted in collaboration with Dr. Anass BENAYAD (LITEN/CEA Grenoble). The XPS analyses were performed with a ULVAC PHI 5000 VersaProbe II spectrometer using AlKα X-ray radiation (1486.6 eV). The residual pressure inside the analysis chamber was 7×10^{-8} Pa. A fixed analyzer pass energy of 23 eV was used for core level scans, leading to an overall energy resolution of 0.6 eV. Survey spectra were captured at a pass energy of 117 eV. All spectra were referenced against an internal signal, typically by adjusting the Ti2p 3/2 level peak at a binding energy of 457.9 eV. The XPS spectra were fitted using Multipak V9.1 software in which a Shirly background is assumed and the fitting peaks of the experimental spectra are defined by a combination of Gaussian (80%) and Lorentzian (20%) distributions.

3. Synthesis

3.1. General conditions: In case of air-sensitive syntheses, a Schlenk technique or a glovebox was used. The flasks and other glassware were dried in oven overnight prior to the syntheses. Loadings of metal complexes on NPs were roughly estimated by measuring the UV-vis absorbance of supernatant solutions after centrifugation which indicates the amount of unadsorbed complexes.

3.2. Ligands and complexes

[Ru(bpy)₂(dmbpy)](PF₆)₂. A mixture of [Ru(bpy)₂Cl₂] (52 mg, 0.10 mmol) and 4,4'-dimethyl-2,2'-bipyridine (dmbpy, 20.3 mg, 0.11 mmol, 1.1 equiv) in ethylene glycol (anhydrous, 5 mL) was refluxed at 120 ^{0}C in 2 hours under Ar. The solution color gradually changed from purple to dark red. After the mixture was allowed to cool to RT, an excess amount of saturated solution of KPF₆ in water was added, resulting in immediate red precipitates. The powder was filtered, then solubilized in acetone to remove the excess KPF₆ salt. Subsequently, the solution was evaporated to give red crude product. Small amounts of acetone and diethyl ether were used to solubilize the crude product and then evaporated several times to completely eliminate water. Finally a red fine powder was obtained (70 mg, 80 % yield). **¹H NMR** (400 MHz, CD₃CN): δ (ppm) = 8.49 (d, *J* = 7.9 Hz, 4H), 8.35 (s, 2H), 8.06 – 8.01 (m, 4H), 7.73 (t, *J* = 5.0 Hz, 4H), 7.53 (d, *J* = 5.8 Hz , 2H), 7.41 – 7.35 (m, 4H), 7.23 (d, *J* = 5.1 Hz , 2H), 2.53 (s, 6H). **Electrochemistry** (WE = C disk, RE = Ag/AgNO₃ 0.01 M, electrolyte = MeCN + 0.1 M TBAPF₆, *v* = 100 mV.s^{-1}): $E_{1/2}$ (V) = 0.91, -1.66, -1.86, -2.12.
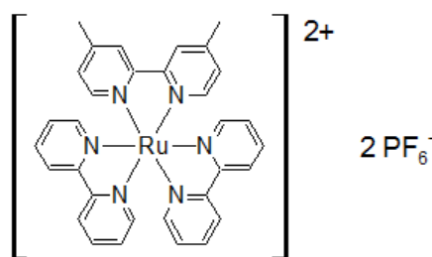
bpy-PO₃Et₂. The synthesis of this ligand requires two steps. In the first step, lithium diisopropylamine (LDA) was prepared by dissolving diisopropylamine (DIPA, 630 μl, 1.29 mmol) in 3 mL THF under Ar in an oven-dried flask. The solution was cooled to -40 ^{0}C, stirred for 30 minutes before slowly adding *n*-butyllithium solution (2.5 M in hexane, 0.58 mL, 1.29 mmol). The LDA solution was kept stirring for one hour while the temperature was raised to 0 ^{0}C, forming a pale green solution. In another oven-dried flask, a solution of 4,4'-

dimethyl-2,2'-dipyridine (dmbpy, 227.5 mg, 1.235 mmol) in 8 mL dried THF was prepared under Ar and cooled to -40 ^{0}C. The LDA solution was added dropwise to the dmbpy solution at -40 ^{0}C, and the mixture was stirred for 1.5 hour.

In the second step, diethyl(3-bromopropyl)phosphonate (0.3 mL, 1.56 mmol) was added to the mixture, and the temperature was slowly raised to room temperature overnight. The reaction was stopped by adding 10 mL saturated NH_4Cl aqueous solution, then extracted with $CHCl_3$ (x2) and washed with ethanol + H_2O. The product was subsequently separated by chromatography. First, SiO_2 column was washed with pentane + 10 % trimethylamine (2 times) before the separation step. A mix of CH_2Cl_2/MeOH was used as eluent. The amount of MeOH was gradually increased from 1 to 3 %. The solution was evaporated and the product was dried under vacuum to yield a white powder (397.6 mg, yield: 90%). **^{1}H NMR** (400 MHz, $CDCl_3$): δ (ppm) = 8.59 – 8.56 (m, 2H), 8.29 (s, 2H), 7.28 (s, 3H), 7.17 (s, 2H), 4.12 – 4.06 (m, 6H), 2.75 (t, J = 7.1 Hz, 2H), 1.85 – 1.79 (m, 4H), 1.32 (t, J = 6.9 Hz, 6H).
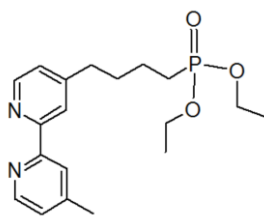
[Ru(bpy)$_2$(bpy-PO$_3$Et$_2$)]Cl$_2$ (denoted as **[Ru-PO$_3$Et$_2$]$^{2+}$**). Precursors *cis*-bis(2,2′-bipyridine)-dichlororuthenium(II) dihydrate ([Ru(bpy)$_2$Cl$_2$].2H$_2$O, 167 mg, 0.345 mmol) and the **bpy-PO$_3$Et$_2$** ligand (150 mg, 0.414 mmol, 1.2 equiv) were solubilized in EtOH/H$_2$O (8/2 v/v) mixed solvent under Ar for 30 minutes. Afterwards, the mixture was refluxed at 85 ^{0}C overnight. The solution color changed to bright red. Addition of an excess amount of acetone lead to formation of red precipitates. The solvent mixture was evaporated under vacuum. The solid part was solubilized again in ethanol and acetone then evaporated several times to remove water. The crude product was purified with flash chromatography using acetonitrile/H$_2$O/saturated aqueous KNO$_3$ solution (100/5/0.5) as mobile phase and silica to yield a bright red powder (230 mg, 76 %).

^{1}H NMR (400 MHz, CD$_3$CN): δ (ppm) = 8.49 (d, J = 7.7 Hz, 4H), 8.41 (s, 1H), 8.37 (s, 1H), 8.06 – 8.02 (m, 4H), 7.74 – 7.70 (m, 4H), 7.55 – 7.52 (m, 2H), 7.42 – 7.36 (m, 4H), 7.23 – 7.22 (m, 2H), 4.04 – 3.93 (m, 4H), 2.83 (t, J = 7.5 Hz, 2H), 2.53 (s, 3H), 1.82 – 1.72 (m, 4H), 1.64 – 1.55 (m, 2H), 1.24 (t, J = 7.0 Hz, 6H). **Electrochemistry** (WE = C disk, RE =

Ag/AgNO$_3$ 0.01 M, electrolyte = MeCN + 0.1 M TBAPF$_6$, v = 100 mV.s^{-1}): $E_{1/2}$ (V) = 0.92, -1.67, -1.86, -2.12.
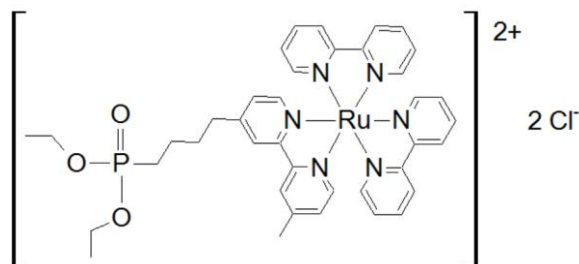
[Ru(bpy)$_2$(bpy-PO$_3$H$_2$)]Cl$_2$ (denoted as **[RuP]$^{2+}$**). The complex was synthesized by hydrolysis of **[Ru-PO$_3$Et$_2$]$^{2+}$** (180 mg, 0.213 mmol) in acidic solution containing 10 mL H$_2$O and 10 mL saturated HCl solution. The mixture was refluxed at 100 ^{0}C for 48 hours. The color changed to slightly dark red during the reaction. After the reaction, the solvent was evaporated under vacuum. The solid part was solubilized in ethanol/acetone mixture then evaporated several times to eliminate the water content. Finally the solid product was dried under vacuum to give a dark red powder (110 mg). Reaction yield cannot be determined due to the presence of remaining HCl.

^{1}H NMR (400 MHz, CD$_3$CN): δ (ppm) = 8.50 (d, J = 7.9 Hz, 4H), 8.39 (s, 1H), 8.36 (s, 1H), 8.06 – 8.02 (m, 4H), 7.77 – 7.72 (m, 4H), 7.56 – 7.52 (m, 2H), 7.40 – 7.36 (m, 4H), 7.23 (m, 2H), 2.83 (t, J = 7.4 Hz, 2H), 2.52 (s, 3H), 1.81 – 1.73 (m, 4H), 1.68 – 1.63 (m, 2H). **Electrochemistry** (WE = C disk, RE = Ag/AgNO$_3$ 0.01 M, electrolyte = MeCN/H$_2$O (95/5 v/v) + 0.1 M TBAPF$_6$, v = 100 mV.s^{-1}): $E_{1/2}$ (V) = 0.92, -1.20 (irreversible), -1.89 (irreversible).
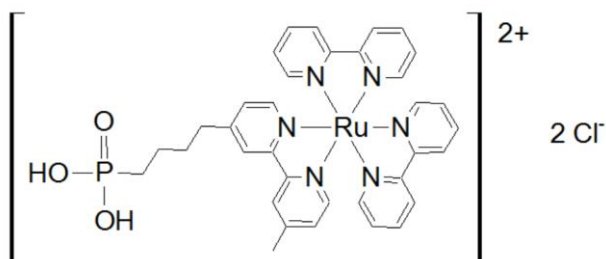
[Cr(ttpy)$_2$](ClO$_4$)$_3$. To 4'-tolyl-2,2':6',2"-terpyridine (ttpy, 0.50 g, 1.55 mmol) in a suspension of 50 mL H$_2$O and 5 mL EtOH was added CrCl$_2$ (0.19 g, 1.55 mmol, 1 equiv) in an Ar glove box. The suspension immediately turned purple upon addition and was then stirred for 1 h at RT. An excess amount of LiClO$_4$ was added and precipitation was observed. The flask was

removed from the glove box and bubbled through with air for 2 h which produced an orange suspension. The solid was separated by filtration and dried under high vacuum to afford desired product as an orange solid (0.66 g, 61 %).

Elemental Analysis (EA): Calc. for $C_{44}H_{28}N_6Cr$: C, 52.99; H, 2.83; N, 8.43. Found: C, 52.17; H, 3.73; N, 8.64. **UV-vis**: λ_{max} (MeCN) = 368 nm (ε = 36500 $M^{-1}.cm^{-1}$). **Electrochemistry** (WE = C disk, RE = Ag/AgNO$_3$ 0.01 M, electrolyte = MeCN + 0.1 M TBAPF$_6$, v = 100 mV.s^{-1}): $E_{1/2}$ (V) = -0.47, -0.85, -1.35, -2.25. **^{1}H NMR** cannot be done because the material is paramagnetic.
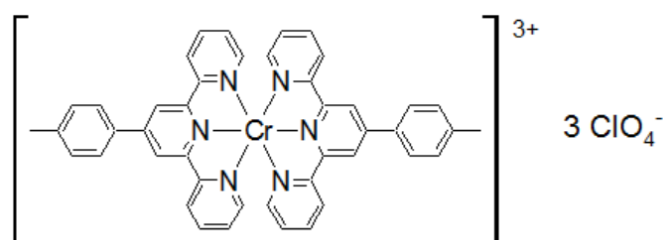
ttpy-PO₃Et₂.
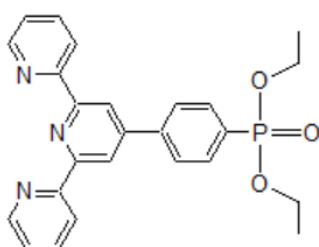
The synthesis of this ligand requires two steps:

(i) *Step 1: Synthesis of 4'-(4-bromophenyl)-2, 2':6', 2"-terpyridine*

To acetyl pyridine (2.62 g, 21.6 mmol) in 100 mL EtOH mixed with 60 mL NH$_4$OH was added KOH (1.28 g, 21.6 mmol, 1 equiv) then 4-bromo-benzaldehyde (2.0 g, 10.8 mmol, 0.5 equiv). The reaction mixture turned yellow then green in color. The reaction was heated to 55 °C and stirred for 12 h. The solid was filtered, recrystallized from EtOH then dried under high vacuum with gentle heating to afford a fluffy, white solid (1.56 g, 36 %).

EA: Calc. for $BrC_{21}H_{14}N_3$: C, 66.96; H, 3.64; N, 10.82. Found: C, 62.10; H, 4.09; N, 10.35. **^{1}H NMR** (400 MHz, CDCl$_3$): δ (ppm) = 8.72 (d, J = 4.0 Hz, 2H), 8.70 (s, 2H), 8.67 (d, J = 8.0 Hz, 2H), 7.88 (td, J_1 = 8.0 Hz, J_2 = 1.6 Hz, 2H), 7.78 (d, J = 8.0 Hz, 2H), 7.64 (d, J = 8.0, 2H), 7.36 (m, 2H). **ESI-MS**: m/z = 388 (M+H, 95 %), 361 (52), 242 (19).

(ii) *Step 2: Synthesis of diethyl [4-(2,2':6',2"-terpyridin-4'-yl)phenyl]phosphonate*

To a degassed mixture of 4′-(4-bromophenyl)-2,2′:6′,2″-terpyridine (0.97 g, 2.50 mmol) and [1,1-bis-(diphenylphosphino)ferrocene]dichloropalladium(II) (0.10 g, 0.13 mmol) was added 25 mL anhydrous toluene then Et_3N (0.28 g, 2.75 mmol) and diethylphosphite (0.38 g, 2.76 mmol). The orange solution was stirred for 48 h at 90 °C under an Ar atmosphere. The solvent was removed *in vacuo* and the residue recrystallized from MeCN three times and dried under high vacuum to give a purple solid (0.63 g, 56%)

EA: Calc. for $C_{25}H_{24}N_3O_3P$: C, 67.40; H, 5.44; N, 9.43. Found: C, 67.71; H, 5.37; N, 9.74. **^{1}H NMR** (400 MHz, $CDCl_3$): δ (ppm) = 8.75 (s, 2H), 8.73 (d, J = 4.0 Hz, 2H), 8.68 (d, J = 8.0 Hz, 2H), 7.98 (m, 4H), 7.89 (td, J_1 = 8.0 Hz, J_2 = 4.0 Hz, 2H), 7.37 (m, 2H), 3.12 (q, J = 4.0 Hz, 4H), 1.44 (t, J = 4.0 Hz, 6H). **^{31}P NMR** (400 MHz, $CDCl_3$): δ (ppm) = 19.43. **ESI-MS:** *m/z* = 446 (M+H, 47 %).

ttpy-PO₃H₂. A degassed sample of **ttpy-PO₃Et₂** (0.63 g, 1.52 mmol) was dissolved in 6 mL anhydrous CH_2Cl_2. Then TMSBr (0.84 g, 5.48 mmol) was added and the purple solution was stirred at 20 °C for 48 h under an argon atmosphere. The solvent was evaporated to dryness *in vacuo* before the solid was dissolved in 25 mL MeOH and stirred at 20 °C for 3 h. The grey/lilac solid was filtered and washed with EtOH twice and acetone twice. The solid was dissolved in water by adding NaOH 10 % solution and precipitated by adding HCl 10 % aqueous solution until pH 3 was reached. The solid was filtered off, washed with water and dried under high vacuum to give a light brown powder (0.29 g, 49 %).

^{1}H NMR (400 MHz, $CDCl_3$): δ (ppm) = 8.85 (t, J = 12.0 Hz, 6H), 8.21 (td, J_1 = 8.0 Hz, J_2 = 4.0 Hz, 2H), 8.12 (dd, J_1 = 8.0 Hz, J_2 = 4.0 Hz, 2H), 7.95 (m, 2H), 7.69 (m, 2H). **^{31}P NMR** (400 MHz, $CDCl_3$): δ (ppm) = 11.91. **ESI-MS:** *m/z* = 371 (M−OH, 91 %).
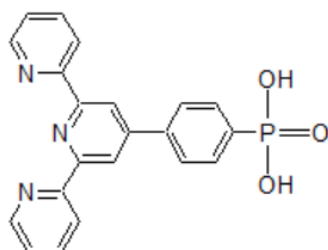

[Cr(ttpy-PO₃Et₂)₂](ClO₄)₃. To a suspension of **ttpy-PO₃Et₂** (0.10 g, 0.22 mmol) was added 2 mL of a solution of $CrCl_2$ (11 mg, 0.086 mmol) in H_2O in an Ar glovebox. Approximately 5 mL EtOH was added and the solution turned very dark in color. The mixture was left to stir for 1 h at 25 ^{0}C then an excess amount of $LiClO_4$ were added. The solution was removed from

the glove box and compressed air was bubbled through for 30 mins upon which a color change from purple to dark yellow was observed. The solution exposed to air was left stirring for 12 h. The bright yellow suspension was filtered and the resulting yellow solid recrystallized from a solution of H_2O and EtOH and dried under high vacuum to give the product as a dark yellow solid (41 mg, 38 %). **Electrochemistry** (WE = C disk, RE = Ag/AgNO$_3$ 0.01 M, electrolyte = MeCN + 0.1 M TBAPF$_6$, v = 100 mV.s^{-1}): $E_{1/2}$ (V) = -0.34, -0.77, -1.30, -2.21. **^{1}H NMR** cannot be done because the product is paramagnetic.
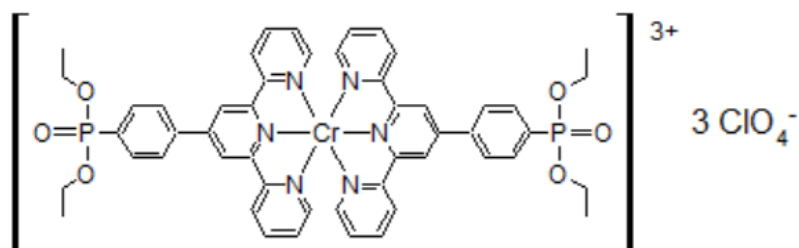
[Cr(ttpy-PO₃H₂)₂](ClO₄)₃ ([Cr2P]³⁺). In a glove box, **ttpy-PO₃H₂** (30 mg, 0.077 mmol) was dissolved in 5 mL DMSO. To this was added CrCl$_2$ (4.5 mg, 0.037 mmol) dissolved in 2 mL H_2O. Upon addition, the solution turned dark purple in color. A further 40 mL of H_2O was added and the solution stirred for 1 h at 25 ^{0}C. Three spatula-fulls of LiClO$_4$ were added but no precipitation was observed. The purple solution was removed from the glove box and stirred for 12 h at RT whilst exposed to air. The resulting dark yellow solution was filtered to afford the product [Cr2P]$^{3+}$ as a pale yellow solution. The solvent was evaporated under vacuum to afford a grey/yellow solid (25 mg, 60 %).

^{1}H NMR cannot be done because the product is paramagnetic. **UV-vis**: λ_{max} (MeCN) = 370 nm (ε = 36500 M^{-1}.cm^{-1}). **Electrochemistry:** CVs cannot be done directly due to its poor solubility in any solvent except for DMSO. Instead, its redox potentials were studied by grafting [Cr2P]$^{3+}$ on a ITO electrode and used it as WE: $E_{1/2}$ (V) = -0.42, -0.79, -1.32. (WE: area = 1.2 cm^2, RE = Ag/AgNO$_3$ 0.01 M, electrolyte = MeCN + 0.1 M TBAPF$_6$, v = 100 mV.s^{-1}).
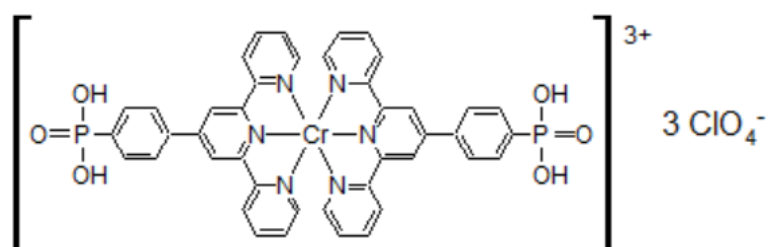
[Cr(ttpy)Cl₃]. The complex has been synthesized following reported procedures.[2,3] To 10 mL EtOH was added anhydrous CrCl₃ (0.19 g, 1.17 mmol) then 4'-tolyl-2,2':6',2"-terpyridine (ttpy, 0.48 g, 1.49 mmol). The mixture was heated to reflux then granulated zinc (42 mg, 0.64 mmol) was added. The mixture color turned to khaki green. It was stirred vigorously for 12 h at 80 °C. The khaki green precipitate was filtered, washed twice with EtOH and dried under high vacuum (0.45 g, 79 %). **¹H NMR** cannot be done because the product is paramagnetic.
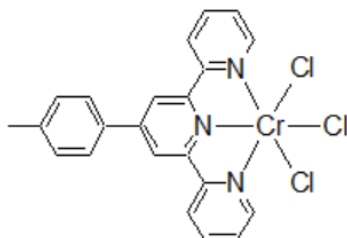
[Cr(ttpy)(OTf)₃] (OTf = CF₃SO₃⁻). The complex has been synthesized following reported procedures.[2,3] To **[Cr(ttpy)Cl₃]** (0.20 g, 0.42 mmol) was added CF₃SO₃H (3.68 g, 24.5 mmol) giving a yellow/brown solution which was stirred for 12 h at RT. The reaction was cooled to 0 °C and 30 mL Et₂O was added. The solid produced was separated by filtration, washed with Et₂O and the resulting brown solid dried under high vacuum (0.21 g, 59 %). **¹H NMR** cannot be done because the product is paramagnetic.
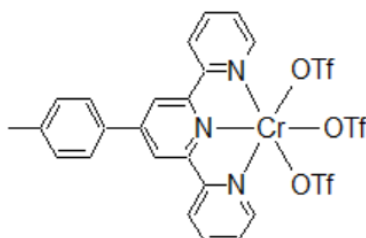

[Cr(ttpy)(ttpy-PO₃H₂)](PF₆)₃ ([Cr1P]³⁺). The complex has been synthesized following reported procedures.[2,3] Precursors **[Cr(ttpy)(OTf)₃]** (25 mg, 0.029 mmol) and **ttpy-PO₃H₂** (10.5 mg, 0.027 mmol) were dissolved in 8 mL degassed MeCN plus 8 mL degassed DMSO and the brown solution was stirred at 80 ⁰C under an Ar atmosphere for 48 h. The solution was cooled to RT and an excess amount of KPF₆ in water added. No obvious precipitate was formed, so the solution was filtered to remove any insoluble impurities prior to be used for grafting [Cr1P]³⁺ onto ITO electrodes or TiO₂ NPs.

¹H NMR cannot be done because the product is paramagnetic. **Electrochemistry:** CVs cannot be done directly due to the poor background signal of DMSO. Instead, the redox

potentials of $[Cr1P]^{3+}$ were studied by grafting it on a ITO electrode and used it as WE: $E_{1/2}$ (V) = -0.44, -0.81, -1.34. (WE: area = 1.2 cm^2, RE = Ag/AgNO$_3$ 0.01 M, electrolyte = MeCN + 0.1 M TBAPF$_6$, v = 100 mV.s^{-1}).
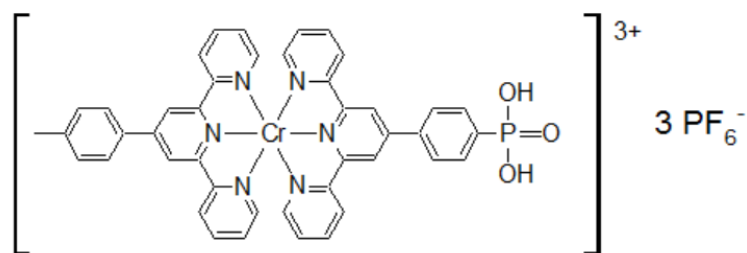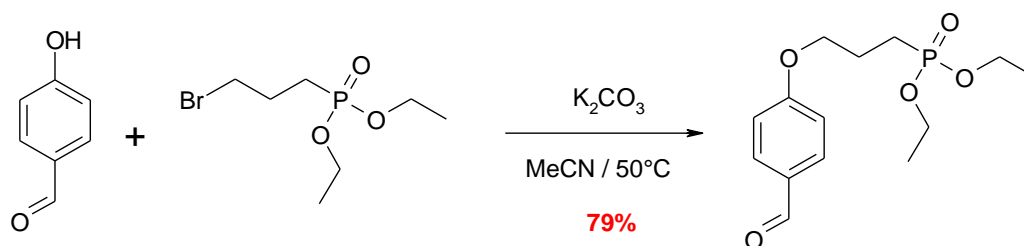

**ttpy-(CH₂)₃-PO₃H₂.**
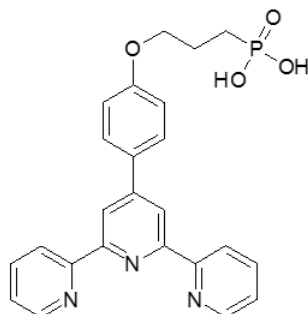
The synthesis requires three consecutive steps as follows:

(i)   Step 1: Synthesis of [3-(4-formyl-phenoxy)-propyl]-phosphonic acid diethyl ester:

4-hydroxybenzaldehyde (200 mg, 1.637 mmol) was dissolved in 5 mL of acetonitrile before addition of K₂CO₃ (340 mg, 2.457 mmol, 1.5 equiv) and diethyl(3-bromopropyl)phosphonate (0.35 mL, 1.802 mmol, 1.1 equiv). The reaction was heated at 50°C overnight. After cooling to RT, 50 mL of water were added and the solution was extracted with 50 mL of CH₂Cl₂ (3 times). The organic layer was washed with brine before being dried with MgSO₄. After filtration and evaporation, the crude was purified by chromatography on silica gel with ethyl acetate as eluent to give 389 mg (1.295 mmol) of the pure compound as a white solid with 79 % yield.

¹H NMR (300 MHz, CDCl₃): δ (ppm) = 9.85 (s, 1H), 7.80 (d, *J* = 8.7 Hz, 2H), 6.96 (d, *J* = 8.7 Hz, 2H), 4.10 (m, 6H), 2.18-1.86 (m, 4H), 1.30 (t, *J* = 7.0 Hz, 6H). **¹³C NMR** (75 MHz, CDCl₃): δ (ppm) = 190.8, 163.9, 132.1, 130.1, 114.8, 67.9, 67.7, 61.8, 61.7, 23,3, 22.6, 21.4, 16.6, 16.5. **³¹P NMR** (121 MHz, CDCl₃): δ (ppm) = 31.2. **MS-APCI**: *m/z* = 301 [M+H]⁺

(ii) Step 2: Synthesis of [3-(4-[2,2';6',2'']-terpyridin-4'-yl-phenoxy)-propyl]-phosphonic acid diethyl ester
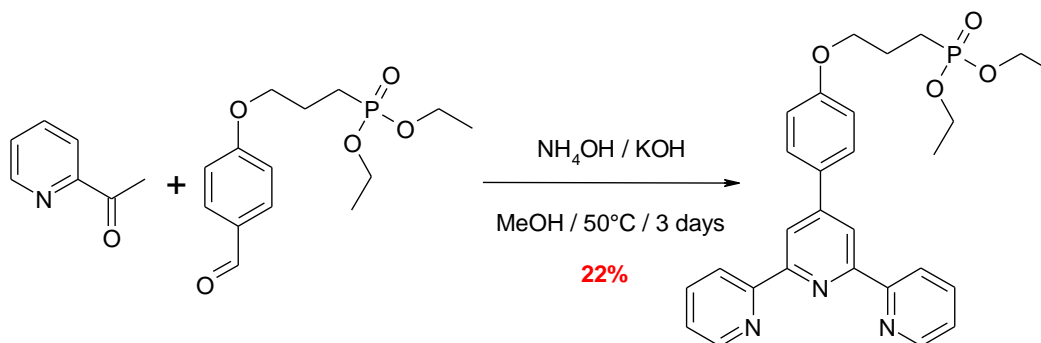
The aldehyde (558 mg, 1.858 mmol) was dissolved in 12 mL of methanol before addition of 2-acetylpyridine (0.42 mL, 3.1716 mmol, 2 equiv), KOH (208 mg, 3.1716 mmol, 2 equiv) and 12 mL of NH₄OH (30%). The reaction was heated at 50 °C during 3 days. After cooling to RT, the solvent was evaporated and the crude was purified by chromatography on silica gel. The elution started with AcOEt and went on with MeOH 2%, 5% before finishing with a mixture of AcOEt/MeOH/Et₃N (94/5/1). The crude compound was dissolved in EtOH and precipitated with addition of water. After filtration, the compound was recrystallized twice with a mixture of AcOEt/Cyclohexane to give 209 mg (0.415 mmol) of a white powder with a 22 % yield.

¹H NMR (400 MHz, CDCl₃): δ (ppm) = 8.75-8.73 (m, 4H), 8.68 (d, *J* = 8.0 Hz, 2H), 7.92-7.88 (m, 4H), 7.38-7.35 (m, 2H), 7.02 (d, *J* = 8.5 Hz, 2H), 4.17-4.09 (m, 6H), 2.19-2.09 (m, 2H), 2.02-1.94 (m, 2H), 1.34 (t, *J* = 7.0 Hz, 6H). **¹³C NMR** (100 MHz, CDCl₃): δ (ppm) = 159.9, 156.3, 155.7, 150.0, 149.0, 137.4, 130.9, 128.8, 124.0, 121.7, 118.7, 115.1, 67.7, 67.6, 61.8, 61.7, 23.2, 22.9, 21.8, 16.7, 16.6. **³¹P NMR** (162 MHz, CDCl₃): δ (ppm) = 31.6. **MS-APCI**: *m/z* = 504 [M+H]⁺

*(iii) Step 3: Synthesis of [3-(4-[2,2';6',2'']-terpyridin-4'-yl-phenoxy)-propyl]-phosphonic acid*
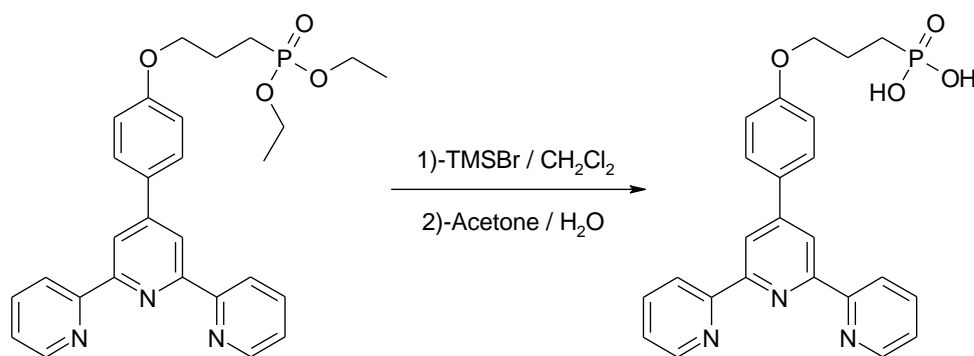
To a solution of bromotrimethylsilane (TMSBr, 0.315 mL, 2.383 mmol, 10 equiv) in 5 mL of anhydrous CH_2Cl_2 under inert atmosphere, 120 mg of the phosphonic ester dissolved in 5 mL of CH_2Cl_2 was added dropwise in 5 minutes at RT. After two hours of reaction, 1 mL of a mixture acetone/water (1/1) was added. After one more hour, the solvent was evaporated and the crude was triturated in 20 mL of hot ethanol. After cooling to RT, the compound was filtrated and dried. A yellow powder was obtained (126 mg). The yield cannot be determined because of the unknown amount of HBr in the molecule.

^{1}H NMR (400 MHz, [D$_6$]DMSO): δ (ppm) = 9.02 (d, J = 8.0 Hz, 2H), 8.94 (d, J = 4.8 Hz, 2H), 8.86 (s, 2H), 8.44-8.40 (m, 2H), 8.05 (d, J = 8.7 Hz, 2H), 7.87-7.84 (m, 2H), 7.19 (d, J = 8.8 Hz, 2H), 4.16 (t, J = 6.3 Hz, 2H), 2.02-1.92 (m, 2H), 1.76-1.68 (m, 2H). **^{13}C NMR** (100 MHz, [D$_6$]DMSO): δ (ppm) = 160.2, 152.1, 151.2, 150.1, 146.7, 141.6, 128.6, 128.2, 126.0, 123.0, 119.2, 115.2, 67.8, 67.6, 24.6, 23.2, 22.8. **^{31}P NMR** (162 MHz, [D$_6$]DMSO): δ (ppm) = 25.9. **MS-MALDITOF**: *m/z* = 448 [M+H]$^+$

dmbpy-pyr. The synthesis of this ligand consists of two steps. In the first step, a lithium diisopropylamine (LDA) was prepared by dissolving diisopropylamine (DIPA, 630 μl, 4.07 mmol) in 5 mL THF under Ar. The solution was cooled to -20 ^{0}C, stirred for 30 minutes before slowly adding *n*-butyllithium solution (2.5 M in hexane, 1.85 mL, 4.07 mmol). The LDA solution was kept stirring for one hour. In another oven-dried flask, a solution of 4,4'-dimethyl-2,2'-dipyridine (dmbpy, 500 mg, 2.714 mmol) in 20 mL dried THF was prepared under Ar and cooled to -70 ^{0}C. The LDA solution was added dropwise to the dmbpy solution at -70 ^{0}C, and the mixture was stirred for 1 hour. In the second step, 1-(10-bromodecyl)pyrrole (Br-pyr, 776 mg, 2.714 mmol) was added to the mixture, then the temperature was slowly raised to RT overnight. The reaction was stopped by adding water, then extracting with CH_2Cl_2 (x3), dried under vacuum, and the product was separated by chromatography (CH_2Cl_2/Ethyl acetate, 98/2 v/v) to yield a white powder (270 mg, 26 %).

¹H NMR (400 MHz, CDCl₃): δ (ppm) = 8.57 (t, *J* = 4.0 Hz, 2H), 8.28 (s, 2H), 7.17 (d, *J* = 8.0 Hz, 2H), 6.64 (d, *J* = 4.0 Hz, 2H), 6.13 (d, *J* = 4.0 Hz, 2H), 3.85 (t, *J* = 7.9 Hz, 2H), 2.70 (t, *J* = 8.0 Hz, 2H), 2.46 (s, 3H), 1.73 (m, 4H), 1.25 (m, 14H).
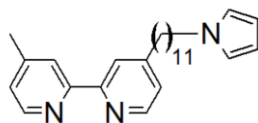
[Ru(dmbpy-pyr)₂]Cl₂. To an oven-dried round-bottom flask was added RuCl₃.3H₂O (56 mg, 214 μmol) and dried DMF (5 mL). The mixture was stirred and heated to 110 ⁰C, then the **bpy-pyr** ligand (167 mg, 429 μmol, 2 equiv) was added. It was refluxed for 3 hours. After that, it was cooled to RT, then added 30 mL diethyl ether leading to the precipitation of the product. The solid was subsequently filtered, rinsed with 50 mL acetone/diethyl ether (1/4, v/v) to yield a dark purple solid (120 mg, yield: 59 %).

¹H NMR: similar to the dmbpy-pyr ligand. **Electrochemistry** (in CH₂Cl₂ + 0.1 M TBAPF₆, WE = C disk, *v* = 20 mV.s⁻¹): $E_{1/2}$ = 1.2 V (irreversible), 0.03 V, -1.55 V, -1.86 V. **ESI-MS**: *m/z* = 986 [M-Cl]⁻
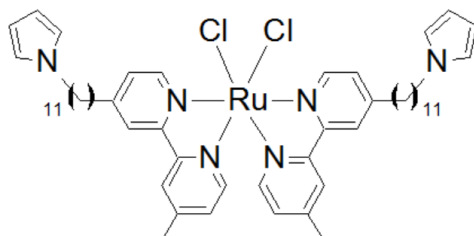
***fac*-[Mn(ttpy)(CO)₃Br]**. The complex has been synthesized according to literature.[4] In a typical experiment, [Mn(CO)₅Br] (200 mg, 0.73 mmol) and 4'-(4-methylphenyl)terpyridine (ttpy, 120 mg, 0.37 mmol) were dissolved in 30 mL diethyl ether. The resulting solution was refluxed for 3 h, and allowed to cool down to RT before the orange solid was filtered. Excess [Mn(CO)₅Br] precursor was eliminated by stirring the solid in 50 mL diethyl ether for 30 mins, then the remaining solid was filtered and washed with diethyl ether. The solid product was dried under vacuum for 2 h, yielding a pale yellow powder (170 mg, 85 %).

¹H NMR (400 MHz, [D₆]DMSO): δ (ppm) = 9.25 (d, *J* = 5.1 Hz, 1H), 9.00 (m, 2H), 8.80 (d, *J* = 4.8 Hz, 1H), 8.29 (m, 1H), 8.09 (m, 4H), 7.96 (m, 1H), 7.75 (m, 1H), 7.65 (m, 1H), 7.42

(d, J = 8.4 Hz, 2H), 2.50 (s, 3H). **FT-IR** (KBr pellet, C=O stretching): ν (cm^{-1}) = 2022, 1948, 1916.
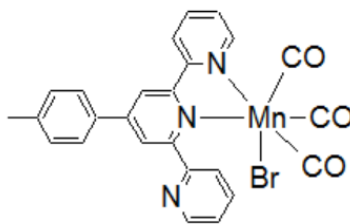


3.3. *Nanoparticles and their surface modifications*

SiO₂ nanoparticles. The ultrasound-assisted synthesis of SiO₂ NPs follows the Stober's method[5] with some modifications[6]. To a mixture of 50 mL ethanol and water was added 4 mL tetraethyl orthosilicate (TEOS), then sonicated for 2 h. Ammonia was added to the mixture at different feed rates to achieve >100 nm NPs (dropwise) or <10 nm NPs (0.05 mL.min^{-1}). A milky gel was formed after 5 hours of sonication. It was separated from the solution by centrifugation, washed with ethanol, dried in an oven at 80 ^{0}C overnight and calcined at 250 ^{0}C for 2 hours to yield a white powder.

TiO₂ nanoparticles. The synthesis of anatase TiO₂ NPs follows a modified sol-gel process.[7] To a flask containing 50 mL pure ethanol was dropwise added 6 mL (0.02 mol) titanium isopropoxide (TTIP), then the mixture was vigorously stirred for 30 minutes to obtain a milky solution. A solution of 2 mL H₂O/HCl (3/1, v/v) was added dropwise to the TTIP mixture. After 2 hours the solution became clear, and allowed for peptization by refluxing it at 70 ^{0}C for 24 hours, followed by aging at RT overnight. The nanoparticles were then separated and washed in pure ethanol by centrifugation (1 hour, 5000 rpm). They were subsequently dried in an oven at 80 ^{0}C overnight and calcined at 450 ^{0}C for 2 hours to yield a white powder (276 mg).

Titania NPs with a mixed anatase – rutile (80% - 20%) phase were achieved by calcination of the anatase TiO₂ NPs at 700 ^{0}C instead of 450 ^{0}C for 2 hours.

TiO₂/Ru^{II} and SiO₂/Ru^{II}. In a typical experiment, a suspension of the TiO₂ NPs (anatase, 50 mg) or SiO₂ (d < 20 nm, 50 mg) in ethanol/acetone (8/2, v/v) was sonicated for 20 minutes. Subsequently, the **[RuP]$^{2+}$** complex (14.2 mg, 14 μmol) was added to the suspension, and the

mixed solvent was also added to a total volume of 25 mL. The mixture was vigorously stirred in 60 hours. The dye-sensitized NPs were excessively washed and separated by centrifugation (4000 rpm, 45 minutes), then dried in an oven overnight to yield an orange fine powder (~46 mg). The loading on the sol-gel synthesized NPs is 0.19 mmol.g^{-1} (TiO$_2$/Ru^{II}) and 0.02 mmol.g^{-1} (SiO$_2$/Ru^{II}). The Ru loading on commercially available NPs is estimated to be 0.21 mmol.g^{-1} (TiO$_2$/Ru^{II}) and 0.076 mmol.g^{-1} (SiO$_2$/Ru^{II}). For the commercially available anatase TiO$_2$ NPs, assuming they are all spherical with diameter of 25 nm and bulk density of 3.9 g.cm^{-3}, one can roughly estimate the Ru^{II} loading to be 4000 Ru^{II} molecules per particle or 2 Ru^{II} molecules per nm^2. Similar estimation for Ru loading on commercially available SiO$_2$ NPs, taken into account the diameter of 20 nm and density of 2.4 g.cm^{-3}, gives 460 Ru^{II} molecules per particle or 0.5 Ru^{II} molecules per nm^2. **Electrochemistry** (in MeCN + 0.1 M TBAPF$_6$, WE = Pt microcavity electrode, v = 100 mV.s^{-1}): $E_{1/2}$ = 0.92 V (SiO$_2$/Ru^{II}) or 0.98 V (TiO$_2$/Ru^{II}).
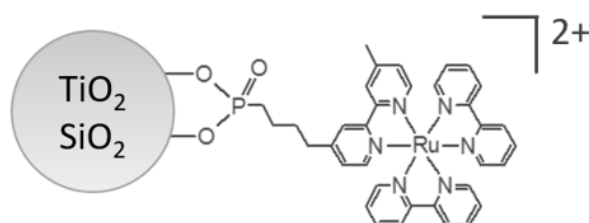

TiO$_2$/[Cr2P]$^{3+}$. A suspension of TiO$_2$ (anatase, 50 mg) in 25 mL DMF/DMSO (8/2, v/v) solution containing **[Cr2P]$^{3+}$** (17 mg, 15 μmol) was sonicated for 20 minutes. The mixture was then stirred vigorously for 60 hours in dark. Afterwards, the NPs were separated by centrifugation, washed in DMF/DMSO, DMF and ethanol, respectively, and dried in an oven overnight to yield a light purple powder (58.3 mg). The loading of [Cr2P]$^{3+}$ is estimated to be ~0.20 mmol.g^{-1} (about 3800 Cr^{III} molecules per particle or 2 Cr^{III} molecules per nm^2).
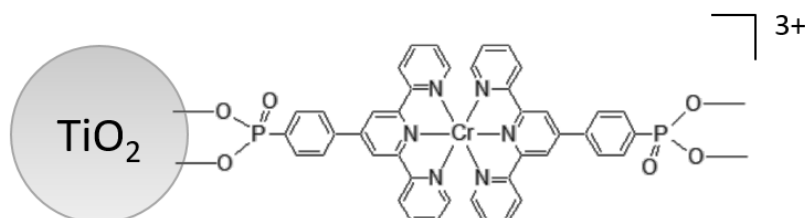
C$_6$H$_5$-CH$_2$-PO$_3$H$_2$/TiO$_2$/[Cr2P]$^{3+}$ (C$_6$H$_5$-CH$_2$-PO$_3$H$_2$ = benzylphosphonic acid, BPA). Similar to the case of **TiO$_2$/[Cr2P]$^{3+}$**, but a mixture of **[Cr2P]$^{3+}$** and BPA was used instead of

only $[Cr2P]^{3+}$. In a typical experiment for 10% spacer + 90% $[Cr2P]^{3+}$, a mixture of BPA (1.35 μmol) and $[Cr2P]^{3+}$ (1.5 μmol) in 25 mL DMF/DMSO (8/2 v/v) solution was used to graft onto anatase TiO_2 NPs (50 mg), yielding 54.3 mg product. The loading of $[Cr2P]^{3+}$ on TiO_2 is estimated to be 0.03 mmol.g^{-1} (about 570 Cr^{III} molecules per particle or 0.3 Cr^{III} molecules per nm^2).

$Ru^{2+}/TiO_2/[Cr2P]^{3+}$ (Ru:Cr = 1:1). A suspension of TiO_2 (anatase, 50 mg) in DMF/DMSO (8/2, v/v) solvent and a mixture of **$[Cr2P]^{3+}$** (5.7 mg, 5 μmol) and **$[RuP]^{2+}$** (5.1 mg, 5 μmol) in the same solvent were sonicated for 20 minutes. They were then mixed together and stirred vigorously for 60 hours in dark. Afterwards, the NPs were separated by centrifugation, washed in DMF/DMSO, DMF and ethanol, respectively, and dried in an oven overnight to yield an orange powder (54.7 mg). Both complexes are expected to be grafted quantitatively. The loadings of $[Cr2P]^{3+}$ and $[Ru-PO_3H_2]^{2+}$ are estimated to be 0.10 mmol.g^{-1} (about 1600 molecules per particle or 1 molecule per nm^2).
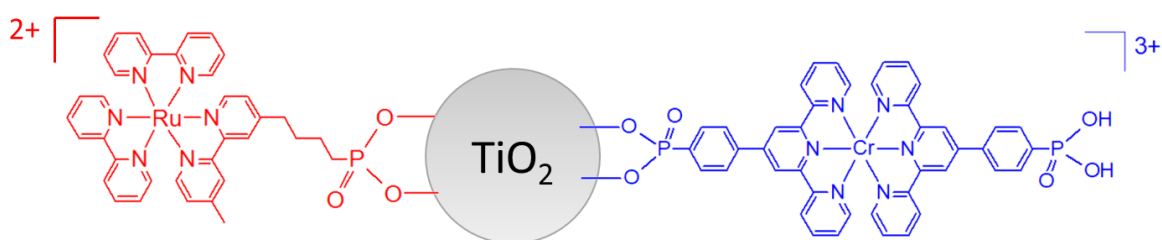
$Ru^{2+}/TiO_2/[Cr2P]^{3+}$ and BPA spacers. Similar to the $Ru^{2+}/TiO_2/[Cr2P]^{3+}$ triad but the $[Cr2P]^{3+}$ content was reduced. In a typical experiment for 20 % Ru, 2 % Cr and 78 % spacer, we used a mixture as follows: TiO_2 (50 mg), $[Cr2P]^{3+}$ (0.3 mg, 0.3 μmol), $[Ru-PO_3H_2]^{2+}$ (3.0 mg, 3 μmol) and BPA (2.1 mg, 11.7 μmol).

TiO₂/Mnᴵ (Mnᴵ = [Mnᴵ(ttpy-(CH₂)₃-PO₃H₂)(CO)₃Br]). It has been synthesized following a two-step procedure. First, the **ttpy-(CH₂)₃-PO₃H₂** ligand (4.5 mg, 10 µmol) and TiO₂ anatase NPs (50 mg) were solubilized in 25 mL DMSO. The mixture was stirred at RT for 20 h in dark. Afterwards, the modified NPs were separated by centrifugation and washed multiple times with DMSO and acetone to remove unadsorbed ligands. In the second step, the NPs were mixed with Mn(CO)₅Br (2.8 mg, 10 µmol) in 25 mL acetone and refluxed at 45 ^{0}C for 3 h in dark. Finally, the TiO₂/Mnᴵ NPs were centrifuged and washed thoroughly with acetone prior to be dried under vacuum to yield a pale yellow powder (40.7 mg). Loading of Mnᴵ on TiO₂ is estimated to be ~0.20 mmol.g^{-1} (about 3800 Mnᴵ molecules per particle or 2 Mnᴵ molecules per nm²). **FT-IR** (KBr pellet, C=O stretching): ν (cm^{-1}) = 2022, 1900-1950 (broad).
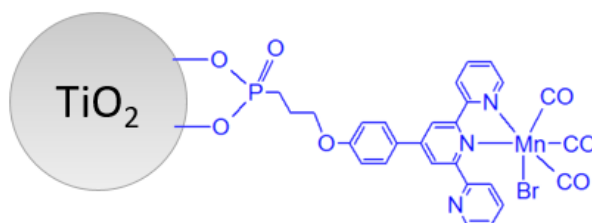

Ruᴵᴵ/TiO₂/Mnᴵ (Ruᴵᴵ = [Ru-PO₃H₂]²⁺ and Mnᴵ = [Mnᴵ(ttpy-(CH₂)₃-PO₃H₂)(CO)₃Br], Mn:Ru = 1:10). It has been synthesized by stepwise grafting the Mn and Ru complexes on TiO₂ anatase NPs (50 mg), respectively. The grafting procedure for Mnᴵ is similar to that described for TiO₂/Mnᴵ NPs in the above paragraph, except that the contents of **ttpy-(CH₂)₃-PO₃H₂** and Mn(CO)₅Br have been reduced to 0.7 µmol (ie. 0.31 mg for ttpy-(CH₂)₃-PO₃H₂ and 0.19 mg for Mn(CO)₅Br). After being washed thoroughly with acetone and dried under vacuum, the TiO₂/Mnᴵ NPs were mixed with **[RuP]²⁺** (7.1 mg, 7 µmol) in 25 mL H₂O. The mixture was stirred at RT for 20 h in dark. Afterwards, the modified NPs were separated by centrifugation and washed thoroughly with water, then acetone to remove water from the particles. Finally, the acetone solvent was evaporated to yield a pale orange powder (23.6 mg).
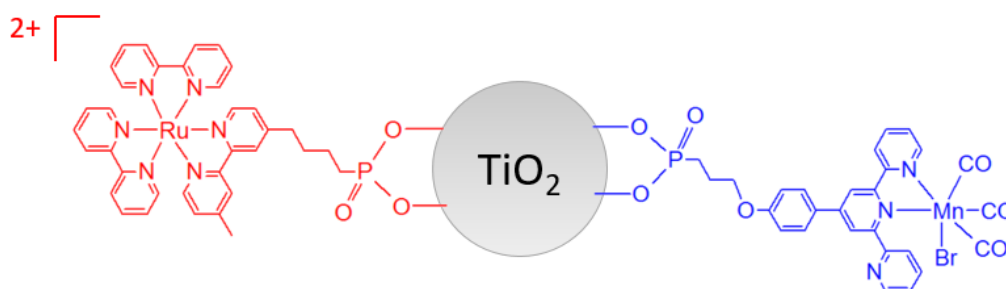
TiO₂/[Ru-pyr]²⁺. This modification of anatase TiO_2 NPs requires two steps. In the first step, a suspension of the NPs (50 mg) in distilled water was sonicated for 20 minutes, before addition of **bpy-PO₃H₂** (38 μmol, 11.7 mg) and water to make a total volume of 25 mL. The mixture was vigorously stirred at RT overnight to functionalize the surface with bpy ligands. The NPs were then excessively washed with water and separated by centrifugation (4000 rpm, 45 minutes) until the solution turns from acidic to neutral pH, and no bpy-PO_3H_2 was spectroscopically detected from the supernatant solution. The particles were then washed two times with ethanol prior to their complexation. In the second step, a suspension of **TiO₂/bpy** NPs in ethanol/acetone (8/2, v/v) was sonicated for 20 minutes, before the addition of **[Ru(dmbpy-pyr)₂]Cl₂** (15.3 μmol, 14.6 mg) and the mixed solvent to a total volume of 25 mL. The mixture was refluxed for 60 hours. The TiO₂/[Ru-pyr]²⁺ NPs were washed in ethanol/acetone and ethanol excessively, separated by centrifugation (4000 rpm, 45 minutes) and dried in an oven overnight to yield a dark red powder (44.4 mg). Loading of [Ru-pyr]²⁺ is estimated to be ~0.20 mmol.g⁻¹ (about 3800 molecules per particle or 2 molecules per nm²). **Electrochemistry** (in MeCN + 0.1 M TBAPF₆, WE = Pt microcavity electrode, v = 100 mV.s⁻¹): $E_{1/2}$ = 0.82 V (irreversible).
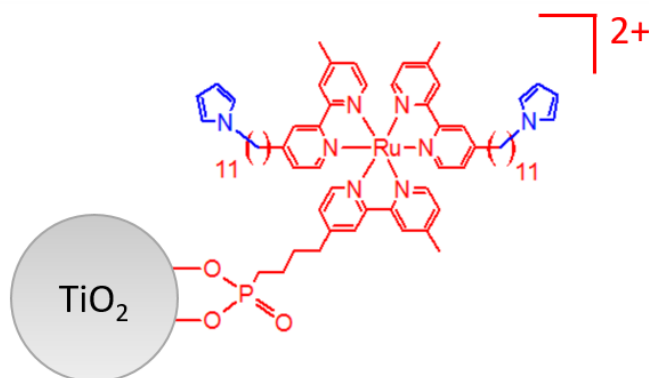
References

1   J. V Caspar and T. J. Meyer, *J. Am. Chem. Soc.*, 1983, **105**, 5583–5590.

2   R. Farran, "Transfert d'électron photoinduit au sein d'assemblages hétérométalliques associant le [Ru(bpy)$_3$]$^{2+}$ à des complexes bisterpyridine du Fe(II), Co(III) et Cr(III)", *PhD Dissertation,* Université Grenoble-Alpes, 2015.

3   E. C. Constable, C. E. Housecroft, M. Neuburger, J. Schönle and J. A. Zampese, *Dalt. Trans.*, 2014, **43**, 7227–7235.

4   J.-D. Compain, M. Stanbury, M. Trejo and S. Chardon-Noblat, *Eur. J. Inorg. Chem.*, 2015, 5757–5766.

5   W. Stober and A. Fink, *J. Colloid Interface Sci.*, 1968, **26**, 62–69.

6   I. A. Rahman, P. Vejayakumaran, C. S. Sipaut, J. Ismail, M. A. Bakar, R. Adnan and C. K. Chee, *Colloids Surfaces A Physicochem. Eng. Asp.*, 2007, **294**, 102–110.

7   X. Chen and S. S. Mao, *Chem. Rev.*, 2007, **107**, 2891–2959.

TiO$_2$/[Ru(bpy)$_3$]$^{2+}$ based hybrid nanomaterials associated with [Cr(ttpy)$_2$]$^{3+}$ or [Mn(ttpy)(CO)$_3$Br] or a pyrrole moiety: Synthesis, spectroscopic studies and applications in solar energy conversion

Résumé: Ce mémoire vise à montrer l'intérêt de nanoparticules (NPs) de TiO$_2$ comme plateforme pour immobiliser dans un environnement proche des complexes de coordination pouvant interagir par transfert d'électron photoinduit. Nous nous sommes intéressés à l'étude de nanomatériaux hybrides associant le complexe [Ru(bpy)$_3$]$^{2+}$ (bpy = 2,2'-bipyridine) comme photosensibilisateur aux complexes [Cr(ttpy)$_2$]$^{3+}$ ou [Mn(ttpy)(CO)$_3$Br] (ttpy = 4'-(p-tolyl)-2,2':6',2"-terpyridine) comme accepteurs d'électrons. Pour immobiliser les différents complexes à la surface du TiO$_2$, une fonction acide phosphonique a été introduite sur une des bipyridines du centre [Ru(bpy)$_3$]$^{2+}$ et sur la terpyridine des complexes [Cr(ttpy)$_2$]$^{3+}$. L'étude des processus de transferts de charges photo-induits sous irradiation en lumière visible sur le colloïde TiO$_2$/Ru^{II} montre que l'état à charges séparées (e⁻)TiO$_2$/Ru^{III} possède une longue durée de vie, ce qui rend possible l'utilisation des charges dans des réactions successives d'oxydation ou de réduction. Notamment l'irradiation du colloïde TiO$_2$/Ru^{II} en présence de [Cr(ttpy)$_2$]$^{3+}$ et de triéthanolamine (TEOA) comme donneur d'électron sacrificiel permet la réduction à deux électrons du [Cr(ttpy)$_2$]$^{3+}$. Par la suite, le complexe [Cr(ttpy)$_2$]$^{3+}$ est immobilisé sur les NPs de TiO$_2$/Ru^{II} pour former un assemblage Ru^{II}/TiO$_2$/Cr^{III} au sein duquel les processus de transfert d'électrons photo-induits sont étudiés. De manière à proposer un système pour la réduction photocatalytique du CO$_2$, le complexe [Mn(ttpy)(CO)$_3$Br] a été co-immobilisé avec le [Ru(bpy)$_3$]$^{2+}$ suivant une approche de chimie sur surface pour former le colloïde Ru^{II}/TiO$_2$/Mn^{I}. Ce système présente une excellente sélectivité vis-à-vis du HCOOH comme seul produit de la photoréduction du CO$_2$ en présence de 1-benzyl-1,4-dihydronicotinamide (BNAH) comme donneur d'électron sacrificiel. Un système hybride associant le [Ru(bpy)$_3$]$^{2+}$ portant des fonctions pyrroles et immobilisé sur TiO$_2$ a également été synthétisé et étudié. Sous irradiation lumineuse, le transfert de charge (e⁻)TiO$_2$/[Ru-pyr]$^{3+}$ permet d'induire la polymérisation du pyrrole. Le nanocomposite TiO$_2$/poly(Ru-pyr) obtenu et déposé sur une électrode génère, en présence de TEOA, un photocourant anodique stable de plus de 10 µA.cm^{-2}. L'ensemble des résultats montre que les NPs de TiO$_2$ peuvent être un moyen d'assembler des complexes dans un environnement proche en limitant les interactions à l'état fondamental, mais permettant des transferts d'électron photoinduits entre eux. Suivant les potentiels redox des différents composants, les transferts d'électron ont lieu soit via la nanoparticule soit en surface de celle-ci.

Abstract: This thesis aims to investigate the possibility of using TiO$_2$ nanoparticles (NPs) as a platform to immobilize proximal coordination complexes that can interact with each other by photoinduced electron transfer. We have studied hybrid nanomaterials combining [Ru(bpy)$_3$]$^{2+}$ (bpy = 2,2'-bipyridine) as a photosensitizer and [Cr(ttpy)$_2$]$^{3+}$ or [Mn(ttpy)(CO)$_3$Br] (ttpy = 4'-(p-tolyl)-2,2':6',2"-terpyridine) as electron acceptors. To immobilize the various complexes on the surface of TiO$_2$, a phosphonic acid functional group was introduced on one of the bipyridines of the [Ru(bpy)$_3$]$^{2+}$ center and on the terpyridines of the [Cr(ttpy)$_2$]$^{3+}$ complex. Under visible light, the TiO$_2$/Ru^{II} colloid undergoes a photo-induced charge transfer process leading to a long-lived charge separation state (e⁻)TiO$_2$/Ru^{III}, which makes it possible to be engaged in successive oxidation or reduction reactions. In particular, the visible irradiation of the TiO$_2$/Ru^{II} colloid in the presence of [Cr(ttpy)$_2$]$^{3+}$ and triethanolamine (TEOA) as a sacrificial electron donor allows the two-electron reduction of [Cr(ttpy)$_2$]$^{3+}$. Subsequently, the [Cr(ttpy)$_2$]$^{3+}$ complex has been immobilized on the TiO$_2$/Ru^{II} NPs to form a Ru^{II}/TiO$_2$/Cr^{III} assembly in which the photoinduced electron transfer processes were investigated. In order to propose a system for the photocatalytic reduction of CO$_2$, the [Mn(ttpy)(CO)$_3$Br] and [Ru(bpy)$_3$]$^{2+}$ complexes were co-immobilized on TiO$_2$ NPs following a chemistry on surface approach to form a Ru^{II}/TiO$_2$/Mn^{I} triad. Under irradiation at 470 nm, this system exhibits excellent selectivity towards HCOOH as the only product of CO$_2$ photoreduction in DMF/TEOA solvent mixture, in the presence of 1-benzyl-1,4-dihydronicotinamide (BNAH) as a sacrificial electron donor. Another hybrid system linking a [Ru(bpy)$_3$]$^{2+}$ unit to two pyrrole functions and being immobilized on TiO$_2$ has also been synthesized and studied. Under visible light, the transient (e⁻)TiO$_2$/[Ru-pyr]$^{3+}$ species induce the polymerization of pyrrole to form a TiO$_2$/poly(Ru-pyr) nanocomposite. The nanocomposite deposited on an electrode generates, in the presence of TEOA, a stable anodic photocurrent of more than 10 µA.cm^{-2}. All the results show that TiO$_2$ NPs can be used to associate different complexes in a close environment by limiting the interactions in the ground state but allow photoinduced electron transfer processes between them. Depending on the redox potentials of the different components, the electron transfer takes place either through the semiconducting NPs or on the surface.